University of Ferrara

Physics and Earth Science Department

Ph.D. in Physics

Nano-structured Germanium anodes for Lithium-ion batteries

Candidate
Alfredo Andreoli

Supervisor
Prof. Donato Vincenzi

Co-supervisor
Ph.D. Silvio Fugattini

Ph.D. Coordinator
Prof. Eleonora Luppi

XXXIII Cycle – 2017/2021
FIS/01

Per aspera ad astra

Abstract

Lithium-Ion Batteries represent the leading technology of the nowadays energy storage systems and are expected to play a fundamental role in the transition towards a green and sustainable economy. Nevertheless, the current commercial devices are close to meet their theoretical limits, thereby new materials with higher capacity, energy density and superior rate capability, are required.

Among the various possibilities, germanium is regarded with particular interest to replace the actual standard for the negative electrode, which is graphite, as it shows a higher theoretical capacity and promising electrochemical properties that could make it suitable for fast charge and discharge applications. The major drawback hindering the direct exploitation of this material is represented by a huge volumetric expansion through the charge and discharge processes, leading to the pulverization of bulk materials within few cycles. A possible solution to overcome this issue is to nano-structure the semiconductor material down to a size in which it becomes compliant to the volumetric variations.

In this thesis work, two processes to realize efficient and reliable germanium-based nano-structured anodes for high capacity and superior rate capability Lithium-Ion Batteries are presented, accompanied by a thoroughly physical and electrochemical characterization of the electrodes.

The fabrication processes make use of standard techniques that are already widely employed in the industry of semiconductors that are not typically exploited by the battery industry. In this process a thin germanium film is realized first, by means of a Low Energy Plasma Enhanced Chemical Vapor Deposition and is subsequently nano-structured recurring to one out of two techniques, represented by Hydrofluoric acid Electrochemical Etching and Ion Implantation. The electrodes realized do not require any binder, conductive agent, or seed layer, that is important to enhance the overall gravimetric capacity of the cells as well as simplifying the fabrication process. The details of the fabrication process, as well as a review of the experimental results in comparison with previous works, theoretical models, and the literature, are presented.

The extensive physical and electrochemical characterizations of the electrodes are deepened in specific chapters, where brief introductions of the techniques and methods used are also reported. The electrodes show very high capacities, well above that of graphite, which are retained for hundreds or even thousands of cycles. Remarkable retention at elevated rates is also observed, as well as a promising performance in a wide temperature range (-30 °C ÷ 60 °C). These interesting results are demonstrated to be completely ascribed to the nano-structured germanium, irrespective of the substrate materials, the nano-structuration technique, or the cell testing procedure used.

The nano-structured germanium anodes presented in this work are particularly appealing for aerospace applications, where highly reliable materials are required. Part of the activities here presented were carried out in the framework of a project financed by the Italian Space Agency and named “ANGELS”. The promising results observed since the first prototypes, led also to the filing of a patent family (original application IT201800006103A) on the fabrication process consisting in the deposition and the subsequent electrochemical dissolution.

Abstract (Italiano)

Le Batterie agli Ioni di Litio sono la tecnologia di punta tra i sistemi di accumulo dell'energia attuali e ci si aspetta che giocheranno un ruolo fondamentale nella transizione verso una economia verde e sostenibile. Tuttavia, la tecnologia odierna è vicina al raggiungimento dei propri limiti teorici e sono pertanto richiesti nuovi materiali con densità energetica superiore e una migliore risposta ad elevati ratei di carica e scarica.

Tra le varie possibilità, il germanio è particolarmente interessante per rimpiazzare il materiale attualmente utilizzato come standard negli anodi delle batterie, rappresentato dalla grafite. Il germanio ha infatti una capacità teorica superiore e promettenti performance elettrochimiche lo renderebbero particolarmente adatto per applicazioni di potenza. Il principale limite che ne impedisce lo sfruttamento diretto è rappresentato da una forte variazione volumetrica durante i cicli di carica e scarica, che porta alla polverizzazione del materiale massiccio nell'arco di pochi cicli. Una possibile soluzione per risolvere questo problema consiste nella nano-strutturazione del materiale, per creare strutture in grado di accomodare reversibilmente le deformazioni.

In questo lavoro di tesi si presentano due processi articolati in due fasi per la realizzazione di anodi nano-strutturati a base di germanio con capacità superiori e migliori performance ad elevati ratei di carica e scarica, presentando anche una approfondita campagna di caratterizzazioni fisiche ed elettrochimiche dei campioni realizzati.

I processi di fabbricazione in due fasi fanno ricorso a tecniche che rappresentano già degli standard nell'industria dei semiconduttori, ma che non sono ancora diffusi in quella delle batterie. In particolare, si tratta di approcci "top-down" nei quali si realizza in primis un film sottile di germanio ricorrendo a una deposizione chimica da fase vapore assistita da un plasma a bassa energia, per poi realizzare la nano-struttura ricorrendo a una delle due tecniche tra l'attacco elettrochimico con acido fluoridrico o l'impiantazione ionica. Gli elettrodi così prodotti non necessitano di additivi per incrementare l'adesione o la conducibilità, e non occorrono deposizioni preliminari per assisterne la crescita: questi costituiscono aspetti importanti per incrementare la capacità per unità di massa degli elettrodi oltre a semplificare i processi di fabbricazione. I dettagli dei processi di realizzazione degli elettrodi e una rassegna dei risultati sperimentali sono illustrati e confrontati con precedenti lavori, con modelli teorici e con la letteratura.

Le caratterizzazioni fisiche ed elettrochimiche effettuate sono presentate in appositi capitoli, fornendo brevi introduzioni delle tecniche e delle metodologie di analisi utilizzate. Gli elettrodi hanno dimostrato ottime capacità, superiori alla grafite, che vengono mantenute per centinaia o migliaia di cicli. L'elevata capacità degli elettrodi è mantenuta anche ad elevati ratei di carica e scarica ed in un ampio range di temperature. Inoltre, si dimostra che i promettenti risultati osservati sono ascrivibili esclusivamente al germanio nano-strutturato, e sono indipendenti dal materiale substrato, dalla tecnica di nano-strutturazione usata e dal particolare test elettrochimico effettuato.

Gli anodi presentati in questo lavoro risultano particolarmente promettenti per applicazioni aerospaziali. Parte delle attività presentate è stata svolta nell'ambito di un progetto finanziato dall'Agenzia Spaziale Italiana e denominato ANGELS. In virtù dei risultati ottenuti sin dai primi prototipi, il processo di realizzazione degli anodi tramite la deposizione e la successiva nano-strutturazione mediante dissoluzione anodica è stato protetto da una famiglia di brevetti, con capostipite il brevetto italiano IT201800006103A.

Table of Contents

List of Figures

List of Tables

1. Introduction

1.1. Motivation of the work and thesis outline

The climate changes and environmental pollution caused by human activities are posing serious concerns about the actual carbon-based economy and require urgent solutions. The reduction of the greenhouse gases, the transition toward renewable energy sources, and the development of a zero-emission mobility, represent crucial steps to mitigate the environmental issues and to permit a sustainable development. The availability of efficient and reliable energy storage system is a key aspect in the switch toward a carbon-free economy, in which lithium-ion batteries represent the leading technology. [1]
Although lithium-ion batteries show unparalleled capacity and energy density among the various electrochemical storage technologies, the current commercial devices are close to meet their theoretical limits. Thereby, new materials with higher capacity, energy density and superior rate capability, are required [2]. Many research efforts are focusing on new materials to replace the negative electrode as the actual standard, which is graphite, suffers for a poor maximum theoretical capacity and limited rate capability. Among the various possibilities, germanium is regarded with particular interest thanks to a theoretical capacity more than 4 times that of graphite, as well as a high lithium-ion diffusivity and good electronic conductivity, which could make it suitable for fast charge and discharge applications [3]. The major drawback hindering the exploitation of this material is represented by a huge volumetric expansion through the charge and discharge processes, leading to the pulverization of bulk materials within few cycles. A possible solution to overcome this issue is to nano-structure the semiconductor material down to a size in which it becomes compliant [4].

This thesis work inserts in this research context, with the aim to realize and characterize germanium-based nano-structured anodes for lithium-ion batteries with high capacity and superior rate capability, realized by means of standard techniques which are already widely used in the industry of semiconductors.
The fabrication process adopted in this work offers some advantages over the actual electrode materials and other research works, as it enables the production of electrodes that do not require any binder, conductive agent, or seed layer. These usually represent non-active materials that typically lower the overall gravimetric capacity of the electrodes [5],

thereby avoiding their use represents a strength of the process that is presented in this thesis.

The electrode production consists of two processes representing a top-down approach, which differentiate this work from the main research path represented by bottom-up solutions. Firstly, a thin germanium film is directly deposited onto the current collector substrate, by means of a low energy plasma enhanced chemical vapor deposition technique. This is followed by a nano-structuration step, represented by one out of two different techniques: the hydrofluoric acid electrochemical attack or the ion implantation. All the aspects of the fabrication processes are covered in this thesis, including a thorough review of their uniformity and the analysis and comparison with the theoretical models, previous works, or the literature.
The electrodes realized have been also completely characterized under the morphological, compositional, and structural point of views by means of independent and complementary techniques. Their electrochemical performances were also analysed, performing several tests, and the best results obtained so far are introduced and discussed.

In this Chapter, a general introduction regarding the state-of-the-art of the actual anodic and cathodic materials for lithium-ion batteries is presented. The focus is then placed on the most promising chemistries regarding the anode, with an in-depth analysis of germanium. A particular attention is posed on some of the key factors that affect the electrode performances, like the solid-electrolyte interphase and the effects of eventual binders or conducting agents. Some considerations on the future perspectives about the lithium-ion batteries and the germanium anodes are drawn in conclusion of the Chapter.

In Chapter 2, the details of the fabrication process are presented. The main features of the low energy plasma enhanced chemical vapor deposition technique are introduced and a review is performed about the uniformity of the films produced, in comparison with the results from previous works. Then, the hydrofluoric acid electrochemical etching, which is the first of the two nano-structuration techniques employed, is deepened. The most recent model of germanium dissolution in hydrofluoric acid is reported and the agreement of the etching data with the model is discussed. The second nano-structuration technique, namely ion implantation, is exposed afterwards, deepening its most important peculiarities and the rationale behind the choice of the implantation recipes.

Chapter 3 is dedicated to the morphological, compositional, and structural characterizations of the samples. Firstly, a very brief review of the techniques employed is presented. Afterwards, the experimental results are introduced and discussed, treating the relevant features of the substrate material, the as deposited samples, and the nano-structured ones.

In Chapter 4 the electrochemical characterization of the electrodes is presented. The instrumentation used and the analysis methods are treated first. Then, some of the preliminary results that lead us in the choice of the best etching recipe and in the definition of the standard electrolyte solution are presented. Some of the best results achieved so far are subsequently deepened, for both the kinds of the nano-structured electrodes. A particular attention is devoted to the electrochemical features of the lithiation and de-lithiation processes, which are interpreted according to the most reliable results from the literature. The analogies and differences observed in the various samples are deepened, for both the nano-structuration techniques, taking into account also the ageing and the current drawn in each specific case.

Finally, the main conclusion that can be drawn from this whole work are summarized in Chapter 5.

1.2. **Basics of batteries**

A battery is an energy storage device in which the chemical energy stored in its components is converted in electrical energy via redox reactions [6]. A battery consists of an assembly of single elements, called cells, which can be arranged in series or in parallel. Every cell usually constitutes a closed system and is composed by two electrodes, in contact with an electrolyte that is ionically conducting but electronically insulating. The chemical reactions occur within the electrodes and at their interphase with the electrolyte. The electrodes are divided by a separator that permits a selective migration of the chemical species contained in the electrolyte and prevents their direct contact. [7] A schematic representation of a battery is shown in Figure 1:

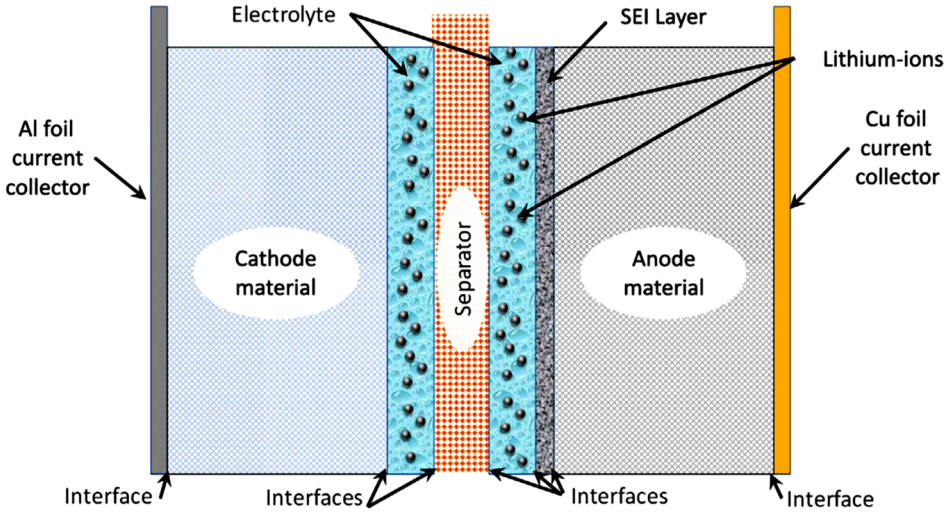

Figure 1: Schematic drawing of the battery elements. From ref. [4].

The driving force behind any chemical reaction is the variation of the Gibbs free energy of the species participating to the reaction [8]. For electrochemical reactions, this involves the transfer of charged species, which is exploited in batteries to produce electrical work by separating the ionic from the electronic transfer. The ions are transferred between the electrodes within the electrolyte, while electrons flux through an external circuit to reach the opposite electrode and sustain the reaction. For a generic reaction of the type:

$$(1) \quad (Oxidation)\ aA \leftrightarrow cC + ne^-$$

$$(2) \quad (Reduction)\ bB + ne^- \leftrightarrow dD$$

$$(3) \quad (Overall\ reaction)\ aA + bB \leftrightarrow cC + dD$$

The overall Gibbs free energy variation can be written as:

$$(4) \quad \Delta G = \sum \Delta G(products) - \sum \Delta G(reactants)$$

And recurring to the van't Hoff isotherm this relationship can be rewritten as [6]:

$$(5) \quad \Delta G = \Delta G^0 + RTln\left(\frac{a_C^c a_D^d}{a_A^a a_B^b}\right)$$

Where ΔG^0 represents the standard Gibbs free energy (at 25 °C and unit activity), R is the gas constant, T is the absolute temperature and a_x^y are the activities of the species involved. Under open circuit conditions, the chemical potential difference between the reactants guides the mobile ionic species within the electrolyte until the build-up of a balancing electrostatic field that opposes to further migration. Taking this into account for the previous generic reaction, the following energy balance can be expressed [9]:

$$(6) \quad \Delta G = -nFE$$

Where n is the total charge transferred, F is the Faraday constant, and E is the cell voltage that can be experimentally measured. The combination of this relation with to the previous equation (5) leads to the Nernst equation for the electrochemical reactions [10]:

$$(7) \quad E = E^0 - \frac{RT}{nF} ln \frac{a_C^c a_D^d}{a_A^a a_B^b}$$

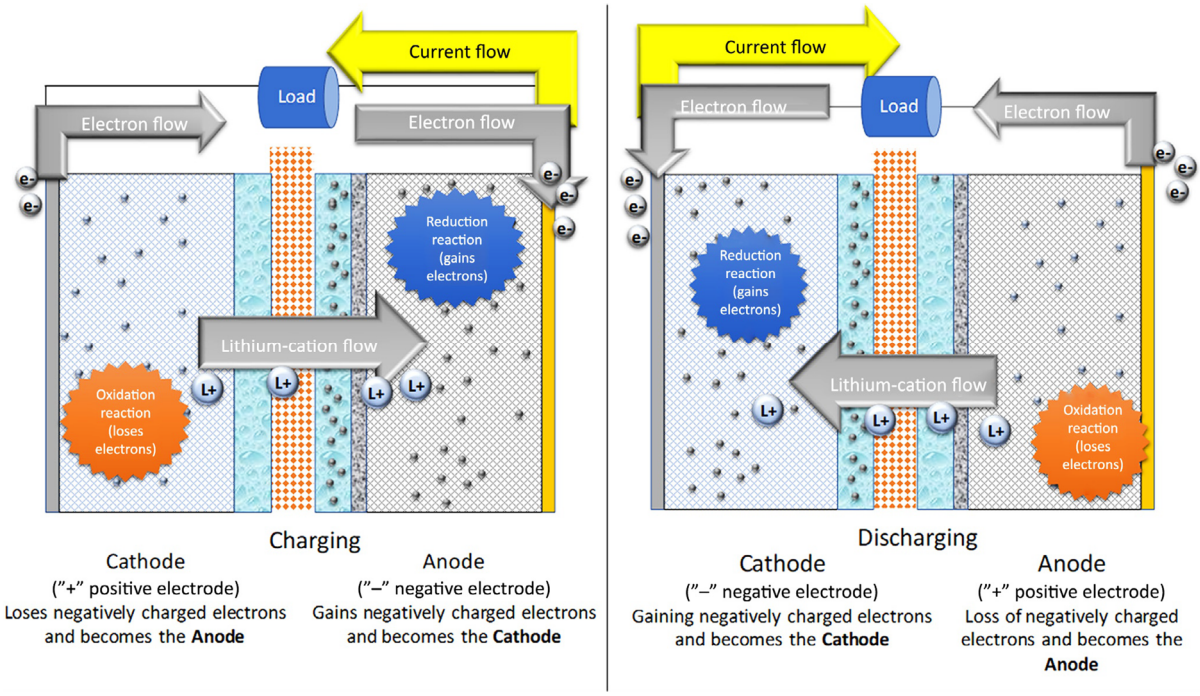

Figure 2: Schematic of the operating principle of a battery during forced recharge (A) and spontaneous discharge (B). The image is from ref. [4].

Conventionally, the electrodes are labelled according to the reactions taking place there: the anode is the electrode where oxidation occurs, while the cathode is the electrode in which reduction happens. For non-rechargeable batteries, these are defined once and are never exchanged. In rechargeable systems, instead, the role of the anode and the cathode switches between the charge and discharge phases. In fact, oxidation occurs at one electrode in one phase, while reduction takes place at the same electrode in the opposite phase.

During the discharge the reaction proceeds spontaneously with oxidation taking place at the anode, which is the negative electrode. This can be observed in right part of Figure 2. Always during the discharge, reduction proceeds at the cathode, which is the positive electrode. On the contrary, the reverse chemical reaction is forced to occur during the

recharge. At the anode, the negative electrode, electrons are supplied by lowering the potential, so that the reduction takes place. In this way, the anode effectively becomes a cathode. For the same reason, during the charge, the cathode is brought to a higher potential and oxidation takes place. Thus, the former cathode effectively becomes the anode of the system. The forced charge process is schematically depicted in the left part of Figure 2 [11].

1.3. Fundamental parameters: definitions of specific capacity and C-rate.

Various parameters are fundamental to design a battery and to characterize its performances. They lead the research and development designers and give the possibility to the users to choose which systems suit better for their purposes [7]. Of course, one is represented by the cell voltage presented before, but also the specific capacity (sometimes named also Coulombic or gravimetric capacity), the energy and power densities, the cycle-life, and the C-Rate, represent all important parameters.
The specific capacity expresses the theoretical amount of charge that an electrode can store per unit of mass of the active material, while the cell voltage is the potential difference between the electrodes and is determined from the Nernst equation for the overall reaction occurring in the cell. The energy content is simply given by the product of the two previous quantities, while the power is the product of the cell voltage times the current drawn.
The cycle-life identifies the useful life of a battery in terms of charge and discharge cycles that can afford before its capacity drops below the 80 % of the nominal value. Finally, the C-rate is related to the current and express the velocity with which a particular cell is cycled. [11]

In this thesis, only gravimetric quantities have been considered that can be derived from their corresponding parameters dividing them by the mass of the active material. Some of these values can also be derived in a pure theoretical way, as for instance the specific capacity.

1.3.1. **Specific capacity**

As previously said, the specific capacity defines the amount of charge that an electrode can store per unit of mass of its active material and is usually expressed in mAh/g. In principle, this can be calculated directly from the stoichiometric expressions of the reaction products, by considering the amount of charge involved in the reaction for an equivalent of the pristine active material. [7]

Let us consider, for example, the graphite, which is the standard anodic material of the actual Lithium-Ion Batteries (LIBs). The pristine material is simply represented by carbon, C, while the final lithiation product is the LiC_6 composite. Upon incorporation of that lithium-ion inside the hosting graphite lattice, one electron is absorbed from the external circuit. So, once the reaction has reach completion, one electron is inserted in the hosting material every 6 atoms of carbon. By reasoning in terms of equivalents, the specific capacity is obtained starting from this ratio as follows:

$$\text{Gravimetric capacity}_{\text{Graphite}} = \frac{1}{6}\frac{\text{F}}{\text{Carbon molar mass}} = 372\ \text{mAh/g} \quad (8)$$

This expression defines the amount of charge that can be stored by a unit of mass of graphite, as a maximum. Of course, the same method can be applied to determine the specific capacity of other compounds. For example, considering the $Li_{22}Ge_5$ compound of lithium and germanium (see section 1.6.4.2), its theoretical capacity results in:

$$\text{Gravimetric capacity}_{\text{Germanium}} = \frac{22}{5}\frac{\text{F}}{\text{Ge molar mass}} = 1624\ \text{mAh/g} \quad (9)$$

One disadvantage of this way of calculating the capacity is that the lithium mass is neglected. This could lead to some paradox, with materials having theoretical capacities higher than the elemental material itself.

Starting from this definition, the theoretical capacity that a real electrode can attain is simply found by multiplying its specific capacity by the mass of active material present.

1.3.2. **C-rate**

Another important parameter is the C-rate. This is a measure of the rate at which a battery is charged or discharged, relative to its maximum capacity. It is introduced to normalize the current against the capacity, as the latter depends on the specific battery tested. In this way, comparisons between different cells and different chemistries are enabled. [10]

The C-rate is simply defined as the ratio between the rated cell capacity and the time, expressed in hours, in which the cell is fully charged or discharged:

$$\text{C-rate} = \frac{\text{Rated electrode capacity}}{\text{h}} = \frac{\text{Specific capacity (mAh/g)} \cdot \text{Mass loading (g)}}{\text{Charge (or discharge) time (h)}} \quad (10)$$

According to this definition, a current of 1C is the current to fully charge (or discharge) an electrode in 1 hour. Similarly, 2C represents the current to fully charge/discharge and electrode in half an hour, and so on.

1.4. **The key role of Lithium-Ion Batteries**

Since the invention of the "pile" by Alessandro Volta, around 1800, a tremendous effort has been spent in the development of batteries [12]. A variety of different chemistries has been investigated and some of them eventually became standards. Three examples, currently representing the most relevant rechargeable systems at a commercial level, are the lead-acid, the nickel metal hydride (Ni-MH) and nickel-cadmium (Ni-Cd), and the Lithium-Ion Batteries (LIBs) [13][14][15].

The first ones were discovered in the mid of the 19th century and still represent a significative market share, as industrial and automotive application still rely on them [16]. The Ni-MH and Ni-Cd were developed starting from the 1940-1950 and dominated for a long time the portable electronic and standby power markets [2], representing the system of choice also for aerospace applications [7][17]. However, the most disruptive technology is represented by the youngest one: that of the LIBs. Since their first appearance, in the 1991, this system completely revolutionized the energy storage technology with its inventors that have been honoured with the Chemistry Nobel prize in 2019[12].

The disruptiveness of LIBs over the other chemistries is associated to several unparalleled characteristics, like the high energy and power densities, high open circuit voltage, low self-discharge, nearly zero-memory effect, long cycle-life and a high efficiency. [2][14][15] [18][19][20][21]. Some of these features are listed in Table 1, taken from ref. [21], where they can be compared with those of the other battery systems. The superior characteristics of LIBs can be ascribed to the intrinsic properties of this element, which is the lightest metal and one of the most electropositive elements on the periodic table. Furthermore, its small ionic radius allows for fast diffusion rates through the electrode materials as well as in the electrolytes. [9][14][22]

Technical characteristics of energy storage technologies.

Storage type	Power density (volumetric) (kW/m^3)	Energy density (volumetric) (kWh/m^3)	Energy density (mass) (Wh/kg)	Cycle efficiency (%)	Lifetime (cycles)
Battery					
Li-ion	1300–10,000 [151] 1500–10,000 [148] 150–360 [126] 60–800 [146]	300–750 [126] 200–400 [151] 200–500 [148] 90–500 [146]	100–300 [126] 60–200 [151] 75–200 [148] 200 [102] 150–200 [5] 30–300 [146]	85–98 [151] 90–97 [148] 95 [5],[102] 85–95 [94] >95 [126] 70–100 [146]	500–10^4 [151] 1000–10^4 [148, 5] 3000 [102] 250–10^4 [146]
NiMH sealed	500–3000 [151] 8–600 [146]	80–200 [151] 40–300 [146]	40–80 [151] 30–90 [146]	65–75 [151] 50–80 [146]	600–1200 [151] 300–3000 [146]
Lead acid	90–700 [151] 10–400 [148, 146]	50–80 [151, 148] 25–90 [146]	30–45 [151] 30–50 [148] 35–50 [5] 10–50 [146]	65–80 [102] 75–90 [151, 94] 70–80 [148] 80 [5] 60–90 [146]	250–1500 [151] 500–1000 [148] 500–1500 [5] 100–2000 [146]
NiCd[2]	40–140 [146]	15–150 [146]	10–80 [146]	60–90 [146]	300–10^4 [146]
NiCd vented	75–700 [151]	15–80 [151]	15–40 [151]	60–80 [151]	1500–3000 [151]
NiCd sealed	80–600 [148]	80–110 [151] 60–150 [148]	30–45 [151] 50–75 [148] 75 [5]	60–70 [151, 148] 80 [5]	500–800 [151] 2500 [5]

Table 1: Technical characteristics of different battery systems. Taken from ref. [21], the reader is forwarded there for the references listed in the table.

The advent of this energy storage technology represented a breakthrough and led the base for the development of the modern electronic devices over the last three decades [2]. Besides this, in the recent years, a further increased interest in this technology has been prompted by the necessity of mitigating the climate changes and air pollution [20][23]. For this purpose, the electrification of transportation has been identified as a crucial component to reduce mankind's greenhouse gas emission [19][22][24]. To avoid the worsening of the climate issues, many governments are adopting solutions that foresee the complete stop of petrol-based vehicles in the long term, looking for a full transition towards electric mobility [15][22]. Another important strategy which is pursued to alleviate the climate changes is the switch toward renewable energy sources. In this field, energy storage emerges a key factor to efficiently harvest the energy from these sources, tempering the inconstancies which are intrinsic in some of them, like photovoltaics or wind energy. In addition, energy storage systems could be extremely beneficial also for the electric grid, allowing for the

load levelling and peak shaving, frequency regulation, damping energy oscillations, and improving power quality and reliability. [9][20][21][25]
LIBs represent the system of choice for this transition, which is growing at impressive rates. In the decade 2008/2018 the compound annual growth rate (CAGR) of the global market volume for LIBs increased at a rate of about 24 % per year [16]. But this trend is foreseen to continue, with expected revenues for 69 billion $ and a CAGR of over 16 % by 2022 [19] and a further increase until 2030 [14], with a market CAGR of about 20 % [16].

The relentless market evolution engaged the lithium-ion technology in a continuous chase for better performances as new and more demanding electronic devices are produced or long-range vehicles are required. For this reason, the state-of-the-art of this technology is always a step behind the increasingly challenging requests in terms of charge capacity, energy and power densities, efficiencies, rate capabilities [2][18][26]. This is why, since their first commercialization, LIBs underwent continuous research activities, attaining notable performance increases [22] but never meeting pace with the unsatiable demand from the market [2]. In particular, immense efforts have been focused on developing anode, cathode, or electrolyte materials to improve this battery technology [19][22].
This work perfectly inserts in this context, pursuing the research of a novel anodic material to push forward the performances with respect to the actual standards. In the following sections, the state-of-the-art of the actual anodic and cathodic materials for LIBs is presented. The focus is then placed on the most promising chemistries regarding the anode, with an in-depth analysis of germanium. Some of the key factors that affect the electrode performances are also disclosed, like the Solid-Electrolyte Interphase (SEI) or the presence of binders or conducting agents. In the end, some future perspectives regarding the expected evolution of LIBs and germanium anodes and some considerations of the economical aspects are given.

1.5. Cathode materials

The cathodic materials that are currently used in commercial LIBs are all intercalation compounds of metal oxides. The main ones are 5 materials that differ in terms of capacities, thermal stability, cycle-life, or power capability. The precise choice of one chemistry or

another is dictated by the specific application as each of them has particular advantages at the expense of other characteristics.

The first of these materials is the layered lithium-cobalt oxide $LiCoO_2$ (LCO), which was originally introduced by Goodenough *et al.* [27]. It shows a practical specific capacity of 130-150 mAh/g, good cycling performance, high discharge voltage, good mechanical strength, and good rate capability. However, it has a low thermal stability and can not withstand deep cycling. In addition, it is subject to the volatile cost of the cobalt. LCO is not used anymore in large format applications today, while is still employed in portable devices. [4][19][28]

Secondly, there is the spinel lithium-manganese oxide $LiMn_2O_4$ (LMO), which is cheaper and more environmental-friendly than LCO. It exhibits a high lithium-ion diffusivity, low internal resistance, and good rate capability. It also has a high thermal stability and is a safe material, tolerating high currents. However, its practical capacity is less than 130 mAh/g, below that of LCO. Moreover, deep discharge result in fast deterioration of the material and a long cycle-life can be attained only if low currents are used. [13][19][22][29]

The third cathodic composite for LIBs is the olivine structured lithium-iron phosphate $LiFePO_4$ (LFP): this is an environmental-friendly low-cost material with excellent cycle-life and both thermal and chemical stability, for enhanced safety. It shows a low practical capacity of about 120 mAh/g, but it can withstand harsh conditions and hazard events better than other batteries since it does not explode or catch fire. Furthermore, it possesses a high pulse-rate capability of up to 10C - 20C. As a trade-off, its lower operating nominal voltage of 3.2 V reduces the overall energy density. It represents the material of choice when safety is mandatory, like in maritime applications. [4][19][30].

Another common cathodic material is the layered $LiNiMnCoO_2$ (NMC), which combines the high capacity from Ni, the high electrical conductivity from Co and the structural stability from Mn. It has similar or higher capacity than LCO, depending on the Ni content, and a similar operating voltage (ranging between 2.5V to 4.2V, with a sloping trend), but is cheaper due to the lower amount of Co. By incorporating more Ni, higher capacity and energy density can be achieved, at the expense of its thermal stability and life span. The specific capacity ranges from 160 mAh/g of NMC111 ($LiNi_{1/3}Mn_{1/3}Co_{1/3}O_2$) to 200 mAh/g of NMC811 ($LiNi_{0.85}Mn_{0.1}Co_{0.1}O_2$) [14][18][19][31].

Finally, the last material is the layered $LiNiCoAlO_2$ (NCA). Analogously to NMC, the high capacity from Ni is combined to the conductivity from Co, but the structural stability is due to Al. This cathodic material shows a specific capacity up to 180-200 mAh/g and can endure 1000–1500 full cycles. An operative voltage of about 3.6 V allows for high energy

density. However particular care must be taken as elevated voltages or temperatures initiate a fast capacity fade. [19][28][32]

Thanks to their superior capacities and overall performances, NCA and NMC have been selected as cathodic materials by many automobile manufacturers for the next generation of hybrid electric vehicles [19][33][34], and are expected to be of primary importance in the near future [32].

Material	**$LiCoO_2$**	**$LiMn_2O_4$**	**$LiFePO_4$**	**$LiNiMnCoO_2$**	**$LiNiCoAlO_2$**
Abbreviation	**LCO**	**LMO**	**LFP**	**NMC**	**NCA**
Specific capacity (mAh/g)	130-150	~ 130	~ 120	160 - 200	180 – 200
Operating voltage (V)	3.9	3.7	3.2	~ 3.7	3.6
Cycle-life	500-1000	300-700	1000-2000	1000-1500	> 500

Table 2: Fundamental characteristics of the typical cathode materials. Data from [4][35][36] and the other references listed in the text.

1.6. **Anode materials**

The anode is the electrode where oxidation spontaneously takes place during the discharge process. The present standard material is graphite, whose properties are presented in this section aside some of the most promising candidates as the next anodic materials for the LIBs of the future. These are mainly represented by graphene, metallic lithium, and the elements of the 4^{th} group of the periodic table. The reason for the interest in these materials is mainly represented by their elevated gravimetric capacities, which are well above that of the actual standard, as it can be ascertained from Table 3. However, their exploitation is hindered by various issues that arise upon the charge and discharge cycles.

The properties of these materials and the latest results from the frontier of the research are now presented, with particular attention to Germanium, which is the subject of this work.

Material or element	Final lithiation compound	Specific capacity (mAh/g)	Volumetric capacity (mAh/cm3)
Soft carbon (C)	< LiC_6	255 [4]	293 [4]
Graphite (C)	LiC_6 [37]	372 [37]	837 [4]
Hard carbon (C)	> LiC_6	480 [4]	553 [4]
Graphene (C)	>> LiC_6	~ 1000 [4]	~ 4000 [4]
Tin (Sn)	$Li_{22}Sn_5$ [38]	994 [38]	7216 [39]
Germanium (Ge)	$Li_{22}Ge_5$ [39]	1624 [39]	8645 [39]
Lithium (Li)	Li metal	3860 [40]	2061 [4]
Silicon (Si)	$Li_{22}Si_5$ [41]	4200 [41]	9765 [4]

Table 3: Maximum theoretical capacities conceivable and final lithiation products of some anodic materials or elements.

1.6.1. **The Solid-Electrolyte Interphase**

Before deepening the various chemistries, and the related properties, it is necessary to introduce what is usually called the Solid-Electrolyte Interphase (SEI). This is a thin film that is typically formed on the surface the negative electrode due to the decomposition of the electrolyte components. When the potential of the negative electrode falls below the thermodynamic stability limit of the electrolyte [42][43], this is reduced, and the insoluble products of the reaction are deposited at the interface [44][45][46][47]. For the most common liquid electrolytes, the low potential limit of the stability window is around 0.8 V vs Li/Li^+ (see Figure 3) [44][46][48][49]. So, SEI production begins from this potential but can continue up to the lower cut-off voltage. [46][50]

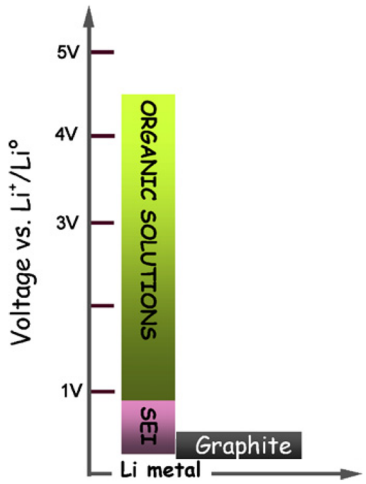

Figure 3: Electrochemical stability window of the most common electrolyte solutions, adapted from ref. [48].

The SEI production is a self-limiting process that continues up to the point in which its thickness is enough to prevent electron tunneling from the anode [7][51]. The most important property of the resulting film is that it is electrically insulating but still permeable to the lithium-ions [4][44][45][47][51][52]. This, which constitutes a side reaction, is actually a fundamental step to assure the effective LIBs functioning [43][46][47][50][51]. Indeed, it extends the electrochemical stability window of the electrolyte and prevents its further decomposition [46][53], while ensuring lithium-ions accessibility to the electrode [43][44].

The SEI passivation layer is clearly a source of impedance inside the LIB [4][43][51][54]. In order to minimize this impedance and to reduce the amount of electrolyte and lithium consumed in its formation, it is desirable that a thin, uniform and robust SEI layer [26][43][44][50] is completely formed during the first cycles of a battery life. [44][45][46] [55]. The effective layer thickness, as well as its precise composition and the potential at which electrolyte reduction is triggered, depend upon the electrolyte solution composition, the lithium salt, the presence of additives for the electrolyte solution, the presence of coatings on the active material, and on the active material itself [33][36][37][41][43][44].

It is quite accepted that the SEI layer is composed by a multi-layer structure comprising both crystalline and amorphous phases, with an inner compact region that is mainly made of inorganic compounds and an outer porous and less-compact region containing organic compounds [46][47][50][51][52][53]. For a typical electrolyte solution on a graphite electrode, the main SEI constituents are inorganic lithium compounds, such as Li_2O, Li_2CO_3, and LiF, in the inner layer, close to the electrode, while oligomer organic compounds, such as semicarbonates and polyolefins, are found in the outer region towards the electrolyte [46][47][50][51]. A naive representation of the SEI layer on a graphite anode is depicted in Figure 4.

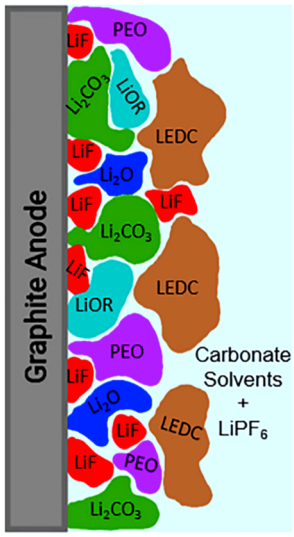

Figure 4: Commonly accepted SEI components for typical organic electrolyte solutions on graphite anodes. Adapted from ref. [47].

1.6.2. **Graphite and carbonaceous materials**

Since LIBs birth, the most common anodes have been the carbonaceous materials, which are represented by graphite, soft and hard carbon and, more recently, graphene.

Among them, graphite undoubtedly dominates [19][26][56] thanks to a combination of factors and excellent properties: first of all, graphite is very abundant, easy to process, and constitutes a low-cost material [4][56]; secondly, it presents a constant potential for lithium insertion that is the lowest among all the carbonaceous materials [7][56], enabling high energy content LIBs; thirdly, it exhibits only small volume variations around 10 % upon lithium insertion/extraction [57], which enables for a long cycle-life. Graphite also shows a good theoretical capacity of 372 mAh/g, corresponding to LiC_6 as a final compound (Table 3), and that is almost met in actual batteries by natural graphite. This material is nowadays commercially available in many "formats", the most frequently used including MesoCarbon MicroBeads (MCMB), Mesophase pitch-based Carbon Fibres (MCF) and Vapour Grown Carbon Fibres (VGCF). [56] The outclass of graphite over the other carbonaceous materials, or other chemistries, can be inspected in Figure 5, which gives a survey of the anodes market share in 2015. As it can be seen, graphite alone constitutes more than 93 % of the whole market, while the carbonaceous material as a whole make up about the 98 % of the total share. [4]

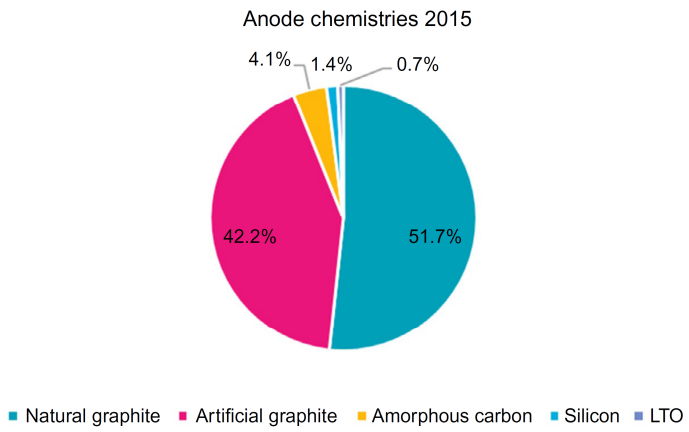

Figure 5: Market share of the anode chemistries in 2015, taken from ref. [4].

The amorphous materials that appear in Figure 5 are mainly hard and soft carbon, as graphene is still under study. Soft carbons differ from graphite in that their crystal structure does not have the same long-range order or repeatability. They also show a lower capacity than graphite (cf. Table 3) and therefore are mainly used as conductive additives or material coatings in commercial LIBs. [4]

Hard carbons differ from both graphite and soft carbon in that they have an entirely random arrangement of the carbon atoms. This provides a lot of voids in their reticular structure that can accommodate lithium-ions, enabling a higher practical capacity. Hard carbons are also less subject to lithium dendrites growth because the intercalation occurs at higher potential compared to the other carbon materials. In addition, lithium intercalation occurs at almost zero volume change. However, hard carbons display low initial coulombic efficiency and require a higher deintercalation voltage than graphitic carbons. Moreover, they typically show high fading with cycling. [4]

Graphene is not yet implemented in today LIBs, since it is one of those new materials studied at the frontier of the research. Graphene is "simply" a sheet of single carbon atoms arranged in a two-dimensional hexagon formation, having a single atom thickness. This material attains promising capacities ranging between 780 mAh/g and 1116 mAh/g when used alone [4], but it is usually coupled to other elements, like those of the 4th group (see section 1.6.4), to obtain synergic effects of their benefits [58][59][60][61][62][63]. Thanks to other interesting properties, like a tensile strength that is 100 times that of steel, a thermal conductivity that is 3 times that of diamond, and an electron mobility that is more than 10 times greater than silicon, it is often found in studies as a coating material or conductive additive. [4][58]

1.6.3. **Lithium metal**

One might question why lithium metal is not directly used as an anode in LIBs, forcing this laborious search for other materials which could host lithium-ions. The answer is related to the safety issues when this material is used in its metal form. These are mainly related to two aspects: the first is the high lithium reactivity with oxygen and water, but also with the electrolyte solvents and salts, thus posing concerns on the battery safety in case of accidents [4] and leading to continuous side reactions [64]; the second is mechanical in nature, since lithium metal is plated and stripped without a host material, resulting in low spatial control and leading to unstable morphologies including dendrites [8][45][64][65][66]. These are particularly hazardous since they typically grow towards the cathode, which could result in internal short circuits [4][45][51][56][40]. The uncontrolled deposition induces also mechanical instability to the SEI layer, with continuous consumption of electrolyte [45][51][64][66]. Furthermore, the dendritic structures get often detached from the underlying metal through the cycles, resulting in a progressive capacity fade [8][65]. It is for these reasons that insertion anode materials are used in commercial LIBs, instead of lithium metal, involving the lithium-ions in the process that is usually referred to as the "rocking-chair" LIB. [14][37]

Extensive research efforts have been spent during the years to address the aforementioned problems. The most promising studies involve coatings to inhibit dendrite growth [4], innovative electrolytes or additives to suppress the side reactions while enhancing uniform growth pathways [64], solid polymeric and ceramic electrolytes having larger mechanical strength than lithium [64][66]. But also other approaches have been tested, like ex-situ SEI "pre-formation" prior to the cell assembly [66], or the use of nano-structured templates with "lithiophilic" functional groups to create virtual hosting structures [65]. Although the significant efforts, no reliable solutions have been found yet [4][40] and fundamental progresses are still required regarding both the comprehensions of the phenomena behind the mentioned issues, as well as on their possible solutions. [65][66]

1.6.4. **Alloying materials: the elements of the 4th group**

The 4th group elements undergo a completely different reaction mechanism with lithium, compared to intercalation materials. This is not simply inserted inside the host reticular

structure but rather induces a complete transformation and results in heavily lithiated compounds as a product. This mechanism is termed “alloying” and Silicon (Si), Germanium (Ge) and Tin (Sn) are some of the elements which gathered the highest attention [3][54][67]. Thanks to their very high lithium intake, these materials show theoretical capacities which are more than 2 to 10 times higher than graphite (see Table 3). In addition, they show a relatively low voltage versus lithium [3][26][41][68], giving a good trade-off between retaining high open-circuit voltage and avoiding adverse lithium plating [41][69]. Unfortunately, all the cited materials share a common issue, which is represented by an enormous volumetric modification upon the alloying process that can lead to changes of more than 300 % [22][54][68]. The continuous expansion and contraction can break these materials apart over time, by their progressive fragmentation and delamination from the electrode through the cycles [70]. This typically results in a short cycle-life, with a rapid capacity fading due to the loss of active material [39][54][68] [71]. Additionally, the volumetric expansion and the active material fragmentation lead to continuous SEI formation, consuming lithium and electrolyte and increasing also the cell impedance [26][54][69]. All of these things further reduces the capacity and the cycle-life.[54]

Many strategies have been proposed or are currently studied to render these materials available as long-term solutions for LIB anodes.
One way is to mix or co-structure them with carbon-based composites, which could act as a buffer for the volumetric expansion [56][61][71][72][73]. Of course, this reduces the overall gravimetric capacity, but still results in a much higher capacity than graphite, while helping to alleviate the cycle-life challenges [4][56][61].
Another promising solution is represented by the nano-structuration of the active materials. This has the potential to reduce the stress and strain associated with the expansion [4][61][71] up to the point in which the material can reversibly accommodate it [26][74]. Furthermore, besides relieving the volume variation, nano-structuration offers several additional advantages, like an enhanced surface-to-volume ratio leading to more active sites available for lithium storage, and a larger surface in contact with the electrolyte resulting in a better ionic transfer and reduced diffusion lengths. [56][74][75][76]

In designing the nano-structures a particular care should be taken regarding some delicate aspects. The first is the preservation of the SEI layer, as its breaking and reformation at each cycle traduces in a waste of energy, lithium and electrolyte [4][26][43][50]. The

second aspect regards the possibility that these structures undergo an aggregation through the cycles [68][70][77][78]. Such a process could destroy the nano-structured morphology and increase the resistance to electron and lithium-ion transfer [54][79][38]. The mitigation of these risks could be achieved by providing adequate room for the expansion [37][71][76][80][81][82] or adopting particular coatings for the active material or additives for the electrolyte solution. [26][83]

Before deepening the material that is the subject of this work, namely germanium, few words are spent about silicon. This is one of the most promising materials for the future LIBs because it offers a high theoretical capacity of about 4200 mAh/g, but is also one of the more abundant elements in nature [3][56][84], it is cheap [3][54][85], and it has no negative environmental impacts. [4][56][72]. As all the other alloying elements, silicon suffers for the tremendous volumetric expansion during the charge and discharge processes. Another drawback is also represented by a poor conductivity, which limits the rate capability [26][69][68][86]. This is due to the fact that generally only the lithium ions that are inserted near the surface are able to participate to the electrochemical reactions during fast charge or discharge, leaving lithium trapped in the innermost regions and causing reduced capacity and poor power capability [4]. Both these aspects hinder the direct exploitation of this material and there are many research paths ongoing [69]. One example is seen in the efforts to create carbon-based shells or cages around the Si, buffering its volumetric expansion [87][88]. Many works point in the direction of using silicon nano-materials, like nano-particles, nano-wires and nano-tubes, porous structures and many others, eventually employing additives, to overcome the limitations [26][68][69][86].
Today, some Silicon is already used in commercial LIBs (see Figure 5), blended with carbonaceous materials [87][89][90][91], but the previously mentioned issues have not been solved yet, and its usage results in a shrinkage of the device useful life. [4]

1.6.4.1. **Germanium**

Germanium has received less attention with respect to Li metal and Si due to its lower specific capacity (see Table 3)[3]. Despite this, it shows some advantages when compared to Si, which make it particularly interesting. Indeed, it possess a 10^4 higher electrical conductivity and a 400 times faster lithium-ion diffusivity [3][54][85][92][93], advising a superior rate capability over silicon and a particular suitability for high power applications

[3][4][67][85]. Furthermore, in spite the lower specific capacity, its volumetric capacity (8645 mAh/cm^3) is not so far from that of silicon (9765 mAh/cm^3) [39].

Unfortunately, as for the other alloying materials, also germanium experiences dramatic volumetric expansions and contractions when reacting with lithium. And similarly, the downsizing of the material to nanometric structure design is one of the strategies that is usually adopted to solve this issue [71][39]. In this regard, the nano-structuration of Germanium present another advantage over silicon, that is an isotropic lithiation process and a beneficial plastic behaviour which make it far more resilient to fractures [4][54][74][80][85][94][95]. Thanks to these properties, the dimension of the germanium features that can reversibly accommodate the volumetric changes could be appreciably bigger than those necessary for Si. Indeed, the diameters at which cracks form in Si have been determined to be about 150 nm for nano-particles and between 200 ÷ 360 nm for nano-pillars and nano-wires [26][50][54][70][96]. In germanium, instead, nano-particles with dimensions from 100 nm to submicron have been observed by Liu *et al*. to undergo multiple lithiation/de-lithiation cycles without fractures [74]. More recently, Lee *et al*. observed that fractures developed in crystalline pillars with diameters of ~1.2 μm [97].

During the time, a large number of nano-structures have been proposed to find a reliable solution for all the aforementioned problems. Many examples can be found ranging from 0D to 3D geometries, in which germanium is often combined with different materials looking for synergic effects. Tubes or wires [98][99][100][101][102], quantum dots or particles [103][104][105][106][107], inverse opal [108][109], or porous structures [76] [110][111] represent only few examples.

1.6.4.2. **Germanium lithiation process**

The lithiation of germanium is a multi-step process that involves amorphous phases containing increasing amounts of lithium, up to the $Li_{15}Ge_4$ alloy as a final compound. The overall process could be summarized by the following reaction [26][67][99][111][112] [113][114][115]:

$$(11) \quad Ge \rightarrow a\text{-}Li_xGe \rightarrow a\text{-}Li_{15}Ge_4 + c\text{-}Li_{15}Ge_4\,,\ (0 < x < 3.75)$$

The final lithiation compound, $Li_{15}Ge_4$, could be produced both in crystalline as well in amorphous phase. This is usually related to the current rate and to the cut-off potential [3] [67][98][116], but could also be related to the germanium feature dimensions [3]. When the lithiated germanium is oxidised in the de-lithiation process, it is recovered in a final amorphous phase, with possibly some residual amorphous Li_xGe compound [3][67][111]. The various lithiation and de-lithiation steps produce specific features in the galvanostatic profiles of charge and discharge (cf. sect. 4.2.1). In the electrochemical characterization chapter (Chapter 4) these features are interpreted by comparisons with the literature.

The previous reaction equation could seem somehow trivial. However, its identification required a long process and involved many studies. In fact, especially in the initial works, there was no unanimous consensus regarding the precise lithiation steps, the presence of intermediate crystalline compound and even the precise final compound. Regarding this last aspect, some of the first works claimed the presence of the crystalline $Li_{22}Ge_5$ alloy among the products [92][117] but many others identified only the $Li_{15}Ge_4$ compound as the final lithiation product. [3][67][112][113][116][118]

As a heritage of the former uncertainty about the final lithiation compound, many authors still consider the $Li_{22}Ge_5$ as the maximum theoretical capacity and use it for the calculation of the C-rate. According to this literature trend, the $Li_{22}Ge_5$ phase is considered for the calculation of the C-rate or the maximum theoretical capacity also in this work.

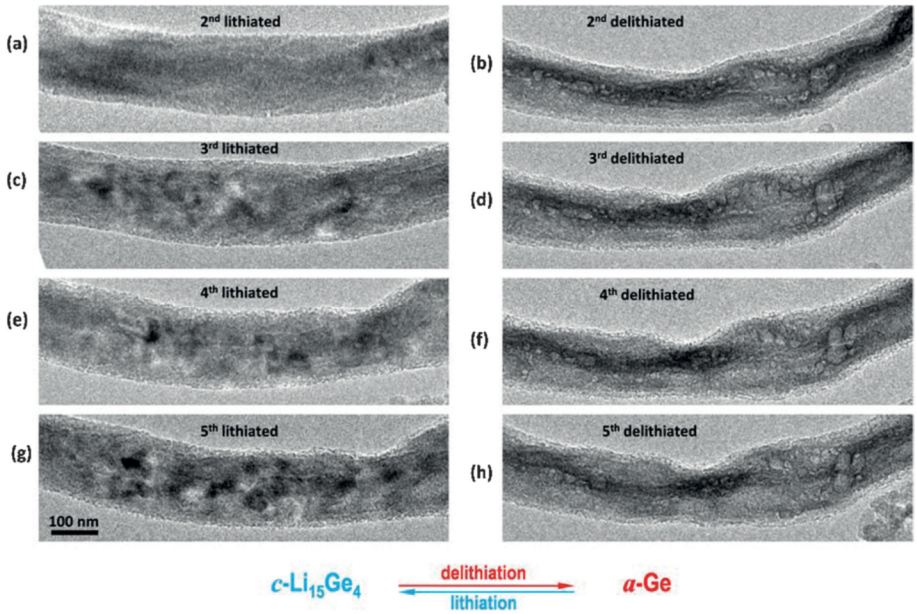

Figure 6: The self-organized nano-porous structure that form on germanium through its lithiation and de-lithiation. The image is from ref. [74].

As a last remark on the lithiation of germanium, an interesting phenomenon is reported that is the spontaneous formation of a nano-porous structure on the surface upon the electrochemical reactions with lithium [37][119][120][121]. This porous structure is self-organized and shows a memory effect i.e., the pore position does not change once these are formed. Such a structure can be inspected in Figure 6, reported from ref [74], showing the change of a germanium nano-wire morphology through the cycles during an in-situ TEM experiment [74][119]. This self-reorganization process is ascribed to a local aggregation of vacancies that are created during lithium-ion extraction [37][74][119]. Such a structure could be beneficial for stress relaxation during the volumetric expansion, in buffering the volumetric expansion [37], but could also help in minimizing the SEI layer deterioration and hindering the formation of new one. [74]

1.7. A binder and additive free approach

The active materials are typically synthesized in the form of powders with a bottom-up approach. The electrodes are then fabricated by mixing these powders with conducting agents and binders, which usually are non-active elements, forming slurries that are deposited onto the current collector [81][82][122][123][124][125]. However, this practice presents several drawbacks as:

1) It lowers the overall specific capacity of the electrodes [5][102][126], as their total weight could be constituted up to the 60 % by these inactive yet necessary materials [101][122][127],
2) The electrode production from slurries represents one of the longest steps in the fabrication process, involves expensive materials [128], and requires a drying phase that could consume up to the 40 % of the total energy required in the whole fabrication, thus contributing significantly to the final electrode cost [124],
3) The appropriate selection of the binders and eventual additives, as wells as their precise proportion, could represent a complicated task. Indeed, their compatibility between themselves and with the active material, the electrolyte, and the current collector should be carefully evaluated as it influences the overall performance of the electrode [127][129][130][131].

4) Another aspect regards the mechanism that holds together the various components, relying on van der Waals bonding, which could result in weak cohesion of the components or poor adhesion to the current collector [123],
5) Non-uniform distribution of the active and inactive materials could occur, leading to detrimental aggregation phenomena [82][108][123][132],
6) The tortuous distribution of the various elements and their non-perfect contact could increase the electrode impedance [82][130][133],
7) Finally, the present binders and additives are not suitable for the emerging active materials, like the alloying ones, since they are un-able to withstand these materials volumetric expansion, leading to the electrode breakdown through the cycles. [82][102][130][132]

An alternative approach is represented by a fabrication process in which the anodic material is directly produced and arranged onto the current collector substrate, favouring growth and nano-structuration techniques with high throughputs and which are already industrial standards. This is precisely the methodology used in the present work, in which the anodic materials have been realized and nano-structured directly onto the current collectors.
The fabrication processes of this work consist of two main steps: first, a thin Germanium film is realized onto the current collector by means of Low Energy Plasma Enhanced Chemical Vapor Deposition technique (LEPECVD); then, this film is nano-structured recurring to one of the two distinct techniques which have been studied and consisting in electrochemical etching in HydroFluoric acid (HF) or Ion Implantation. This represents a top-down approach to produce the final electrodes and it does not require any binder or conductive agent. Thus, the fabrication process presented in this work permits to get-rid of most of the previously cited issues, simultaneously offering several additional benefits. Firstly, the whole mass loading of the final electrode is constituted uniquely by active material, thus enhanching the overall gravimetric capacity. Secondly, the lack of inactive materials leaves room for the volumetric expansion of the alloying material [81][82][125][133] as well as increasing its surface in contact with the electrolyte, to the advantage of the reaction kinetics [132]. Thirdly, the direct contact of the active material with the current collector could enhance the electrical conductivity, fostering the electrode high-rate capability [81][115][123] [126][132]. Additionally, the lack of other materials permits to ascribe all the features observed in the electrochemical characterizations exclusively to the active material (and eventually the electrolyte), providing insight into the

lithiation mechanisms. [70][101][133] Finally, the absence of binders and additives is also beneficial as it could simplify the electrode fabrication process.

The use of standard industrial techniques in the fabrication process, could be helpful in terms of large-scale production and would ease the practical implementation of the novel material, since already existing facilities could be exploited.

1.8. Future perspectives

Besides the key sectors of portable electronics, electric mobility, and energy storage for renewable energies harvesting, LIBs are also gradually expanding in other sectors like the aerospace [14][19] and the medical one [16]. However, despite the important progresses already made (and those foreseen), it is hard to think that LIBs alone could meet all the future demands for the energy storage systems. For this reason, it is expected that hybrid systems, in which different energy storage solutions are coupled together to combine their collective advantages, will be highly developed in the near future [9][20][21][134][135].
In Hybrid Energy Storage Systems (HESS), the heterogeneous storage devices will be such that the short term high power requirements is supplied by high power devices, while long term energy needs is met by high energy devices [20]. In the near term, HESS are particularly promising for the transportation field [20][21][136][137], where a combination of fuel cells, supercapacitors and LIBs together could bridge the gap with respect to the power and energy content of conventional combustion fuels, as it can be ascertained from the Ragone plot[1] presented in Figure 7. Many works on this topic testify the interest on hybrid systems in view of a zero-emission mobility. [135][136][138][139][140][141]

Regarding the Ge-based LIBs, their development and short-term implementation is hindered by two relevant obstacles, in addition to those previously listed. The first is represented by an extremely limited production ranging around a hundreds of tons of germanium manufactured per year worldwide [142], leading to its classification as a critical raw material by the European Union [143]. The second is that it is particularly expensive compared to other elements [4][41][93][144]. However, nano-structured Ge as a novel

[1] This is constituted by the Power vs. Energy graph and is typically used to compare various energy production or storage systems. [153]

anodic material could be particularly interesting in those fields where the costs are not the main driver, like in the aerospace sector.

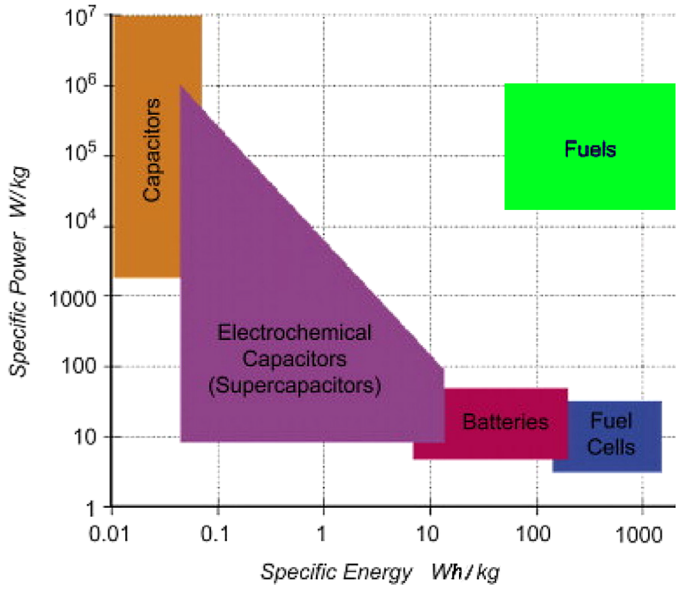

Figure 7: Ragone plot of the energy content for LIBs, capacitors, supercapacitors, fuel cells and fuels. Adapted from the references [6] and [21].

LIBs gained increasing interest in aerospace applications since the first mission implementing this technology in 2001 [17], the European Space Agency (ESA) satellite Proba-1 [145], and nowadays represent the standard choice in nearly all the spacecraft applications, like for instance the CubeSat nanosatellites [19][145][146][147]. Furthermore, they have recently substituted the Ni-H_2 batteries of ISS, in an operation started in 2017 [148], and nowadays represent the 98 % of the energy storage systems commissioned for new spacecrafts [17]. However, the space LIB technology is essentially the same as that for terrestrial applications, with graphitic anodes and intercalation cathodes [147]. Therefore, further advances are required to support the customer demand for higher power payloads [146]. Also an extended temperature window [146] and further mass and volume reduction [17][145] are required for the future space LIBs, to allow for additional payload capability and extend the mission operativity ranges.

The attention toward new technologies involves all the aerospace sector stakeholders, and in particular the national space agencies. This is highlighted by two recent research projects financed by the Italian Space Agency (ASI) regarding novel anodic materials based on nano-structured germanium. The first of these projects, named ANGELS (Standing for the Italian "*Sviluppo di anodi in germanio nano-poroso per batterie al litio per applicazioni*

aerospaziali"), started in 2018, as a part of the invitation to tender "New Ideas for Future Space Tools". Some of the activities presented in this thesis were carried out within the framework of that project. A new project, named GLITTERY (Standing for "*Sviluppo di batterie agli ioni di litio con anodo in germanio nano-poroso per applicazioni aerospaziali*"), started in 2021 within the "Interdisciplinary Enabling Technologies" program. The aim of this project is to increase the Technology Readiness Level (TRL) [149], of the germanium anodes up to a TRL 6, corresponding to system adequacy demonstrated in simulated relevant environment [150].

1.9. Economical considerations

Besides the scientific and technological aspects of a battery, an important factor in the choice of its components is represented by their costs and their influence on the overall price of the final product.

A review of these economical aspects was performed by Berckmans *et al.* [151]. The cost breakdown of a standard chemistry lithium-ion battery obtained in that study is reported in Figure 8. As it can be seen, the electrode materials represent about half of the total cost of a battery, and in particular the anode represents the 24 %. The detailed breakdown analysis of the negative electrode (right part of the same figure) shows that more than the 80 % of this cost is due to the electrode active material2 and to its production process.

This could represent an additional disadvantage for the commercial exploitation of germanium since, as previously mentioned, this is classified as a critical raw material by the European Union. Moreover, according to the 2021 U.S. Minerals Yearbook, its price averaged around $ 1,000,000 per ton, to be compared with $ 1,400 per ton of graphite [152]. This difference in price would surely influence the final electrode cost, however the relatively low TRL of the technology presented in this work does not allow for a precise economical evaluation at this stage. In particular, some savings could come from the production process that does not involve binders or conductive agents, as well as the lack of any drying step that is typical for the standard graphite electrodes.

[2] Intended as the graphite plus the conductive agents and the binder.

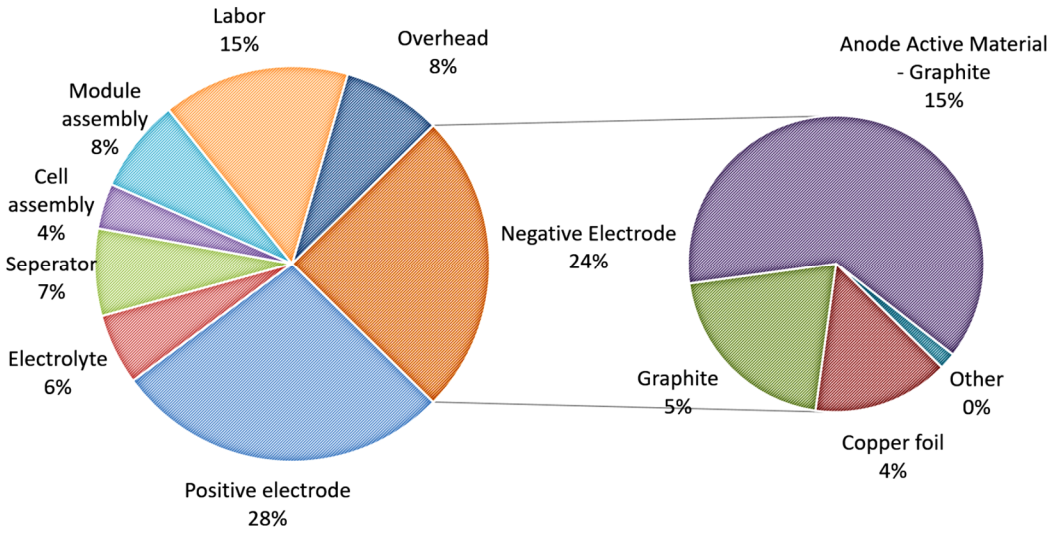

Figure 8: Cost breakdown of a typical graphite-based battery, with a special focus on the anode composition. The image is from ref. [151].

1.10. Convention about the terms “charge” and “discharge”

In conclusion of this chapter, some words are spent about the terms “charge” and “discharge”, which sometimes might be misleading. For example, if we consider a novel anodic material that is tested in a half-cell configuration (i.e., directly facing lithium metal as counter and reference electrode), the spontaneous process corresponds to the lithiation of the anodic material. Naturally, this is the spontaneous discharge of the half-cell. However, the lithiation of the anodic material corresponds to the charging process in full batteries, where the anode is faced for instance to an NMC cathode. This “ambiguity” arises because in the half-cell configuration the tested material actually constitutes the cathode of the cell. For this reason, the terms “charge” and “discharge” could be sometimes confusing, and expression like “lithiation” and “de-lithiation” or “reduction” and “oxidation” are usually preferred.

In this thesis, the terms “charge” and “discharge” are occasionally used in a generic way in Chapter 4 when referring to complete cycles of lithiation and de-lithiation.

References

[1] European commission - Directorate-general for Energies, “In focus: Batteries – a key enabler of a low-carbon economy,” Mar. 15, 2021. https://ec.europa.eu/info/news/focus-batteries-key-enabler-low-carbon-economy-2021-mar-15_en (accessed Apr. 09, 2021).

[2] Y. Liang *et al.*, “A review of rechargeable batteries for portable electronic devices,” *InfoMat*, vol. 1, no. 1, 2019, doi: 10.1002/inf2.12000.
[3] H. Jung *et al.*, “Elucidation of the local and long-range structural changes that occur in germanium anodes in lithium-ion batteries,” *Chem. Mater.*, vol. 27, no. 3, 2015, doi: 10.1021/cm504312x.
[4] J. T. Warner, *Lithium-Ion Battery Chemistries: A Primer*. Elsevier Science, 2019.
[5] J. Hao *et al.*, “A general method for high-performance Li-ion battery Ge composites electrodes from ionic liquid electrodeposition without binders or conductive agents: The cases of CNTs, RGO and PEDOT,” *Chem. Eng. J.*, vol. 346, 2018, doi: 10.1016/j.cej.2018.04.007.
[6] M. Winter and R. J. Brodd, “What are batteries, fuel cells, and supercapacitors?,” *Chem. Rev.*, vol. 104, no. 10, 2004, doi: 10.1021/cr020730k.
[7] T. B. Reddy, *Linden’s Handbook of Batteries, Fourth Edition*, 4th ed. New York: McGraw-Hill Education, 2011.
[8] R. A. Huggins, *Advanced batteries: Materials science aspects*. 2009.
[9] T. M. Gür, “Review of electrical energy storage technologies, materials and systems: Challenges and prospects for large-scale grid storage,” *Energy and Environmental Science*, vol. 11, no. 10. 2018, doi: 10.1039/c8ee01419a.
[10] C. Julien, A. Mauger, A. Vijh, and K. Zaghib, *Lithium Batteries: Science and Technology*. Springer International Publishing, 2015.
[11] A. Andreoli, “Porous germanium films as anode materials for lithium ion batteries,” University of Ferrara, Ferrara, 2016.
[12] O. Ramström, “Scientific Background on the Nobel Prize in Chemistry 2019 - Lithium-Ion Batteries,” *R. Swedish Acad. Sci.*, vol. 50005, pp. 1–13, 2019, [Online]. Available: https://www.nobelprize.org/prizes/chemistry/2019/advanced-information/.
[13] E. Kamali-Heidari, A. Kamyabi-Gol, M. Heydarzadeh Sohi, and A. Ataie, “Electrode materials for lithium ion batteries: a review,” *J. Ultrafine Grained Nanostructured Mater.*, vol. 51, no. 1, pp. 1–12, 2018.
[14] G. Zubi, R. Dufo-López, M. Carvalho, and G. Pasaoglu, “The lithium-ion battery: State of the art and future perspectives,” *Renewable and Sustainable Energy Reviews*, vol. 89. 2018, doi: 10.1016/j.rser.2018.03.002.
[15] W. Chen, J. Liang, Z. Yang, and G. Li, “A review of lithium-ion battery for electric vehicle applications and beyond,” in *Energy Procedia*, 2019, vol. 158, doi: 10.1016/j.egypro.2019.01.783.
[16] C. Pillot, “The rechargeable battery market and main trends 2018-2030,” 2019.
[17] Y. Borthomieu, “Satellite Lithium-Ion Batteries,” in *Lithium-Ion Batteries: Advances and Applications*, 2014.
[18] T. Kim, W. Song, D. Y. Son, L. K. Ono, and Y. Qi, “Lithium-ion batteries: outlook on present, future, and hybridized technologies,” *Journal of Materials Chemistry A*, vol. 7, no. 7. 2019, doi: 10.1039/C8TA10513H.
[19] X. Zeng *et al.*, “Commercialization of Lithium Battery Technologies for Electric Vehicles,” *Advanced Energy Materials*, vol. 9, no. 27. 2019, doi: 10.1002/aenm.201900161.
[20] F. Nadeem, S. M. S. Hussain, P. K. Tiwari, A. K. Goswami, and T. S. Ustun, “Comparative review of energy storage systems, their roles, and impacts on future power systems,” *IEEE Access*, vol. 7. 2019, doi: 10.1109/ACCESS.2018.2888497.
[21] S. Koohi-Fayegh and M. A. Rosen, “A review of energy storage types, applications and recent developments,” *Journal of Energy Storage*, vol. 27. 2020, doi: 10.1016/j.est.2019.101047.
[22] M. Li, J. Lu, Z. Chen, and K. Amine, “30 Years of Lithium-Ion Batteries,” *Advanced Materials*, vol. 30, no. 33. 2018, doi: 10.1002/adma.201800561.
[23] H. J. Kim *et al.*, “A comprehensive review of li-ion battery materials and their recycling techniques,” *Electronics (Switzerland)*, vol. 9, no. 7. 2020, doi: 10.3390/electronics9071161.
[24] Y. K. Sun, “High-Capacity Layered Cathodes for Next-Generation Electric Vehicles,” *ACS Energy Letters*, vol. 4, no. 5. 2019, doi: 10.1021/acsenergylett.9b00652.
[25] X. N. Penisa, M. T. Castro, J. D. A. Pascasio, E. A. Esparcia, O. Schmidt, and J. D. Ocon, “Projecting the price of lithium-ion NMC battery packs using a multifactor learning curve model,” *Energies*, vol. 13, no. 20, 2020, doi: 10.3390/en13205276.

[26] T. D. Bogart, A. M. Chockla, and B. A. Korgel, “High capacity lithium ion battery anodes of silicon and germanium,” *Current Opinion in Chemical Engineering*, vol. 2, no. 3. 2013, doi: 10.1016/j.coche.2013.07.001.
[27] K. Mizushima, P. C. Jones, P. J. Wiseman, and J. B. Goodenough, “LixCoO2 (0< x⩽ 1): A new cathode material for batteries of high energy density,” *Solid State Ionics*, vol. 3, pp. 171–174, 1981.
[28] A. Eftekhari, *Future Lithium-ion Batteries*. Royal Society of Chemistry, 2019.
[29] A. Manthiram, “A reflection on lithium-ion battery cathode chemistry,” *Nature Communications*, vol. 11, no. 1. 2020, doi: 10.1038/s41467-020-15355-0.
[30] D. Andrea, *Lithium-Ion Batteries and Applications: A Practical and Comprehensive Guide to Lithium-Ion Batteries and Arrays, from Toys to Towns, Volume 1, Batteries*, no. v. 1. Artech House, 2020.
[31] N. Voronina, Y.-K. Sun, and S.-T. Myung, “Co-Free Layered Cathode Materials for High Energy Density Lithium-Ion Batteries,” *ACS Energy Lett.*, vol. 5, no. 6, pp. 1814–1824, Jun. 2020, doi: 10.1021/acsenergylett.0c00742.
[32] F. Duffner, M. Wentker, M. Greenwood, and J. Leker, “Battery cost modeling: A review and directions for future research,” *Renewable and Sustainable Energy Reviews*, vol. 127. 2020, doi: 10.1016/j.rser.2020.109872.
[33] J. Kim, H. Lee, H. Cha, M. Yoon, M. Park, and J. Cho, “Prospect and Reality of Ni-Rich Cathode for Commercialization,” *Advanced Energy Materials*, vol. 8, no. 6. 2018, doi: 10.1002/aenm.201702028.
[34] S. Zhang, J. Ma, Z. Hu, G. Cui, and L. Chen, “Identifying and Addressing Critical Challenges of High-Voltage Layered Ternary Oxide Cathode Materials,” *Chemistry of Materials*, vol. 31, no. 16. 2019, doi: 10.1021/acs.chemmater.9b01557.
[35] H. Pan *et al.*, “Li- and Mn-rich layered oxide cathode materials for lithium-ion batteries: A review from fundamentals to research progress and applications,” *Molecular Systems Design and Engineering*, vol. 3, no. 5. 2018, doi: 10.1039/c8me00025e.
[36] R. Reinhardt, B. Amante García, L. Canals Casals, and S. Gassó Domingo, “A Critical Evaluation of Cathode Materials for Lithium-Ion Electric Vehicle Batteries,” 2019.
[37] J. D. Ocon, J. K. Lee, and J. Lee, “High energy density germanium anodes for next generation lithium ion batteries,” *Applied Chemistry for Engineering*, vol. 25, no. 1. 2014, doi: 10.14478/ace.2014.1008.
[38] H. Ying and W. Q. Han, “Metallic Sn-Based Anode Materials: Application in High-Performance Lithium-Ion and Sodium-Ion Batteries,” *Advanced Science*, vol. 4, no. 11. 2017, doi: 10.1002/advs.201700298.
[39] W. Li, X. Sun, and Y. Yu, “Si-, Ge-, Sn-Based Anode Materials for Lithium-Ion Batteries: From Structure Design to Electrochemical Performance,” *Small Methods*, vol. 1, no. 3. 2017, doi: 10.1002/smtd.201600037.
[40] X. Q. Zhang, X. B. Cheng, and Q. Zhang, “Advances in Interfaces between Li Metal Anode and Electrolyte,” *Advanced Materials Interfaces*, vol. 5, no. 2. 2018, doi: 10.1002/admi.201701097.
[41] D. Liu *et al.*, “Group IVA Element (Si, Ge, Sn)-Based Alloying/Dealloying Anodes as Negative Electrodes for Full-Cell Lithium-Ion Batteries,” *Small*, vol. 13, no. 45. 2017, doi: 10.1002/smll.201702000.
[42] P. Peljo and H. H. Girault, “Electrochemical potential window of battery electrolytes: The HOMO-LUMO misconception,” *Energy Environ. Sci.*, vol. 11, no. 9, 2018, doi: 10.1039/c8ee01286e.
[43] H. Zhao *et al.*, “Film-forming electrolyte additives for rechargeable lithium-ion batteries: Progress and outlook,” *Journal of Materials Chemistry A*, vol. 7, no. 15. 2019, doi: 10.1039/c9ta00126c.
[44] P. Verma, P. Maire, and P. Novák, “A review of the features and analyses of the solid electrolyte interphase in Li-ion batteries,” *Electrochimica Acta*, vol. 55, no. 22. 2010, doi: 10.1016/j.electacta.2010.05.072.
[45] M. Winter, “The solid electrolyte interphase - The most important and the least understood solid electrolyte in rechargeable Li batteries,” *Zeitschrift fur Phys. Chemie*, vol. 223, no. 10–11, 2009, doi: 10.1524/zpch.2009.6086.
[46] S. J. An, J. Li, C. Daniel, D. Mohanty, S. Nagpure, and D. L. Wood, “The state of

understanding of the lithium-ion-battery graphite solid electrolyte interphase (SEI) and its relationship to formation cycling," *Carbon*, vol. 105. 2016, doi: 10.1016/j.carbon.2016.04.008.

[47] S. K. Heiskanen, J. Kim, and B. L. Lucht, "Generation and Evolution of the Solid Electrolyte Interphase of Lithium-Ion Batteries," *Joule*, vol. 3, no. 10. 2019, doi: 10.1016/j.joule.2019.08.018.

[48] B. Scrosati and J. Garche, "Lithium batteries: Status, prospects and future," *Journal of Power Sources*, vol. 195, no. 9. 2010, doi: 10.1016/j.jpowsour.2009.11.048.

[49] L. Wang *et al.*, "Identifying the components of the solid–electrolyte interphase in Li-ion batteries," *Nat. Chem.*, vol. 11, no. 9, 2019, doi: 10.1038/s41557-019-0304-z.

[50] E. Peled and S. Menkin, "Review—SEI: Past, Present and Future," *J. Electrochem. Soc.*, vol. 164, no. 7, 2017, doi: 10.1149/2.1441707jes.

[51] A. Wang, S. Kadam, H. Li, S. Shi, and Y. Qi, "Review on modeling of the anode solid electrolyte interphase (SEI) for lithium-ion batteries," *npj Computational Materials*, vol. 4, no. 1. 2018, doi: 10.1038/s41524-018-0064-0.

[52] X. Yu and A. Manthiram, "Electrode-electrolyte interfaces in lithium-based batteries," *Energy and Environmental Science*, vol. 11, no. 3. 2018, doi: 10.1039/c7ee02555f.

[53] B. Horstmann, F. Single, and A. Latz, "Review on multi-scale models of solid-electrolyte interphase formation," *Current Opinion in Electrochemistry*, vol. 13. 2019, doi: 10.1016/j.coelec.2018.10.013.

[54] Z. Hu, S. Zhang, C. Zhang, and G. Cui, "High performance germanium-based anode materials," *Coordination Chemistry Reviews*, vol. 326. 2016, doi: 10.1016/j.ccr.2016.08.002.

[55] C. Liu, Z. G. Neale, and G. Cao, "Understanding electrochemical potentials of cathode materials in rechargeable batteries," *Materials Today*, vol. 19, no. 2. 2016, doi: 10.1016/j.mattod.2015.10.009.

[56] S. Goriparti, E. Miele, F. De Angelis, E. Di Fabrizio, R. Proietti Zaccaria, and C. Capiglia, "Review on recent progress of nanostructured anode materials for Li-ion batteries," *Journal of Power Sources*, vol. 257. 2014, doi: 10.1016/j.jpowsour.2013.11.103.

[57] V. Etacheri, R. Marom, R. Elazari, G. Salitra, and D. Aurbach, "Challenges in the development of advanced Li-ion batteries: A review," *Energy and Environmental Science*, vol. 4, no. 9. 2011, doi: 10.1039/c1ee01598b.

[58] C. Zhong, J. Z. Wang, X. W. Gao, D. Wexler, and H. K. Liu, "In situ one-step synthesis of a 3D nanostructured germanium-graphene composite and its application in lithium-ion batteries," *J. Mater. Chem. A*, vol. 1, no. 36, 2013, doi: 10.1039/c3ta11796k.

[59] S. Fang, L. Shen, H. Zheng, and X. Zhang, "Ge-graphene-carbon nanotube composite anode for high performance lithium-ion batteries," *J. Mater. Chem. A*, vol. 3, no. 4, 2015, doi: 10.1039/c4ta04350b.

[60] Z. Luo, Q. Xiao, G. Lei, Z. Li, and C. Tang, "Si nanoparticles/graphene composite membrane for high performance silicon anode in lithium ion batteries," *Carbon N. Y.*, vol. 98, 2016, doi: 10.1016/j.carbon.2015.11.031.

[61] N. Liu *et al.*, "Facile high-voltage sputtering synthesis of three-dimensional hierarchical porous nitrogen-doped carbon coated Si composite for high performance lithium-ion batteries," *Chem. Eng. J.*, vol. 343, 2018, doi: 10.1016/j.cej.2018.02.111.

[62] S. Sauze *et al.*, "Integration of 3D nanographene into mesoporous germanium," *Nanoscale*, vol. 12, no. 47, 2020, doi: 10.1039/d0nr04937a.

[63] J. Zhu, A. Liu, and D. Wang, "Study on the synergistic lithium storage performance of Sn/graphene nanocomposites via quantum chemical calculations and experiments," *Appl. Surf. Sci.*, vol. 416, 2017, doi: 10.1016/j.apsusc.2017.04.252.

[64] J. Lu, Z. Chen, F. Pan, Y. Cui, and K. Amine, "High-Performance Anode Materials for Rechargeable Lithium-Ion Batteries," *Electrochem. Energy Rev.*, vol. 1, no. 1, 2018, doi: 10.1007/s41918-018-0001-4.

[65] Z. A. Ghazi *et al.*, "Key Aspects of Lithium Metal Anodes for Lithium Metal Batteries," *Small*, vol. 15, no. 32. 2019, doi: 10.1002/smll.201900687.

[66] H. Wu, H. Jia, C. Wang, J. G. Zhang, and W. Xu, "Recent Progress in Understanding Solid Electrolyte Interphase on Lithium Metal Anodes," *Advanced Energy Materials*, vol. 11, no. 5. 2021, doi: 10.1002/aenm.202003092.

[67] L. Y. Lim, S. Fan, H. H. Hng, and M. F. Toney, "Storage Capacity and Cycling Stability in

Ge Anodes: Relationship of Anode Structure and Cycling Rate," *Adv. Energy Mater.*, vol. 5, no. 15, 2015, doi: 10.1002/aenm.201500599.
[68] Y. Yang *et al.*, "Silicon-nanoparticle-based composites for advanced lithium-ion battery anodes," *Nanoscale*, vol. 12, no. 14. 2020, doi: 10.1039/c9nr10652a.
[69] X. Zuo, J. Zhu, P. Müller-Buschbaum, and Y. J. Cheng, "Silicon based lithium-ion battery anodes: A chronicle perspective review," *Nano Energy*, vol. 31. 2017, doi: 10.1016/j.nanoen.2016.11.013.
[70] T. Kennedy, M. Brandon, and K. M. Ryan, "Advances in the Application of Silicon and Germanium Nanowires for High-Performance Lithium-Ion Batteries," *Adv. Mater.*, vol. 28, no. 27, 2016, doi: 10.1002/adma.201503978.
[71] H. Tian, F. Xin, X. Wang, W. He, and W. Han, "High capacity group-IV elements (Si, Ge, Sn) based anodes for lithium-ion batteries," *Journal of Materiomics*, vol. 1, no. 3. 2015, doi: 10.1016/j.jmat.2015.06.002.
[72] C. M. Park, J. H. Kim, H. Kim, and H. J. Sohn, "Li-alloy based anode materials for Li secondary batteries," *Chem. Soc. Rev.*, vol. 39, no. 8, 2010, doi: 10.1039/b919877f.
[73] D. Li, H. Wang, H. K. Liu, and Z. Guo, "A New Strategy for Achieving a High Performance Anode for Lithium Ion Batteries - Encapsulating Germanium Nanoparticles in Carbon Nanoboxes," *Advanced Energy Materials*, vol. 6, no. 5. 2016, doi: 10.1002/aenm.201501666.
[74] Y. Liu, S. Zhang, and T. Zhu, "Germanium-Based Electrode Materials for Lithium-Ion Batteries," *ChemElectroChem*, vol. 1, no. 4, 2014, doi: 10.1002/celc.201300195.
[75] X. Zhang, X. Cheng, and Q. Zhang, "Nanostructured energy materials for electrochemical energy conversion and storage: A review," *Journal of Energy Chemistry*, vol. 25, no. 6. 2016, doi: 10.1016/j.jechem.2016.11.003.
[76] S. Choi *et al.*, "Mesoporous Germanium Anode Materials for Lithium-Ion Battery with Exceptional Cycling Stability in Wide Temperature Range," *Small*, vol. 13, no. 13, 2017, doi: 10.1002/smll.201603045.
[77] B. Xu, "Silicon-based anode materials for lithium-ion batteries," The University of Queensland, 2016.
[78] P. Dou, Z. Cao, C. Wang, J. Zheng, and X. Xu, "Ultrafine Sn nanoparticles embedded in shell of N-doped hollow carbon spheres as high rate anode for lithium-ion batteries," *Appl. Surf. Sci.*, vol. 404, 2017, doi: 10.1016/j.apsusc.2017.01.253.
[79] L. S. Roselin *et al.*, "Recent advances and perspectives of carbon-based nanostructures as anode materials for Li-ion batteries," *Materials*, vol. 12, no. 8. 2019, doi: 10.3390/ma12081229.
[80] X. Xiao, X. Li, S. Zheng, J. Shao, H. Xue, and H. Pang, "Nanostructured Germanium Anode Materials for Advanced Rechargeable Batteries," *Advanced Materials Interfaces*, vol. 4, no. 6. 2017, doi: 10.1002/admi.201600798.
[81] W. Zhang, Y. Zhang, Z. Yang, G. Chen, G. Ma, and Q. Wang, "In-situ design and construction of lithium-ion battery electrodes on metal substrates with enhanced performances: A brief review," in *Chinese Journal of Chemical Engineering*, 2016, vol. 24, no. 1, doi: 10.1016/j.cjche.2015.07.015.
[82] L. Zhang *et al.*, "Advanced Matrixes for Binder-Free Nanostructured Electrodes in Lithium-Ion Batteries," *Advanced Materials*, vol. 32, no. 24. 2020, doi: 10.1002/adma.201908445.
[83] W. Qi, J. G. Shapter, Q. Wu, T. Yin, G. Gao, and D. Cui, "Nanostructured anode materials for lithium-ion batteries: Principle, recent progress and future perspectives," *J. Mater. Chem. A*, vol. 5, no. 37, 2017, doi: 10.1039/c7ta05283a.
[84] W. F. Sheehan, "Periodic table of elements with emphasis," *Chemistry (Easton).*, vol. 49, no. 3, pp. 17–18, 1976.
[85] A. M. Chockla, K. C. Klavetter, C. B. Mullins, and B. A. Korgel, "Solution-grown germanium nanowire anodes for lithium-ion batteries," *ACS Appl. Mater. Interfaces*, vol. 4, no. 9, 2012, doi: 10.1021/am3010253.
[86] F. Dou, L. Shi, G. Chen, and D. Zhang, "Silicon/Carbon Composite Anode Materials for Lithium-Ion Batteries," *Electrochem. Energy Rev.*, vol. 2, no. 1, 2019, doi: 10.1007/s41918-018-00028-w.
[87] P. Li *et al.*, "Recent progress on silicon-based anode materials for practical lithium-ion battery applications," *Energy Storage Materials*, vol. 15. 2018, doi:

10.1016/j.ensm.2018.07.014.
[88] X. Shen *et al.*, "Research progress on silicon/carbon composite anode materials for lithium-ion battery," *Journal of Energy Chemistry*, vol. 27, no. 4. 2018, doi: 10.1016/j.jechem.2017.12.012.
[89] J. W. Choi and D. Aurbach, "Promise and reality of post-lithium-ion batteries with high energy densities," *Nature Reviews Materials*, vol. 1. 2016, doi: 10.1038/natrevmats.2016.13.
[90] T. Chen, J. Wu, Q. Zhang, and X. Su, "Recent advancement of SiOx based anodes for lithium-ion batteries," *Journal of Power Sources*, vol. 363. 2017, doi: 10.1016/j.jpowsour.2017.07.073.
[91] A. Kwade, W. Haselrieder, R. Leithoff, A. Modlinger, F. Dietrich, and K. Droeder, "Current status and challenges for automotive battery production technologies," *Nature Energy*, vol. 3, no. 4. 2018, doi: 10.1038/s41560-018-0130-3.
[92] S. Yoon, C. M. Park, and H. J. Sohn, "Electrochemical characterizations of germanium and carbon-coated germanium composite anode for lithium-ion batteries," *Electrochem. Solid-State Lett.*, vol. 11, no. 4, 2008, doi: 10.1149/1.2836481.
[93] J. Hao, Y. Wang, Q. Guo, J. Zhao, and Y. Li, "Structural Strategies for Germanium-Based Anode Materials to Enhance Lithium Storage," *Particle and Particle Systems Characterization*, vol. 36, no. 9. 2019, doi: 10.1002/ppsc.201900248.
[94] W. Liang *et al.*, "Tough germanium nanoparticles under electrochemical cycling," *ACS Nano*, vol. 7, no. 4, 2013, doi: 10.1021/nn400330h.
[95] M. Pharr, Y. S. Choi, D. Lee, K. H. Oh, and J. J. Vlassak, "Measurements of stress and fracture in germanium electrodes of lithium-ion batteries during electrochemical lithiation and delithiation," *J. Power Sources*, vol. 304, 2016, doi: 10.1016/j.jpowsour.2015.11.036.
[96] M. Shao, "In situ microscopic studies on the structural and chemical behaviors of lithium-ion battery materials," *Journal of Power Sources*, vol. 270. 2014, doi: 10.1016/j.jpowsour.2014.07.123.
[97] S. W. Lee, I. Ryu, W. D. Nix, and Y. Cui, "Fracture of crystalline germanium during electrochemical lithium insertion," *Extrem. Mech. Lett.*, vol. 2, no. 1, 2015, doi: 10.1016/j.eml.2015.01.009.
[98] T. Kennedy, E. Mullane, H. Geaney, M. Osiak, C. O'Dwyer, and K. M. Ryan, "High-performance germanium nanowire-based lithium-ion battery anodes extending over 1000 cycles through in situ formation of a continuous porous network," *Nano Lett.*, vol. 14, no. 2, pp. 716–723, 2014, doi: 10.1021/nl403979s.
[99] E. Mullane, T. Kennedy, H. Geaney, and K. M. Ryan, "A rapid, solvent-free protocol for the synthesis of germanium nanowire lithium-ion anodes with a long cycle life and high rate capability," *ACS Appl. Mater. Interfaces*, vol. 6, no. 21, pp. 18800–18807, 2014, doi: 10.1021/am5045168.
[100] S. Goriparti *et al.*, "Facile synthesis of Ge-MWCNT nanocomposite electrodes for high capacity lithium ion batteries," *J. Mater. Chem. A*, vol. 5, no. 37, 2017, doi: 10.1039/c7ta04971d.
[101] H. Geaney *et al.*, "Enhancing the performance of germanium nanowire anodes for Li-ion batteries by direct growth on textured copper," *Chem. Commun.*, vol. 55, no. 54, 2019, doi: 10.1039/c9cc03579f.
[102] N. Bensalah, F. Z. Kamand, N. Mustafa, and M. Matalqeh, "Silicon–Germanium bilayer sputtered onto a carbon nanotube sheet as anode material for lithium–ion batteries," *J. Alloys Compd.*, vol. 811, 2019, doi: 10.1016/j.jallcom.2019.152088.
[103] U. Gulzar *et al.*, "Nitrogen-doped single walled carbon nanohorns enabling effective utilization of Ge nanocrystals for next generation lithium ion batteries," *Electrochim. Acta*, vol. 298, 2019, doi: 10.1016/j.electacta.2018.11.130.
[104] Y. Wang, S. Luo, M. Chen, and L. Wu, "Uniformly Confined Germanium Quantum Dots in 3D Ordered Porous Carbon Framework for High-Performance Li-ion Battery," *Adv. Funct. Mater.*, vol. 30, no. 16, 2020, doi: 10.1002/adfm.202000373.
[105] T. H. Kim, H. K. Song, and S. Kim, "Production of germanium nanoparticles via laser pyrolysis for anode materials of lithium-ion batteries and sodium-ion batteries," *Nanotechnology*, vol. 30, no. 27, 2019, doi: 10.1088/1361-6528/ab0aa1.
[106] M. Zhao, D. L. Zhao, X. Y. Han, H. X. Yang, Y. J. Duan, and X. M. Tian, "Ge nanoparticles embedded in spherical ordered mesoporous carbon as anode material for high performance

lithium ion batteries," *Electrochim. Acta*, vol. 287, 2018, doi: 10.1016/j.electacta.2018.08.050.
[107] W. Wei *et al.*, "Confined metal Ge quantum dots in carbon nanofibers for stable rechargeable batteries," *Nanoscale*, vol. 10, no. 15, 2018, doi: 10.1039/c8nr00153g.
[108] D. McNulty, H. Geaney, D. Buckley, and C. O'Dwyer, "High capacity binder-free nanocrystalline GeO2 inverse opal anodes for Li-ion batteries with long cycle life and stable cell voltage," *Nano Energy*, vol. 43, 2018, doi: 10.1016/j.nanoen.2017.11.007.
[109] S. Geier, R. Jung, K. Peters, H. A. Gasteiger, D. Fattakhova-Rohlfing, and T. F. Fässler, "A wet-chemical route for macroporous inverse opal Ge anodes for lithium ion batteries with high capacity retention," *Sustain. Energy Fuels*, vol. 2, no. 1, 2018, doi: 10.1039/c7se00422b.
[110] D. Kwon *et al.*, "Synthesis of dual porous structured germanium anodes with exceptional lithium-ion storage performance," *J. Power Sources*, vol. 374, 2018, doi: 10.1016/j.jpowsour.2017.11.044.
[111] K. Mishra, X. C. Liu, F. S. Ke, and X. D. Zhou, "Porous germanium enabled high areal capacity anode for lithium-ion batteries," *Compos. Part B Eng.*, vol. 163, 2019, doi: 10.1016/j.compositesb.2018.10.076.
[112] X. H. Liu *et al.*, "In situ TEM experiments of electrochemical lithiation and delithiation of individual nanostructures," *Advanced Energy Materials*, vol. 2, no. 7. 2012, doi: 10.1002/aenm.201200024.
[113] L. Y. Lim, N. Liu, Y. Cui, and M. F. Toney, "Understanding phase transformation in crystalline Ge anodes for Li-ion batteries," *Chem. Mater.*, vol. 26, no. 12, 2014, doi: 10.1021/cm501233k.
[114] J. Doherty *et al.*, "Germanium tin alloy nanowires as anode materials for high performance Li-ion batteries," *Nanotechnology*, vol. 31, no. 16, 2020, doi: 10.1088/1361-6528/ab6678.
[115] D. McNulty, S. Biswas, S. Garvey, C. O'Dwyer, and J. D. Holmes, "Directly Grown Germanium Nanowires from Stainless Steel: High-performing Anodes for Li-Ion Batteries," *ACS Appl. Energy Mater.*, vol. 3, no. 12, pp. 11811–11819, 2020, doi: 10.1021/acsaem.0c01977.
[116] L. Baggetto and P. H. L. Notten, "Lithium-Ion (De)Insertion Reaction of Germanium Thin-Film Electrodes: An Electrochemical and In Situ XRD Study," *J. Electrochem. Soc.*, vol. 156, no. 3, 2009, doi: 10.1149/1.3055984.
[117] J. Graetz, C. C. Ahn, R. Yazami, and B. Fultz, "Nanocrystalline and Thin Film Germanium Electrodes with High Lithium Capacity and High Rate Capabilities," *J. Electrochem. Soc.*, vol. 151, no. 5, 2004, doi: 10.1149/1.1697412.
[118] Y. Kim, H. Hwang, K. Lawler, S. W. Martin, and J. Cho, "Electrochemical behavior of Ge and GeX2 (X = O, S) glasses: Improved reversibility of the reaction of Li with Ge in a sulfide medium," *Electrochim. Acta*, vol. 53, no. 15, 2008, doi: 10.1016/j.electacta.2007.12.015.
[119] X. H. Liu, S. Huang, S. T. Picraux, J. Li, T. Zhu, and J. Y. Huang, "Reversible nanopore formation in Ge nanowires during lithiation- delithiation cycling: An in situ transmission electron microscopy study," *Nano Lett.*, vol. 11, no. 9, 2011, doi: 10.1021/nl2024118.
[120] F. W. Yuan, H. J. Yang, and H. Y. Tuan, "Alkanethiol-passivated Ge nanowires as high-performance anode materials for lithium-ion batteries: The role of chemical surface functionalization," *ACS Nano*, vol. 6, no. 11, 2012, doi: 10.1021/nn303519g.
[121] X. Zhou *et al.*, "In Situ Focused Ion Beam-Scanning Electron Microscope Study of Crack and Nanopore Formation in Germanium Particle during (De)lithiation," *ACS Appl. Energy Mater.*, vol. 2, no. 4, 2019, doi: 10.1021/acsaem.9b00380.
[122] C. K. Chan, X. F. Zhang, and Y. Cui, "High capacity Li ion battery anodes using Ge nanowires," *Nano Lett.*, vol. 8, no. 1, 2008, doi: 10.1021/nl0727157.
[123] Y. Yue and H. Liang, "3D Current Collectors for Lithium-Ion Batteries: A Topical Review," *Small Methods*, vol. 2, no. 8, 2018, doi: 10.1002/smtd.201800056.
[124] S. Y. Kim, C. H. Kim, and C. M. Yang, "Binder-free silicon anodes wrapped in multiple graphene shells for high-performance lithium-ion batteries," *J. Power Sources*, vol. 486, 2021, doi: 10.1016/j.jpowsour.2020.229350.
[125] K. T. Chen, W. C. Chang, H. J. Yang, C. Y. Tsai, S. B. Huang, and H. Y. Tuan, "Free standing Si (Ge) nanowire/Cu nanowire composites as lithium ion battery anodes," *J.*

Taiwan Inst. Chem. Eng., vol. 104, 2019, doi: 10.1016/j.jtice.2019.07.014.
[126] K. Stokes, W. Boonen, H. Geaney, T. Kennedy, D. Borsa, and K. M. Ryan, "Tunable Core-Shell Nanowire Active Material for High Capacity Li-Ion Battery Anodes Comprised of PECVD Deposited aSi on Directly Grown Ge Nanowires," *ACS Appl. Mater. Interfaces*, vol. 11, no. 21, 2019, doi: 10.1021/acsami.9b03931.
[127] E. Foreman *et al.*, "A Review of Inactive Materials and Components of Flexible Lithium-Ion Batteries," *Advanced Sustainable Systems*, vol. 1, no. 11. 2017, doi: 10.1002/adsu.201700061.
[128] T. Chen, Q. Zhang, J. Xu, J. Pan, and Y. T. Cheng, "Binder-free lithium ion battery electrodes made of silicon and pyrolized lignin†," *RSC Adv.*, vol. 6, no. 35, 2016, doi: 10.1039/c6ra03001g.
[129] M. A. González, A. C. Marschilok, and E. Reichmanis, "Perspective—Enhancing Active Anode Material Performance for Lithium-Ion Batteries via Manipulation of Interfacial Chemistry," *J. Electrochem. Soc.*, vol. 167, no. 5, 2020, doi: 10.1149/1945-7111/ab6a8a.
[130] Y. Shi, X. Zhou, and G. Yu, "Material and Structural Design of Novel Binder Systems for High-Energy, High-Power Lithium-Ion Batteries," *Acc. Chem. Res.*, vol. 50, no. 11, 2017, doi: 10.1021/acs.accounts.7b00402.
[131] S. N. Bryntesen, A. H. Strømman, I. Tolstorebrov, P. R. Shearing, J. J. Lamb, and O. Stokke Burheim, "Opportunities for the State-of-the-Art Production of LIB Electrodes—A Review," *Energies*, vol. 14, no. 5, 2021, doi: 10.3390/en14051406.
[132] Y. Kang *et al.*, "Binder-Free Electrodes and Their Application for Li-Ion Batteries," *Nanoscale Research Letters*, vol. 15, no. 1. 2020, doi: 10.1186/s11671-020-03325-w.
[133] K. K. Sarode, R. Choudhury, and S. K. Martha, "Binder and conductive additive free silicon electrode architectures for advanced lithium-ion batteries," *J. Energy Storage*, vol. 17, 2018, doi: 10.1016/j.est.2018.04.002.
[134] H. Rezk, A. M. Nassef, M. A. Abdelkareem, A. H. Alami, and A. Fathy, "Comparison among various energy management strategies for reducing hydrogen consumption in a hybrid fuel cell/supercapacitor/battery system," *Int. J. Hydrogen Energy*, vol. 46, no. 8, 2021, doi: 10.1016/j.ijhydene.2019.11.195.
[135] A. A. Kamel, H. Rezk, and M. A. Abdelkareem, "Enhancing the operation of fuel cell-photovoltaic-battery-supercapacitor renewable system through a hybrid energy management strategy," *Int. J. Hydrogen Energy*, vol. 46, no. 8, pp. 6061–6075, 2021.
[136] H. Zhang, J. Yang, J. Zhang, P. Song, and M. Li, "Optimal energy management of a fuel cell-battery-supercapacitor-powered hybrid tramway using a multi-objective approach," *Proc. Inst. Mech. Eng. Part F J. Rail Rapid Transit*, vol. 234, no. 5, 2020, doi: 10.1177/0954409719849804.
[137] Y. Wang, D. F. Ruiz Diaz, K. S. Chen, Z. Wang, and X. C. Adroher, "Materials, technological status, and fundamentals of PEM fuel cells – A review," *Materials Today*, vol. 32. 2020, doi: 10.1016/j.mattod.2019.06.005.
[138] H. Fathabadi, "Novel fuel cell/battery/supercapacitor hybrid power source for fuel cell hybrid electric vehicles," *Energy*, vol. 143, 2018, doi: 10.1016/j.energy.2017.10.107.
[139] A. Opitz, P. Badami, L. Shen, K. Vignarooban, and A. M. Kannan, "Can Li-Ion batteries be the panacea for automotive applications?," *Renewable and Sustainable Energy Reviews*, vol. 68. 2017, doi: 10.1016/j.rser.2016.10.019.
[140] S. Gherairi, "Hybrid electric vehicle: Design and control of a hybrid system (fuel cell/battery/ultra-capacitor) supplied by hydrogen," *Energies*, vol. 12, no. 7, 2019, doi: 10.3390/en12071272.
[141] S. Changizian, P. Ahmadi, M. Raeesi, and N. Javani, "Performance optimization of hybrid hydrogen fuel cell-electric vehicles in real driving cycles," *Int. J. Hydrogen Energy*, vol. 45, no. 60, 2020, doi: 10.1016/j.ijhydene.2020.01.015.
[142] S. Wu *et al.*, "Germanium-Based Nanomaterials for Rechargeable Batteries," *Angewandte Chemie - International Edition*, vol. 55, no. 28. 2016, doi: 10.1002/anie.201509651.
[143] European Commission, "Study on the EU's list of Critical Raw Materials (2020)," 2020.
[144] J. Qin and M. Cao, "Multidimensional Germanium-Based Materials as Anodes for Lithium-Ion Batteries," *Chemistry - An Asian Journal*, vol. 11, no. 8. 2016, doi: 10.1002/asia.201600005.
[145] T. P. Barrera and M. L. Wasz, "Spacecraft li-ion battery power system state-of-practice: A

critical review," 2018, doi: 10.2514/6.2018-4495.
[146] K. B. Chin *et al.*, "Energy Storage Technologies for Small Satellite Applications," *Proc. IEEE*, vol. 106, no. 3, 2018, doi: 10.1109/JPROC.2018.2793158.
[147] V. Knap, L. K. Vestergaard, and D. I. Stroe, "A review of battery technology in cubesats and small satellite solutions," *Energies*, vol. 13, no. 15. 2020, doi: 10.3390/en13164097.
[148] P. J. Dalton, E. Bowens, T. North, and S. Balcer, "International Space Station Lithium-Ion Battery Start-Up and Cycling," *NASA Aerospace Battery Workshop*. 2017.
[149] I. Tzinis, "Technology Readiness Level," *National Aeronautics and Space Administration*, Oct. 28, 2012. https://www.nasa.gov/directorates/heo/scan/engineering/technology/technology_readiness_level (accessed Apr. 07, 2021).
[150] ESA-ESTEC, "ECSS-E-HB-11A Space engineering Technology readiness level (TRL) guidelines," *ECSS Standard*, no. March. ESA-ESTEC, 2017, Accessed: Apr. 07, 2021. [Online]. Available: https://ecss.nl/home/ecss-e-hb-11a-technology-readiness-level-trl-guidelines-1-march-2017/.
[151] G. Berckmans, M. Messagie, J. Smekens, N. Omar, L. Vanhaverbeke, and J. Van Mierlo, "Cost projection of state of the art lithium-ion batteries for electric vehicles up to 2030," *Energies*, vol. 10, no. 9, 2017, doi: 10.3390/en10091314.
[152] U.S. Geological Survey, "Mineral Commodity Summaries 2021," 2021.
[153] D. V. Ragone, "Review of battery systems for electrically powered vehicles," 1968, doi: 10.4271/680453.

2. Materials and methods

2.1. Introduction

As previously stated, the motivation of this thesis work was to realize and characterize germanium-based nano-structured anodes to be tested in LIBs, recurring to fabrication processes that make use of techniques which are already standards in the industry of semiconductor. In this chapter, the details of this fabrication processes are presented.

The germanium anodes that are realized and characterized in this work consist in nano-structured thin films which are fabricated by means of two processes using a top-down approach.

Both the processes start with the deposition of a thin germanium film onto the current collector substrate. This is performed by means of the LEPECVD technique, which is the first described in this chapter. The main features of this instrumentation are presented, illustrating the best deposition parameters and the expected film properties derived from previous works. Then, the experimental data of many depositions is analysed as a check.

Afterwards, the thin films are nano-structured: this is necessary to realize the compliant structures that can reversibly accommodate the volumetric variations of the active material and is performed recurring to one out of two different techniques, the HF electrochemical attack or the Ion Implantation. The use of different nano-structuration techniques permitted to obtain samples with different morphologies to be compared.

The electrochemical etching is treated first, presenting the theoretical basis of the germanium anodic dissolution in HF. The lab-made experimental setup that was used and the macroscopic appearance of the processed samples are also presented. Some of the main experimental results are deepened and their correspondence with the theoretical model is evaluated.

Finally, the Ion Implantation process is introduced, starting from the basic principles of the nano-structure formation and their main morphological features. The need for a different deposition time as well as some possible drawbacks of the dedicated deposition masks are explained. The motivation behind the choice of the implantation recipes adopted to produce different morphologies is also covered on the basis of the damage map model developed by Darby *et al.* [1].

The overall processes presented in this chapter represent a top-down approach in the fabrication of the electrodes. This differentiates the present work from that which represent the main research path, consisting of bottom-up solutions [2]. This is a convenient approach as it permits to avoid the use of materials that typically lower the overall gravimetric capacity of the electrodes, as they represent "dead-weight" in the final balance. Furthermore, the use of techniques that already represent standards in the semiconductor industry could be helpful for the technological transfer from the academic research to real applications, as high throughput and already existing facilities could be exploited.

Before drawing some conclusions for this chapter, a brief explanation regarding the specific choice of Molybdenum and Stainless Steel as substrate materials is given.

2.2. **Plasma Enhanced Chemical Vapor Deposition**

A variety of Chemical Vapor Deposition (CVD) techniques exist that are all based on the same working principles: firstly, the precursors of the elements or compounds to be deposited are decomposed and then, the resulting reactive species, react chemically to produce a film on the target substrate.
The main difference between the various CVD techniques lies in the method by which the activation energy is delivered to the precursors and sustains the reaction. In most cases, this energy is furnished thermally by means of resistances, radiofrequency induction or photon irradiation from lamps. In general, also the target substrates are required to be kept at high temperature. [3][4][5]
Some advantages of CVD techniques, when compared to other systems like Molecular Beam Epitaxy (MBE) or Physical Vapor Deposition (PVD), are represented by a conformal growth of the layers, even on elaborately shaped pieces, and by relatively high deposition rates with high purity and good process control [4][6][7][8]. Instead, one main drawback, is the necessity to keep the substrates at high temperatures, which limits the substrate choice possibilities. [4][8][9]

Most of the samples studied in this work were fabricated using a particular type of CVD, namely a Plasma Enhanced Chemical Vapor Deposition (PECVD). In this system, non-thermal energy is provided by a glow discharge induced by a radio frequency (RF) that

dissociates the carrier and precursor gases employed. This permits to grow films on low temperature substrates, thus overcoming the main issue of standard CVD techniques, and enables deposition even on substrates that do not have the thermal stability to accept coating by other methods. [3][4][10][11] Furthermore, the film composition results to be strictly equivalent to the precursor gas mixtures. [12][13]

The highly reactive species and the energetic ions generated in the plasma hit continuously the sample substrate thus favouring the mobility of the adsorbed particles, facilitating the rearrangement of the growing structures and helping the desorption of passivating species like hydrogen. [6][9][14]

This technique allows also for very high deposition rates, up to 10 nm/s [6][15], which represent a key point to achieve high throughputs as required by the semiconductor industry. Thanks to these advantages, PECVD represents nowadays a common industrial technique and is extensively used in many fields like microelectronics, photovoltaic and photonic, optics (antireflective coatings, optical waveguides, interference filters), sensors and packaging [3][15][16].

2.2.1. The low energy PECVD equipment

The schematic of the PECVD equipment installed in the clean rooms of the Physics and Earth Science Department of the University of Ferrara is shown in Figure 9.

The PECVD reactor chamber is made out of stainless steel with the RF antenna placed at its bottom. Hydrogen (H_2) is fluxed to ignite the plasma and has a function of carrier for the precursor gases during the process. Both the carrier and the precursor gases are injected from a molybdenum ring placed in proximity of the sample, on the bottom part of the chamber. For this work, only germane (GeH_4) was used as precursor gas.

The samples are hosted in a quartz holder placed in front of the plasma plume, in proximity of the gas ring. This is electrically insulated, inducing a negative self-biasing during the discharge which accelerates the ions towards the samples. Furthermore, the samples are loaded facing down to prevent that eventual particles present could fall and accumulate on their surface. Finally, graphite heaters, placed above the sample holder, permit the temperature management during the deposition process.

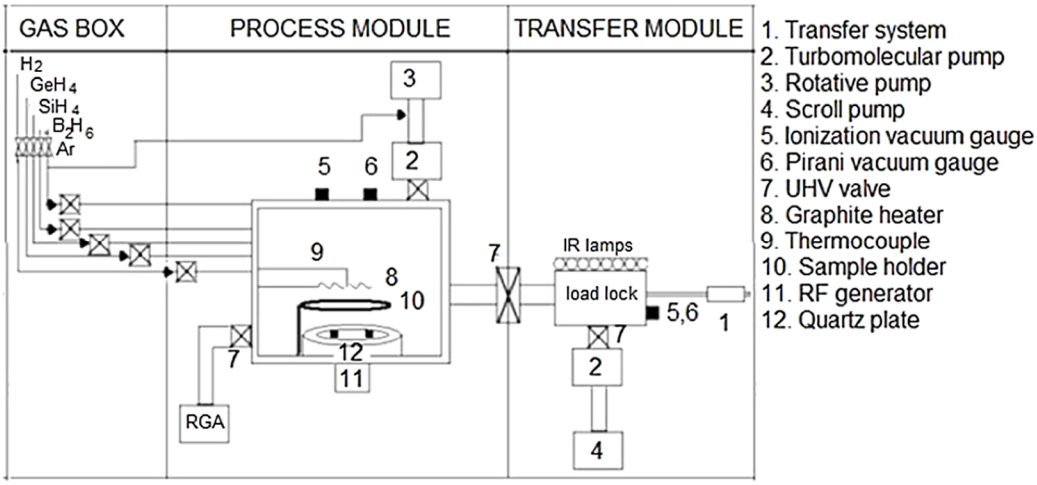

Figure 9: Schematic of the PECVD equipment at University of Ferrara, from ref. [6].

The plasma is excited at a frequency of 13.56 MHz, which allows only electrons to be effectively accelerated [14], and the energy transfer to the heavy particles occurs via collisions. The resulting plasma has a low degree of ionization, around 1 % at maximum, and the energy distribution is strongly asymmetric with electrons being far more energetic than ions (which remain essentially at room temperature): this is usually referred to as a "non-equilibrium" plasma [9]. The ion energy was measured as a function of the chamber pressure by the PECVD manufacturer and is shown in Figure 10. To prevent sample damages or sputtering from ion bombardment, the ion energy should be less than 15 eV [12]: for this reason, the pressure is kept in the range of $10^{-2} \div 10^{-3}$ mbar during deposition. This configuration, with reduced ion energy, is usually referred to as Low Energy PECVD (LEPECVD).

To guarantee minimal contaminations of the reaction chamber, a turbomolecular and a rotary pre-vacuum pump evacuate the chamber at a base pressure of 10^{-8} mbar. For the same reason, the samples are loaded by means of a load lock separated from the main chamber via a gate valve. In addition, the load lock is equipped with infrared lamps to promote desorption of water and other species.

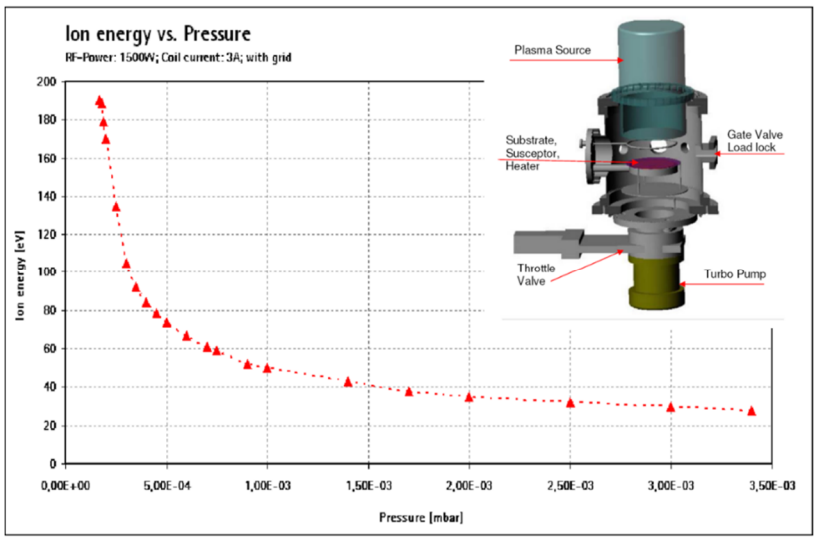

Figure 10: Ion energy inside the plasma as a function of the pressure in the PECVD reactor [17].

2.2.2. Seed-layer-free deposition and substrates cleaning procedure

The LEPECVD process previously described enabled the direct deposition of thin films onto the metallic current collectors, which is an essential requirement to permit the production of anodes without resorting to the slurry-based procedure. The good-adhered films are subsequently nano-structured to obtain the final electrode morphologies, without requiring any binder or conductive agents as these are already strongly connected mechanically and electrically to their substrates. An additional advantage, which was experimentally observed, is that LEPECVD permit the deposition without the needing of any seed-layer on the current collectors. This brings a two-fold benefit that is the lack of any additional material that could interfere in the reactions, eventually influencing the overall capacity of the electrochemical process, and the reduction of the fabrication steps. [18]

A cleaning process of the substrate materials is the only preliminary step performed prior to the deposition. This consists of a sequential rinsing in dichloromethane (RPE grade, CARLO ERBA Reagents), acetone (purity > 99.5 %, CARLO ERBA Reagents), 2-propanol (purity > 99.8 %, Sigma-Aldrich) and de-ionized water.

2.2.3. Deposition parameters and growth rate

The "best" deposition parameters were identified in some previous works [17][19] as those process chamber settings that enabled the better trade-off between the film thickness homogeneity across the surface and fast deposition processes (namely, high growth rates). These parameters are the gas carrier and precursor fluxes, the graphite heater power and the RF antenna power, whose values are all reported in Table 4:

Main chamber heater		**Gas fluxes (sccm)**	
Power (%)[1]	**Substrate temperature (°C)**	**H2 (carrier)**	**GeH4 (precursor)**
20	420	35	15

Table 4: LEPECVD deposition parameters

To identify this as the best combination, various depositions were performed varying the experimental conditions. The thin films were realized on flat silicon wafers and their profiles, composition and surface roughness were evaluated. In particular, for the deposition recipe presented in Table 4, a thickness variance of 10 % was measured from interferometric profile analysis between the highest and the lowest points across the entire wafer surface. In addition, a root mean square roughness of 2.8 nm was determined using AFM [17].

The growth rate was calculated from the profile measurements, and independently confirmed by SIMS analysis [17][19], and its value was estimated to be:

$$\text{Growth rate} = r = 1.27 \pm 0.07 \text{ nm/s} \quad (12)$$

Since the same parameters were used for all the depositions realized in this work, the growth rate was the same in all the cases. According to this, the deposition time was varied to produce films of different thicknesses.

[1] This is expressed as the percentual of the maximum heater power, this being 1600 W.

2.2.4. Sample holders and film thickness

The quartz sample holder of the LEPECVD was originally designed to host standard 100 mm wafers, so specific masks were realized to lodge the metallic substrates used in this project. Two layouts were designed to host the two kinds of metallic substrates: the 3x3 cm square foils, for the electrochemical etching, and the 1.5 cm diameter disks for the ion implantation.

Both masks are made of stainless steel (AISI 316L) and the number of samples that each of them can host is the maximum allowed by the dimensional constraints from the quartz holder and the metallic substrates. For the etching-oriented mask, a maximum of 5 samples can be loaded for each deposition, while the ion implantation mask can accommodate up to 19 metallic disks.

Both types of masks are depicted in Figure 11: the samples are put in correspondence of the mask holes, through which the deposition occurs. The hole diameter in the etching mask (A) is 2.8 cm, while is 1.4 cm in the mask for ion-implantation (B).

A)

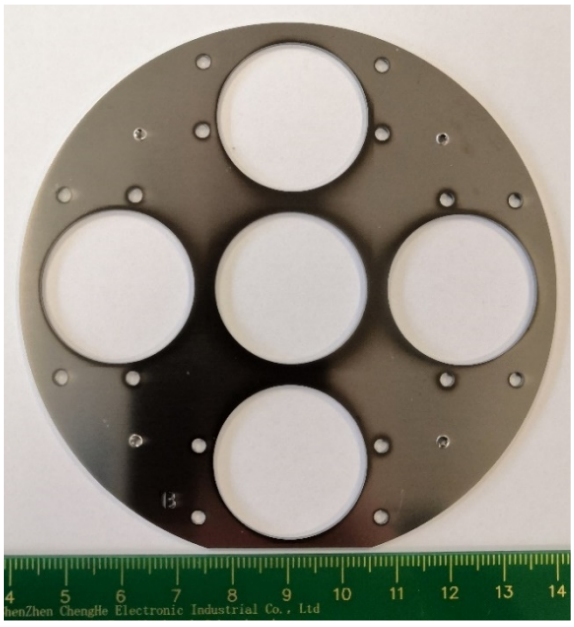

B)

Figure 11: The stainless-steel deposition masks for samples to be etched (A) or ion implanted (B).

Samples with different thicknesses were realized depending on the nano-structuration process. The reason behind this is that in the anodic oxidation process part of the germanium is removed, while for the samples that undergo ionic implantation the mass is not affected (sections 2.3 and 2.4). Therefore, thicker films were necessary for those samples destined to etching to compensate for the mass reduction.

When this thesis work started, a deposition thickness of 1 µm was chosen for the samples to be etched. For these samples, an average mass of about 0.3 mg of nano-structured germanium is calculated to remain in the electrode area after anodic oxidation (see section 2.3.6). To obtain similar mass loadings for the implanted anodes, 0.3 mg represents the target mass to be deposited. This loading was chosen as it was comparable to those found in other studies at the time of the beginning of this work [20][21][22][23][24][25].

The deposition times were calculated starting from the growth rate and making the following assumptions:

1) The deposition occurs uniformly across the substrate surface, namely same thickness and same density are achieved in all the points of the film,
2) The germanium density is considered equal to that of bulk germanium.

The first assumption implies considering an average thickness of the deposition, neglecting the 10 % of variance in thickness previously reported. Regarding the second assumption, this could be considered quite reasonable since crystalline domains were identified in the layers (see section 3.3.3). Taking this into account, the deposition times can be easily calculated from the growth rate as follows:

$$(13)\quad t_{deposition,\ etching} = \frac{film\ thickness}{growth\ rate} = \frac{h_{etch}}{r} = \frac{1\ \mu m}{1.27\ nm \cdot s^{-1}} \sim 787\ s \sim 13.1\ minutes$$

To find the deposition time for the implanted samples we must determine their thickness first, based on the target mass loading of 0.3 mg. It is important to consider that in this case the deposited area is smaller, being equal to that of the 1.4 cm holes in the deposition mask:

$$(14)\quad \text{Estimated thickness, implantation samples} = h_{impl} = \frac{m_{Ge,\ implantation}}{A_{deposted,\ implantation} \cdot \rho_{Ge}}$$

$$= \frac{0.3\ 10^{-3}\ g}{1.54 cm^2 \cdot 5.325\ g \cdot cm^{-3}} = 3.66 \cdot 10^{-5}\ cm = 366\ nm$$

And the deposition time is found as before:

$$(15)\quad t_{deposition,\ implantation} = \frac{h_{impl}}{r} = \frac{366\ nm}{1.27\ nm \cdot s^{-1}} \sim 288\ s$$

These values were then approximated to those listed in Table 5, which have been the effective deposition times used for all the depositions:

Samples for	Deposition time	Expected film thickness (nm)
Etching	14 min	1067
Ion Implantation	4 min 37 sec	352

Table 5: Deposition times for samples destined to etching or ion implantation.

For each deposition time, all the samples fabricated in this work were considered as identical, independently form their position on the deposition mask or the specific batch of production. Because of this, in the remainder of the text, they are distinguished only according to the deposition time. Of course, the effective mass of each sample has been always measured, to perform an estimation of the real thickness deposited. These values were used to perform the deposition uniformity review that is now presented.

2.2.5. Deposition uniformity review

A review was conducted on the deposition data from different batches of samples to assess the uniformity of the deposition process inside the reaction chamber. This constitutes a check of the evaluations carried out in the previous works, which highlighted a variance of 10 % on the thickness uniformity (cf. sec. 2.2.3).
The uniformity was analysed considering the mass of germanium deposited as a function of the samples position on the holder. These positions were labelled observing the holders from above and so, as described in section 2.2.1, the deposited side is the opposite.

For the etching-type samples, deposition data was analysed for the last 10 batches, corresponding to a total of 50 samples. A high replicability of the deposition process can be argued from part A of Figure 12, where the same trend can be clearly identified through all the 10 depositions. However, the graph highlights also a systematic inhomogeneity of the mass deposited on different positions. Furthermore, a certain degree of variability is observed also for each specific position. These things constitute an evidence that the deposition occurs in a non-uniform way over the mask surface exposed to the plasma.

The thickness variance can be considered equivalent to an analogous gravimetric quantity, given the assumption that the germanium density is constant. Under this hypothesis, a mass variability can be defined to be compared with the thickness variance as follows:

$$(16)\quad m_{var} = \frac{\overline{m_{Ge\ heaviest}} - \overline{m_{Ge\ lightest}}}{\overline{m_{Ge\ lightest}}} * 100 = 15.75\ \%$$

Where $m_{Ge\ heaviest}$ and $m_{Ge\ lightest}$ represent the mean values of the heaviest and lightest samples. That mass variability is undoubtedly higher than the thickness variance and confirms that the deposition occurred in a non-uniform way. Although, despite the ~6 % difference, this value is still considered in quite good agreement with that observed in the previous studies. In part C of Figure 12 is visually highlighted that more germanium is deposited on the central and bottom-left parts of the masks.

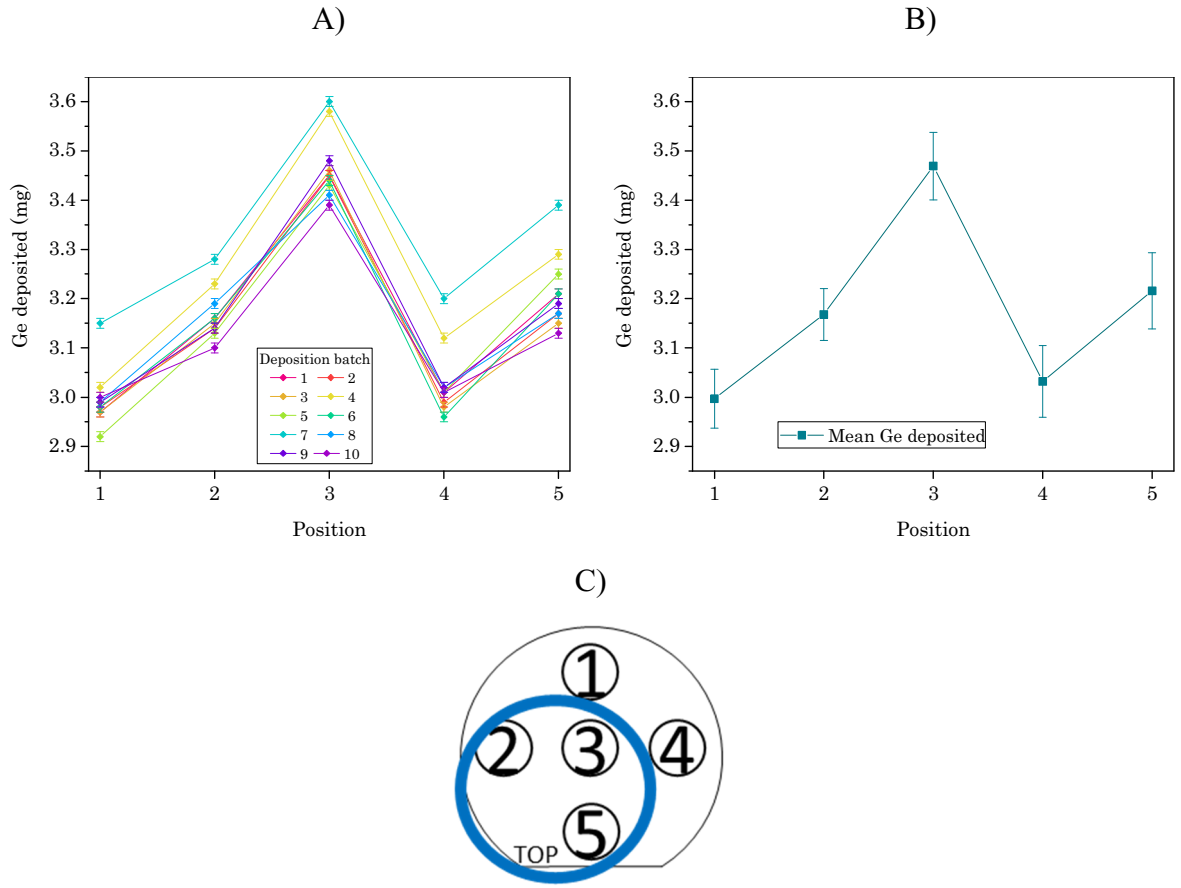

Figure 12: Mass of Ge deposited on the various positions of the etching-type masks. The masses deposited over the last 10 batches are depicted in A, while their mean values are reported in B. The position labelling is shown in C, where the blue circle highlights the region in which more Ge is deposited.

For the implantation mask, the deposition data of 3 batches were analysed, corresponding to a total of 57 samples. In this case, no clear deposition trend was identified apart from a slightly higher amount of germanium deposited in the central region. However, the mass variability is more than doubled with respect to the previous case:

$$(17)\quad m_{var} = \frac{\overline{m_{Ge\ heaviest}} - \overline{m_{Ge\ lightest}}}{\overline{m_{Ge\ lightest}}} * 100 = 35.82\ \%$$

This high variability reflects the large fluctuations of the deposited mass as a function of the position on the mask that can be seen in Figure 13. In addition, substantial differences are observed also for the mass deposited in each specific position. Such a variation could be related to the shorter deposition time required for the implanted samples, as this is the only variable modified between the two kinds of deposition. A possible explanation for this could be related to fluctuations of the plasma density inside the chamber that might self-balance over longer deposition times like that of the etching samples. Even the region where more germanium is deposited is different with respect to the etching mask, this time being the central part of the mask (orange circle in part C of Figure 13).

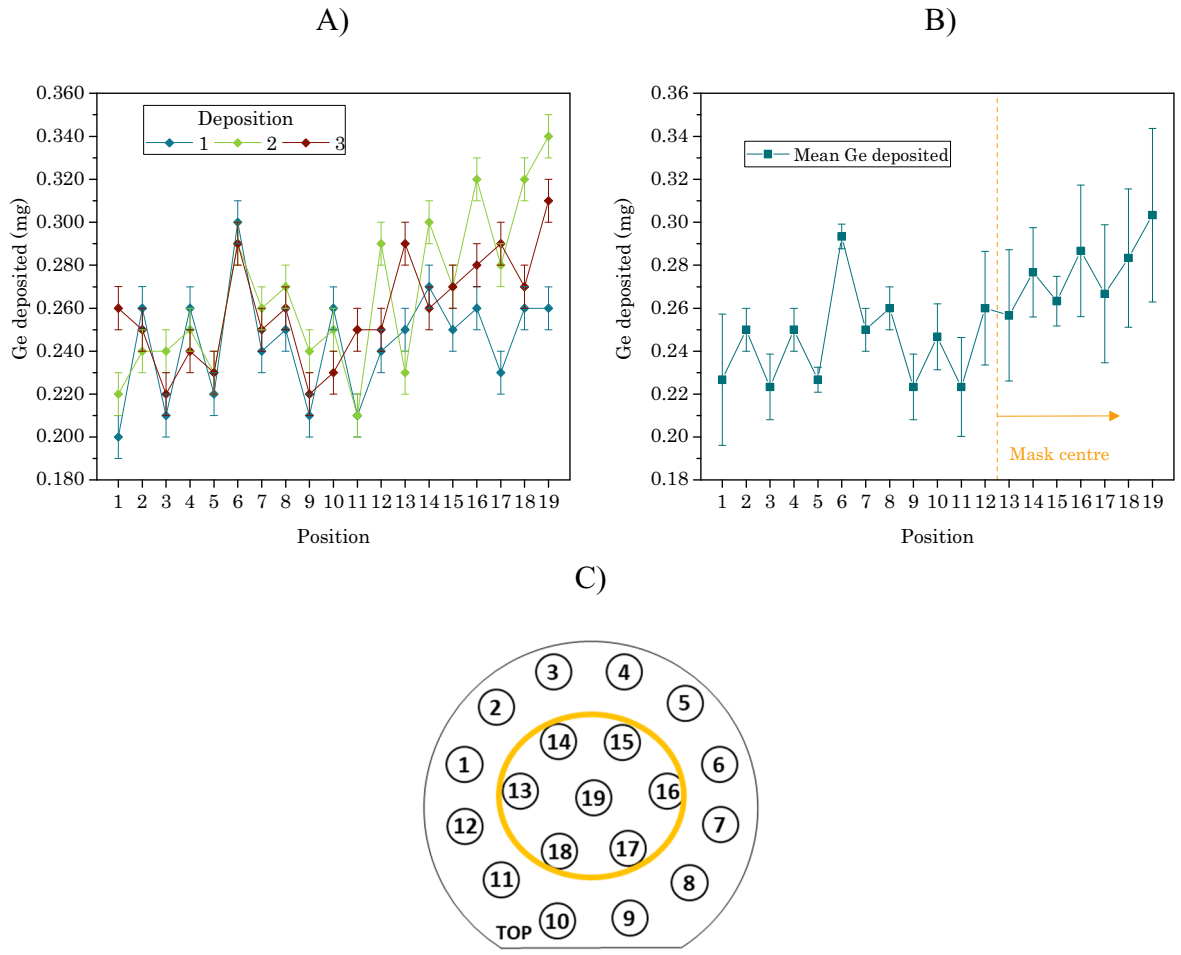

Figure 13: Mass of Ge deposited when using the ion-type masks. The masses deposited as a function of the position over the last 3 batches are depicted in A. In B their mean values are reported. The position labelling is shown in C, where the orange circle highlights the region where more Ge is deposited.

Due to the high uncertainty and to the reduced number of batches analysed, these results were considered only in a qualitative way as a confirmation that some deviations occurred with respect to the previous homogeneity studies.

2.3. **Electrochemical etching**

Electrochemical etching was one of the techniques used to realize the nano-structured electrodes of this thesis. This was carried out using HF electrolyte and a "laboratory-made" setup realized in the Physics Department of the University of Ferrara.

In general, electrochemical etching represents an industrial standard [26] that is based on a well-established, simple and inexpensive technology [27][28][29], and which is particularly suitable for in-line mass production of components due to its high throughput [26]. The technique is largely employed in the integrated-circuit (IC) industry [27] and related fields like display fabrication [26], structuring or removal of oxide layers in Si [30], MEMS fabrication [31], Si wafer cleaning [32] and many others. Additionally, the recent interest in porous Si for its possible employment in photovoltaic, electronics, sensors and photonic applications [33][34][35][36][37][38] has fostered its further development, involving also germanium [39][40][41][42][43][44].

From a chemical-physical point of view, electrochemical etching involves non-spontaneous reactions that imply an increase of the Gibbs free energy between the reactants and the products. This energy must be provided from the outside as electric work, by applying a potential. In this regard, the configuration of an electrochemical etching system reminds very much that of batteries, since it is composed of two electrodes which are immersed in an electrolytic solution through which a current is made to flow. Like all the electrochemical reactions, and precisely as for batteries, also the etching processes are governed by the Nernst law seen in the first Chapter. [45]

In this section, a brief introduction of the theoretical basis and a description of the setup employed is given. Some of the main experimental results are deepened and their correspondence with the theoretical model is analysed. Instead, the treatment of the morphologies and the electrochemical performances of samples realized by means of the various etching recipes are presented in section 3.3.

2.3.1. The etching setup

The process was performed using a custom tank, depicted in Figure 14, composed by a cylinder made of PolyTetraFluoroEthylene (PTFE) which is closed on one side. The sample is positioned in correspondence of the open side of the cylinder, on an aluminium plate as mechanical support and current collector. The cylinder is tightened to the plate by means of nylon screws and the sealing between the tank chamber and the sample is achieved by means of HF resistant Viton® O-rings, of 2.5 cm in diameter. In the figure are depicted also the electrical connections to achieve the anodic dissolution of the Ge layer: the positive electrode is connected to the aluminium plate while the negative one is clamped to a graphite rod that is inserted in the tank chamber. The wirings are arranged in a 4-wire configuration to enable a reliable measurement of the potential difference between the terminals during the etching process. Silicone wires and stainless-steel (AISI 304) clamps were used due to the HF acidic environment. The replicability in the positioning of the graphite bar is guaranteed by a specific housing in the tank. The electrolyte is poured from a hole realized on the top of the etching tank. Hydrogen is produced in the reactions (cf. sec. 2.3.2) and flows out from the chamber through this top hole, helped by the tapered design of the tank.

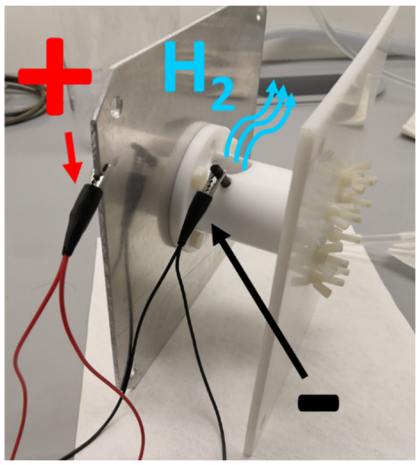

Figure 14: The etching tank assembly with the 4-wire electrical connections.

The hole dimensions in the etching-oriented deposition mask (cf. sect. 2.2.4) were designed to maximise the number of samples and to allow some tolerance for their positioning in the etching tank. Since the etching area can be identified as that inscribed by the O-rings (2.5 cm in diameter), slightly larger holes were realized in the deposition mask (2.8 cm in diameter, as previously stated).

The final aspect of the samples after deposition and etching is depicted in Figure 15. In part A of this figure, the general scheme of a sample is presented, while part B reports the picture of a processed one. The final electrode for the 2032 coin-cells is hollow punched form the inner part of the sample, resulting in a 1.5 cm disk (blue central region of the drawing in Figure 15). The effect of the hollow punching process on the external portion can be inspected in part C of this figure.

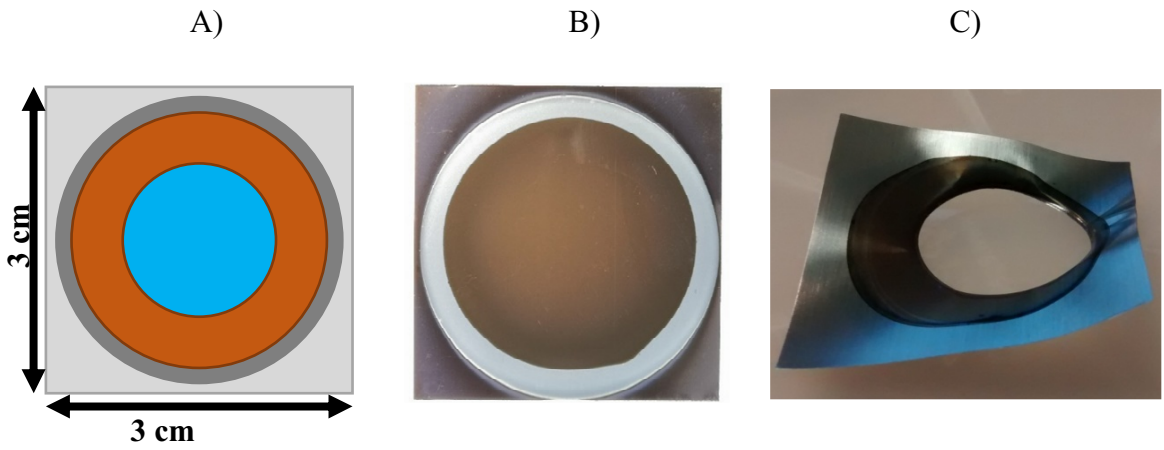

Figure 15: Schematic drawing of an etched sample (A) showing the substrate material as the external light grey square, the deposited Ge as the largest dark grey circle, the etched region as the orange circle and the inner blue circle representing the final electrode. A picture of an etched sample is presented in (B) and its external part after the electrode is hollow-punched is presented in (C) (this image is taken from [45]).

An important assumption was made regarding the etching, which is that it occurs in a uniform way over all the points of the sample surface. This means assuming that similar amounts of Ge are removed independently from the precise position over the sample. In other words, we exclude the possibility that the Ge layer could be completely ablated in some regions while remaining untouched in others. This is quite reasonable as the macroscopic morphology resulted to be uniform, as it can be in seen in part B of Figure 15. Furthermore, this is further supported by the homogeneity observed in the microscopic morphology of the samples, whose main results are reported in section 3.4.1.

2.3.2. Basic of Ge anodic dissolution in HF

Whereas a vast literature is present regarding Si etching, relatively few works can be reported about Ge [12][13][47]. Nevertheless, the basic principles regarding its

electrochemical etching in HF solutions seems to be quite clear and two main mechanisms are identified for its anodic dissolution [46][48][49][50][51], consisting of:

1) A divalent dissolution reaction, foreseeing hydrogen evolution:

$$(18) \quad Ge + 6HF + 2h^+ \rightarrow GeF_6^{2-} + 4H^+ + H_2$$

2) A tetravalent dissolution reaction, for which no hydrogen evolution is expected:

$$(19) \quad Ge + 6HF + 4h^+ \rightarrow GeF_6^{2-} + 6H^+$$

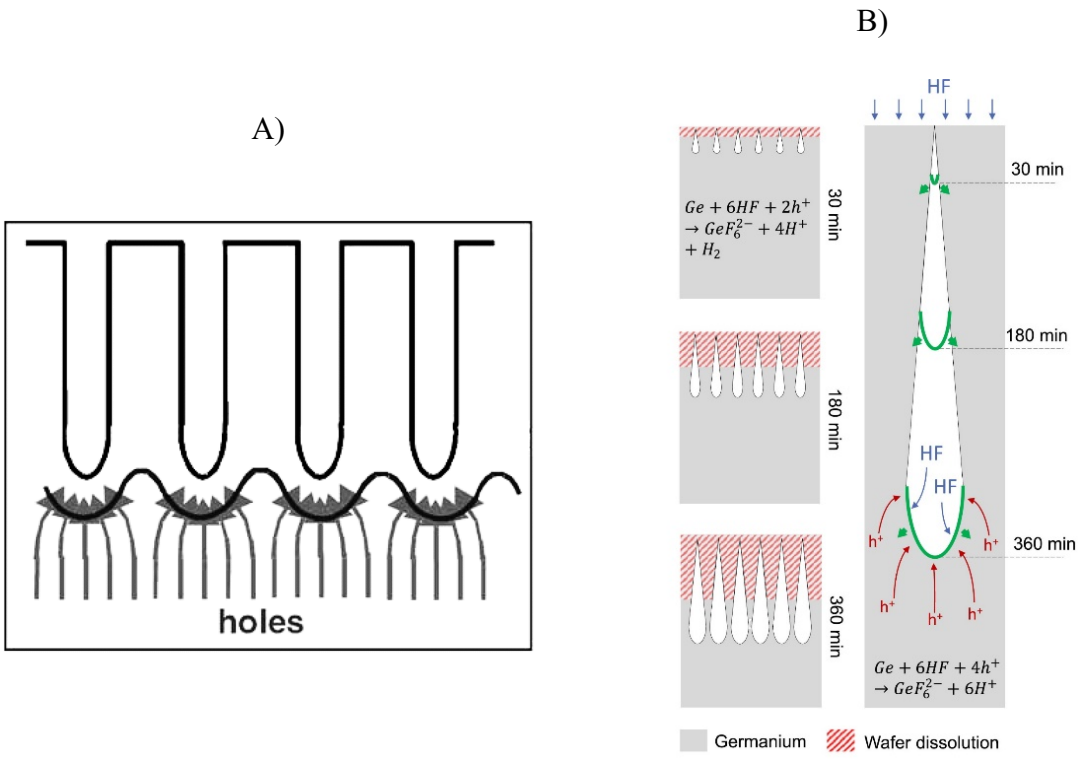

Figure 16: Enhanced pore growth at their base due to the electric field lines concentration (A). The tetravalent and divalent mechanisms responsible for porous layer growth and dissolution, respectively (B). Part (A) is adapted from [53], (B) is taken from [51].

The most recent model for the anodic dissolution of Ge in HF is based on the general pore formation theory by Lehmann *et al.*[52], initially developed for Si but that was associated also to Ge [51], for which a preferential pore growth occurs at their base due to a concentration of the electric field in that region (smaller radius of curvature, see part A of Figure 16). The model associates the vertical growth of the pores to the tetravalent reaction,

while the divalent process should be responsible for the continuous dissolution of the already porosified region, gradually increasing the pore diameter and thinning the layer [50][51], as depicted in part B of Figure 16.

2.3.3. The etching recipes

In this work, samples were electrochemically etched using an electrolytic solution composed by acqueous HF (50 % diluted, MOS grade, CARLO ERBA Reagents) and ethanol (RS grade, CARLO ERBA Reagents) in a ratio of 3:1 v/v. Different etching recipes were tested based on that electrolyte, upon variation of the current density, some of which are listed in Table **6**.

To allow for a comparison between the various recipes, the same amount of charge was made to flow in each case. As a total etching time of 180 s was chosen for the recipe Etch1, the total charge fluxed can be simply found by multiplying the current (see Table 6) by the etching time:

$$\text{(20)} \quad \text{Total charge fluxed: } Q = I \cdot t = 40mA \cdot 180s = (7.2 \pm 0.2)C$$

So, the electrochemical attacks were conducted increasing or reducing the etching time, depending on the current density, to obtain this precise value.

In all the cases, the current was made to flow inside the electrolytic cell by means of a Keithley 2400 Sourcemeter® controlled by a LabVIEW software. The potential and currents were registered for each sample. As it can be seen in Figure 17, a steady potential is observed during the whole process apart from a brief initial transient.

Etching recipe	Current (mA)	Current density (mA/cm^2)[2]
Etch1	40±1	8.2±0.2
Etch2	80±1	16.3±0.3
Etch3	20±1	4.1±0.2

Table 6: List of the etching recipes tested.

[2] Uncertainties were calculated by means of the general formulae for error propagation [83].

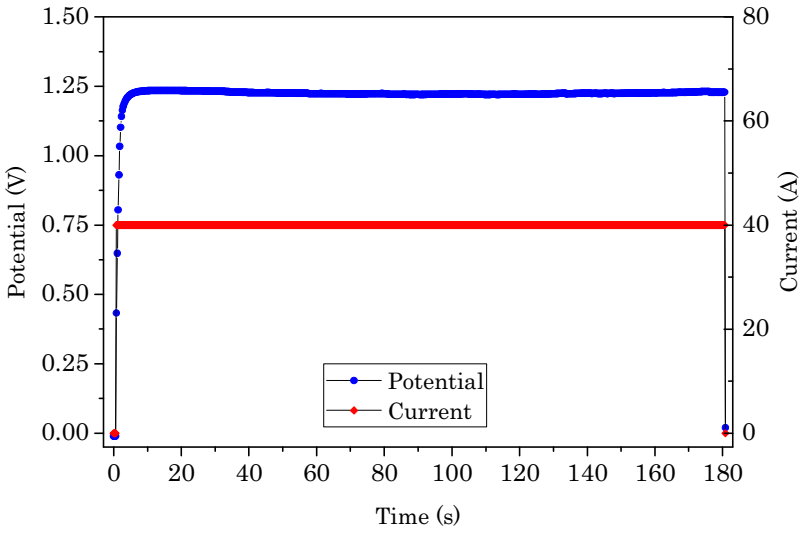

Figure 17: Potential and current profiles of a sample during an etching process with the Etch1 recipe.

2.3.4. The etching process replicability and experimental valence number

As is reported in section 4.5, the Etch1 recipe was selected as standard based on the electrochemical performances of prototype (half-cell) batteries realized with these electrodes.

The amount of Ge removed using this recipe over more than 70 samples was very stable, as it can be inspected from Figure 18, with an average of (1.61 ± 0.05) mg of material dissolved each time. This stability, with a standard deviation representing only the 3 % of the measure, testifies that a high replicability of the etching process has been achieved.

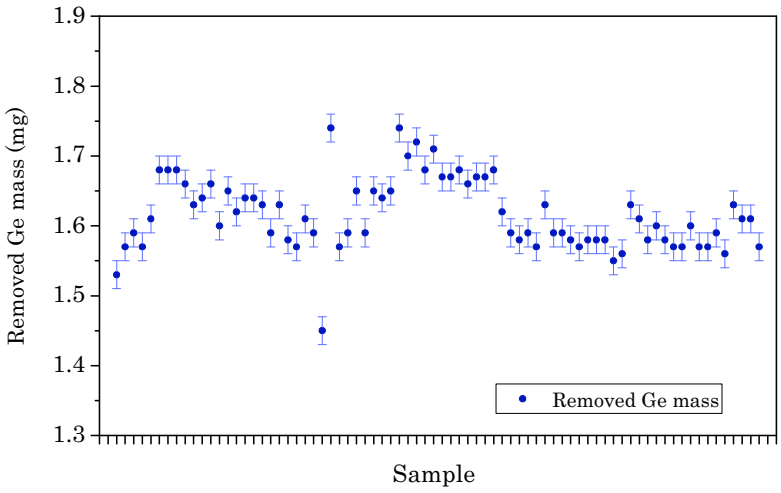

Figure 18: Mass of Ge removed with the Etch1 recipe for all the samples realized.

The Faraday law of electrolysis was used to calculate the valence number of the dissolution process, as a check of the electrochemical processes involved. This basic electrochemical relation states that the amount of mass involved in an electrochemical reaction is directly proportional to the charge transferred [54], according to the relation:

$$(21) \quad \text{Faraday law:} \quad m=\frac{qA}{zF}$$

Where m represents the mass transferred, z is the valence number of the process, q is the total charge fluxed, A stands for the molar mass of the material and F is the Faraday constant (corresponding to the charge of a mole of electrons).
By inverting this relation, the experimental mean valence number over the more than 70 samples was calculated:

$$(22) \quad z = 3.36 \pm 0.11$$

This value matches well with the dissolution model introduced before, by considering the simultaneous occurrence of both the divalent and the tetravalent processes.

In the investigation for some factors affecting the electrochemical etching, the amount of Ge removed was compared to the principal parameters that could have influenced the process. In particular, the following variables were considered:

1) the mass of Ge deposited,
2) the mean potential difference measured during the dissolution process,
3) the time in which the sample remained in contact with the HF solution, while the etching was not occurring (namely, the time in which the electrolyte was poured or removed from the etching cell).

As it can be inspected form the graphs reported in Figure 19, none of these parameters influenced the electrochemical dissolution of Ge, since the correlation coefficient is close to zero in all the cases.

It is interesting to note that the independence of the removed mass from the immersion time in HF means that any spontaneous dissolution process of Ge is negligible with respect to the forced divalent and tetravalent reactions. This is in agreement with other works, where spontaneous dissolution of Ge in HF solutions and water was observed to occur at very low rates [51].

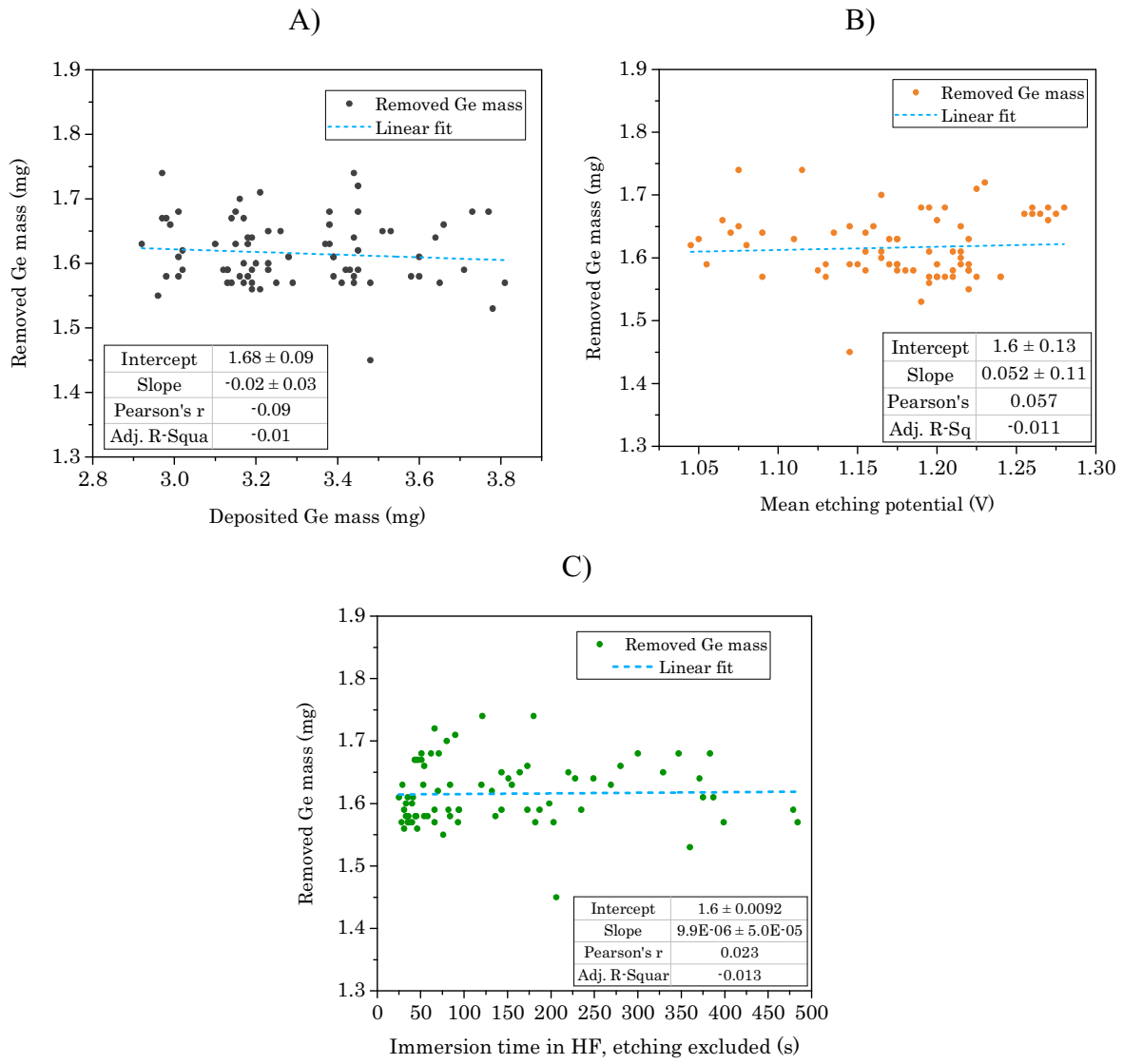

Figure 19: Analysis of the Ge mass removed using the Etch1 recipe as a function of: the amount of Ge deposited (A); the mean etching potential (B); the time in which the sample remained in contact with the HF solution, etching excluded (C).

2.3.5. Analysis of the alternative etching recipes

The etching currents listed in Table 6 were chosen according to a dissolution model developed by Garralaga [48]. This model identifies essentially the same divalent and tetravalent processes introduced before as responsible for the anodic dissolution of Ge. However, it states that their relative importance is different depending on the current density applied. In particular, the tetravalent reaction should predominate at low etching currents $j < 7.5\ \mathrm{mA/cm^2}$, while the divalent process becomes the leading mechanism above that threshold. Moreover, this model identifies the divalent reaction as the one responsible for the pore formation.

Compared to Etch1, a reduced statistic is available for the other recipes since few electrodes were specifically prepared for this comparison to select the most promising recipe. Nevertheless, a very high replicability was achieved anyway, as it can be ascertained from Figure 20 where the amount of Ge dissolved and the mean etching potentials are reported in the various cases.

The Etch1 recipe is not reported in that graph, because it has already been deepened before, but a new one is present, namely Etch4. This was not introduced in Table 6 because the same current as Etch1 was employed, but with etching time halved: so, this would not really be a new recipe, as it does not involve a new current density. However, this was introduced after the selection of Etch1 as standard to investigate how the etching process evolve.

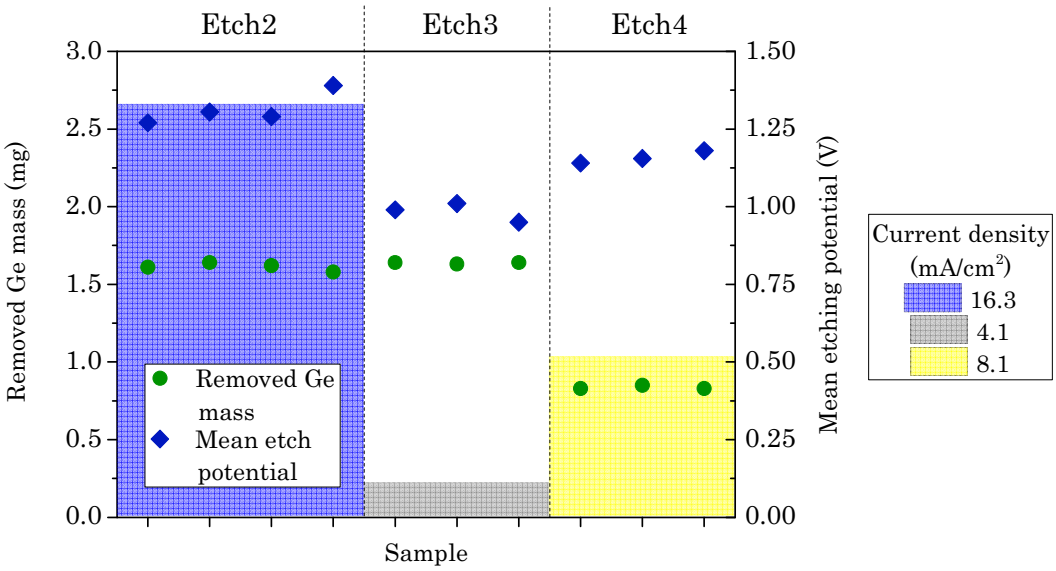

Figure 20: Ge mass removed, current densities and mean dissolution potentials of the etching recipes different from Etch1.

The etching data for the various recipes are summarized in Table 7. The most important thing to note is that a valence number very close to that of Etch1 is observed in all the cases. The same occurs for the amounts of Ge dissolved with Etch2 and Etch3, which perfectly agrees with the Faraday law because the same amount of charge was made to flow in both the cases as for Etch1. Additionally, about half the Ge mass is removed in the case of Etch4, that is consistent with the fact that the same process as Etch1 was carried out but for half the time.

Etching recipe	Mean valence number	Mean Ge mass removed (mg)
Etch2	3.36 ± 0.05	1.61 ± 0.03
Etch3	3.31 ± 0.01	1.637 ± 0.006
Etch4	3.24 ± 0.04	0.84 ± 0.01

Table 7: Mean valence numbers and amounts of Ge dissolved with the alternative etching recipes[3].

The fact that the same valence number is observed upon variations of the current density or the total charge fluxed discredits the model of Garralaga. Indeed, based on these data, it is not possible to confirm a prevalence of the tetravalent mechanism at low current densities or a prevalence of the divalent reaction at higher currents. On the contrary, the fact that we observe the same valence as for Etch1 suggests us that the same reactions occurred in all the cases. As a result, both the divalent and the tetravalent reaction pathways must take place simultaneously, retaining similar proportions in the whole current density range analysed.

One last thing to note is the difference in the mean etching potentials between the various etching recipes, as it appears from Figure 20. Evident discrepancies can be clearly observed when the current density is varied. This could be interpreted as a results of changes in the reaction overpotentials, as the potential rises concordantly with the current density (see ref. [55] and section 4.2.1).

2.3.6. The electrode mass loading

Since we could only measure in a direct way the amount of Ge removed from the overall etching area, the final mass loadings of the electrodes were calculated via simple proportions between the etched and the electrode area (see sec. 2.3.1). The average values for all the samples realize are listed in Table 8.

[3] The uncertainties reported in this table should be considered as qualitative values due to the poor statistic. However, it is interesting to note that they are all extremely low.

Etching recipe	Average mass loading (mg)[4]
Etch1	0.286 ± 0.067
Etch2	0.286 ± 0.045
Etch3	0.292 ± 0.044
Etch4	0.607 ± 0.056

Table 8: Average mass loadings of all the etching recipes.

Very similar values of about 0.3 mg are found for the recipes Etch1, Etch2 and Etch3, while Etch4 is about twice, since only half of the material was removed in that case. This further demonstrates that the mass of Ge dissolved is proportional to the total charge fluxed in each case, according to the Faraday law of electrolysis.

2.3.7. The Void Space Fraction

The structures realized by means of this nano-structuration technique can be characterized in terms of the amount of void space produced. For this reason, it is introduced the concept of the Void Space Fraction (VSF). This is equivalent to the fraction of mass removed, thereby can be expressed either referring to the volume or to the mass according to the following definition:

$$\text{VSF} = \frac{\text{total voids-pores volume}}{\text{total layer volume}} = \frac{\text{m}_1\text{-m}_2}{\text{m}_1\text{-m}_3} \quad (23)$$

where m_1 is the mass of the pristine sample, m_2 is the mass of the sample after the etching, and m_3 is the mass of the sample prior to the thin film deposition (in other words, the substrate mass).

The generality of this definition in terms of volumes or masses allows for a certain flexibility and enables the application of such an expression even to structures realized by means of a variety of techniques. This way, depending on the data available or on the specific nano-structuration technique used, one form of the VSF formulae could result more convenient than the other.

[4] As for the footnote of Table 7, the uncertainties for the etching recipes different from Etch1 should be considered only as qualitative values.

The mean VSF for the various etching recipes were calculated using the gravimetric expression and are listed in Table 9. An average value of about the 70 % is observed for the recipe chosen as standard, Etch1, meaning that about the 70 % of the layer final volume is constituted by empty space.

Etching recipe	Average VSF (%)[4]
Etch1	69.2 ± 5.7
Etch2	69.3 ± 3.6
Etch3	69.2 ± 3.1
Etch4	35.5 ± 2.4

Table 9: Average VSF of all the etching recipes.

Even in this case, similar VSF as that of Etch1 are also found for Etch2 and Etch3. Regarding the half-bulk samples, Etch4, a roughly halved value is obtained, confirming the linearity with time of the etching process.

2.4. Ion Implantation

Ion Implantation was used as an alternative approach to nano-structure the thin germanium films. A brief introduction of this technique is presented in this Chapter, which is inspired by the PhD thesis of Maria Secchi, a researcher of Bruno Kessler Foundation (FBK) who studied the nano-structure formation on Ge by ion implantation. [56]
The morphology of the samples realized by means of this technique and their electrochemical performances are reported in the following sections (cf. sections 3.3 and 4, respectively).

2.4.1. Introduction

Ion Implantation is an industrial technique commonly used to introduce dopants in semiconductors and represents one of the most important fabrication methods that is able to reach the high standards required in IC technology at affordable costs [56][57][58] [59][60].

The technique consists in bombarding the surface of the sample material with charged energetic ions or molecules. The species to be implanted are typically extracted from a high purity source and accelerated at the desired energy by means of electric fields. These are then focused on the material to be irradiated by electrostatic lenses and deflectors to raster its surface. The acceleration energies can span over a wide range from 10 keV and up to several MeV. [56]
Some of the key-features of this technique are the extreme purity of the implanted species, achieved thanks to selectors on the extraction source, high dopant concentrations as high as 10^{21} ions/cm^3, and a precise control over the number of atoms introduced in the target material in areas as large as wafers. [56]

The main effects of ion implantation on semiconductors are the introduction of a dopant distribution and the formation of lattice damage induced by the ion collisions. In particular conditions, the latter can lead to a spontaneous development of nano-structures on the surface of some covalent semiconductors, like GaSb, InSb and, in particular, Ge [56][61][62][63][64][65]. In the following sections, the description is focused only on Ge, but most of the observations may be applicable also for the other materials.

2.4.2. The ion beam interaction with matter

The lattice damage and its reorganization are due to elastic and inelastic interactions of the impinging ions with the nuclei and the electronic clouds of the target material. These interactions are ruled by the Bethe-Bloch relation, that expresses the mean rate of energy loss per unit of length travelled by a heavy charged particle inside matter. Usually, the electronic and nuclear collisions represent the main contributions, and the energy loss rate can be expressed as:

$$\frac{dE}{dx} = \left(\frac{dE}{dx}\right)_n + \left(\frac{dE}{dx}\right)_e \quad (24)$$

The energy E and the atomic number Z of the implanted species determine the relative importance of the two terms, but in general electronic collisions give a main contribution at high energies while the nuclear ones prevail at low energies, as depicted in Figure 21:

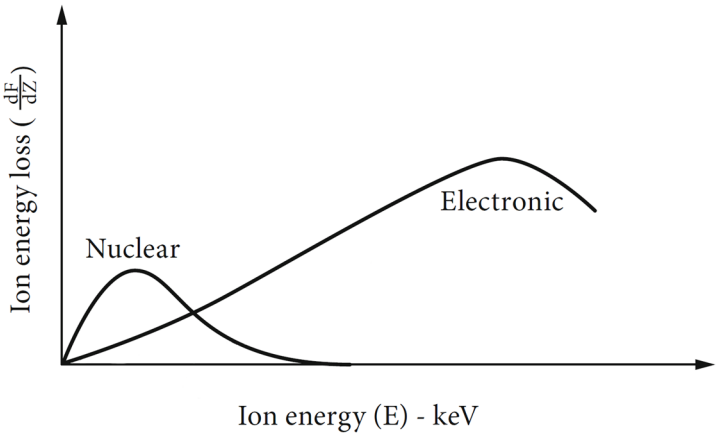

Figure 21: Ion energy loss contributions from nuclear and electronic interactions. Adapted from [66].

Once the impinging ion has lost all of its original energy due to the series of random collisions, it finally comes to rest inside the target material. The total distance travelled by an ion before it stops is usually called its range (R). In principle, this value could be calculated upon integration of the inverse of the energy-loss rate dE/dx. However, this is typically determined experimentally by bombarding different thicknesses of the target materials with beams of particles at the desired energy. From a statistical point of view, and in a first approximation, the range follows a distribution that is gaussian in form. [67]

2.4.3. Theory of nano-structure formation and main morphological features

The most accredited theory about the nano-structure formation is a vacancy clustering process. In fact, upon ionic bombardment, the lattice atoms can be dislodged from their original positions due to collisions in which the energy transfer exceed the displacement energy. This results in the creation of point defects, namely vacancies and interstitial atoms, that cumulates up to the point in which the material becomes amorphous. The further irradiation of the amorphized material results in a "porous" surface, due to an unbalanced formation kinetics and mobility of vacancies and interstitials, with the first that are favoured. The excess of vacancies migrates inside the material and produce clusters, while interstitials are quickly reabsorbed in the amorphous matrix. These vacancy clusters gradually grow and give rise to nano-voids that finally produce the porous structure [60][61][64][68][69]. A representative depiction of this process is reported in Figure 22:

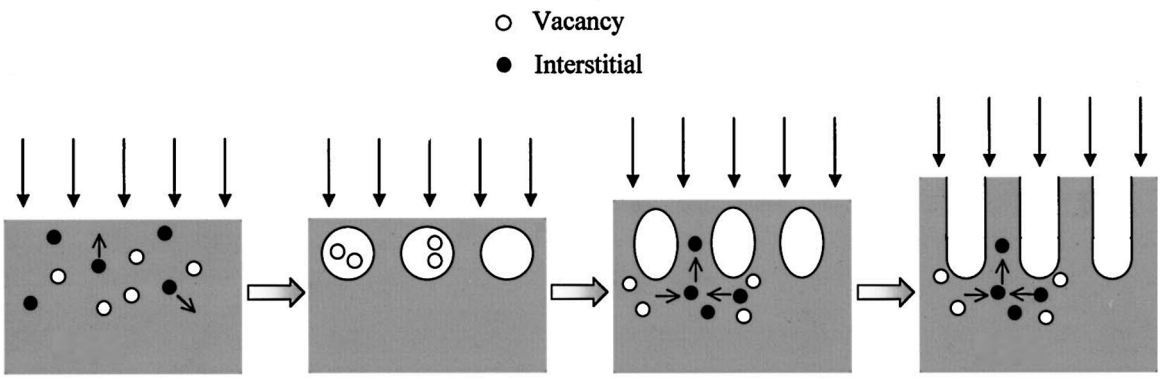

Figure 22: The various steps leading to the nano-structure formation upon ion implantation. Adapted from [61].

The morphologies obtained could be very different and are generally affected by many factors (see the following section). However, some common features have been observed in many works. In particular, nano-voids developing with a sort of cylindrical symmetry on the plane of the irradiated surface have been extensively reported. These are arranged in a quite regular way and extend in orthogonal direction with respect to the sample surface. The final shape of these structures resembles that of a bee nest, like that reported in Figure 23, and this explains why they are usually referred to as "honeycomb" nano-voids [56][64][68][70][71]. In the most recent works, also other kinds of morphologies have been reported, like nano-wires [72][73], sponge-like structures and neuron-like arrangements [74].

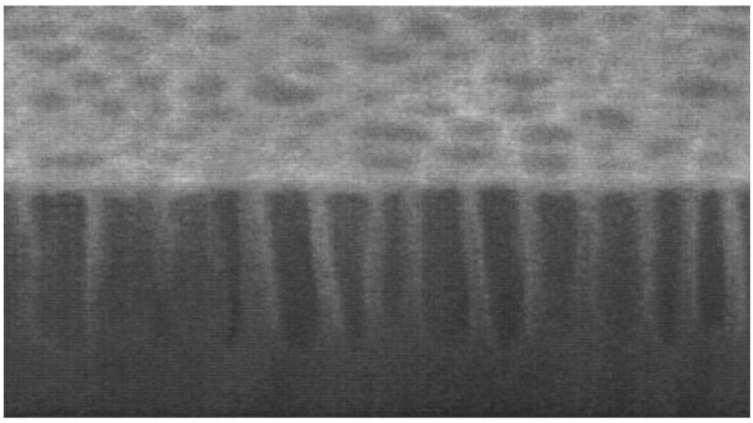

Figure 23: An example of the honeycomb structure of an ion implanted sample, from [68]

Besides the morphological evolution, a swelling of the implanted surface is also generally reported, with the walls of the nano-structures developing in both directions below and above the original surface plane [64][65][75]. However, particularly for very high doses and heavy ions, the implantation could also result in sputtering processes [72][76].

2.4.4. Features affecting the nano-structuration process

Many variables affect the onset of the spontaneous structure formation and their morphologies, like the ion incidence angle with respect to the lattice planes, the target nature (i.e., whether is amorphous, crystalline, or polycrystalline) or the energy of the impinging ions. However, some thresholds were identified related to the atomic number Z of the implanted species, the temperature of the target material, and the total number of ions deposited per unit of the implanted area [1][56][64][65][74].

The last cited quantity, which is usually referred to as fluence or dose, represents the amount of dopant atoms introduced in the irradiated material. If the ion beam intensity I is constant, the fluence can be calculated as:

$$\Phi = \frac{It}{qA} \quad (25)$$

Where q is the charge transported by each ion, A is the area of the beam spot on the sample and t is the total time of the implantation process.

The fluence empirically demonstrated to be one of the most critical parameters in achieving the nano-structuration of the layer [65]. In fact, an accurate study by Darby *et al.* correlated the development of nano-structures for self-implantation of Ge with the fluence of the incident ions, which is not modified even by variations of orders of magnitude of the ion energy [1].

Regarding the atomic number, a threshold mass for inducing nano-structuration was identified as that of chromium, ^{52}Cr [74]. The existence of such a threshold could be related to a stronger dependence of the nuclear energy-loss term in the Bethe-Bloch formula on the atomic number of the implanted ions, leading to a higher defects production with heavy ions.

Finally, a temperature threshold, or even better a temperature window, for nano-void formation in Ge was identified by Stritzker *et al.* and resulted to be -80°C<T<200°C [65][76]. At low temperature only amorphization occurs while at high temperature only partial damage is observed, without amorphization or void formation. This suggests that thermally activated phenomena may participate to the nano-structuration process. [56]

2.4.5. The ion damage map and the choice of the implantation recipes

In this work, self-implantation of germanium was selected to avoid any alteration in the chemical composition of the layer. In this way, any eventual doping effect is also excluded ab initio.

The choice of the ion implantation recipes was based on the study of Darby *et al.* [1], that realised a "damage map" for self-implantation of Ge. In this map, which is depicted in Figure 24, the nature of the film after the implantation process is correlated to the ion fluence and energy. The dashed lines clearly demonstrate how the fluence is the crucial parameter in determining the final phase, that is not affected by the ion energy, as previously mentioned.

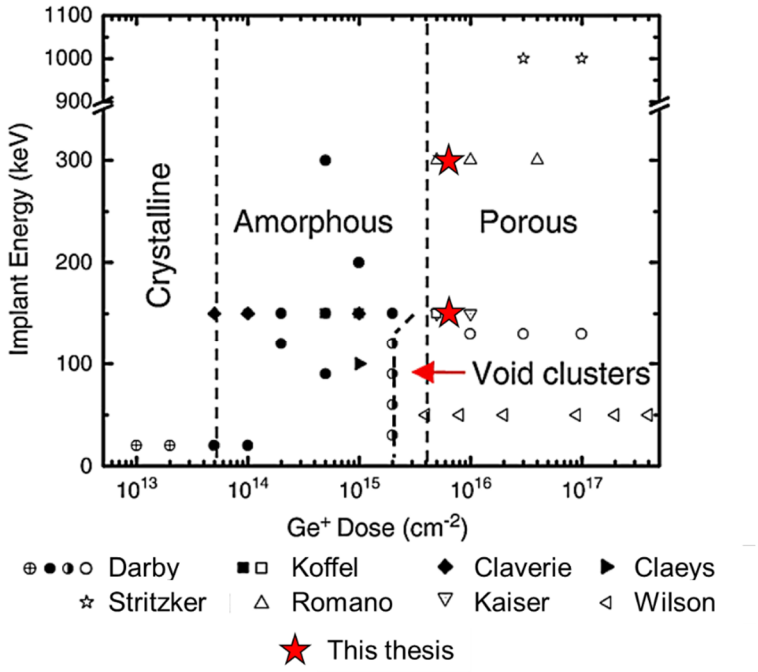

Figure 24: Ion "damage map" for Ge self-implantation. The nature of the layer after the implantation is reported and the symbols refer to the works considered in the Darby et al. study [1]. The red stars identify the implantation energies and fluences selected for this work.

Two implantation recipes were selected above the fluence threshold for nano-structure formation, according to the damage map, whose energy and fluence are reported in Table

10. The reason for choosing a couple of recipes, rather than a single one, was to compare the effects of eventual morphology differences on the electrochemical performances in the lithium-ion batteries. Furthermore, this undoubtedly reduced the overall risk of failures.

Implantation recipe (label)	Fluence (atoms/cm^2)	Ion energy (keV)
Ion 1	2.5E16	150
Ion 2	2.0E16	300

Table 10: Implantation recipes fluence and energy.

All the ion implanted samples presented in this thesis were realised at the Ion Beam Services facility of Peynier, France.

2.4.6. Monte-Carlo simulations of the ion implantation process

As previously stated, from a theoretical point of view the penetration range could be directly calculated from the Bethe-Bloch relation.
Despite this could be quite complicated, many Monte-Carlo simulation techniques have been developed from the basic ion interaction models to predict depth distributions of large fluences of implanted species. In particular, the Stopping and Range of Ions in Matter (SRIM) represents one of the most important software packages for this purpose. This software was developed to allow the calculation of the implanted ion distribution, the associated damage cascade, and the detailed energy release inside the material. [56][77]

Monte-Carlo simulations with SRIM software were performed for both the implantation recipes of this project by the Bruno Kessler Foundation of Trento, Italy. The results showed that the same amount of damage is produced in both the cases, and this was considered as a further check to confirm the chosen recipes. However, the simulation aspects and their results are not deepened in this thesis since these were activities performed by the FBK foundation, on which I have not contributed in a direct way.

2.4.7. The ion implantation mask and sample positioning

As mentioned in section 2.2.4, a specific deposition mask was realized for the ion implanted samples. Since this process does not imply a mass removal[5], shorter deposition times are required to obtain mass loadings comparable to those of the etched samples. As listed in the previous Table 5, this time was calculated to correspond to a deposition thickness of about 350 nm.

As depicted in the previous Figure 11, the mask for ion implantation can host up to 19 substrates that are already cut in the form of disks of 1.5 cm diameter. To hold the substrates in place, the implantation mask is made of 3 components: two outer plates, with holes of 1.4 cm in diameter to keep the samples in place, and an intermediate one, with holes of 1.55 cm in diameter to allow for the substrates loading and managing. A three-dimensional rendering model of this mask is depicted in Figure 25.

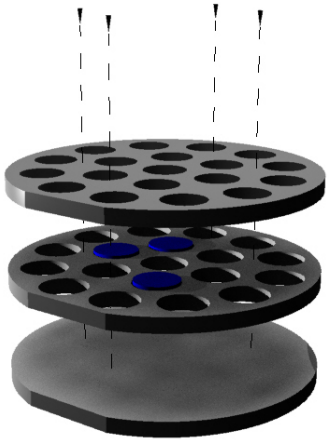

Figure 25: Rendering model of the implantation mask, showing the samples location inside the mask. The mask is tightened by the four screws displayed in the model.

After the Ge film deposition, the masks were disassembled to weigh the samples. Then, they were assembled again, with the samples in their original positions, for the implantation. However, the small margin left to ease the samples loading allowed for some displacements respect to their initial positions. Of course, the ideal situation would be that in which the deposited area is perfectly superposed to the implanted one. But unfortunately, the difference between the diameters of the inner mask holes and the samples leaves the

[5] In principle, ion implantation could increase the sample mass because the implanted ions become part of the film. For the fluences used in this work this corresponds to a few µg increments, which is negligible with respect to the mass loadings (< 1 %).

possibility of a translation between the deposition and the implantation, that could be equal to 0.05 cm in the worst case.

The resulting areal mismatch is depicted in Figure 26, where a single sample inside the mask is rendered, in top-view and in perspective, for the worst-case scenario. The colours in the figure correspond to the maximum areal mismatch (green), the minimum nano-structured germanium area (red), and the undeposited substrate exposed to implantation as a result of the displacement (blue).

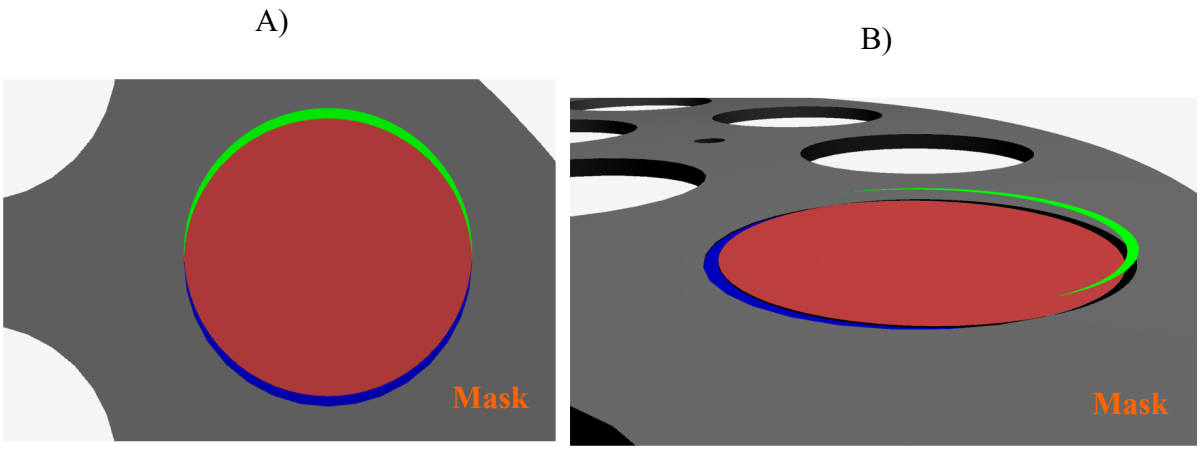

Figure 26: Worst-case displacement mismatch between deposition and ion implantation, in top-view (A) and perspective (B). The grey regions represent the mask; the green slice is the maximum area of bulk Ge that could be shielded by the mask during implantation; the red part is the minimal implanted Ge area, and the blue slice represents the bare substrate exposed to implantation as a result of the displacement. In part B, the green area is displayed above the plane of the mask and the sample for the sake of clarity.

Naturally, the maximum care was adopted about the precise positioning of the samples, when these have been weighted and inserted again inside the mask. However, in some cases, traces of bulk Ge have survived to the implantation process since the typical signature of crystalline Ge is clearly recognized in some electrochemical tests. This is further discussed in section 4.8.1.

It is important to underline that the amount of bulk Ge that could remain is very low compared to the nano-structured (and amorphous) material. In fact, in the worst case, the area of bulk Ge remained would be less than the 5 % of the area of the nano-structured material in the electrode, as reported in Table 11.

Total deposited area (mm^2)	153.94
Max. area of bulk Ge slice (mm^2)	7.00
Min. area of nano-structured Ge region (mm^2)	146.94
Max. amount of bulk Ge, worst case (%)	4.76

Table 11: Worst-case displacement area of the bulk and nano-structured regions.

2.5. **Molybdenum and stainless steel as substrate materials**

The electrodes for LIBs are typically composed by an active material deposited onto a metallic substrate acting as a current collector. The most common metals used for this purpose are copper (negative electrode) and aluminium (positive electrode) due to their high electric conductivity, low production costs, and their stability at the respective electrode potentials. [1][78][79]

In this work different materials were required because of constraints related to the deposition equipment and the main nano-structuration technique, namely the electrochemical etching.
The main issue regarding the LEPECVD setup is related to the introduction of pollutants inside the reaction chamber, as it would be the case for low vapour pressure metals. The principal concern about the electrochemical etching is associated to the stability of the substrate material in HF environments. [45]
For these reasons, Molybdenum (Mo) and Stainless Steel (SS) were selected as substrate materials. Indeed, they present full compatibility with the deposition equipment since they are already present in various components of the main chamber (see section 2.2.1). In addition, they are both HF resistant materials according to the literature [80][81][82] and to experimental evidences [11][31].

The substrates used in this work were 25 µm thick foils of pure Mo (purity higher than 99.9 %) purchased from Sigma-Aldrich, and AISI 316 SS (annealed) furnished by GoodFellow. In the characterization chapter, their morphological evaluation is presented.

2.6. **Summary and conclusions to Chapter 2**

The details of the standard industrial techniques that are adopted in the two processes of fabrication of the electrodes were presented in this chapter. The main features of the deposition technique, the LEPECVD, and of both the nano-structuration processes, the HF anodic dissolution and the Ion Implantation, were extensively treated.

The deposition parameters and the expected film properties, which were derived from previous works, were presented. To obtain similar mass loadings (~0.3 mg) in both the kinds of the nano-structured electrodes, the necessity of depositing film having different thickness (~1μm and ~350 nm) was explained. Furthermore, a review of the deposition data from many samples was conducted and the uniformity of the deposition process was assessed. This shows a thickness uniformity of about 15.75 %, which is considered compatible with the variability determined in the previous works (~10 %)[6].

Regarding the etching process, some of the main experimental results were deepened and their correspondence with the theoretical model was evaluated. The etching process replicability was analysed recurring to the Faraday law of electrolysis by calculating the experimental valence number for all the etching recipes. The results match well with the most recent theoretical model, considering the simultaneous occurrence of the divalent and tetravalent dissolution mechanisms. This is also confirmed by the etching recipe whose time was halved, for which the same valence number of the other recipes was found, and that demonstrated the linearity with time of the dissolution process.

Regarding the Ion Implantation, the theoretical bases and the expected morphologies were introduced. The rationale for the choice of the implantation recipes was presented, based on the damage map model developed by Darby et *al*. [1]. The possibility for the presence of bulk germanium after the ion implantation process was explained, linking it to a small degree of freedom of the samples inside the deposition masks.

Finally, a brief explanation about the choice of Molybdenum and Stainless Steel as substrate materials was given.

[6] As previously stated, the thickness variability for the ion-implantation samples was not considered reliable under a quantitative point of view due to the poor statistic available.

References

[1] B. L. Darby, B. R. Yates, N. G. Rudawski, K. S. Jones, A. Kontos, and R. G. Elliman, "Insights for void formation in ion-implanted Ge," Thin Solid Films, vol. 519, no. 18, 2011, doi: 10.1016/j.tsf.2011.03.040.

[2] T. Kennedy, M. Brandon, and K. M. Ryan, "Advances in the Application of Silicon and Germanium Nanowires for High-Performance Lithium-Ion Batteries," Adv. Mater., vol. 28, no. 27, 2016, doi: 10.1002/adma.201503978.

[3] Y. Hamedani, P. Macha, T. J. Bunning, R. R. Naik, and M. C. Vasudev, "Plasma-Enhanced Chemical Vapor Deposition: Where we are and the Outlook for the Future," in Chemical Vapor Deposition - Recent Advances and Applications in Optical, Solar Cells and Solid State Devices, 2016.

[4] S. Wolf and R. N. Tauber, Silicon Processing for the VLSI Era - Volume 1: Process Technology, vol. 1. Lattice Press, 1986.

[5] A. Rockett, Ed., "Chemical Vapor Deposition," in The Materials Science of Semiconductors, Boston, MA: Springer US, 2008, pp. 573–609.

[6] G. Calabrese, "Relaxed germanium epilayers on porous silicon buffers for low dislocation content Ge on Si virtual substrates," University of Ferrara, Ferrara, 2014.

[7] X. T. Yan and Y. Xu, Chemical Vapour Deposition: An Integrated Engineering Design for Advanced Materials. Springer London, 2010.

[8] J. R. Creighton and P. Ho, "Introduction to chemical vapor deposition (CVD)," Chem. Vap. Depos., vol. 2, pp. 1–22, 2001.

[9] P. M. Martin, Handbook of Deposition Technologies for Films and Coatings, 3rd edition. Elsevier, 2010.

[10] A. C. Jones and M. L. Hitchman, "Overview of chemical vapour deposition," Chem. Vap. Depos. Precursors, Process. Appl., vol. 1, pp. 1–36, 2009.

[11] K. K. Schuegraf and K. Seshan, "Handbook of Thin Film Deposition Processes and Techniques: Principles, Methods, Equipment and Applications," Angew. Chemie, vol. 101, 2002.

[12] C. Rosenblad, H. R. Deller, A. Dommann, T. Meyer, P. Schroeter, and H. von Känel, "Silicon epitaxy by low-energy plasma enhanced chemical vapor deposition," J. Vac. Sci. Technol. A Vacuum, Surfaces, Film., vol. 16, no. 5, 1998, doi: 10.1116/1.581422.

[13] M. Kummer et al., "Low energy plasma enhanced chemical vapor deposition," in Materials Science and Engineering B: Solid-State Materials for Advanced Technology, Feb. 2002, vol. 89, no. 1–3, pp. 288–295, doi: 10.1016/S0921-5107(01)00801-7.

[14] A. Boogaard, "Plasma-enhanced chemical vapor deposition of silicon dioxide," University of Twente, Enschede, The Netherlands, 2011.

[15] L. Martinu, O. Zabeida, and J. E. Klemberg-Sapieha, Handbook of Deposition Technologies for Films and Coatings-Plasma-Enhanced Chemical Vapor Deposition of Functional Coatings. 2010.

[16] M. I. Pech-Canul and N. M. Ravindra, Eds., Semiconductors, 1st ed. Cham: Springer International Publishing, 2019.

[17] M. Boschetti, "PECVD growth of Ge for nanoporous lithium-ion battery anodes," University of Ferrara, Ferrara, 2015.

[18] D. McNulty, S. Biswas, S. Garvey, C. O'Dwyer, and J. D. Holmes, "Directly Grown Germanium Nanowires from Stainless Steel: High-performing Anodes for Li-Ion Batteries," ACS Appl. Energy Mater., vol. 3, no. 12, pp. 11811–11819, 2020, doi: 10.1021/acsaem.0c01977.

[19] S. Fugattini, "Binder-free porous germanium anode for Li-ion batteries," University of Ferrara, Ferrara, 2018.

[20] L. Y. Lim, N. Liu, Y. Cui, and M. F. Toney, "Understanding phase transformation in crystalline Ge anodes for Li-ion batteries," Chem. Mater., vol. 26, no. 12, 2014, doi: 10.1021/cm501233k.

[21] B. Farbod et al., "Array geometry dictates electrochemical performance of Ge nanowire lithium ion battery anodes," J. Mater. Chem. A, vol. 2, no. 39, 2014, doi:

10.1039/c4ta03805c.
[22] E. J. Powell, S. M. Wood, H. Celio, A. Heller, and C. B. Mullins, “Obviating the need for nanocrystallites in the extended lithiation/de-lithiation of germanium,” J. Mater. Chem. A, vol. 3, no. 46, 2015, doi: 10.1039/c5ta04941e.
[23] D. T. Ngo et al., “Carbon-Interconnected Ge nanocrystals as an anode with ultra-long-term cyclability for lithium ion batteries,” Adv. Funct. Mater., vol. 24, no. 33, 2014, doi: 10.1002/adfm.201400888.
[24] R. A. Susantyoko, X. Wang, L. Sun, W. Sasangka, E. Fitzgerald, and Q. Zhang, “Influences of annealing on lithium-ion storage performance of thick germanium film anodes,” Nano Energy, vol. 12, 2015, doi: 10.1016/j.nanoen.2015.01.024.
[25] Y. Chen, C. Yan, and O. G. Schmidt, “Strain-driven formation of multilayer graphene/GeO2 tubular nanostructures as high-capacity and very long-life anodes for lithium-ion batteries,” Adv. Energy Mater., vol. 3, no. 10, 2013, doi: 10.1002/aenm201300575.
[26] J. Chen, W. Cranton, and M. Fihn, Handbook of visual display technology. 2016.
[27] J. D. Plummer, M. D. Deal, and P. B. Griffin, Silicon VLSI Technology: Fundamentals, Practice and Modeling. Prentice Hall, 2000.
[28] Y. Yue and N. Zhen, “Porous Silicon Fabrication for MEMS Applications,” Saudi J. Eng. Technol., vol. 04, no. 10, 2019, doi: 10.36348/sjeat.2019.v04i10.003.
[29] C. YANG, D. YU, and L. YU, “ACCELEROMETER AND MANUFACTURING PROCESS THEREOF,” WO2014044015A1, 2014.
[30] D. M. Knotter, “The Chemistry of Wet Etching,” in Handbook of Cleaning in Semiconductor Manufacturing: Fundamental and Applications, 2011.
[31] P. Pal, V. Swarnalatha, A. V. N. Rao, A. K. Pandey, H. Tanaka, and K. Sato, “High speed silicon wet anisotropic etching for applications in bulk micromachining: a review,” Micro and Nano Systems Letters, vol. 9, no. 1. 2021, doi: 10.1186/s40486-021-00129-0.
[32] D. Yang, Handbook of Photovoltaic Silicon. Springer Berlin Heidelberg, 2019.
[33] G. Korotcenkov and B. K. Cho, “Silicon porosification: State of the art,” Crit. Rev. Solid State Mater. Sci., vol. 35, no. 3, 2010, doi: 10.1080/10408436.2010.495446.
[34] F. A. Harraz, “Porous silicon chemical sensors and biosensors: A review,” Sensors Actuators, B Chem., vol. 202, 2014, doi: 10.1016/j.snb.2014.06.048.
[35] N. K. Kozlov et al., “Recycling of silicon: From industrial waste to biocompatible nanoparticles for nanomedicine,” Mater. Res. Express, vol. 4, no. 9, 2017, doi: 10.1088/2053-1591/aa8c33.
[36] S. H. Lee, J. S. Kang, and D. Kim, “A mini review: Recent advances in surface modification of porous silicon,” Materials, vol. 11, no. 12. 2018, doi: 10.3390/ma11122557.
[37] N. Abu-Thabit and E. Ratemi, “Hybrid Porous Silicon Biosensors Using Plasmonic and Fluorescent Nanomaterials: A Mini Review,” Frontiers in Chemistry, vol. 8. 2020, doi: 10.3389/fchem.2020.00454.
[38] S. Arshavsky-Graham, N. Massad-Ivanir, E. Segal, and S. Weiss, “Porous Silicon-Based Photonic Biosensors: Current Status and Emerging Applications,” Analytical Chemistry, vol. 91, no. 1. 2019, doi: 10.1021/acs.analchem.8b05028.
[39] E. Garralaga Rojas, J. Hensen, J. Carstensen, H. Föll, and R. Brendel, “Porous germanium multilayers,” Phys. Status Solidi Curr. Top. Solid State Phys., vol. 8, no. 6, 2011, doi: 10.1002/pssc.201000130.
[40] H. H. Abdelmaksoud, T. M. Guinan, and N. H. Voelcker, “Fabrication of Nanostructured Mesoporous Germanium for Application in Laser Desorption Ionization Mass Spectrometry,” ACS Appl. Mater. Interfaces, vol. 9, no. 6, 2017, doi: 10.1021/acsami.6b14362.
[41] S. Acikgoz, H. Yungevis, E. Özünal, and A. Şahin, “Low-cost, fast and easy production of germanium nanostructures and interfacial electron transfer dynamics of BODIPY–germanium nanostructure system,” J. Mater. Sci., vol. 52, no. 22, 2017, doi: 10.1007/s10853-017-1434-6.
[42] O. NALAMASU and S. VERHAVERBEKE, “ENERGY STORAGE DEVICE WITH POROUS ELECTRODE,” US2010221606A1, 2010.
[43] E. Garralaga Rojas, J. Hensen, J. Carstensen, H. Föll, and R. Brendel, “Porous Germanium Layers by Electrochemical Etching for Layer Transfer Processes of High-Efficiency Multi-Junction Solar Cells,” ECS Trans., vol. 33, no. 17, 2011, doi: 10.1149/1.3553351.

[44] N. Alkurd, “Demonstration of functional III-V photovoltaic cell via processing of porous Ge substrates,” Colorado School of Mines , 2019.
[45] A. Andreoli, “Porous germanium films as anode materials for lithium ion batteries,” University of Ferrara, Ferrara, 2016.
[46] S. Tutashkonko et al., “Mesoporous Germanium formed by bipolar electrochemical etching,” Electrochim. Acta, vol. 88, 2013, doi: 10.1016/j.electacta.2012.10.031.
[47] E. Garralaga Rojas et al., “Mesoporous Germanium Formation by Electrochemical Etching,” J. Electrochem. Soc., vol. 156, no. 8, 2009, doi: 10.1149/1.3147271.
[48] E. J. Garralaga Rojas, “Thesis: Mesoporous Germanium Layer Formation by Electrochemical Etching,” 2010.
[49] S. Tutashkonko, S. Alekseev, and T. Nychyporuk, “Nanoscale morphology tuning of mesoporous Ge: Electrochemical mechanisms,” Electrochim. Acta, vol. 180, 2015, doi: 10.1016/j.electacta.2015.08.112.
[50] Y. A. Bioud et al., “Fast growth synthesis of mesoporous germanium films by high frequency bipolar electrochemical etching,” Electrochim. Acta, vol. 232, 2017, doi: 10.1016/j.electacta.2017.02.115.
[51] A. Dupuy, M. R. Aziziyan, D. Machon, R. Arès, and A. Boucherif, “Anisotropic Mesoporous Germanium Nanostructures by Fast Bipolar Electrochemical Etching,” Electrochim. Acta, 2021, doi: 10.1016/j.electacta.2021.137935.
[52] V. Lehmann, R. Stengl, and A. Luigart, “On the morphology and the electrochemical formation mechanism of mesoporous silicon,” Mater. Sci. Eng. B Solid-State Mater. Adv. Technol., vol. 69, 2000, doi: 10.1016/S0921-5107(99)00286-X.
[53] H. Föll, M. Christophersen, J. Carstensen, and G. Hasse, “Formation and application of porous silicon,” Materials Science and Engineering R: Reports, vol. 39, no. 4. 2002, doi: 10.1016/s0927-796x(02)00090-6.
[54] A. J. Bard and L. R. Faulkner, Electrochemical Methods: Fundamentals and Applications . John Wiley & Sons, Inc., 2001.
[55] R. A. Huggins, Advanced batteries: Materials science aspects. 2009.
[56] Maria Secchi, “Nanostructure formation on Germanium by ion irradiation,” University of Trento, Trento, 2016.
[57] Marie Backman, “Effects of nuclear and electronic stopping power on ion irradiation of silicon-based compounds,” University of Helsinki, Helsinki, 2012.
[58] M. I. Current, “Ion implantation of advanced silicon devices: Past, present and future,” Materials Science in Semiconductor Processing, vol. 62. 2017, doi: 10.1016/j.mssp.2016.10.045.
[59] K. S. Jones and N. G. Rudawski, “STRUCTURES INCLUDING ION BEAM-MIXED LITHIUM ION BATTERY ELECTRODES, METHODS OF MAKING, AND METHODS OF USE THEREOF,” WO2013126372A1, 2013.
[60] N. M. Lyadov et al., “Formation of Pores in Thin Germanium Films under Implantation by Ge+ Ions,” Tech. Phys. Lett., vol. 46, no. 7, 2020, doi: 10.1134/S1063785020070196.
[61] N. Nitta, M. Taniwaki, Y. Hayashi, and T. Yoshiie, “Formation of cellular defect structure on GaSb ion-implanted at low temperature,” J. Appl. Phys., vol. 92, no. 4, 2002, doi: 10.1063/1.1493662.
[62] D. P. Datta et al., “60 keV Ar+-ion induced modification of microstructural, compositional, and vibrational properties of InSb,” J. Appl. Phys., vol. 116, no. 14, 2014, doi: 10.1063/1.4897537.
[63] O. W. Holland, B. R. Appleton, and J. Narayan, “Ion implantation damage and annealing in germanium,” J. Appl. Phys., vol. 54, no. 5, 1983, doi: 10.1063/1.332385.
[64] L. Romano, G. Impellizzeri, M. V. Tomasello, F. Giannazzo, C. Spinella, and M. G. Grimaldi, “Nanostructuring in Ge by self-ion implantation,” J. Appl. Phys., vol. 107, no. 8, 2010, doi: 10.1063/1.3372757.
[65] N. G. Rudawski and K. S. Jones, “Nanostructured germanium prepared via ion beam modification,” Journal of Materials Research, vol. 28, no. 13. 2013, doi: 10.1557/jmr.2013.24.
[66] H. Frey and H. R. Khan, Handbook of Thin-Film Technology. 2015.
[67] W. R. Leo, Techniques for Nuclear and Particle Physics Experiments. 1994.
[68] T. Janssens et al., “Heavy ion implantation in Ge: Dramatic radiation induced morphology in

Ge," J. Vac. Sci. Technol. B Microelectron. Nanom. Struct., vol. 24, no. 1, 2006, doi: 10.1116/1.2151904.
[69] L. Ottaviano et al., "Surface morphology of Mn+ implanted Ge(1 0 0): A systematic investigation as a function of the implantation substrate temperature," Surf. Sci., vol. 601, no. 13, 2007, doi: 10.1016/j.susc.2006.11.075.
[70] M. Secchi et al., "Ge nanostructuring by Sn ion implantation," 2015, doi: 10.1109/NANO.2015.7388655.
[71] S. Prucnal et al., "Electron concentration limit in ge doped by ion implantation and flash lamp annealing," Materials (Basel)., vol. 13, no. 6, 2020, doi: 10.3390/ma13061408.
[72] A. L. Stepanov, V. I. Nuzhdin, V. F. Valeev, A. M. Rogov, V. V. Vorobev, and Y. N. Osin, "Porous germanium formed by low energy high dose Ag+-ion implantation," Vacuum, vol. 152, 2018, doi: 10.1016/j.vacuum.2018.03.030.
[73] A. M. Rogov, Y. N. Osin, V. I. Nuzhdin, V. F. Valeev, and A. L. Stepanov, "Porous germanium with Ag nanoparticles formed by ion implantation," in Journal of Physics: Conference Series, 2018, vol. 1092, doi: 10.1088/1742-6596/1092/1/012125.
[74] A. M. Rogov, V. I. Nuzhdin, V. F. Valeev, and A. L. Stepanov, "Formation of porous germanium layers with various surface morphology in dependence on mass of implanted ions," Compos. Commun., vol. 19, 2020, doi: 10.1016/j.coco.2020.01.002.
[75] A. M. Rogov, A. I. Gumarov, L. R. Tagirov, and A. L. Stepanov, "Swelling and sputtering of porous germanium by silver ions," Compos. Commun., vol. 16, 2019, doi: 10.1016/j.coco.2019.08.013.
[76] B. Stritzker, R. G. Elliman, and J. Zou, "Self-ion-induced swelling of germanium," in Nuclear Instruments and Methods in Physics Research, Section B: Beam Interactions with Materials and Atoms, 2001, vol. 175–177, doi: 10.1016/S0168-583X(00)00597-8.
[77] J. F. Ziegler, J. P. Biersack, and M. D. Ziegler, SRIM - The Sopping and Range of Ions in Matter. SRIM Co., 2008.
[78] J. T. Warner, Lithium-Ion Battery Chemistries: A Primer. Elsevier Science, 2019.
[79] Y. Kang et al., "Binder-Free Electrodes and Their Application for Li-Ion Batteries," Nanoscale Research Letters, vol. 15, no. 1. 2020, doi: 10.1186/s11671-020-03325-w.
[80] L. Zhang et al., "Advanced Matrixes for Binder-Free Nanostructured Electrodes in Lithium-Ion Batteries," Advanced Materials, vol. 32, no. 24. 2020, doi: 10.1002/adma.201908445.
[81] P. Walker and W. H. Tarn, CRC Handbook of Metal Etchants, 1st Edition. CRC Press, 1990.
[82] X. Chen, L. Yang, H. Dai, and S. Shi, "Exploring factors controlling pre-corrosion fatigue of 316L austenitic stainless steel in hydrofluoric acid," Eng. Fail. Anal., vol. 113, 2020, doi: 10.1016/j.engfailanal.2020.104556.
[83] J. R. Taylor, Introduction To Error Analysis: The Study of Uncertainties in Physical Measurements. University Science Books, 1997.

3. Physical characterizations

3.1. Introduction

The characterization of the electrodes is fundamental to better understand their electrochemical behaviour, as this is naturally influenced by their composition, structure, and morphology. The analyses of the sample properties were performed on the bare substrates, on the as deposited samples, and on the nano-structured ones. In order to guarantee the highest reliability, complementary analyses were often used and compared. Their experimental results are summarised in this chapter.

Prior to the detailed discussion of the sample properties, a very brief description of the experimental techniques used in this work is presented. In particular, X-Ray Diffraction (XRD) patterns were combined with the results from Transmission Electron Microscopy (TEM) analysis to gather the structural information. The compositional analysis was carried out recurring to Secondary Ion Mass Spectrometry (SIMS) and independently confirmed by X-ray Photoelectron Spectroscopy (XPS). SIMS was also used to investigate the thickness of the layer deposited, as a check for the deposition technique. This was supported in an independent way also from TEM analysis and Secondary Electron Microscopy (SEM). The sample morphology was determined by means of SEM inspections, both in top-view as well as in cross-section, to evaluate how this evolves across the germanium film thickness. The sample morphology was confirmed by TEM and by the dual beam Secondary Electron Microscopy and Focused Ion Beam technique (SEM-FIB), which was employed to prepare the TEM specimens and to perform localized cross-section analysis. In SEM, TEM and SEM-FIB, Energy Dispersive X-ray Analysis (EDX) verified the composition observed with XPS and SIMS and helped to identify the position of the substrate, the germanium layer, and the eventual protective films.

At the end of the chapter, the main results are summarised.

3.1.1. X-Ray Diffraction

X-Ray diffraction (XRD) can be exploited to investigate the crystallinity degree and the structure of samples. This technique exploits the constructive interference of X-rays scattered on the atoms and electrons of the material under investigation [1]. If these are arranged in regular ways, namely if these have a lattice structure, constructive interference can occur in certain directions. This happens in those directions for which the path difference of the scattered waves is equal to an integer number of wavelengths λ. This is depicted in part A of Figure 27 and is expressed by the Bragg's law of the diffraction [2][3]:

$$2d \sin \theta = n \lambda \quad (26)$$

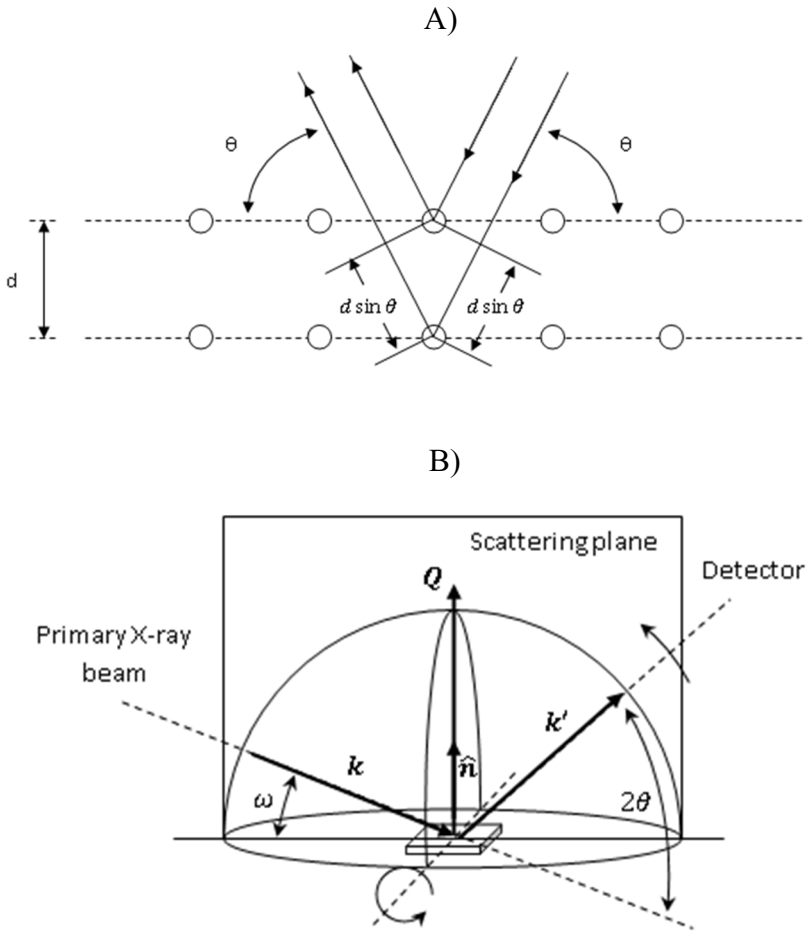

Figure 27: The Bragg's law of diffraction (A) and a typical ω/2θ scan configuration of a diffractometer (B). Both images are adapted from ref. [1].

In a typical X-ray diffractometer, the source of the primary X-ray beam is rotated around an axis centred on the sample. The detector is rotated around the same axis at a doubled angular velocity to measure the diffracted beam intensity. The X-ray source and the detector move on the same plane, on which lies also the normal to the sample surface, which is the scattering plane. The diffraction patterns obtained in this configuration are the so called ω/2θ scans. The working principle of a typical diffractometer is schematically represented in part B of the Figure . There, the wave vectors **k** and **k'** identify the incident and the diffracted rays, forming a 2θ angle between them. The ω angle is that between the surface and the incident beam. [4]

3.1.2. (Scanning) Transmission Electron Microscopy

Transmission Electron Microscopy (TEM) is an analytical technique used to investigate the morphology, microstructure and composition of samples at very high spatial resolution, down to the atomic scale [5]. This is achieved by sending a monochromatic beam of highly energetic electrons onto the sample (typical energies in the range of 80-300 keV, [6]). Some of the electrons are diffracted upon the interaction with the material, some undergo inelastic collisions, and some eventually pass through the sample unaffected. [6][7][8]

The instrument is composed by an Ultra-High Vacuum (UHV) chamber housing the electron gun and a series of electromagnetic lenses and adjustable aperture stops [6] [8]. Depending on the precise lenses and the aperture stops settings, the instrument can be switched between two different operating modes. In the first mode, termed imaging mode, it can be used to compose a direct image of the sample. In the other mode, termed selected area diffraction mode, it can furnish information about its structure and defects (see Figure 28). [9][10] Typically, a TEM instrument can also operate in "scanning mode" (STEM) by adding a scanning coil to the column to raster the electron beam on the sample surface. [8][11]

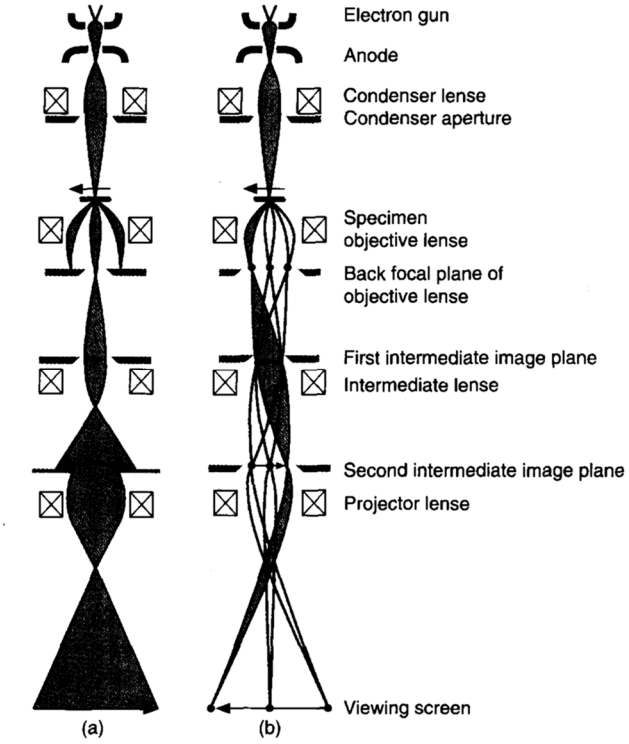

Figure 28: Ray diagram of the TEM operating modes: imaging (a) and selected area diffraction (b). Taken from ref. [10].

This technique permits to investigate only very limited amounts of materials, as the samples must be prepared in the form of extremely thin foils of about 100 nm or less in thickness to let the effective electron transmission [5][10]. For this thesis work, the thin specimens to be analysed with TEM were prepared recurring to the "dual beam secondary electron microscopy and focused ion beam" technique, that is presented in section 3.1.3.1.

3.1.2.1. Electron Energy Loss Spectroscopy

As previously mentioned, the electrons can undergo inelastic collisions upon their interaction with the constituents of the observed specimen. These could span over a wide energy range, as they could be the result of interactions like ionization events or plasmonic excitations [8], whose specific values are on turn related to the elements present and to their bonding states [9][12][13]. The analysis of the energy spectra of the transmitted electrons can thus be exploited to gather information about the specimen chemical composition, its band structure, and the bonding state of its atoms [9][8][12]. This is usually referred to as Electron Energy Loss Spectroscopy (EELS).

An example of an EELS spectra is reported in Figure 29. The zero-loss peak includes the elastically scattered electrons. The energy-loss range up to about 100 eV is dominated by collective electron excitations (plasmons) or energy transfer for transitions from the valence to the conduction band (left part of Figure 29). The latter includes the optical transitions and could be used to determine the specimen optical properties. Excitations from core-levels are found at higher energy losses (from 450 eV and above in Figure 29), appearing as edge-like features. The arrangement of these details and their precise energy permits to identify the elements present and their bonding state, while the area submitted includes information on their concentrations. [8][12][13]

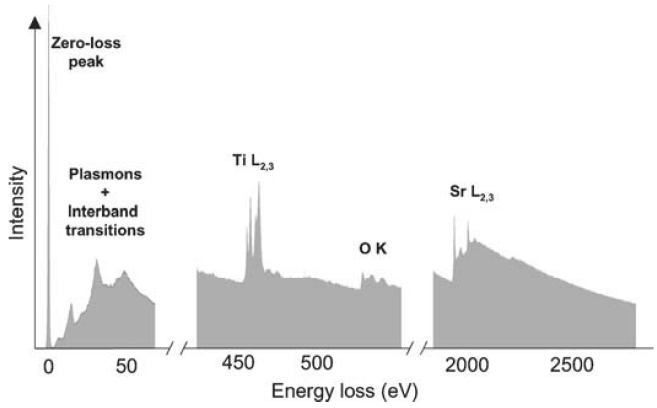

Figure 29: An example of Electron Energy Loss Spectrum, obtained from TEM analysis of a $SrTiO_2$ sample. The image is taken from ref [12]; the right parts of the spectrum are strongly magnified compared to the low-energy segment.

This technique was not used in the analysis of the samples reported in this thesis. It is nevertheless introduced since it represents one of the most useful characterizations available in TEM analysis.

3.1.2.2. Energy Dispersive X-rays analysis

Compositional information can be complementary obtained from the characteristic X-rays produced by electronic relaxation of the atoms that interacted with the electron beam [9]. This is usually carried out by means of semiconductor detectors and permits an independent confirmation of the chemical composition determined in EELS analysis.

This technique is named Energy Dispersive X-rays analysis (EDX) and it is often used as it permits a more straightforward quantification of the chemical species with respect to EELS, with high accuracy. Furthermore, when the TEM instrument is operated in STEM mode, it

enables the superposition of the elemental map onto the specimen image. However, it shows a lower energy resolution with respect to the former analysis. A further disadvantage is represented by the small solid angle of collection for the X-rays, this being limited by the size of the detector crystal [6][12].

For the purpose of this work, EDX was preferred since a complete compositional analysis was already carried out by means of the Secondary Ion Mass Spectroscopy and X-ray Photoemission spectroscopy, which are introduced in the next sections. The elemental maps gathered with this technique independently confirmed the high purity of the germanium films realized by means of LEPECVD. This technique resulted particularly useful in the determination of a detail at the interface of the samples realized on SS (see section 3.3.3).

3.1.3. Scanning Electron Microscopy

Scanning Electron Microscopy (SEM) is a widely used technique to provide topological and compositional information of the samples. In this tool, an electron beam is accelerated and focused onto the sample surface, at energies that are lower than TEM and typically in the range of 100 eV – 40 keV [14][15]. When these electrons enter the sample material, several signals are produced as a result of their interactions with matter. For instance, as it is depicted in Figure 30, they can be backscattered with the same energy, or they could produce the emission of auger electrons, characteristic and bremsstrahlung x-rays, or Secondary Electrons (SE), depending on the specific interactions and whether these are elastic or inelastic. [6][14][16]

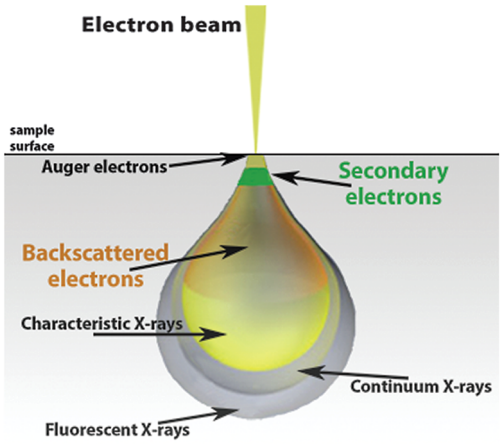

Figure 30: Interaction volume for of the primary electron beam with the sample material and regions where the interactions products are originated. The image is from ref. [17].

The interactions usually result in a “pear-shaped” volume inside the specimen, from which the various interaction products originate. The precise shape and dimensions of this region depend on the primary electron energy and on the sample composition [9][18]. For higher energies, the dimension of the interaction volume increase, as it is depicted in part (a) of Figure 31, since the electrons can travel more space inside the material and cause a higher number of interactions. Vice versa, for lower energies (usually below 5 keV [15]), the primary electrons can travel only for a limited distance in the sample, and the interaction region shrinks (part (b) of Figure 31). This difference in the probed region is typically exploited in SEM to gather information from various depth of the sample under investigation. [15][18]

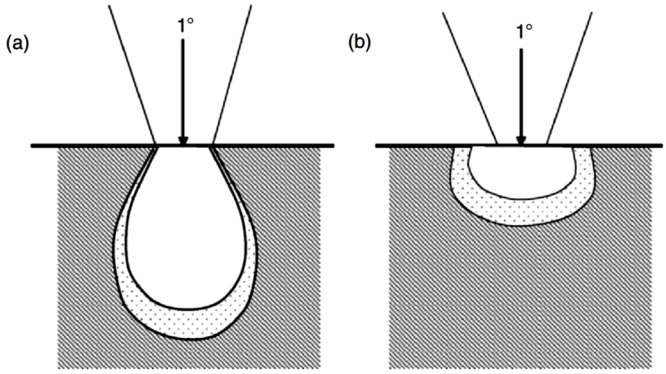

Figure 31: Interaction volume for a higher energy (or lower atomic number sample) (a) or low-energy (or higher atomic number sample) primary electron beam. The image is from ref. [18]

Among all the previously cited signals, the SE are particularly important since they are typically used to obtain the sample surface images [6]. SE are conventionally defined as those having energies of less than 50 eV [18]. Due to their low energy, they typically originate from the topmost nanometres of the sample, as displayed in Figure 30, from a zone that is approximately as large as the electron beam spot on the surface. [6][18]

Topographical images of the samples are commonly obtained as SE intensity maps, that are constructed recording the SE originating from the sample while the primary electron beam is scanned over its surface [19]. SE that are prevented from reaching the detector will generate shadows or darker regions in the final image [6]. For instance, these could be morphological features of the sample acting as barriers between the SEs and the detector, as it is depicted in part A of Figure 32. [18]

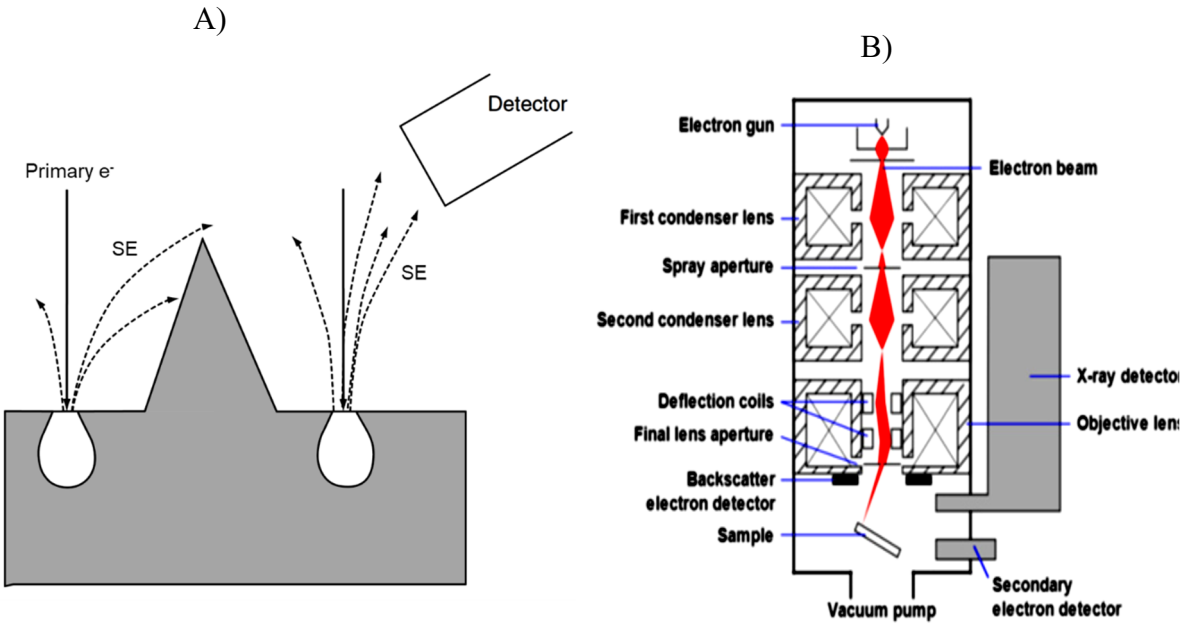

Figure 32: Schematic of SE detection influenced by the sample morphology (A), adapted from [18], and drawing of the typical SEM components (B), taken from [15].

Analogously to TEM, also SEM is usually composed by a vacuum chamber containing an electron gun and a set of electromagnetic lenses. Scanning coils enable to scan the electron beam on the surface of the sample, which is hosted on a specific stage. A series of detectors for SE, backscattered electrons, X-rays, etc... can be placed in the vacuum chamber to gather information from the signals previously listed. The general scheme of a SEM tool is drawn in part B of Figure 32. [6][15][16]

Among the various detectors, there is an analogous of the EDX introduced in TEM. This tool permits the measurement of the characteristic X-rays originating from the sample, enabling a compositional analysis precisely as it occurs in TEM [6][15]. However, differently from the former technique, the accuracy is lower in SEM as typically larger interaction volumes are involved [9][6]. SEM EDX is nevertheless extremely useful to produce elemental maps [6], as it was performed for many samples of this thesis. In particular, elemental maps resulted very useful in the SEM-FIB analysis (introduced in the next chapter) to identify the position of the interface between the Ge layer and the substrate.

3.1.3.1. Dual beam Scanning Electron Microscopy and Focused Ion Beam technique

The SEM column can be coupled to a confocal Focused Ion Beam (FIB), resulting in a versatile multifunctional tool that is termed dual beam SEM-FIB technique. In the dual-beam platforms, in addition to imaging and chemical analysis as for simple SEM, direct manipulation and structuration can be successfully carried out from the micrometre range down to the nanoscale. [20]

The working principle of standard FIB is similar to that of SEM, but in this tool an ion beam is focused onto the sample surface, rather than an electron beam. The ion beam consists of ionized atoms of relatively massive elements, that are typically accelerated up to energies of 50 keV. The elements chosen for the ion beam are typically liquid metals as they simplify the ion extraction and allow for a precise beam control. Among all the possible sources, gallium is commonly preferred in commercial FIBs. [21][22][23]

Depending on the ion energy, their interaction with the specimen could result in sputtering, amorphization, deposition, implantation, or backscattering. The first process is exploited for milling the sample surface, as this is the fundamental application of FIB systems. Ion milling can be used to structure the sample surface, allowing for complex patterning that are difficult to form using conventional processes due to material or geometrical constraints. In addition, compared to standard lithography or etching processes, FIB nano-structuration could be performed without the use of masks. [20][21][24]

Thanks to its capability to perform precise cut with extreme spatial accuracy, dual-beam SEM-FIB is largely employed in the preparation of samples for TEM analysis [23]. These can be cut in the form of ultrathin and uniform lamellae, that can be taken from the desired positions of the sample in a more rapid and safe way compared to traditional methods. [21][22][25][26] The lamellae for TEM inspections of this work were prepared recurring to this technique.

As an investigation technique, the ion beam result in a better compositional contrast compared to single beam SEM. This is due to the strong dependence of the primary ion energy loss with the atomic number [22]. In addition, the secondary ions extracted from the sample during milling can be analysed with a spectrometer, as a further compositional

analysis. This is similar to the technique of Secondary Ion Mass Spectroscopy that is introduced in section 3.1.5. [21]

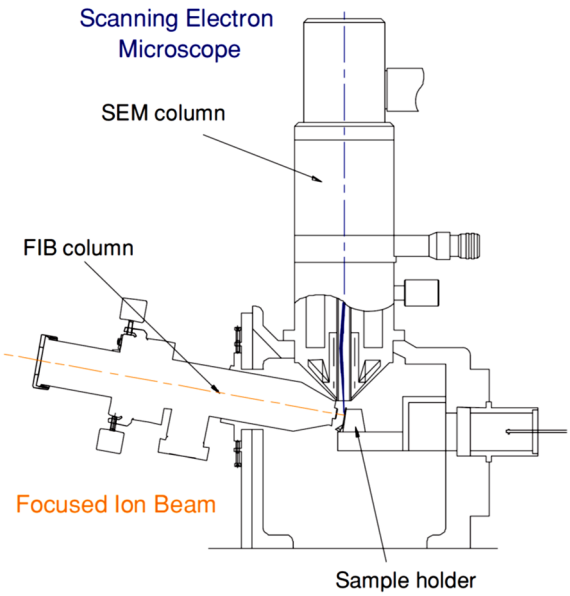

Figure 33: Schematic of the combined SEM-FIB microscope, from ref. [20].

The schematic layout of a dual beam SEM-FIB is depicted in Figure 33. Usually, the SEM electron column is mounted in a vertical position, while the ion column lies at an angle of about 55°, so that the electron and ion beam spots can be coincident on the sample surface. [20][21][22]

When equipped with a Gas Injection System (GIS), dual-beam SEM-FIB can be used also to perform precise deposition of material on localized regions of the specimens. This is achieved by injection of gas precursors that are decomposed by the electron or ion beams, leading to the deposition of small amounts of material. This is particularly useful for micro or nano lithography or to deposit conductive or protective layers for subsequent processing. [20][21][22] Protective Pt layer were often realized on the samples studied in this work and can be recognized in many of the TEM or SEM images presented in this section.

3.1.4. X-ray Photoelectron Spectroscopy

X-ray Photoelectron Spectroscopy (XPS) is a technique used to investigate the surface chemistry of samples. In XPS the sample surface is irradiated with monochromatic X-rays, typically Al-Kα (1486.6 eV) or Mg-Kα (1253.6 eV). Their absorption by the sample atoms

can result in core-level excitation, with the corresponding emission of energetic electrons. This represents the photoelectric effect, and the Kinetic Energy (KE) of the emitted electrons is related to their Binding Energy (BE) by the following equation: [9][27] [28][29][30]

$$\text{KE} = h\upsilon - \text{BE} - \phi \quad (27)$$

Where $h\upsilon$ is the photon energy and ϕ is the spectrometer work function. The KE of the emitted electrons is the quantity measured in XPS: since the BEs are characteristic of each element, the electron energy spectra can be used to identify the elements present in the specimen. Besides the core-level electrons, also auger electrons could be emitted as a result of the relaxation processes that follow the photoelectron emissions. Since also the energies of these electrons are characteristic for each element, they further contribute to the identification of the sample chemical composition. [9][29][30][31][32]

An example of an energy spectra collected with XPS is depicted in Figure 34. The peaks correspond to core-level or auger electrons, while the diffuse background is related to electrons that underwent inelastic collisions in their escape from the specimen. The peaks intensity give quantitative information on the elements present, while their displacements and relative intensities can be related to the chemical state and bonding of the atoms. [30] [31][33]

Due to the low energies of the exciting photons, only the electrons from the topmost layers of the material (depth < 10 nm) could exit without heavily interact with other atoms or electronic clouds. This is clearly visible also in the previous Figure 30, where it can be observed that auger electrons originate from a very thin layer near the sample surface. This is why this technique is particularly useful for surface analysis. [9][27][28][33]

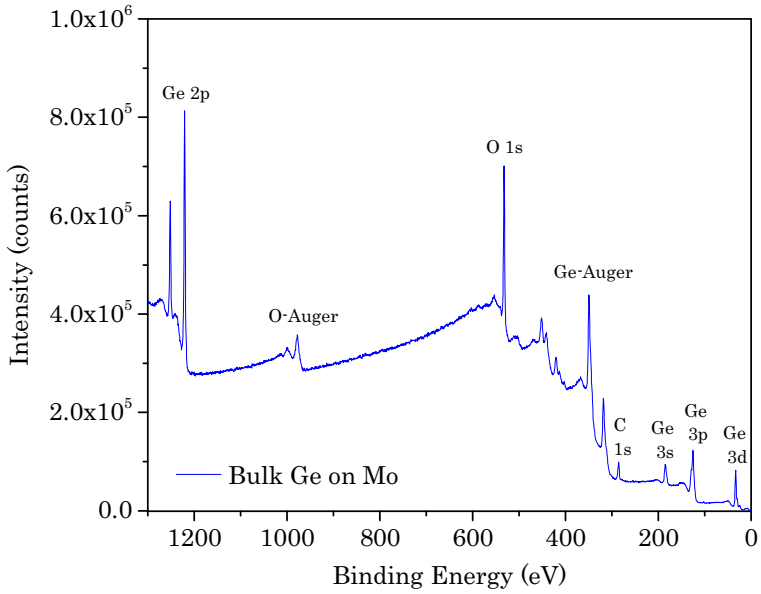

Figure 34: Example of the binding energy survey for a bulk germanium sample obtained using XPS.

A schematic drawing of the main XPS components is depicted in Figure 35. These are basically the X-ray source, which irradiates the sample surface, and a hemispherical analyser where the photoemitted electrons are collected and their energy analysed.

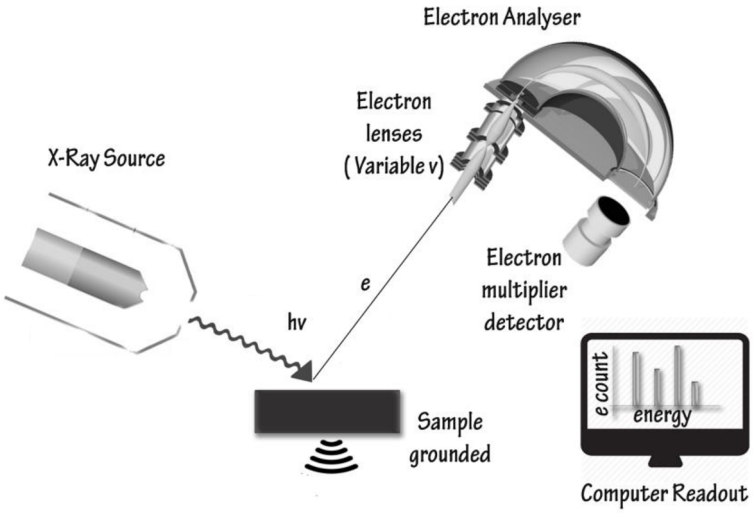

Figure 35: Schematic of the main XPS components. Adapted from ref [28].

3.1.5. Secondary Ion Mass Spectrometry

Secondary Ion Mass Spectrometry (SIMS) is one of the most sensitive surface analytical techniques that is commonly used for compositional analysis. The high sensitivity of this

technique allows for detection of impurities in concentrations as low as parts per billion (ppb). For this reason, SIMS is particularly suitable for doping profile evaluations in the semiconductor industry [9][34][35].

In this technique, the surface of the sample to be analysed is bombarded by an ion beam, with typical energies in the range of 0.1 keV – 50 keV and in UHV conditions, to induce sputtering. The Secondary Ions (SI) produced are then analysed by means of a mass spectrometer. Most of these ions come from the topmost atomic layers of the analysed material, which is what makes this technique a surface analysis tool [29][35][36].

The process of ejection of charged SI, which are the target of the SIMS measurement, are affected by a variety of factors.
The overall efficiency of the sputtering is usually expressed as the "sputtering yield" (Y). This depends on the sample characteristics, as the atomic number of its constituents, the crystalline structure and its orientation, the surface binding energy, and the sample temperature. But the yield is also affected by the primary ion parameters, like the atomic mass and number of the selected ions, the beam current density, the energy, and the incidence angle. The yield can also affect the Sputtering Rate (SR), which is a quantity expressing the thickness of material that is removed per unit of time. [9][29]

Even if the previous variety of factors must be considered when SIMS analysis are carried out, two operative regimes can be distinguished as a function of the primary beam current density. These differ in terms of the Sputtering Rate (SR).
In the first regime, which is termed static SIMS, low current density intensity is used and results in low sputtering rates, of about 1Å/h. This is particularly indicated for surface analysis and ion mapping as it enables precise composition profiling at monoatomic layer level.
The second regime, termed dynamic SIMS, is more suitable for bulk analysis and elemental depth profiling. This is achieved for high beam current densities. In this configuration very high sputtering rates, higher than 10 Å/s, can be achieved, resulting in fast depth profiling of thick samples. [9][29][37]

To use SIMS for quantitative evaluations of a specimen composition, reference samples are required to properly calibrate the sputtering yield. Indeed, this can greatly vary according to the chemical environment from which the ions are ejected. This is usually referred to as

"matrix effect" and prevents a direct quantification deduced from the ion as-measured signal. For this reason, to perform precise quantitative evaluations, sample specimens of high purity and having a matrix environment as similar as possible to the target sample are required to properly calibrate the analysis. [9][34][36]

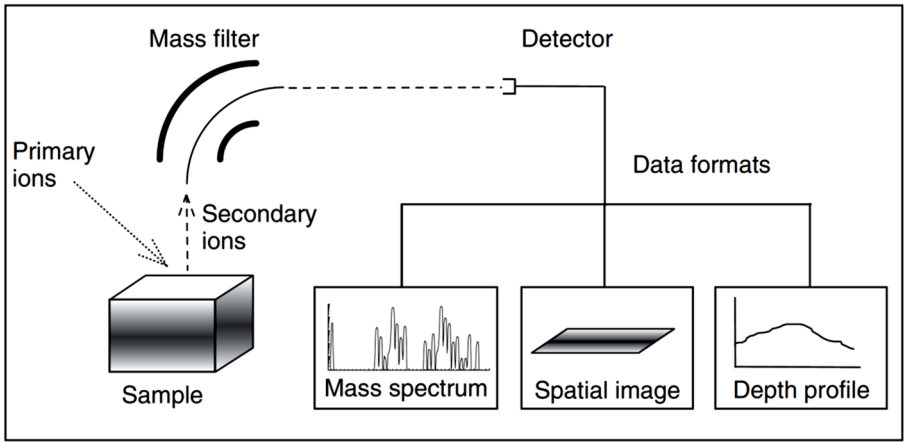

Figure 36: Conceptual drawing of the main components found in a typical SIMS instrument. Taken from ref. [29].

The SIMS main components consist of an ion source, the electromagnetic optics to accelerate and focus the primary ions onto the sample, the analysis chamber where the sample is placed, and the secondary ion collection tool that comprises also a mass selector. [9][29][38] A conceptual representation is presented in Figure 36.

3.2. **Substrates**

The most important physical feature of the pristine substrates is represented by their morphology, which is replicated by the thin films realized on their surface.
This has been investigated by means of Secondary Electron Microscopy (SEM) using a Jeol JSM-7401F. Secondary Electrons (SE) images were acquired using 15 keV accelerating voltage and 10 μA beam current and the samples were conventionally mounted on a holder with conductive carbon tape.

All the other SEM images presented in this work have been acquired with the same equipment and under same conditions; eventual differences are reported from time to time.

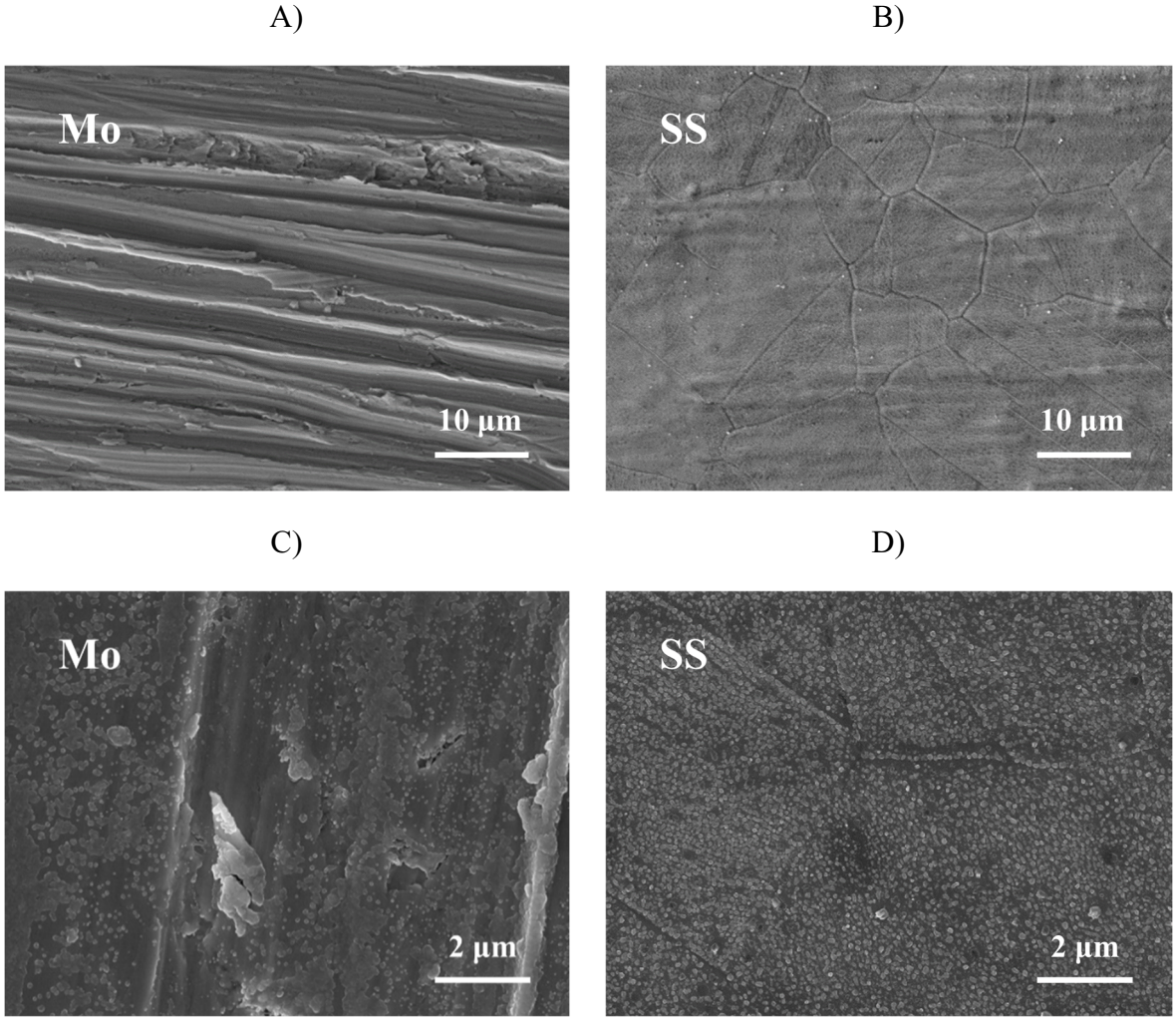

Figure 37: Top-view of the pristine substrates: Mo (A, C) and SS (B, D). Images A, B and D are from ref. [39].

As it can be recognized in Figure 37, Mo substrates appear quite rough with a striped texture (part A of Figure 37) that leads to micrometric variations of the surface height profile. SS, instead, appears essentially flat (figure B). The greater roughness of Mo compared to SS is confirmed also at higher magnification (C, D), even if less evident. For both the materials, some particle-like features are observed on their surface with dimensions of about a hundred nanometres.

3.3. Morphological, structural, and compositional properties of the thin films

The as deposited and nano-structured specimens have been characterized by means of various techniques. The main results are disclosed here, starting from the bulk films and concluding with the morphologies obtained with the two nano-structuration processes.

Most of the characterizations have been performed on 1 μm bulk or etched samples, as the structural and compositional properties of thinner samples are considered to be identical: for this reason, apart from some structural characterization performed for confirmation, only their morphology is presented in this section.

3.3.1. Bulk germanium films

The as-deposited films represent the bulk material prior to the nano-structuration. As it is confirmed by the SEM top-view images A and B of Figure 38, the films replicate the underneath substrate morphology, and so they result rough on Mo and flat on SS. The film surface appears grainy, as it is more evident at higher magnification (parts C and D of Figure 38). This could be related to the partially crystalline nature of these films (cf. structural analysis, sect. 3.3.3).

To inspect the films throughout their thickness, SEM analyses were performed by tilting the sample holder and inspecting regions near the specimen borders. In fact, as a result of the rough hollow punch operation, the Ge film is fragmented near the borders and allows in depth observation across its whole thickness. The cross-section reported in E, shows that the films realized by means of the LEPECVD deposition are dense and uniform across their entire thickness.

The top-view image F confirms the Ge layer fragmentation near the border. The fact that many fragments are still attached, up close to the border, is a hint of the very good adhesion achieved between the layer and the substrate, which is confirmed also from the TEM observations (sect. 3.3.3).

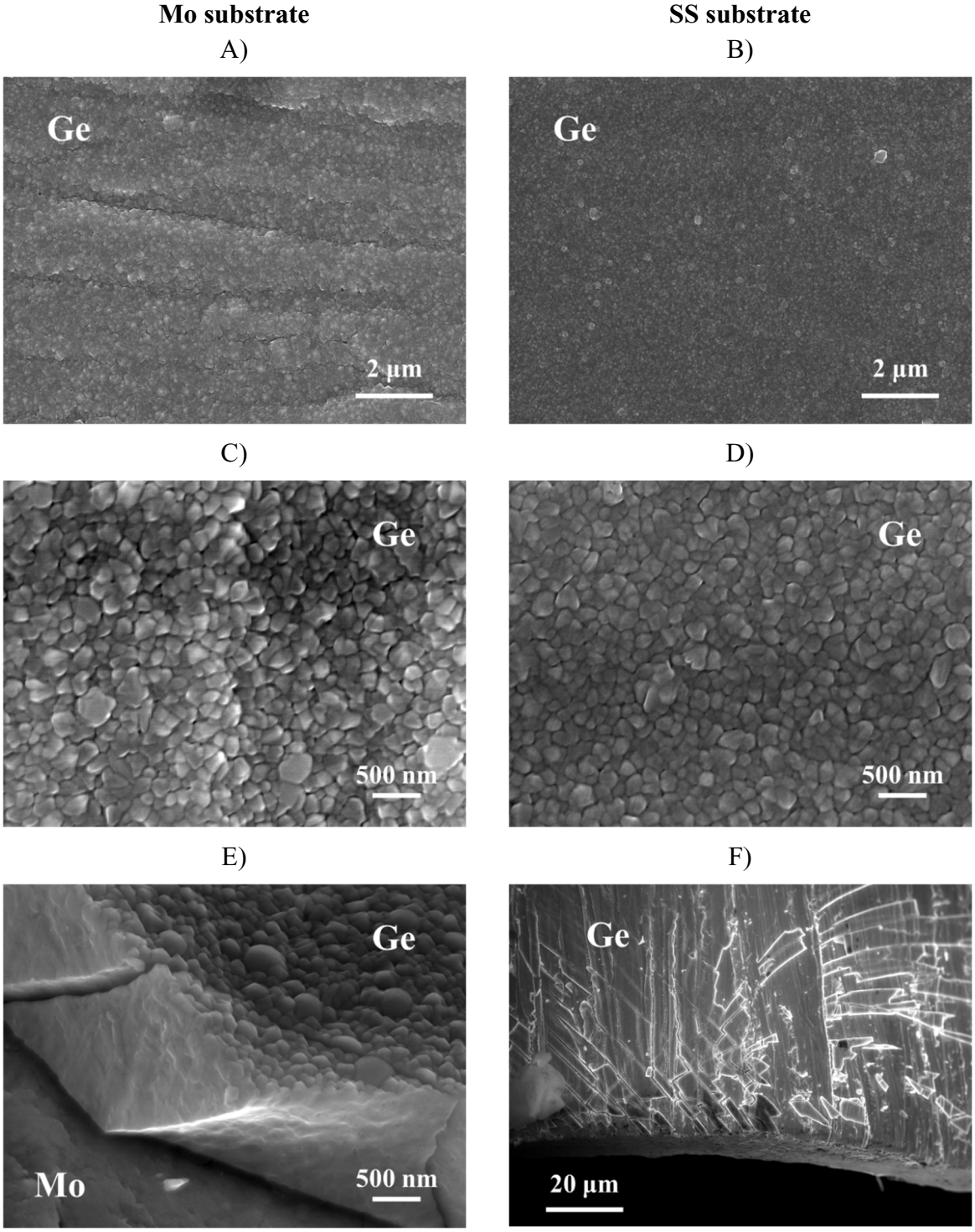

Figure 38: Top-view at low (A, B) and high (C, D) magnification and cross-sections (E, F) of the films realized on Mo and SS. Images C and D are from ref. [39].

3.3.2. **Thin film composition**

The sample composition has been investigated via Secondary Ion Mass Spectroscopy (SIMS) and X-ray Photoelectron Spectroscopy (XPS).

SIMS was carried out with a Cameca SC-Ultra in MCs^+ mode, using 3 keV impact energy Cs^+ as primary ions and collecting the positive secondary ions formed by both the atoms of interest and the re-sputtered Cs^+ ions [40]. To improve the depth resolution, the analysis was carried out in the rotating stage mode, in which the sample is set on rotation around an axis normal to its surface. The rotation axis, primary ion beam and secondary ion beam are all centred on the same point of the sample surface that is under investigation [41]. To allow for thickness evaluations, the sputtering ratio of the LEPECVD deposited samples was determined by performing SIMS analysis on reference samples where thin Ge films were deposited onto flat Si wafers [42].

XPS were performed using a Kratos AXIS $Ultra^{DLD}$ with a beam energy of 1486.6 eV (Aluminium Kα). The samples were attached to the holder by metallic clips and the analysis were carried out on bulk and etched samples surfaces.

The SIMS profile presented in Figure 39 (left graph) shows that the films are composed only by Ge and some impurities, that are probably incorporated during the deposition process.
The three main contaminants are C, Si and, at a lower extent, O. C and O could be related to moisture, atmospheric oxygen or hydrocarbon contaminations [43][44], however all the three contaminants are compatible with occasional sputtering phenomena from various components inside the chamber (like the quartz holder or the graphite heater).

The thickness reported in the x-axis of that SIMS profile was determined by inverse formula from the sputtering time and the sputtering ratio [42]. The film thickness can be identified as the position where the molybdenum signal rises to 50 % of its total value. As it can be seen, this occurs around 1000 nm and perfectly agrees with the estimation based on the growth rate (see sect. 2.2.4).

The increase of the Mo signal inside the Ge film, prior to the interface, is ascribed to a combined effect of the substrate surface roughness and of the rotating stage acquisition method rather than a Mo diffusion towards the layer. This way, the rise of the signal is thought to derive from those substrate features which are locally higher and therefore are detected in advance.

The XPS analysis confirms the composition as determined from the SIMS, with the presence of O and C, as it can be seen in the surveys reported in part B of Figure 39. XPS also highlights the presence of fluorine (F) in the bulk samples, which is suppressed in the etched ones. This is ascribed to contaminations in the deposition process: this could originate either from the fluorinated vacuum oil (perfluoropolyether) of the pre-vacuum pump or from residual traces of the gas used for the process chamber cleaning, which is NF_3.

Regarding the reduction of the F signal after the etching, it is thought that this could be engaged in the etching process, in which HF is used, thus resulting in its depletion in the nano-structured samples.

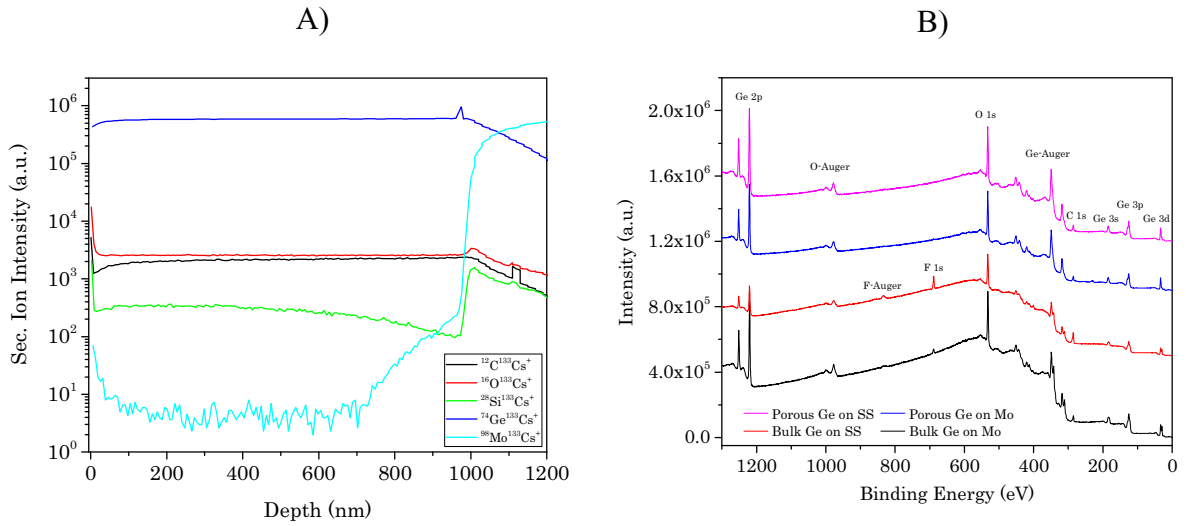

Figure 39: SIMS analysis of a bulk sample deposited on Mo substrate (A) and XPS surveys of the thin film surface for samples realized on both the substrate materials (B).

3.3.3. **Structural analysis**

The film structural properties have been evaluated through XRD and TEM-STEM analysis. XRD was carried out by means of a PANalytical Empyrean X-ray diffractometer equipped with a 1.8kW CuKα ceramic X-ray tube, PIXcel3D 2x2 area detector and operating at 45 kV and 40 mA. The diffraction patterns are collected in air at room temperature using Parallel-Beam geometry and a symmetric reflection mode.

Transmission Electron Microscopy (TEM) and Scanning-TEM (STEM) were performed with a FEI Tecnai F20 ST microscope. To investigate the Ge layer, cross-sectional specimens were prepared by a dual beam SEM-FIB Zeiss CrossBeam 340, using a conventional approach for the fabrication of a cross-sectional sample thin lamella and starting from the deposition at the samples surface of a platinum protective layer. This characterization was carried out on the etched samples to inspect the nano-structures realized while evaluating their crystallinity.

The structural characterization shows that the films are composed by an amorphous matrix in which Ge is locally organized into crystalline domains. This is in accordance with previous works observations [1][45], with the electrochemical behaviour observed during the 1st cycle lithiation (see section 4.7.1), and could be responsible for the grainy morphology noticed before. In addition, the film structural properties are independent from the substrate material.

The XRD curves of 1 µm and 350 nm bulk and nano-structured samples realized on SS and Mo are reported in Figure 40. Crystalline Ge (c-Ge) is clearly present in both the types of bulk samples (A and C), confirming that the structural properties of the thin and thicker samples are the same. These peaks are also clearly visible in the etched sample (B) but are nearly absent in the implanted one (figure D). This means that crystalline Ge is still present after the etching process, while ion implantation result in a layer amorphization. This perfectly agrees with the pore formation mechanism in the implantation process presented in section 2.4.3.

In all the samples, a prominent shoulder is found on the left of the first Ge reflection peak, at about 25.5°, which could be associated to Ge oxide (GeO_2).

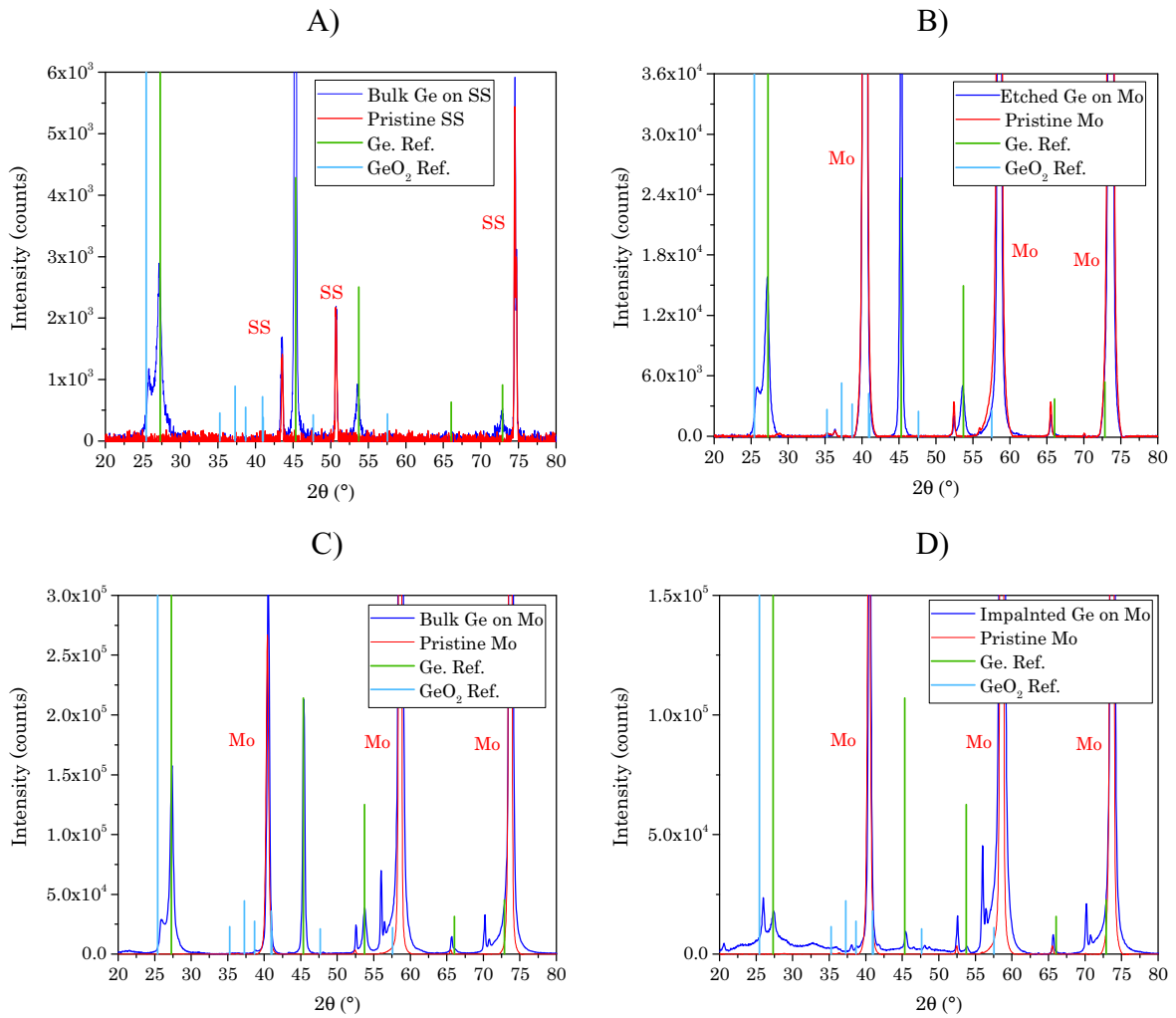

Figure 40: XRD patterns of an as deposited film realized on SS (A), an etched sample realized on Mo (B), a ~320 nm bulk film realized on Mo (C) and an ion implanted sample realized on Mo (D).

The TEM cross-sections of two etched samples realized on Mo (A) and SS (B) by means of the Etch1 recipe are reported in Figure 41. In both the images the substrate is visible on the bottom part and the nano-structured layer is on its top. Above the Ge, the Pt protective layer is visible.

The Ge structures show irregular shapes and variable dimensions: in both the cases they show a mountain-like aspect, with micrometric bulk regions interconnected at their base (particularly evident in A). These structures appear dense and uniform, confirming the previous SEM observations (Figure 38). Fine Ge structures can be noticed on the surface of these bulky regions: these are more evident in the morphologic inspection that is presented in section 3.4. Furthermore, at their base, the films show a perfect continuity with the

substrate materials, which could explain the strong adhesion experimentally observed with both the substrate materials.

The insets show the Selected Area Electron Diffraction pattern (SAED) from zones inside the Ge layer. The broad rings in part A show a local amorphous region, while the sharper ones with bright spots in part B suggest a local presence of Ge crystals. This, combined to the XRD analysis, is compatible with a generally amorphous structure of the Ge layer in which are dispersed small crystalline domains.

A) B)

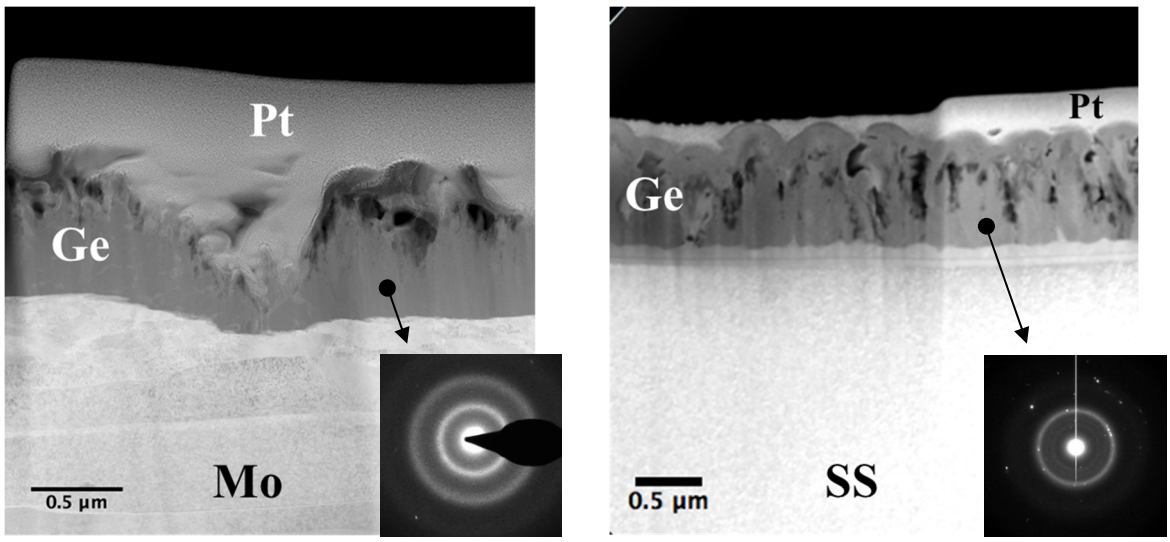

Figure 41: STEM of etched samples on Mo (A) and SS(B). The insets show the SAED performed on the Ge layer.

Some other interesting information comes from the interface region: indeed, the presence of an extended interface between the substrate and the thin film can be noticed in the SS sample. This is depicted at high magnification in Figure 42, where it clearly appears also a thin marked line that runs parallel to the substrate. A STEM Energy Dispersive X-ray analysis (EDX) was performed along the red arrow visible in A and showed a mixed composition region of Ge and Fe spanning over a thickness of about 100 nm. The EDX also shows that the sharp line inside the interface corresponds to a Chromium rich layer. This is identified as the original position of the SS surface before the film deposition. Indeed, Cr represent the 16 ÷ 18 % of the SS 316 alloy, and it is well known that it forms a few nanometres thick layer on the SS surface as a result of natural passivation of this material [46][47].

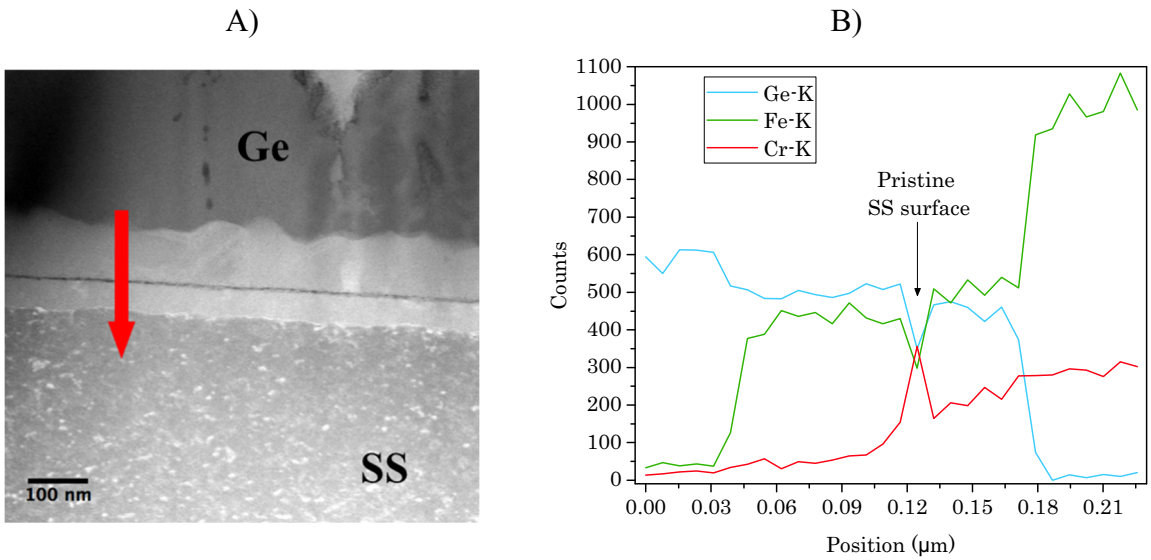

Figure 42: TEM of the extended interface between the Ge layer and the SS substrate (A). EDX analysis performed along the red arrow of part A to investigate the interface thickness and composition (B).

3.4. Morphologies of the nano-structured electrodes

The morphology analysis is performed through top-view and cross-section SEM inspections of the sample surfaces. As for the bulk samples, the cross-sections are obtained by simply tilting the SEM sample holder with respect to the incident electron beam.
The morphology of the electrochemically etched samples is presented first, followed by that of the ion implanted ones.

3.4.1. Etched samples

The etched samples present an irregular morphology which could resemble that of mountain chains, with Ge "crests" divided by "valleys/canyons" where the material has been removed. The top-view and cross-section SEM images of the structures realized by means of the different etching recipes are reported in Figure 43. As it can be seen, the various etching recipes produce similar results in terms of general morphology, but the size of the structures and voids is different from case to case.

The Etch1 recipe (images A, B and C of Figure 43) shows the smaller features and the most homogeneous distribution between the Ge structures and the void spaces, compared to the

other morphologies. In part B, the upmost Ge structures show dimensions in the range of tens to hundreds of nanometres, which become wider in their bottom parts with branches and articulated interconnections. These can be recognized as the mountain-shaped structures observed in the TEM analysis, as it is particularly evident in the cross-section image C.

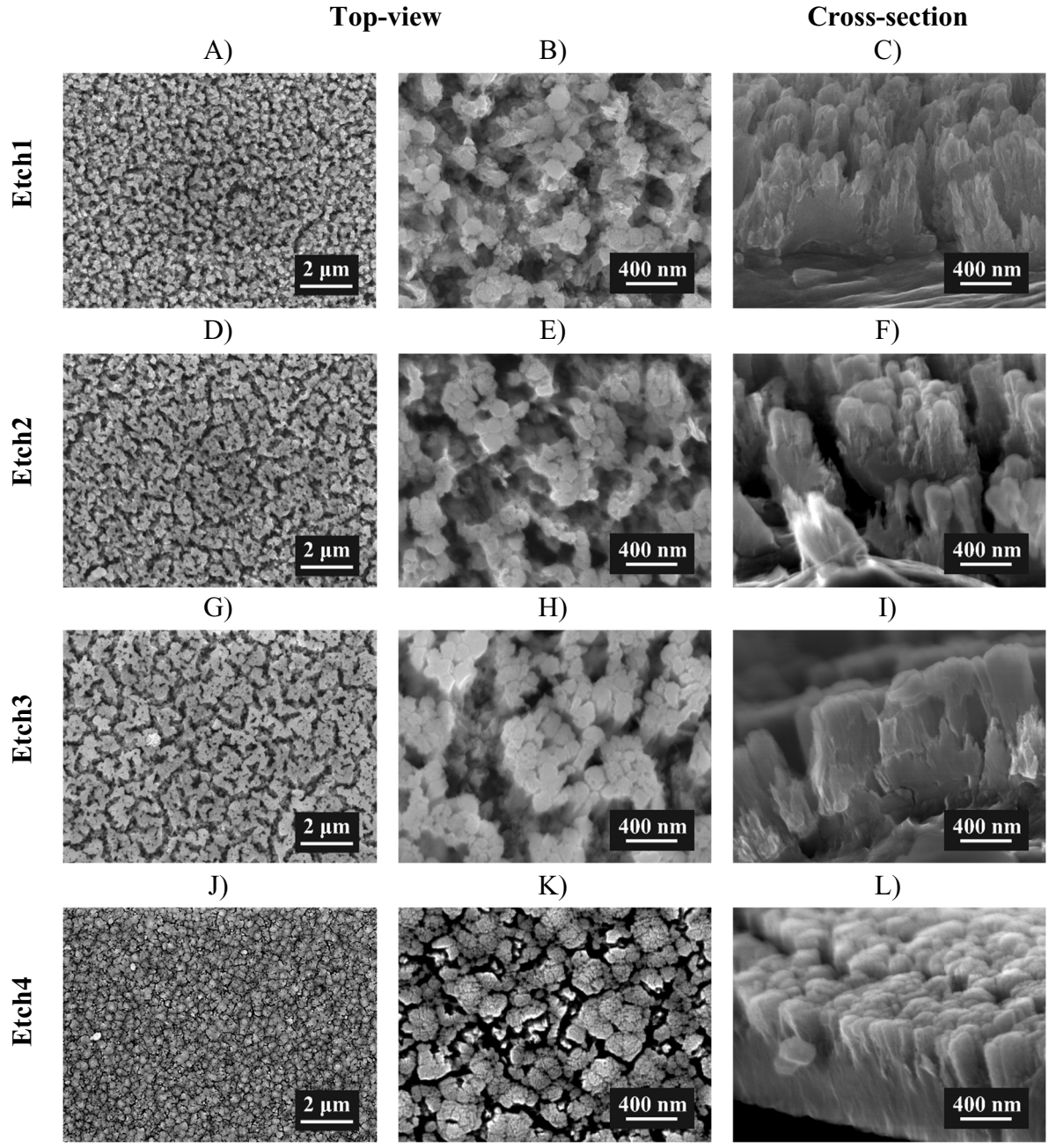

Figure 43: Morphologies produced by means of the different etching recipes. Top view SEM images of the samples surfaces at low (A,D,G,J) and high (B,E,H,K) magnification. Cross-sections of the samples at high magnification (C,F,I,L). Images A, C, F, I and L are from ref. [39].

The Etch2 structures appear bigger than those of Etch1, with Ge clusters of micrometric dimensions clearly visible in all the images (D, E and F). Even the valleys seem to be larger

than for Etch1 and can be identified more easily. When looked in cross-section, as in image F, these appear like deep canyons, while the bottom of the Ge clusters resembles to be composed by unique massive regions.

Etch3 shows the biggest structures and the largest valleys, with big agglomerates that seem to have been only partially affected by the etching. Indeed, the Ge agglomerates appear to be constituted by thick columns with interconnected bases (see image I), rather than showing deep valleys up to the substrate.

The Etch4 morphology is obtained as Etch1 but stopping the electrochemical attack after half of the time, thus showing the starting of the nano-structuration process. As it can be seen, the electrochemical attack starts forming many sharp trenches (black regions in K) that extend up to half the layer thickness (image L). Afterward, these trenches must propagate towards the substrate while the structures above are further consumed to produce the final morphology observed in Etch1.

The features described are quite different from those reported in the works considered for the etching model (cf. section 2.3.2 and ref. [48][49][50][51]), but this is not a contradiction. Indeed, in those works, Bipolar Electrochemical Etching (BEE) was employed. In that technique, the polarity is periodically reversed by introducing cathodic steps, with the purpose of passivating the highest part of the layer from the continuous dissolution due to the divalent reaction mechanism.
In our case, no cathodic steps were introduced, and the etching was performed as a single anodic step for the whole time of the process. For this reason, according to the dissolution model and as it is confirmed by the Etch4 morphology, the dissolution starts digging deep tranches (tetravalent mechanism). Then, the already nano-structured region is further attacked and the pores gradually widen during the etching up to the final morphology observed for Etch1. Always according to the latest dissolution model, this is ascribed to the divalent dissolution mechanism.

As it could be expected, the void space produced by the Etch1, Etch2 and Etch3 recipes is more than that of Etch4, and it appears to be more evenly distributed for Etch1 and Etch2. As anticipated in Chapter 1 (section 1.6.4), this void space is fundamental to permit to the free expansion of the Ge structures during the electrochemical reactions with Li. The fabrication approach used to produce the electrodes, requiring no binders

or conductive agents, leaves this space at complete disposal for the free expansion of the Ge structures. In addition, the lack of "foreign" materials let the whole surface of the Ge layer to be in contact with the electrolyte, thus enhancing the electrode kinetics.

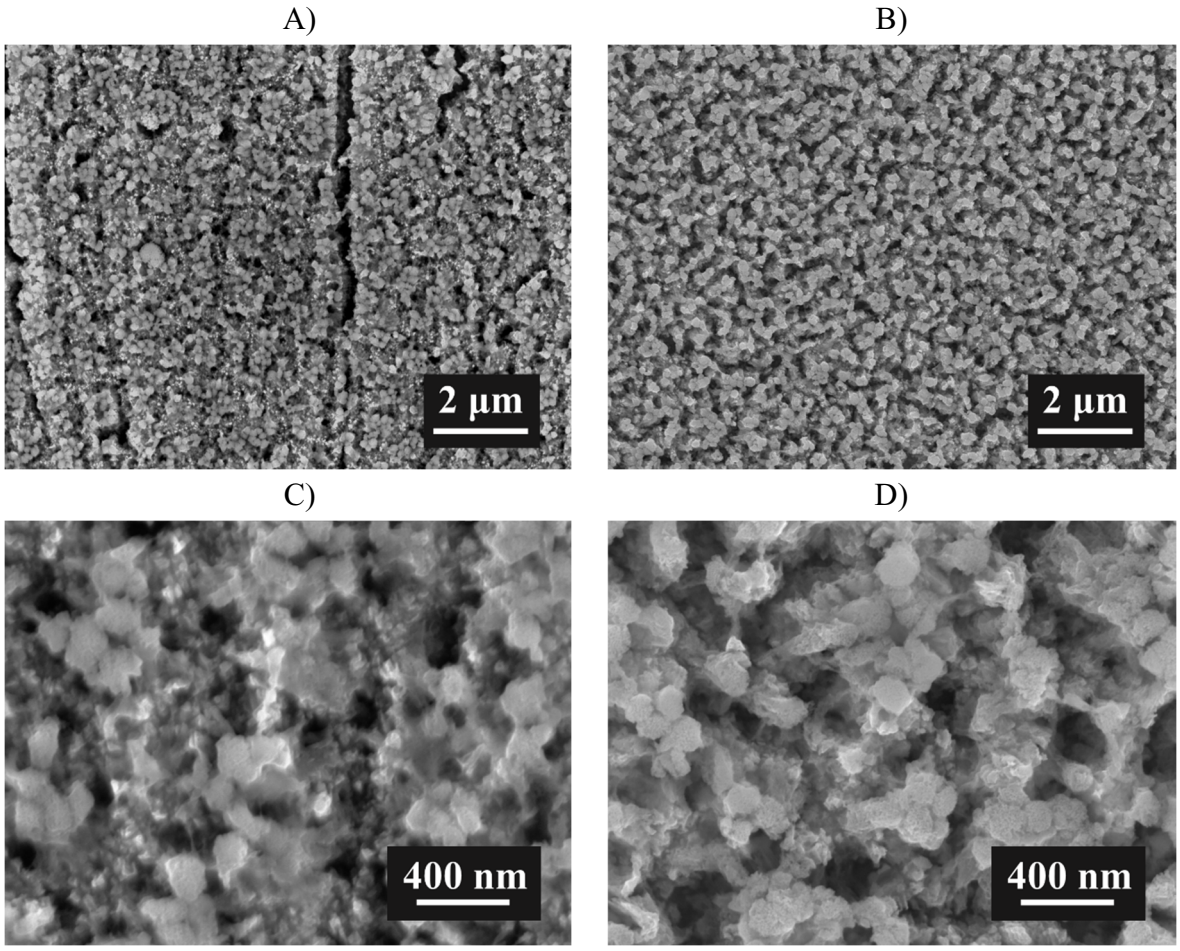

Figure 44: Top-view SEM images at low and high magnification of samples realized on Mo (A, C) and SS (B, D). The substrate materials can influence the macroscopic morphology of the etched samples (A, B) but not their microscopic features (C, D). Image C is from ref. [39].

The morphologies previously reported refer all to samples realized on SS. However, the structures produced are independent from the substrate material used, whose only effect is to influence the final "macroscopic" morphology, as already mentioned.

As a further proof for this, a comparison of the nano-structures realized by means of Etch1 on Mo or SS is reported in Figure 44. As for the bulk samples, the striped texture of the Mo substrate can be recognized also in the etched specimens (A), while those realized on SS do not show particular patterns as these substrates are flatter and more homogeneous (B). Furthermore, at higher magnification, no differences can be distinguished for samples realized on Mo or SS, as it can be observed in the parts C and D of Figure 44.

3.4.2. **Ion implanted samples**

The morphology of the ion implanted samples is completely different from that of the etched ones: for both the implantation recipes, fine Ge structures separated by regular void spaces are observed. These structures appear more homogeneous and evenly spaced for the Ion1 recipe with respect to the Ion2. However, in both cases, the general architecture is quite regular and well-organized. This perfectly agrees with the expectations from the damage map model presented in section 2.4.5.

As for the etched samples, also in these cases the substrate materials do not affect the implanted sample aspect, because the same structures are observed both on Mo and on SS for the same recipe.

According to the introduction given in section 2.4.3, implantation of Ge often results in "honeycomb" arrangements where void cells (or pores) are separated by Ge walls. And the morphologies observed in the SEM images of Figure 45 could match quite well with that kind of structures. In addition, very similar features can be recognized comparing these images with those reported in other works where self-implantation of Ge at similar energies and doses were performed, like those of Darby *et al.* [52], Romano *et al.* [53], Rudawski *et al.* [54] and Koffel *et al.* [55].

The thickness of the Ge walls is in the range of 10 nm for both Ion1 and Ion2, while the void spaces appear bigger and evenly spaced in the case of Ion1 recipe, with an average diameter of about 50 nm. The less regular appearance of the Ion2 samples, compared to Ion1, could be related to the higher ion energy in that case. Indeed, as mentioned in section 2.4.4, the precise morphologies can be influenced by the ion energy, that in this case could have induced an intermixing of the Ge walls.

For both Ion1 and Ion2 some pores are closed: they can be recognized as the regions of the SEM images which appear covered by a semi-opaque film. These films are also made of Ge and are observed in slightly higher quantity in Ion1, as it is particularly evident from parts B and D of Figure 45. This could be related to the slightly higher dose in that case, since a similar phenomenon was observed also by Darby *et al.* [52].

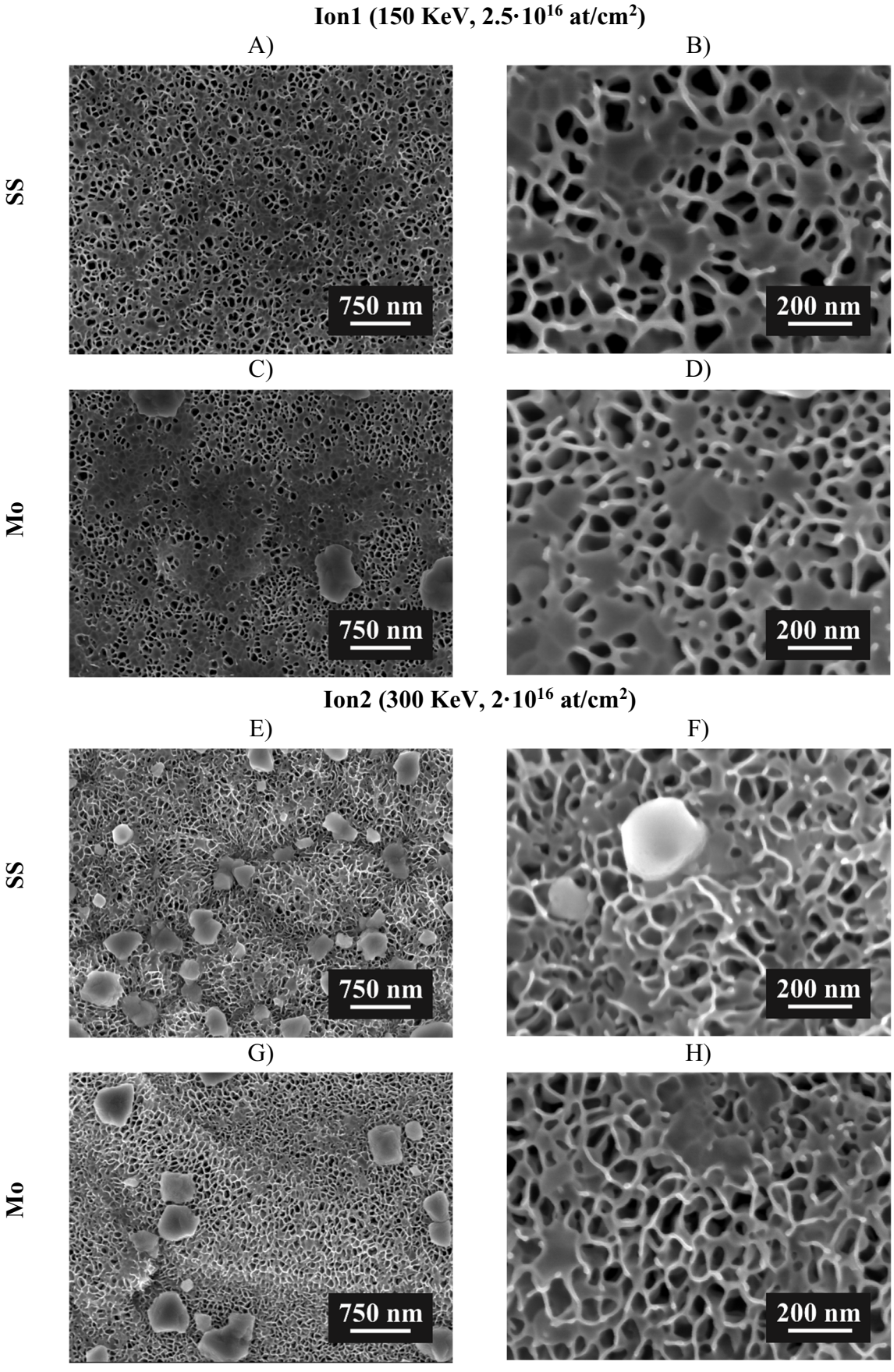

Figure 45: Top view SEM images, at low and high magnification, of samples realized on both the substrate materials by means of Ion1 (A, B, C, D) and Ion2 (E, F, G, H) recipes.

The SEM images also show micrometric particles above the nano-structured surfaces: these are an unpredicted result of the ion implantation process.

More particles are observed in the samples irradiated with higher energy i.e., Ion2, compared to Ion1. EDX analysis, shown in Figure 46, demonstrates that these particles are essentially composed by Ge and some traces of the substrate materials (Mo in the case of the sample in Figure 46). Their origin could be the result of a sputtering and redeposition process, that might be energy dependent.

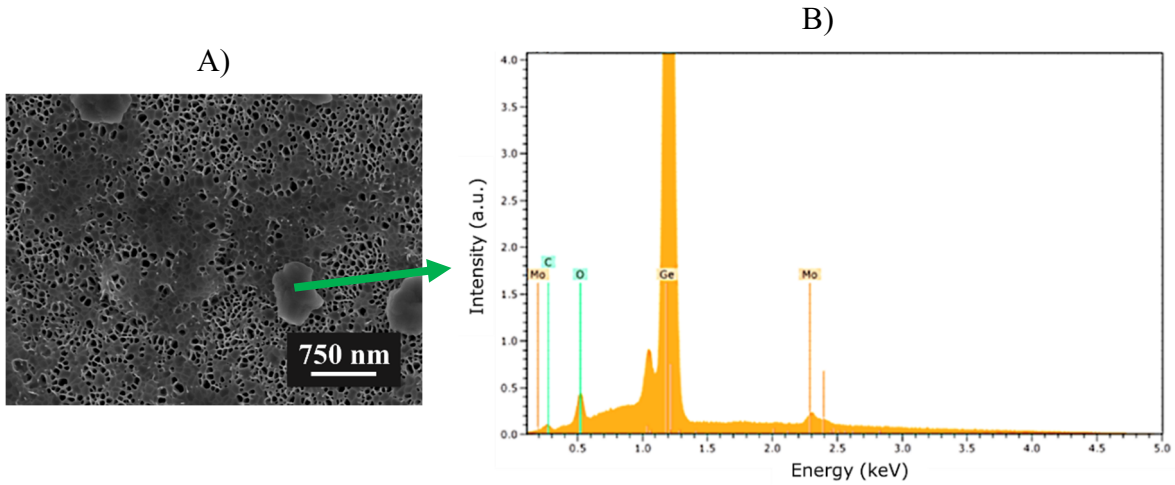

Figure 46: SEM image of some particles on the implanted Ge surface (A) and the EDX spectra performed on one of these particles (B).

SEM-FIB technique was used for cross-section analysis of these samples because, differently from the etched ones, it is not sufficient to tilt them to gain information about their in-depth structure. Their aspect across the nano-structured layer thickness can be inspected in Figure 47. First of all, the Ge structures can be clearly recognized between the Pt protective layer (light grey region on the top) and the Mo substrate (the homogeneous region on the bottom). Secondly, it seems that the nano-structuration process did not occur in a uniform way across the whole film. In fact, in the upmost region some pores and walls of the typical "honeycomb" structure are visible. Instead, in the lower part, spherical-like features are observed which are regularly and densely distributed. Therefore, it seems that the big voids have only a limited extension through the layer thickness and do not reach the interface with the substrates. On the other hand, the regular features on the bottom of the Ge layer suggest that some reorganization process started also in this region but was not completed. Probably, according to the vacancy clustering model introduced in section 2.4.3, these could represent some early stage of the vacancy clusters.

From part A of Figure 47, the final layer thickness after ion irroration can be measured. This resulted in an average value of 428 nm ± 14 nm, with an increment of about the 67 % with respect to the initial one (256 nm ± 12 nm, estimated from the amount of mass deposited)[1]. Such an increase perfectly agrees with the swelling reported in many other works and described in section 2.4.3.

The knowledge of the final layer thickness permits to calculate the VSF for the implanted samples (see sect. 2.3.7). In this case, only the volumetric definition can be used because no mass is removed during the implantation process. The VSF can then be simply calculated as the void volume divided by the total final volume of the layer. The latter can be found from the final layer thickness, after the implantation, while the void volume is simply the difference between the total final volume and that occupied by the initial bulk Ge layer. Assuming that the sample has not displaced between deposition and implantation, the "base" area is the same in both cases and the VSF can be expressed in terms of thicknesses rather than volumes. By performing these calculations, a VSF of about 40 % is found for the ion implanted samples (all data reported in Table 12), to be compared with the 70 % of the etched ones.

Although the VSF in the ion implanted samples is lower than that of the etched samples, the amount of free space produced seems to be significantly higher upon comparison of the SEM morphologies. This is due to the fact that the VSF simply expresses the amount of void introduced in the samples, without specifying how this is arranged. For instance, the same amount of void space produced in the etching could have been obtained through electropolishing, but in that case the remaining layer would have been a bulk structure instead of a nano-structured layer. Although the partial information that can be gathered, the VSF is anyway an important parameter and is the only quantitative factor that can be defined for these samples. Indeed, other techniques which could give some information about the sample porosity or their surface area after the nano-structuration, like the Brunauer-Emmett-Teller (BET) technique, failed to give reliable results due to the low amounts of materials involved.

[1] This value is lower than the aimed thickness of the as deposited samples for ion implantation (350 nm) but is compatible with elevated variability in thickness (~35.82 %) discussed in section 2.2.5.

A)

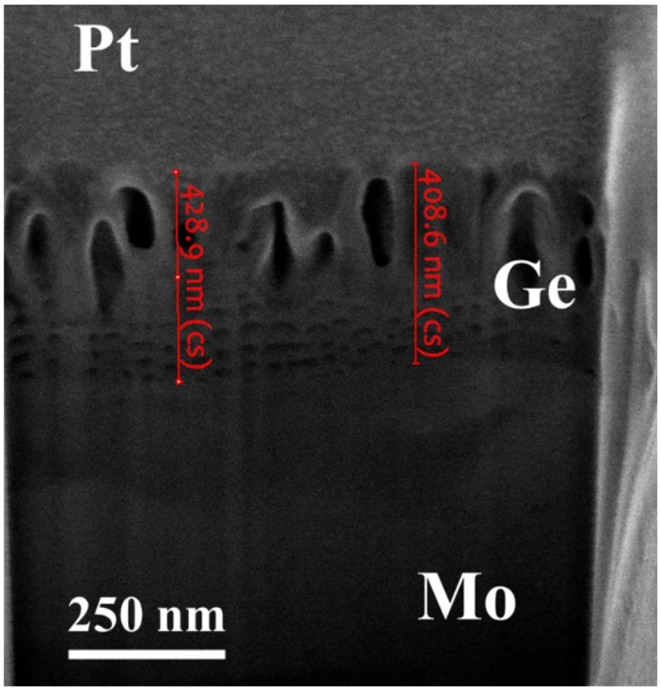

B) C)

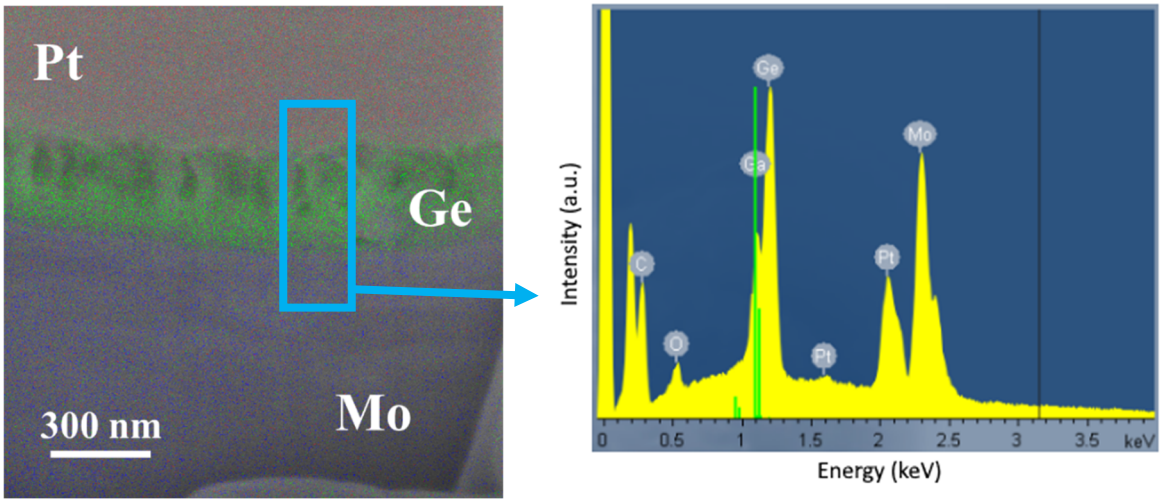

Figure 47: SEM-FIB cross-section of a Ion1 implanted sample on Mo (A). The nano-structured Ge layer thickness is reported by a couple of marks. EDX on the layer cross-section (B) and its spectra from the region outlined by the blue rectangle (C).

These things considered, the important aspect is that the nano-structuration process resulted in the production of significative amounts of void space, which are fundamental to permit to the free expansion of the Ge structures when reacting with Li. As for the etched samples, the lack of any binders or conductive agents leaves more space for this volumetric expansion and let the whole surface of the Ge layer to be in direct contact with the electrolyte, to the benefit of the electrochemical reaction rates.

An EDX analysis was performed on the sample cross-section and the corresponding elemental map is shown in part B of Figure 47, superposed on the corresponding SEM image. This analysis clearly shows a sharp interface between the substrate and the Ge layer. In particular, no intermixing can be identified between the Ge film and the substrate material, meaning that Ge and Mo are sharply divided under the compositional point of view, at the sensitivity level of EDX.

Bulk Ge initial thickness (nm)	256 ± 12
Implanted nano-structured Ge final thickness (nm)	428 ± 14
Height difference (nm)	172 ± 18
VSF (%)	40.2 ± 4.5

Table 12: Thicknesses, height difference and VSF of an ion implanted sample.

3.5. Summary and conclusions to Chapter 3

The characterization of the morphological, compositional, and structural properties of the samples was presented in this chapter, by analysing data from complementary techniques. The characterizations were performed on the bare substates, on the as deposited samples, and on the nano-structured ones.

The sample structure was investigated by means of XRD and TEM analyses. This demonstrated that the films are composed by an amorphous matrix in which Ge is locally organized into crystalline domains, for both the sample thicknesses of 1 μm and 350 nm. The film structure is not affected by the electrochemical etching, while ion implantation produces layer amorphization.

The sample composition was assessed by means of SIMS and XPS and the films resulted to be composed by pure Ge, with traces of contaminants that were ascribed to pollutants in the deposition process (mainly C, O and Si). The SIMS technique allowed also for an experimental verification of the sample thickness, which agreed with that determined from the growth rate, and was further supported also by TEM, SEM and SEM-FIB inspections.

The sample morphology was evaluated by means of SEM, TEM and SEM-FIB observations. The etched sample morphology resulted to be completely different from that

of the ion implanted ones. The first resulted to be “mountain-shaped”, with irregular features. The second appeared to be arranged in more homogeneous structures, which are compatible with the “honeycomb” aspect described in the literature. In all the cases, void spaces were produced to allow for the volumetric expansion of Ge through the cycles. For both the nano-structuration techniques, the observed morphologies are compatible with the respective theoretical models.

The presence of Ge particles on the ion implanted samples was reported. These were an unpredicted result of the ion-implantation process and EDX analysis showed that these are composed by Ge and traces of the substrate elements. EDX also permitted the identification of the former SS surface at the interface with the thin film, highlighted by a Cr rich strip. EDX also helped in the identification of the interface position during SEM-FIB of the ion-implanted samples.

Finally, it was demonstrated that the substrate materials only affected the macroscopic morphology of the samples, as the thin films replicate the main features of the underlying substrate.

References

[1] A. Andreoli, “Caratterizzazione di film epitassiali di SiGe tramite diffrattometria X,” University of Ferrara, Ferrara, 2010.

[2] C. Kittel, P. McEuen, and P. McEuen, *Introduction to solid state physics*, vol. 8. Wiley New York, 1996.

[3] N. W. Ashcroft and N. D. Mermin, “Solid State Physics, Cornell University.” Saunders College Publishing, Harcourt Brace Jovanovich College Publishers …, 1976.

[4] M. Birkholz, *Thin film analysis by X-ray scattering*. John Wiley & Sons, 2006.

[5] C. Y. Tang and Z. Yang, “Transmission Electron Microscopy (TEM),” in *Membrane Characterization*, 2017.

[6] B. J. Inkson, “Scanning Electron Microscopy (SEM) and Transmission Electron Microscopy (TEM) for Materials Characterization,” in *Materials Characterization Using Nondestructive Evaluation (NDE) Methods*, 2016.

[7] P. J. Goodhew, “General Introduction to Transmission Electron Microscopy TEM,” *Aberration-Corrected Analytical Transmission Electron Microscopy*. 2011, doi: 10.1002/9781119978848.ch1.

[8] J. M. Zuo and J. C. H. Spence, *Advanced transmission electron microscopy: Imaging and diffraction in nanoscience*. 2016.

[9] Maria Secchi, “Nanostructure formation on Germanium by ion irradiation,” University of Trento, Trento, 2016.

[10] K. D. Vernon-Parry, “TEM: an introduction,” *III-Vs Rev.*, vol. 6, no. 13, pp. 36+ – 38, 2000.

[11] D. B. Williams and C. B. Carter, *Transmission Electron Microscopy: A Textbook for Materials Science*, no. v. 1. Springer, 2009.

[12] W. Sigle, “Analytical transmission electron microscopy,” *Annual Review of Materials Research*, vol. 35. 2005, doi: 10.1146/annurev.matsci.35.102303.091623.
[13] W. Grogger, F. Hofer, G. Kothleitner, and B. Schaffer, “An introduction to high-resolution EELS in transmission electron microscopy,” *Top. Catal.*, vol. 50, no. 1–4, 2008, doi: 10.1007/s11244-008-9101-4.
[14] K. D. Vernon-Parry, “Scanning electron microscopy: an introduction,” *III-Vs Rev.*, vol. 13, no. 4, pp. 40–44, 2000.
[15] A. Abdullah and A. Mohammed, *Scanning Electron Microscopy (SEM): A Review*. 2019.
[16] M. Abd Mutalib, M. A. Rahman, M. H. D. Othman, A. F. Ismail, and J. Jaafar, “Scanning Electron Microscopy (SEM) and Energy-Dispersive X-Ray (EDX) Spectroscopy,” in *Membrane Characterization*, 2017.
[17] R. Zhang and B. D. Ulery, “Synthetic vaccine characterization and design,” *Journal of Bionanoscience*, vol. 12, no. 1. 2018, doi: 10.1166/jbns.2018.1498.
[18] W. Zhou, R. Apkarian, Z. L. Wang, and D. Joy, “Fundamentals of Scanning Electron Microscopy (SEM),” in *Scanning Microscopy for Nanotechnology: Techniques and Applications*, W. Zhou and Z. L. Wang, Eds. New York, NY: Springer New York, 2007, pp. 1–40.
[19] A. Ul-Hamid and A. Ul-Hamid, “Contrast Formation in the SEM,” in *A Beginners’ Guide to Scanning Electron Microscopy*, 2018.
[20] M. Sezen, “Focused Ion Beams (FIB) — Novel Methodologies and Recent Applications for Multidisciplinary Sciences,” in *Modern Electron Microscopy in Physical and Life Sciences*, 2016.
[21] J. Gierak, “Focused ion beam technology and ultimate applications,” *Semicond. Sci. Technol.*, vol. 24, no. 4, 2009, doi: 10.1088/0268-1242/24/4/043001.
[22] P. R. Munroe, “The application of focused ion beam microscopy in the material sciences,” *Materials Characterization*, vol. 60, no. 1. 2009, doi: 10.1016/j.matchar.2008.11.014.
[23] M. Sugiyama and G. Sigesato, “A review of focused ion beam technology and its applications in transmission electron microscopy,” *Journal of Electron Microscopy*, vol. 53, no. 5. 2004, doi: 10.1093/jmicro/dfh071.
[24] H. Luo, R. Jing, Y. M. Cui, H. A. L. Wang, and R. M. Wang, “Improvement of fabrication precision of focused ion beam by introducing simultaneous electron beam,” *Prog. Nat. Sci. Mater. Int.*, vol. 20, no. 1, 2010, doi: 10.1016/s1002-0071(12)60015-x.
[25] M. E. Curtis, R. J. Ambrose, C. H. Sondergeld, and C. S. Rai, “Transmission and scanning electron microscopy investigation of pore connectivity of gas shales on the nanoscale,” 2011.
[26] J. Loos, J. K. J. van Duren, F. Morrissey, and R. A. J. Janssen, “The use of the focused ion beam technique to prepare cross-sectional transmission electron microscopy specimen of polymer solar cells deposited on glass,” *Polymer (Guildf).*, vol. 43, no. 26, pp. 7493–7496, 2002.
[27] C. J. Powell and A. Jablonski, “Surface sensitivity of X-ray photoelectron spectroscopy,” *Nucl. Instruments Methods Phys. Res. Sect. A Accel. Spectrometers, Detect. Assoc. Equip.*, vol. 601, no. 1–2, 2009, doi: 10.1016/j.nima.2008.12.103.
[28] J. Halim, *An X-Ray Photoelectron Spectroscopy Study of Multilayered Transition Metal Carbides (MXenes)*. Drexel University, 2016.
[29] P. van der Heide, *Secondary Ion Mass Spectrometry: An Introduction to Principles and Practices*. Wiley, 2014.
[30] J. F. Moulder and J. Chastain, *Handbook of X-ray Photoelectron Spectroscopy: A Reference Book of Standard Spectra for Identification and Interpretation of XPS Data*. Physical Electronics Division, Perkin-Elmer Corporation, 1992.
[31] M. Aziz and A. F. Ismail, “X-Ray Photoelectron Spectroscopy (XPS),” in *Membrane Characterization*, 2017.
[32] C. S. Fadley, “X-ray photoelectron spectroscopy: Progress and perspectives,” *J. Electron Spectros. Relat. Phenomena*, vol. 178–179, no. C, 2010, doi: 10.1016/j.elspec.2010.01.006.
[33] F. A. Stevie and C. L. Donley, “Introduction to x-ray photoelectron spectroscopy,” *J. Vac. Sci. Technol. A*, vol. 38, no. 6, 2020, doi: 10.1116/6.0000412.
[34] M. M. L. da Cunha *et al.*, “Overview of chemical imaging methods to address biological questions,” *Micron*, vol. 84. 2016, doi: 10.1016/j.micron.2016.02.005.

[35] E. Zinner, “Depth profiling by secondary ion mass spectrometry,” *Scanning*, vol. 3, no. 2, pp. 57–78, 1980.
[36] A. Benninghoven, “Surface analysis by Secondary Ion Mass Spectrometry (SIMS),” *Surf. Sci.*, vol. 299–300, no. C, 1994, doi: 10.1016/0039-6028(94)90658-0.
[37] H. H. Brongersma and R. A. van Santen, *Fundamental aspects of heterogeneous catalysis studied by particle beams*, vol. 265. Springer Science & Business Media, 2013.
[38] J. Griffiths, “Secondary ion mass spectrometry,” *Analytical Chemistry*, vol. 80, no. 19. 2008, doi: 10.1021/ac801528u.
[39] S. Fugattini, “Binder-free porous germanium anode for Li-ion batteries,” University of Ferrara, Ferrara, 2018.
[40] Y. Gao, “A new secondary ion mass spectrometry technique for III-V semiconductor compounds using the molecular ions CsM+,” *J. Appl. Phys.*, vol. 64, no. 7, 1988, doi: 10.1063/1.341381.
[41] M. Bersani *et al.*, “Boron ultra low energy SIMS depth profiling improved by rotating stage,” *Appl. Surf. Sci.*, vol. 252, no. 19, 2006, doi: 10.1016/j.apsusc.2006.02.282.
[42] M. Boschetti, “PECVD growth of Ge for nanoporous lithium-ion battery anodes,” University of Ferrara, Ferrara, 2015.
[43] K. K. Schuegraf and K. Seshan, “Handbook of Thin Film Deposition Processes and Techniques: Principles, Methods, Equipment and Applications,” *Angew. Chemie*, vol. 101, 2002.
[44] D. M. Mattox, *Handbook of Physical Vapor Deposition (PVD) Processing*. 2010.
[45] G. Calabrese, “Relaxed germanium epilayers on porous silicon buffers for low dislocation content Ge on Si virtual substrates,” University of Ferrara, Ferrara, 2014.
[46] W. Fredriksson, S. Malmgren, T. Gustafsson, M. Gorgoi, and K. Edström, “Full depth profile of passive films on 316L stainless steel based on high resolution HAXPES in combination with ARXPS,” *Appl. Surf. Sci.*, vol. 258, no. 15, 2012, doi: 10.1016/j.apsusc.2012.02.099.
[47] S. Tardio, M.-L. Abel, R. H. Carr, J. E. Castle, and J. F. Watts, “Comparative study of the native oxide on 316L stainless steel by XPS and ToF-SIMS,” *J. Vac. Sci. Technol. A Vacuum, Surfaces, Film.*, vol. 33, no. 5, 2015, doi: 10.1116/1.4927319.
[48] S. Tutashkonko *et al.*, “Mesoporous Germanium formed by bipolar electrochemical etching,” *Electrochim. Acta*, vol. 88, 2013, doi: 10.1016/j.electacta.2012.10.031.
[49] S. Tutashkonko, S. Alekseev, and T. Nychyporuk, “Nanoscale morphology tuning of mesoporous Ge: Electrochemical mechanisms,” *Electrochim. Acta*, vol. 180, 2015, doi: 10.1016/j.electacta.2015.08.112.
[50] Y. A. Bioud *et al.*, “Fast growth synthesis of mesoporous germanium films by high frequency bipolar electrochemical etching,” *Electrochim. Acta*, vol. 232, 2017, doi: 10.1016/j.electacta.2017.02.115.
[51] A. Dupuy, M. R. Aziziyan, D. Machon, R. Arès, and A. Boucherif, “Anisotropic Mesoporous Germanium Nanostructures by Fast Bipolar Electrochemical Etching,” *Electrochim. Acta*, 2021, doi: 10.1016/j.electacta.2021.137935.
[52] B. L. Darby, B. R. Yates, N. G. Rudawski, K. S. Jones, A. Kontos, and R. G. Elliman, “Insights for void formation in ion-implanted Ge,” *Thin Solid Films*, vol. 519, no. 18, 2011, doi: 10.1016/j.tsf.2011.03.040.
[53] L. Romano, G. Impellizzeri, M. V. Tomasello, F. Giannazzo, C. Spinella, and M. G. Grimaldi, “Nanostructuring in Ge by self-ion implantation,” *J. Appl. Phys.*, vol. 107, no. 8, 2010, doi: 10.1063/1.3372757.
[54] N. G. Rudawski and K. S. Jones, “Nanostructured germanium prepared via ion beam modification,” *Journal of Materials Research*, vol. 28, no. 13. 2013, doi: 10.1557/jmr.2013.24.
[55] S. Koffel, P. Scheiblin, A. Claverie, and G. Benassayag, “Amorphization kinetics of germanium during ion implantation,” *J. Appl. Phys.*, vol. 105, no. 1, 2009, doi: 10.1063/1.3041653.

4. Electrochemical characterizations

4.1. Introduction

In this chapter, the electrochemical characterizations of the electrodes are presented, giving an overview of the whole research work prior to deepen the best results achieved so far.

In the beginning of the chapter, a brief overview of the cell assembly and the setup used is presented. The main characterization techniques and the useful information that can be gathered from each of them are presented too. Then, some comparisons are performed, illustrating the paramount importance of the nano-structuration step, the superior performance of the FEC based cells, and the choice of the best etching recipe. Cyclic voltammetry (CV) was carried out to investigate the role played by the substrate materials and to evaluate the main features of the lithiation and de-lithiation processes in the nano-structured samples. Galvanostatic charge and discharge cycles were then performed to investigate the cycle-life behaviours of the electrodes and their capability to sustain elevated currents of charge and discharge. For the etched samples, the electrochemical characterization over a large temperature range is also presented.

In the whole chapter, particular attention is devoted to the electrochemical details of the lithiation and de-lithiation processes, which are presented in the most interesting cases and are interpreted according to the literature. The analogies and differences observed between the various samples are deepened, for both the nano-structuration techniques, taking into account also the ageing and the currents drawn in each specific case.

4.2. Cell assembly and test

The electrodes produced are electrochemically tested in CR 2032 coin-type cells, which are assembled in an Ar-filled MBraun glovebox with H_2O and O_2 levels below 0.1 ppm (part A of Figure 48).

In these cells, the sample electrodes are directly faced to metallic lithium chips (15.6 mm in diameter and 0.45 mm in thickness; MTI Corporations) as counter and reference electrodes: this way they represent two electrodes half-cells (as previously discussed in section 1.10). A dried glass fibre membrane (Whatman GF/D) is used as separator. This configuration and the separator used are both typical in the study of new materials for LIBs [1][2].

A conventional organic liquid electrolyte [3][4] was chosen as base solution, that is the equivolume mixture of Ethylene Carbonate (EC) and DiMethyl Carbonate (DMC), with 1 M Lithium Hexafluorophosphate ($LiPF_6$) dissolved as a conductive salt (LP30, Sigma Aldrich). The precise amount of solution used in each cell varied in the range of 200 µL - 250 µL.

Furthermore, small amounts of Vinylene Carbonate (VC) and FluoroEthylene Carbonate (FEC) were tested as additives for the base electrolyte solution, as these proved to be beneficial on the overall capacity of prototype cells and its retention through the cycles [5][6]. The effects of these additives on the electrochemical performances of cells using the electrodes nano-structured by means of HF anodic dissolution are discussed in section 4.4.

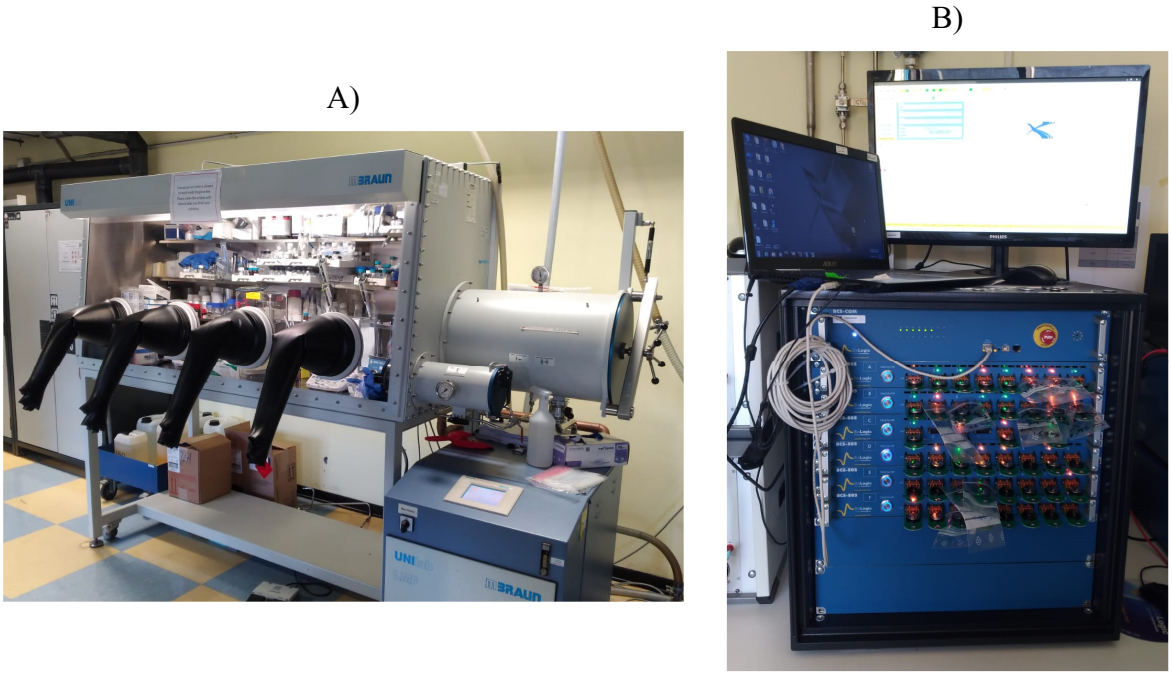

Figure 48: MBraun glovebox (A) where the coin-cells are assembled and the BioLogic BCS-805 multichannel battery unit where they are tested (B).

All the electrochemical tests were performed using a BioLogic BCS-805 multichannel battery unit controlled by BT Lab software, depicted in part B of Figure 48.

A brief introduction of the analysis performed is now presented, focusing the attention on the most important information that each of them can give.

4.2.1. **Galvanostatic cycling**

In galvanostatic cycling a constant current is applied to an electrochemical system while its voltage is recorded. Usually, the constant current is made to flow in a certain potential window: when the voltage drops (or raise) to one of the cut-off limits, the current is reversed. The voltage measured is then plotted against the time or, more commonly, the specific capacity, and the resulting curves are named galvanostatic profiles.
This represents one of the most common and important tools used in the study of the properties of new battery materials [1] and constitutes the primary analysis used in this work.

The shape of the galvanostatic profiles depends on the reactions occurring in the electrochemical cells and their phase transformations. In general, a flat plateau is associated to a two-phase reaction, like a crystalline-amorphous transition could be, during which the potential remains constant according to the Gibbs phase rule. Instead, sloping regions are generally related to one-phase reaction, like species insertion inside solid solutions. Some example profiles are depicted in Figure 49.

The analysis of the derivative of the galvanostatic profiles with respect to the potential is usually performed to better identify the potentials of the various reactions. The resulting curves are usually referred to as Differential Capacity Plot, which are introduced in section 4.2.4.

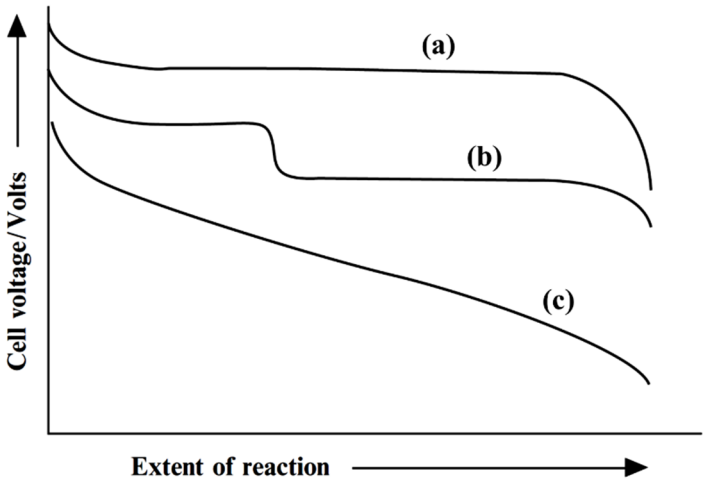

Figure 49: Examples of galvanostatic profiles for a two-phase reaction (a), for a series of multi-phase reactions (b) and for a single-phase reaction (c). Adapted from [7].

In most of the situations, the potential observed in the galvanostatic profiles is not that prescribed by the Nernst relation (see the first Chapter). Indeed, that represents the potential for ideal reversible reactions performed in quasi-static regime, according to thermodynamics, upon flowing of an infinitesimal current.

In real conditions, with finite currents, the measured potential deviates from the ideal one due to overpotentials (also called polarizations). These overpotentials account for irreversible contributions as ohmic drops, activation barriers and concentration polarization due to limited mass transport capabilities [8][9]. In addition, all these factors can depend also on many others, like the temperature, the current drawn, the precise stage of the electrochemical reaction, etc. In general, the effects of these factors on the measured potential E are accounted for by writing:

$$E = E_{th} - iR - \eta \quad (28)$$

In which E_{th} represents the thermodynamic potential of the reaction, iR expresses the global ohmic drop across the electrochemical cell and η accounts for the sum of polarizations listed above. A representation of the possible effects of these overpotentials on the shape of the galvanostatic profiles is presented in Figure 50.

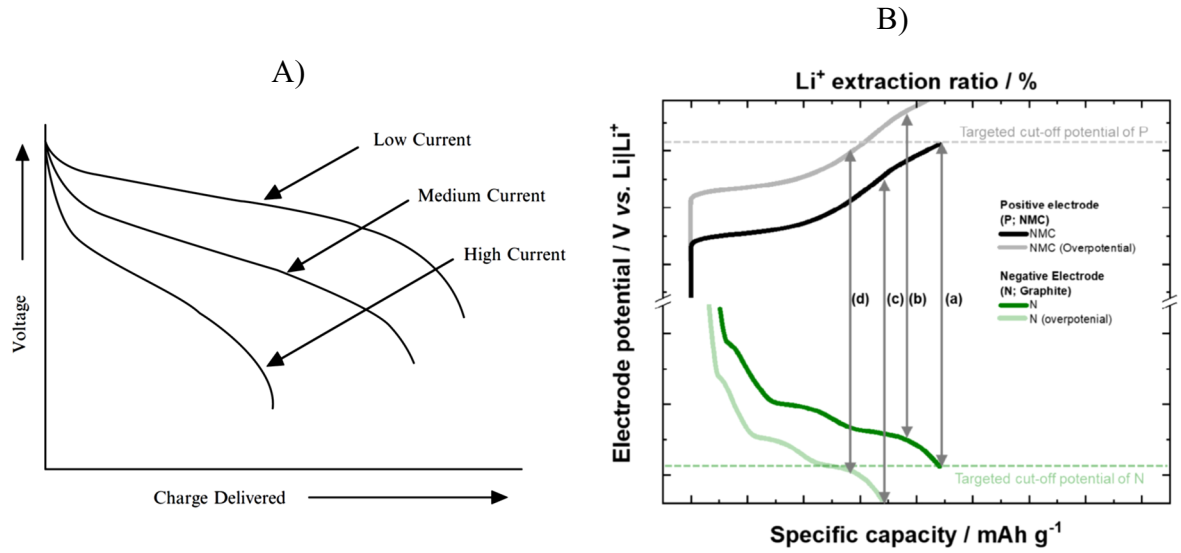

Figure 50: Two representations of the possible effects of a flowing finite current on the electrochemical potential of real systems. A is taken from [7] while B is taken from [2]. Regarding the notation used in this thesis, all the potentials values are expressed with respect to the Li/Li^+ standard redox potential. In other words, the potential of that reaction is assumed as the zero value of the potential.

4.2.2. **Capacity plots and Coulombic Efficiency**

The last capacities recorded in the reduction and oxidation branches of the galvanostatic profiles can be plotted together as a function of the cycle number to obtain the so-called capacity plot. These plots are particularly important since they permit to evaluate the overall capacity of a cell, its stability through the cycles and its efficiency. Of course, from the length of this curve, it is possible to understand the longevity of a new electrode material, but it is also possible to gather information about its behaviour when tested at different C-rates.

An example of a capacity plot is reported in Figure 51. This kind of graphs are always displayed for all the samples presented in this work.

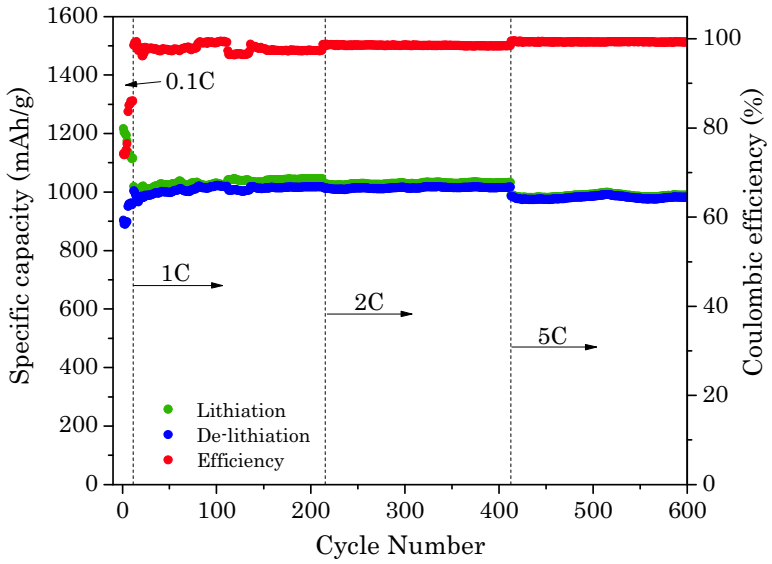

Figure 51: Example of a cell capacity plot, with the lithiation and de-lithiation capacities at different C-rate displayed as a function of the cycle number. The graph reports also the Coulombic Efficiency. The complete version of this graph is presented in Figure 55, part B.

From the capacity plot the efficiency of a cell can be determined, as an expression of the reversibility of the electrochemical processes involved. This can be evaluated from the separation between the lithiation and de-lithiation capacities and expresses the irreversible capacity in each cycle. The formal definition of the efficiency is reported in the following expression, which is usually referred to as Coulombic Efficiency (CE):

$$\text{Coulombic Efficiency} = \frac{\text{de-lithiation capacity}}{\text{lithiation capacity}} \quad (29)$$

4.2.3. **Average capacity**

In the following, average capacities are reported for cells retaining stable behaviours, without evident fading trends, for the cycles performed at the same constant C-rate. This must be considered as a qualitative indicator of the capacity retained during the corresponding cycles, rather than its pure statistical definition as formal quantifier.

These average capacities are then exploited to make comparisons between different cells and are also used in cases when irregular capacity is observed, but no hint of fading can be clearly recognized.

If the capacity is undoubtedly recognized to decrease through the cycles (in other words, if clear fading takes place) the capacity on the first cycles is considered and the focus is put on its retention through the cycles.

4.2.4. **Cyclic Voltammetry and Differential Capacity Plot**

To conclude this review of the electrochemical analysis techniques used in this work, a brief introduction of the cyclic voltammetry and the differential capacity plots is now presented.

Cyclic voltammetry (CV) is one of the most widely used techniques for qualitatively studying the thermodynamics of redox processes and their kinetics [10]. It permits to identify reversible redox couples and to measure the rate constants and transfer coefficients of electrode processes, and can help to unravel complex electrochemical systems [9].

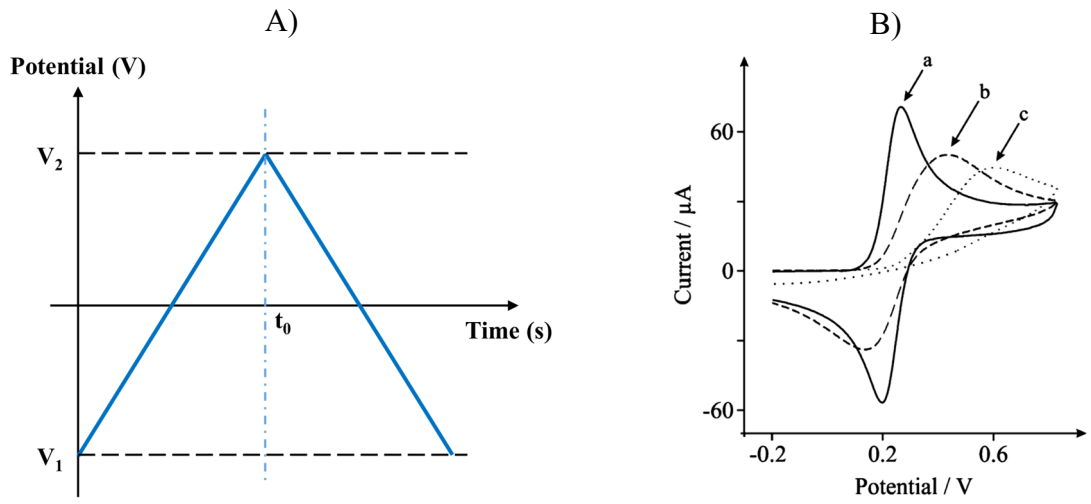

Figure 52: Linear potential sweep (A) and typical voltammograms (B) of a reversible (a), quasi-reversible (b) and irreversible (c) electron transfer. Part B is from ref. [11].

In this kind of analysis, a linear potential sweep is usually performed as a function of time on the target electrode between two cut-off voltages (Figure 52, part A), while the induced current is monitored. The current drawn from the electrode may be plotted as a function of the potential and its shape for complex systems could be quite complicated. Some examples, for a reversible, quasi-reversible and irreversible single redox process involving an electronic transfer, are reported in part B of Figure 52.

The peaks shape and position are governed by the reaction kinetics at the electrode/electrolyte interface of the specific reaction. For a simple fully-reversible n-electron transfer reaction occurring at a planar electrode, the current peak intensity i_p is described by the Randles–Ševćik equation [12]:

$$(30) \quad \mathrm{Ox} + ne^- \leftrightharpoons \mathrm{Red}$$

$$(31) \quad i_p = 0.446 \left(\frac{F^3}{RT}\right)^{1/2} n^{1/2} A C_0 {D_0}^{1/2} v^{1/2}$$

Where F is the Faraday constant, R is the gas constant, T is the temperature (K), n is the number of electrons exchanged in the reaction, A is area of the electrode (cm^2), C_0 is the bulk concentration of the reactant species (mol cm^{-3}), D_0 is the reactant diffusion coefficient ($cm^2\ s^{-1}$), and v is the potential scan rate (V s^{-1}).

Thus, for reversible reactions, the potential of the cathodic or anodic peak is independent from the potential scan rate and this can be exploited to determine an unknown kinetic parameter, provided all the other [10]. Furthermore, the oxidation and reduction peaks separation gives some information about the reversibility of the process involved, since for the previous reaction the following relation holds [9]:

$$(32) \quad \Delta \mathrm{E} = 2.3 \frac{\mathrm{RT}}{\mathrm{nF}}$$

Where the symbols have the same identity as before. Any deviation from this value means a deviation from the ideal reversible process (curves b and c of part B of Figure 52).

While CV could be more useful to gather information about the kinetic aspects, the Differential Capacity Plot (DCP) could be more appropriate to identify the potential stages of the chemical reactions and their contribution to an overall process. In this method, the inverse of the derivative of the potential with respect to the specific capacity is calculated, namely dQ/dE. The result is then plotted against the potential.

Due to this definition, plateaus in the galvanostatic profiles appear as peaks in the dQ/dE plot, as it can be ascertained by inspection of Figure 53. Furthermore, each peak represents a different reaction and the area subtended is the corresponding capacity.

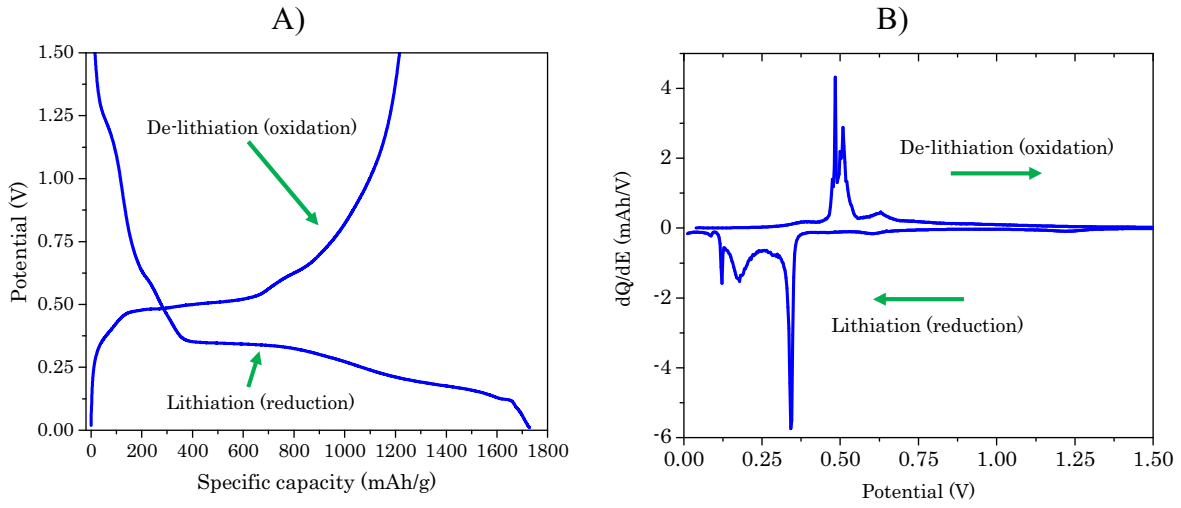

Figure 53: A typical galvanostatic profile of the 1st cycle of an etched germanium half-cell (A) and the corresponding DCP plot (B).

CV and DCP can be considered as complementary techniques because they furnish different kind of information about the same electrochemical reaction. The difference between these methods is that in DCP more time is left to the electrochemical processes to approach completion, as they are carried out at constant current. This permits to highlight the most prominent reactions, in which the largest amounts of charge are consumed. On the other hands, the forced change in the potential induced by the voltage sweep of CV can increase the current beyond the kinetic limit of a system, thereby preventing some capacity from being accessed [1][13].

Both CV and DCP were used in this thesis to highlight the main reactions, which are then identified by comparisons with the literature.

The CV were accomplished using the same BioLogic BCS-805 multichannel battery unit previously mentioned. The potential sweeps were performed at a scan rate of 0.1 mV/s in the 0.01 V – 2.8 V voltage range.

DCP were calculated from the corresponding galvanostatic profiles by using BioLogic BT-Lab® V1.67 software, with dE set equal to 3mV.

4.3. Bulk vs nano-structured

It is well known from the literature that Ge bulk structures can not withstand the volumetric variations produced by the electrochemical reactions inside LIBs [14][15][16][17][18][19].

Nevertheless, a preliminary test was performed at the beginning of this work to confirm the expectations and to assess the effect of the nano-structures on the electrode performance.

All the preliminary tests were performed using VC 5 % v/v as an additive for the electrolyte solution (LP30), based on its beneficial effects as suggested by various works [6] [20][21]. The adoption of FEC as the "standard" additive was effectuated later in this work, after a direct comparison which is presented in the following section.

Both the samples presented in this section were realized on Mo substrates and their mass loadings were of (1.01±0.01) mg for the bulk electrode and of (0.44±0.02) mg for the nano-structured one. The different mass loading is due to the fact that the HF etching removes part of the Ge deposited, as previously described (cf. sect. 2.3). On the contrary, the bulk electrode conserved all of its initial mass.

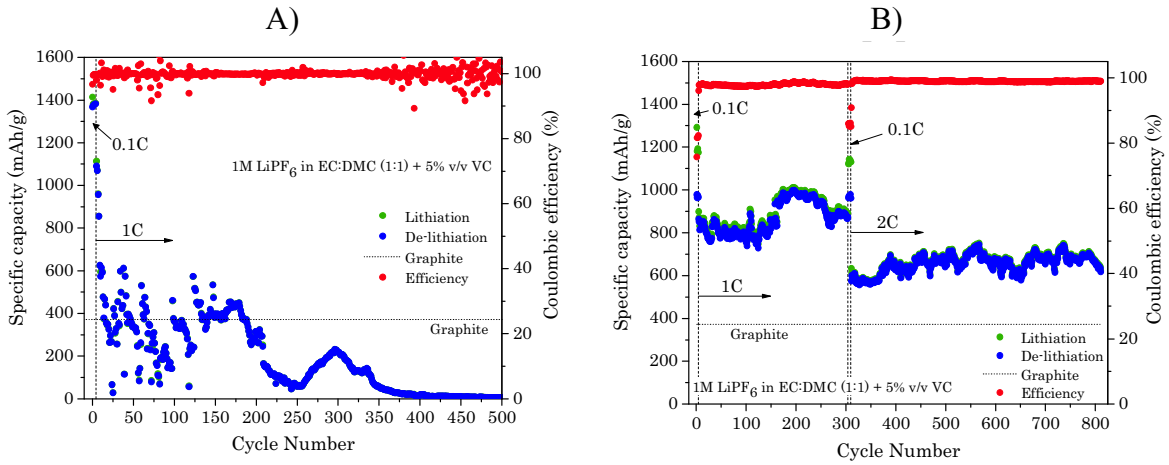

Figure 54: Specific capacity and Coulombic efficiency (CE) as a function of the cycle number of a bulk sample (A) and an electrochemically etched one (B). The horizontal dotted lines represent the graphite theoretical specific capacity while the vertical dashed lines mark the cycles at which the C-rate was changed (the C-rate values are reported in the graphs). Part B of the figure is from ref. [22]

In Figure 54 the specific capacities for the bulk (part A) and nano-structured electrodes (part B) are reported as a function of the cycle number. In both the cases, some initial cycles at the low C-rate of C/10 were performed, before increasing it to 1C, to enable a stable SEI formation [23][24][25].

As it can be observed, the bulk sample capacity heavily drops soon after the first cycles, which is ascribed to a heavy pulverization of the active material. The electrode shows a very high capacity of 1413 mAh/g in the 1st cycle, representing the 87 % of the Ge

theoretical capacity, but drops to less than 100 mAh/g in about 25 cycles. Surprisingly, a partial but very irregular capacity recovery is observed in the following cycles, up to the 300th, before the definitive cell failure. This could be ascribed to participation of new active material, previously buried inside the layer, that takes part to the reactions after the detachment of the material above. Furthermore, a self-reorganization of the Ge structures could occur through the cycles, partially recovering the capacity before their final pulverization. Even the CE is quite irregular and is not considered to be a reliable data, because an improbably high average value of 99.98 % is observed over all the cycles with variations between 89.33 % and 136.60 %.

On the other hand, the nano-structured electrode demonstrates the capability to withstand the volumetric expansions and contractions by reversibly cycling for several hundreds of cycles (part B of Figure 54). In the initial C/10 cycles, an average lithiation capacity of 1210 mAh/g is observed, representing the 75 % of the theoretical Ge capacity. The CE in these cycles is quite poor, with an average value of 80.33 % and attaining a minimum of 75.71 % in the 1st. This is ascribed to SEI formation on the electrode surface [26][27][25] [28].

When the C-rate is raised to 1C, the lithiation capacity drops at about 800 mAh/g. However, the capacity surprisingly increases up to almost 1000 mAh/g after 150 cycles. At this rate, an average lithiation capacity of 885 mAh/g is observed and the irregular behaviour corresponds to a capacity variation of about 7 %. The mean capacity represents only the 54 % of the Ge theoretical one, but it is anyway 2.38 times higher than that of graphite. Furthermore, a very high mean efficiency of 98.79 % is attained in these cycles.

After about 300 cycles at 1C, when the cell is cycled again at the low rate of C/10, an average capacity of 1131 mAh/g is observed. This is only 6.5 % less than the initial one and means that a minimal electrode deterioration occurred even after hundreds of cycles performed at a higher rate. Interestingly, the CE decreases in these new cycles at C/10 close to the values of the first ones, with an average of 85.55 %.

Finally, the cell is cycled in more stressful conditions at a C-rate equal to 2C. Even this time the nano-structured electrode shows the capability to reversibly operate for some more hundreds of cycles. Upon the rate change, the lithiation capacity drops at an average value of 661 mAh/g, reducing by the 45 % and 25 % with respect to the C/10 and 1C capacities.

Nevertheless, this value is still 1.78 times higher than the graphite theoretical one. As for the 1C rate, an irregular capacity is observed even at 2C, with fluctuations of about the 5 %. Despite this, a very stable and high mean CE of 98.92 % is observed.

This test confirms that the bulk samples are not suitable for direct use as anodes in LIBs, as it was expected from the literature. Instead, the nano-structured electrodes are able to withstand reversibly the charge and discharge processes. For this reason, the bulk material was discarded, and all the research efforts were focused only on the nano-structured anodes.

4.4. Comparison between VC and FEC

In order to suppress the capacity irregularity shown in Figure 54, FEC was tested as an alternative additive for the electrolyte solution. In fact, various works suggested that FEC could enhance the electrode capacity, and moreover its stability [29][5][30][31][32], even more than VC [24][33].
Differently from the previous samples, and trying to further enhance the positive effects, a 10 % v/v of additive was added to the LP30 electrolyte solution for both VC and FEC, instead of 5 % v/v.

Both the samples presented in this section were realized on Mo substrate. The mass loadings were or of (0.40±0.02) mg and (0.39±0.02) mg for the samples with VC and FEC, respectively.

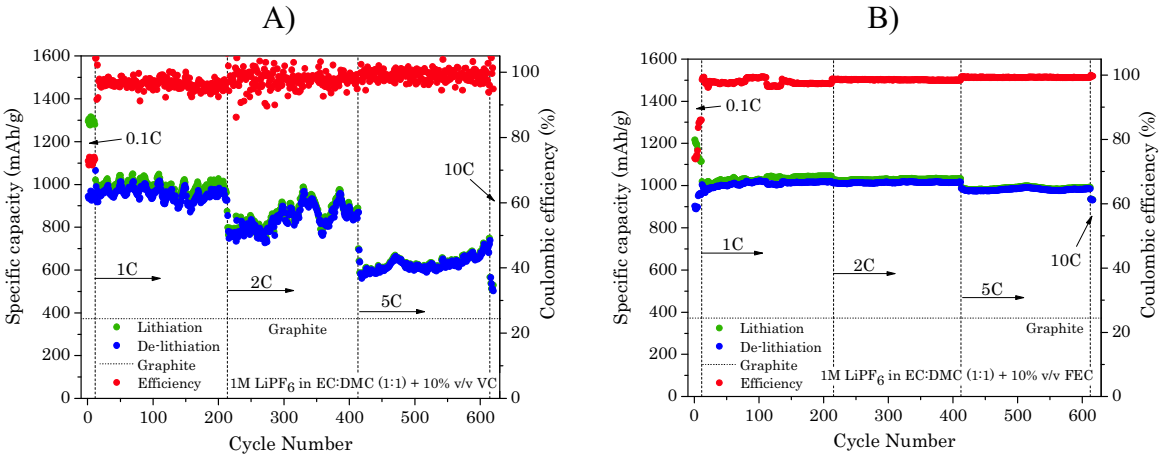

Figure 55: Specific capacity and CE as a function of the cycle number of two cells with etched electrodes and using VC (A) and FEC (B) as additives. The vertical and horizontal dashed or dotted lines have the same meaning as in Figure 54. Both the images are adapted from ref [34].

In Figure 55, the specific capacities as a function of the cycle number of two cells realized with etched samples and using VC (part A) and FEC (part B) as additives are reported. In both the cases, 10 cycles at C/10 were carried out first, for the formation of a stable SEI. Afterwards, the cells were tested performing 200 cycles at the increasing rates of 1C, 2C and 5C, before concluding the tests with some cycles at 10C, to evaluate the effect of the additives on their electrochemical performances.

Already from a first glance at these graphs, it clearly appears that FEC has an extremely positive effect on the electrochemical performance of the electrode. Indeed, the irregular behaviour is suppressed and an enhancement of the specific capacity at the higher rates is observed. This could be related to the production of a thin, low-resistive and elastic SEI layer [4][30][33][35][36] that is more effective in passivating the electrode surface [31][32][37][38] with respect to VC.

Regarding the VC sample (part A) an irregular trend similar to that observed in the previous section can be recognized. However, in this case, the specific capacity is higher both at 1C and at 2C, as it can be seen in Table , with a rise of about 34 % of the latter with respect to the previous case. This is probably due to the higher amount of VC additive used (10 % instead of 5 %), which could have also contributed to reduce the capacity fluctuations. Despite this, a higher variation of the CE is observed. In addition, a low efficiency (72.96 %) is observed in the C/10 cycles, with a minimum of 72.82 % in the 1st. Such a small difference highlights that side reactions occurred during all the cycles at C/10.

Regarding the FEC sample, it showed a slightly higher capacity at 1C with respect to the VC cell at the same rate (Table 13), but this time the fluctuations are greatly suppressed. However, the most important effect of FEC can be seen at the higher rates. Indeed, when the C-rate is raised to 2C, the capacity is essentially unaffected and is even more stable than at 1C. Furthermore, at 5C and 10C the average capacities reduce less than 5 % and 10 % with respect to the 1C value. For comparison, these capacities are 56 % and 77 % higher than the corresponding values of the VC based cell.
The CE of the FEC cell is also higher and much more stable than the VC cell at all the rates. The lowest value is observed in the 1st cycle and is equal to 74.22 %. This is slightly higher than that of the VC cell, but an increase of 7 % is observed for the average efficiency at C/10 by using FEC with respect to the previous case, which could be related to a more stable SEI layer.

Additive	C-rate	C/10	1C	2C	5C	10C
VC	Mean Lit. Capacity (mAh/g)	1293	990	857	633	519
	Mean efficiency (%)	72.96	96.52	97.80	99.26	101.05
FEC	Mean Lit. Capacity (mAh/g)	1157	1032	1030	988	935
	Mean efficiency (%)	80.55	97.77	98.52	99.31	99.76

Table 13: Mean lithiation capacities and CE for the various C-rates for the cells with VC or FEC additives.

Besides the high capacities and efficiencies attained, it must be stressed that both the electrodes have reversibly performed hundreds of cycles of charge and discharge. Furthermore, even at the higher rates, no hints of capacity fading are observed.
This test clearly demonstrated the beneficial effects of FEC over VC for our electrodes. For this reason, the electrolyte solution composed by LP30 plus 10 % v/v of FEC was adopted as standard for all the other cells realized in this work.

4.5. The choice of the etching recipe

A comparison of the electrochemical performances of electrodes realized by means of the various etching recipes (cf. sec. 2.3.3 and 3.3) is presented in this section. The aim is to illustrate the criterion behind the choice of the "best" etching recipe, which was afterward adopted as standard.
The comparison was carried out by performing the same protocol test on all the cells: firstly, 10 cycles at the low rate of C/10 were performed, then the C-rate was increased and 200 cycles at 1C, 2C and 5C were carried out in sequence to stress the electrodes.
According to the previous section, the standard electrolyte solution composed by LP30 and 10 % v/v of FEC as additive was employed for all the cells.

The rationale in the choice of the best etching recipe was to select the one showing the better compromise between high capacity and stable retention through the cycles. Indeed, besides attaining high capacities, one of the most important aspects for secondary batteries is their longevity, that is their capability to sustain a stable capacity for an elevated number of cycles.

This is particularly important in those applications where it is not possible to replace the energy storage systems and where high reliability is necessary, like aerospace, in which a cycle-life of more than 50,000 cycles could be required [39][40].
For this reason, the fading rate was considered as an estimator of the electrodes ageing and was elected as reference parameter for the choice, together with the overall electrode capacity.

To evaluate the fading rates, a simple linear regression of the lithiation and de-lithiation capacities was performed as a function of the cycle number, for each cell and at every C-rate. The angular coefficients of the best fitting curves express the amount of capacity lost per cycle and thereby represent the fading rates for each cell at the various rates.

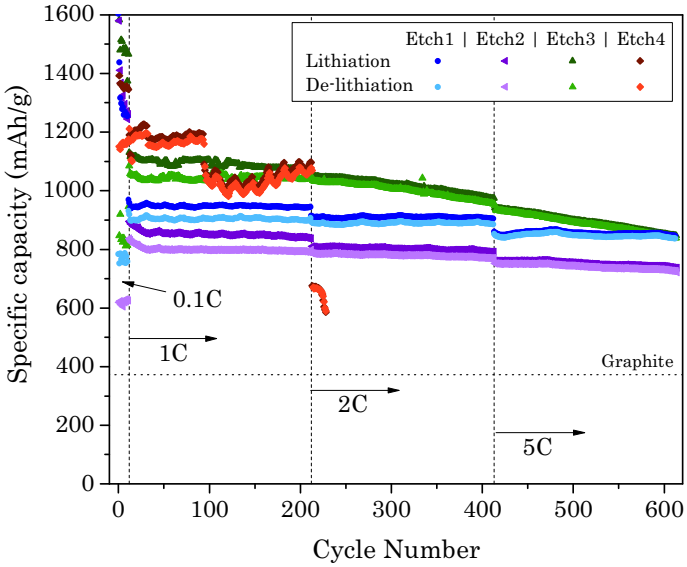

Figure 56: Specific capacities at various C-rates as a function of the cycle number for cells using anodes realized with different etching recipes. The horizontal and vertical dashed or dotted lines have the same meaning as in Figure 54.

In Figure 56, the specific capacities of cells realized using electrodes from different etching recipes are reported. The same labelling as introduced in section 2.3 is employed here referring to the different cells.
The mass loadings were of (0.35±0.02) mg, (0.23±0.02) mg, (0.26±0.02) mg, (0.67±0.02) mg for Etch1, Etch2, Etch3 and Etch4, respectively. This time, the substrate material for all the cells was SS. Since the aim of this section is to present the recipe selected as standard, the focus is put on the cell fading behaviours, with only a brief description of their electrochemical performances.

The highest capacities are shown by the Etch3 and Etch4 cells, being both above 1000 mAh/g at 1C. Although Etch3 shows the highest capacities at 2C and 5C, as reported in Table 14, it also shows the highest fading rates. For this reason, this recipe was discarded. Etch4 shows the highest initial capacity at 1C (1392 mAh/g) but displays an irregular behaviour with a sudden drop after 100 cycles, followed by strong oscillations. When the C-rate is raised to 2C, another important capacity drop is observed, highlighting the cell failure. For this reason, the cell was stopped when the capacity halved its initial 1C value (around 589 mAh/g). This result was expected due to the half-bulk nature of the Etch4 electrode, and its performance was not considered for the stability evaluations.

Etch2 showed the lowest capacity, around 800 mAh/g. A slight fading trend can be recognized already in the 1C cycles and continues even at the higher rates. Due to this, also this recipe was discarded.

The cell that showed the better retention, despite an initial lower capacity compared to the others, is Etch1. Indeed, this cell capacity is about 900 mAh/g, but it retained it stably throughout the cycles even when the rate was raised to 2C and 5C. This is confirmed by the fading rates reported in Table 14, showing the better capacity retention of this electrode compared to the others.

It is interesting to note that the Etch1 morphology showed the smallest and most homogeneous Ge features, as described in section 3.4.1. Furthermore, the Ge structures observed were increasingly larger passing from Etch2 to Etch3, and a corresponding raising trend is displayed by their fading rates. According to this, the worst performances of the other cells, compared to Etch1, were ascribed to active material pulverization due to their bigger Ge structures. A further proof for this is the early failure of the half-bulk cell.

		Capacity fading per cycle (mAh/(g·cycle))		
C-rate		**ETCH1**	**ETCH2**	**ETCH3**
1C	**Lithiation**	-0.023	-0.123	-0.192
	De-lithiation	-0.026	-0.079	-0.006
2C	**Lithiation**	-0.007	-0.078	-0.390
	De-lithiation	0.012	-0.077	-0.403
5C	**Lithiation**	-0.035	-0.128	-0.480
	De-lithiation	-0.045	-0.136	-0.482

Table 14: Lithiation and de-lithiation capacity fading for each C-rate for cells with anodes realized using different etching recipes.

Based on the good capacity and its high retention even at the higher rates, the Etch1 recipe was selected as the standard for the nano-structuration process by means of HF anodic dissolution.

4.6. Independence of the electrochemical performances from the substrate material

Cyclic voltammetry (CV) was carried out to verify the independence of the electrode performances from the substrate materials. In other words, CV were performed to assess if the substrates could represent active materials and the extent of their contributions to the charge storage reactions. To do that, half-cells using pristine substrates as working electrodes were analysed and the results are compared to those of half-cells containing nano-structured Ge electrodes.

The CVs were carried out in the 0.01 V – 2.8 V range at a scan rate of 0.1 mV/s. All the cells were assembled using the standard electrolyte solution, with lithium metal as counter and reference electrode. The mass loadings were of (47.01±0.01) mg, (40.00±0.01) mg, (0.24±0.02) mg (+(46.74±0.01) mg Mo substrate) and (0.31±0.02) mg (+(38.86±0.01) mg SS substrate) for the pristine Mo, pristine SS, etched Ge on Mo, and etched Ge on SS, respectively.

In parts A and B of Figure 57 the CVs for the first 3 cycles of the pristine substrates are reported. Mo shows some cathodic peaks at 1.4 V and below 0.5 V, while on the anodic side a broad peak is observed around 1.5 V plus a smaller one at 2.4 V. Even SS shows two main cathodic peaks, centred at 1.7 V and 0.8 V, and two anodic peaks, centred at 1.5 V and 2.2 V.
In the images C and D, the CV of the cells with etched Ge electrodes are reported, realized on Mo and SS, respectively. The first and most important thing to note is that the current scale range of these graphs are approximately two orders of magnitude higher than those of the pristine substrates. This suggests that the substrate materials do not contribute appreciably to the electrochemical reactions occurring in the cells. As a result, the features observed can be completely ascribed to the Ge layers and to eventual side reactions involving the electrolyte.

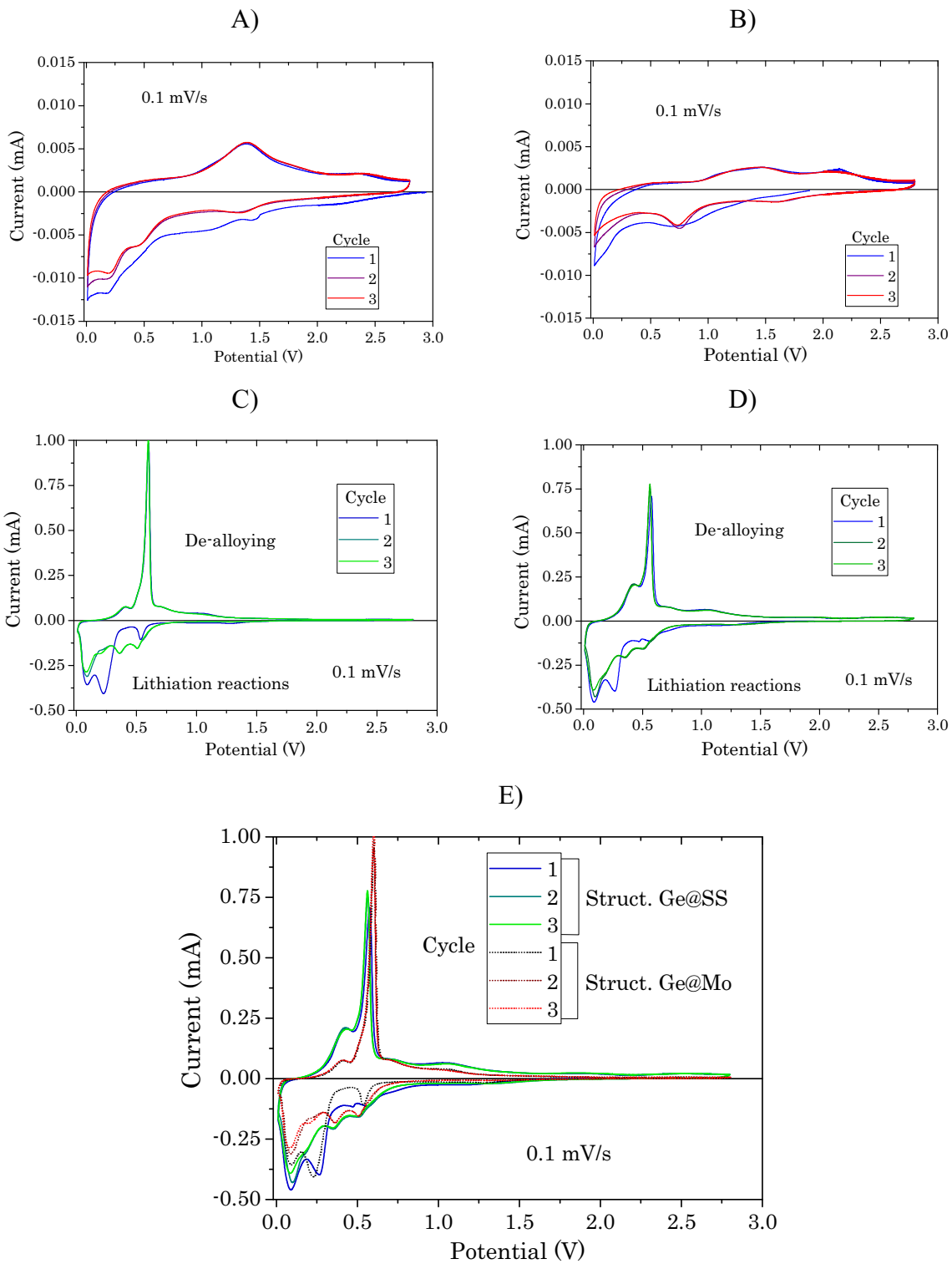

Figure 57: Cyclic voltammetry of pristine Mo (A), pristine SS (B), etched Ge on Mo (C) and etched Ge on SS (D) electrodes. The results for the etched electrodes are also plotted together in part E.

A direct comparison of the CVs of the nano-structured electrodes is reported in part E of Figure 57. The CV curves present different peak intensities and a difference is also observed between the 1st cycles and the following ones, as well as between the 1st cycles for

the different substrates themselves. However, since the peaks positions and the global shapes of the CV curves are essentially identical, the same reactions must occur independently of the substrate material.

On the cathodic scan, for both the samples, the current starts to flow from 1.5 V with an increase around 1.25 V. This is ascribed to electrolyte decomposition and SEI production [30][41]. Then, in the 1st cycles, a clear peak is observed around 0.55 V, followed by two intense ones around 0.25 V and 0.09 V. According to the literature, the first peak could be related to further SEI production [42][30][41] or to lithiation of c-Ge [43], while the others are ascribed to the formation of lithium-germanium (Li-Ge) alloys [42][41][42][100]. Remaining on the cathodic side, the 2nd and 3rd cycles show the same multiple peaks in both the cases, this time starting from ~0.5 V, which could be associated to the development of the Li-Ge alloys [42][43][44].

On the anodic branch, the same reaction pathway occurred for all the three cycles, irrespective of the substrate material, with two main peaks at ~0.42 V and ~0.6 V and a long tail towards higher potential. Again, according to the literature, this multiple peak could be identified as the dealloying process of the Li-Ge composites [14][42][45].

As a further proof of the independence of the electrochemical performances from the substrate materials, two cells were realized and tested in galvanostatic cycles with bare substrates as anodes.
The mass loadings were of (46.59±0.01) mg and (40.16±0.01) mg for Mo and SS, respectively, and the standard electrolyte solution was employed. Currents of 39 µA and 57 µA were used for the Mo and SS cells, respectively, as these represent current values comparable to the typical C/10 values for the Ge nano-structured cells.

The results of this test are presented in Figure 58, where a similar maximum capacity of about 0.10 mAh/g is observed in both cases. This value represents about the 0.01 % of the specific capacity of a typical cell with nano-structured Ge electrodes (mass loadings of about 0.3 mg, see sect. 2.2.4). Furthermore, this is the 1st cycle capacity, in which a great amount of SEI must have formed. Due to this, such a capacity could only represent an over-estimate of the (hypothetical) reversible capacity associated to the substrate materials.

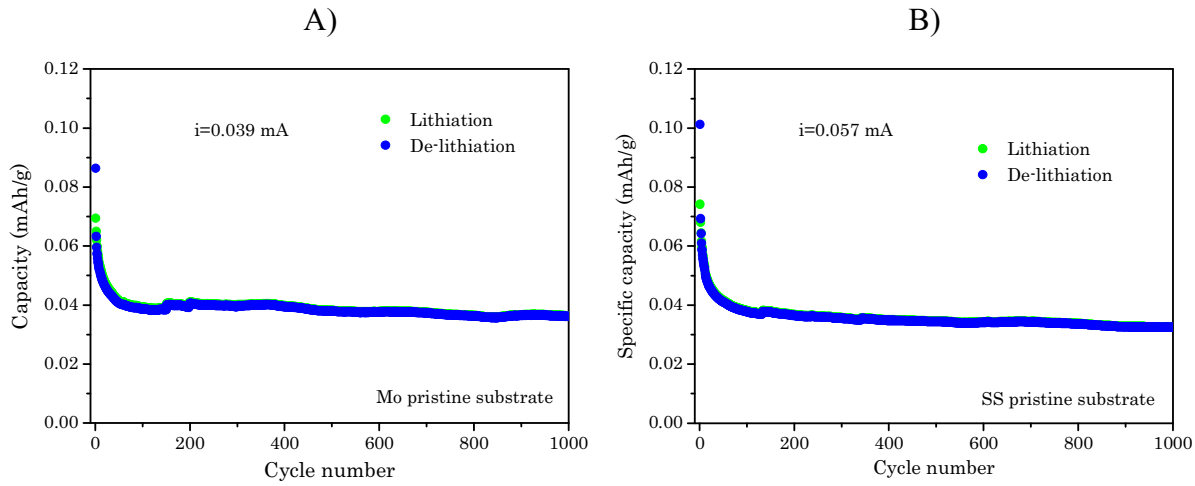

Figure 58: Specific capacity vs cycle number plots of half-cells using pristine Mo (A) and SS (B) substrates as anodes.

From all these observations, it can be concluded that the substrate materials do not participate at an appreciable extent to the electrochemical reactions, so they do not represent active materials. Thanks to this, all the results presented in this work are treated irrespective of the substrate material, which is reported in any case for completeness.

4.7. Electrochemical performances of the etched samples

Some of the best results achieved so far for the electrochemically etched samples are presented in this section. The electrochemical performances of the ion implanted samples are presented in section 4.8.

4.7.1. Cycle-life

Figure 59 reports the capacity plot of a cell using an etched Ge electrode and tested at 1C for its whole life, after some initial cycles at C/10. The electrode mass loading was of (0.22±0.02) mg and the substrate was made of Mo. As usual, the standard electrolyte solution was used (LP30 + 10 % v/v of FEC).

As it can be seen, the cell performed several thousands of cycles with high capacity and high CE, that remained always well above 99 % in all the 1C cycles[1].
The best capacity retention is observed during the first 1500 cycles, in which the cell capacity passes from 1369 mAh/g of the 1st 1C cycle to 1211 mAh/g of the 1500th. This means a retention of 88 % and corresponds to a low fading rate[2] of 0.08 mAh/(g·cycle). It is worth to note that the capacity is always more than 3 times higher than the graphite theoretical one.

Afterwards, an increase of the fading rate up to 0.42 mAh/(g·cycle) is observed between the 1500th and the 3500th cycles. Nevertheless, the cell delivered more than 1000 mAh/g even at the 2000th cycle and retained a capacity well above that of graphite up to the 3500th. Furthermore, even if the fading rate increased, a very high CE was retained with an average value equal to 99.79 %.

Despite some random and small fluctuations, the high and stable capacity as well as its retention through several hundreds of cycles constitute an evidence that the electrodes realized by means of LEPECVD and HF etching can reversibly sustain the charge and discharge processes. This experimentally demonstrates that the electrodes must be able to accommodate in a reversible and efficient way the volumetric variations induced by the electrochemical reactions.

Some of the galvanostatic profiles of this cell are shown in part A of Figure 61. As it can be seen, the 1st cycle differs from the others and shows a high irreversible capacity (CE of 70 %). This was expected and is ascribed to side reactions as SEI production or structural modifications, like the self-organized porous structure described in section 1.6.4.2.

Regarding the following cycles, the curves share very similar behaviours which are replicated through the cycles. The DCP plots shown in part B of the same figure highlight the potentials at which the electrochemical reactions occur, that are identified by means of comparisons with the literature.

[1] Thanks to the high efficiency, the capacity is addressed in general terms in the remainder of this section, without specification to lithiation or de-lithiation. The specific values reported refer to the lithiation half-cycle.
[2] Calculated as the angular coefficient of the lithiation curve as a function of the cycle number, in the same manner as it was done for the choice of the etching recipe in section 4.5.

The first cycle details are now presented, while the main features of the other cycles are subsequently deepened.

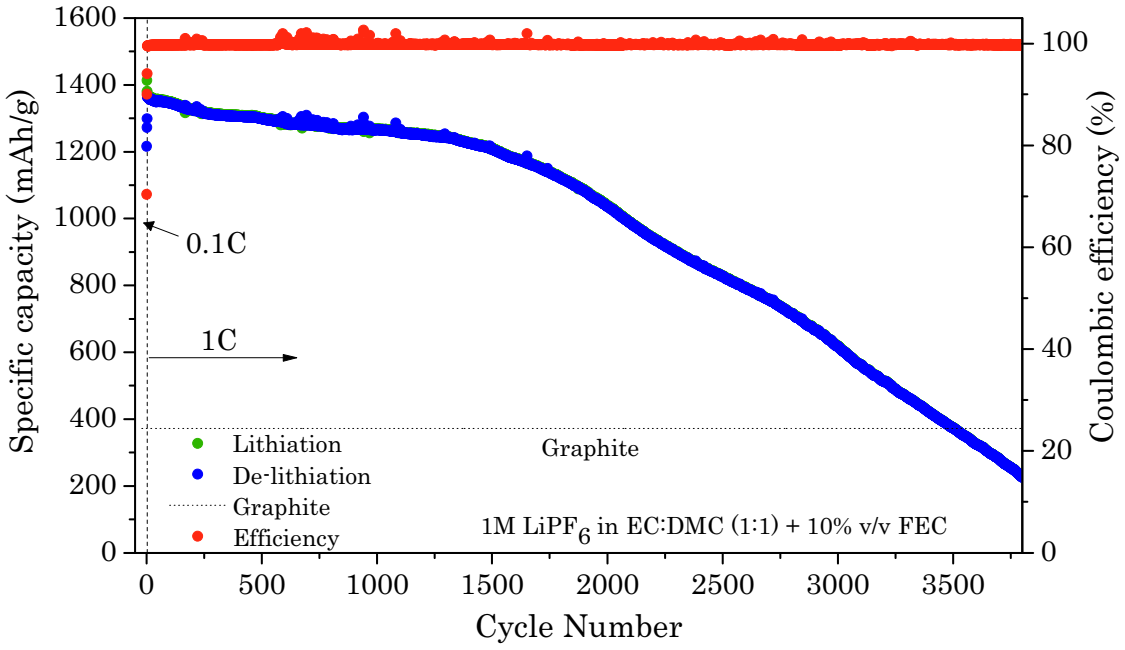

Figure 59: Specific capacity as a function of the cycle number of a cell realized using an etched sample and tested at 1C for its whole life.

As previously stated, the 1st cycle differs from the others and is reported alone in Figure 60. The cathodic peaks are found at 1.23 V (a), 0.6 V (b), 0.34 V (c), 0.18 V (d), 0.12 V (e) plus a small one at 0.08 V (f).
On the anodic side a main double peak is observed around 0.5 V (g) (0.48 V and 0.51 V), with a small satellite at 0.39 V (h) and a more pronounced one at 0.63 V (i), plus an extended tail toward positive potentials.

The reduction peaks above 0.5 V are ascribed to electrolyte decomposition and SEI formation [46][30][41][47], while the intense one at 0.34 V is identified as the characteristic c-Ge lithiation peak [5][6][48][49] (cf. structural analysis, section 3.3.3). The other troughs at lower potentials are ascribed to Li alloying with Ge up to the formation of the final phase c-$Li_{15}Ge_4$ [6][48][50][51].

On the anodic side, the small peak at 0.39 V is ascribed to dealloying from a-$Li_{15}Ge_4$ while that at 0.51 V can be related to de-lithiation from c-$Li_{15}Ge_4$ [6][51][52][49][43] [44]. The tail towards higher potentials is associated to dealloying from less lithiated phases [6][44].

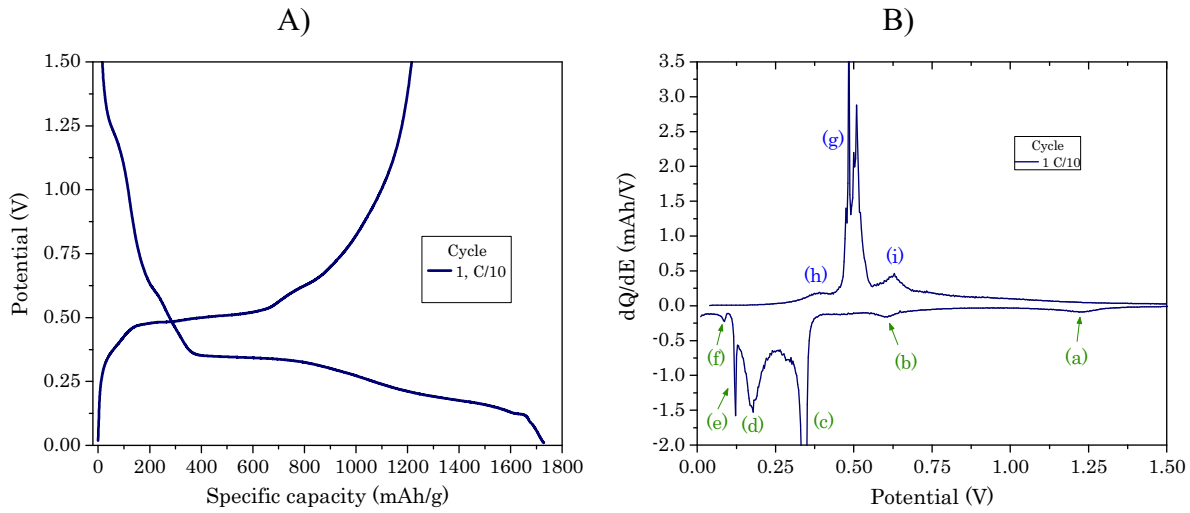

Figure 60: 1st cycle galvanostatic profile (A) and DCP (B) of the sample presented in Figure 59. The letters in B highlight the lithiation (green letters) and de-lithiation (blue characters) peaks.

In the following cycles the lithiation curves assume a multipeak shape, as it can be ascertained in part B of Figure 61. In the 3rd cycle, the main peaks are found around 0.62 V, 0.52 V, 0.38 V, 0.18 V and 0.11 V. The first is again ascribed to SEI production while the others are associated to progressive lithiation of Ge. On the anodic side, the DCP loses the satellite peak at 0.63 V while the rest of the curve retains the same shape as in the 1st cycle, with just a slight shift toward lower potential. These results match well with those of the CV analysis, both for peaks position and general shapes of the curves.

Some important changes are observed in the transition to 1C, that could be ascribed to overpotentials [7][2]. Indeed, all the lithiation troughs are shifted at lower potential. The last peak is the most affected since it loses its small satellite at 0.12V and it does not go to zero anymore. In the galvanostatic profile, this corresponds to a downshift of the curve and to a less articulated and less steep termination. On the anodic side, the sharp oxidation peak at 0.5V is completely faded and is substituted by a broad one centred at ~0.43 V.

A progressive recovery of the 0.5V oxidation peak is observed in the following cycles, accompanied by a suppression of its low potential component, and eventually coming to a conclusion by the 500th cycle. Concurrently, a slight increase and "sharpening" of the final cathodic peak can be recognized. This is pointed out by the black arrows in the inset of Figure 61, where a shallow but clear ending step develops around 0.05V (highlighted by another black arrow in the inset).

Since the sharp oxidation peak at 0.5 V is commonly ascribed to de-lithiation from the c-$Li_{15}Ge_4$ phase, the segment of the anodic curve below 0.5V could be associated to de-lithiation from a-$Li_{15}Ge_4$. This is consistent with the results found in other works [6] [48][51][49][43][44].
Based on these considerations, it could be guessed that a "deterioration" of the final lithiation step leads to a decrease, or even a complete suppression, of the sharp oxidation peak at 0.5 V, in favour of the broad one centred at lower potential.

As a last comment on these "initial" cycles, some changes are observed also in the reduction curves above 0.55V (red arrow in the inset of Figure 61).
These are interpreted as a residual SEI production, which is more evident in the 10th cycle. The process is thought to be completed by the 500th cycle since no more changes are observed thereafter. This is also supported by a slightly lower efficiency in these cycles, with a mean value of 99.77 % to be compared with the 99.90 % attained between the 500th and the 1500th cycles, before the increase of the fading rate.

From the 500th to the 1500th cycle the DCP curves are essentially superposed, and three main reduction peaks are observed at 0.5 V, 0.36 V and 0.16 V. These are consistent with those of the 3rd cycle, even if they are slightly shifted at a lower potential as a result of the overpotentials for the higher rate. In oxidation, an asymmetric peak with maximum at 0.5 V is associated to de-lithiation from c-$Li_{15}Ge_4$ and less lithiated phases.

From the 2000th cycle onward, a gradual decrease of the reduction peak intensities is observed. This is accompanied by their shift towards lower potentials, which is more pronounced for the 0.5 V and the ~0.16 V throughs. Furthermore, also the final lithiation step around 0.05 V is faded out.
On the anodic side, the 0.5 V peak slowly decreases and is completely faded out in the 3500th cycle, where it is substituted by a broad one centred at about 0.43 V.
What happens in these cycles can be considered as the reverse process of that highlighted in the first 500 cycles. Indeed, this time, the 0.5V anodic peak is progressively smoothed through the cycles. Correspondingly, the intensity of the lithiation peaks decreases and shifts towards lower potentials, with the simultaneous fading of their sharp edge at low potential.

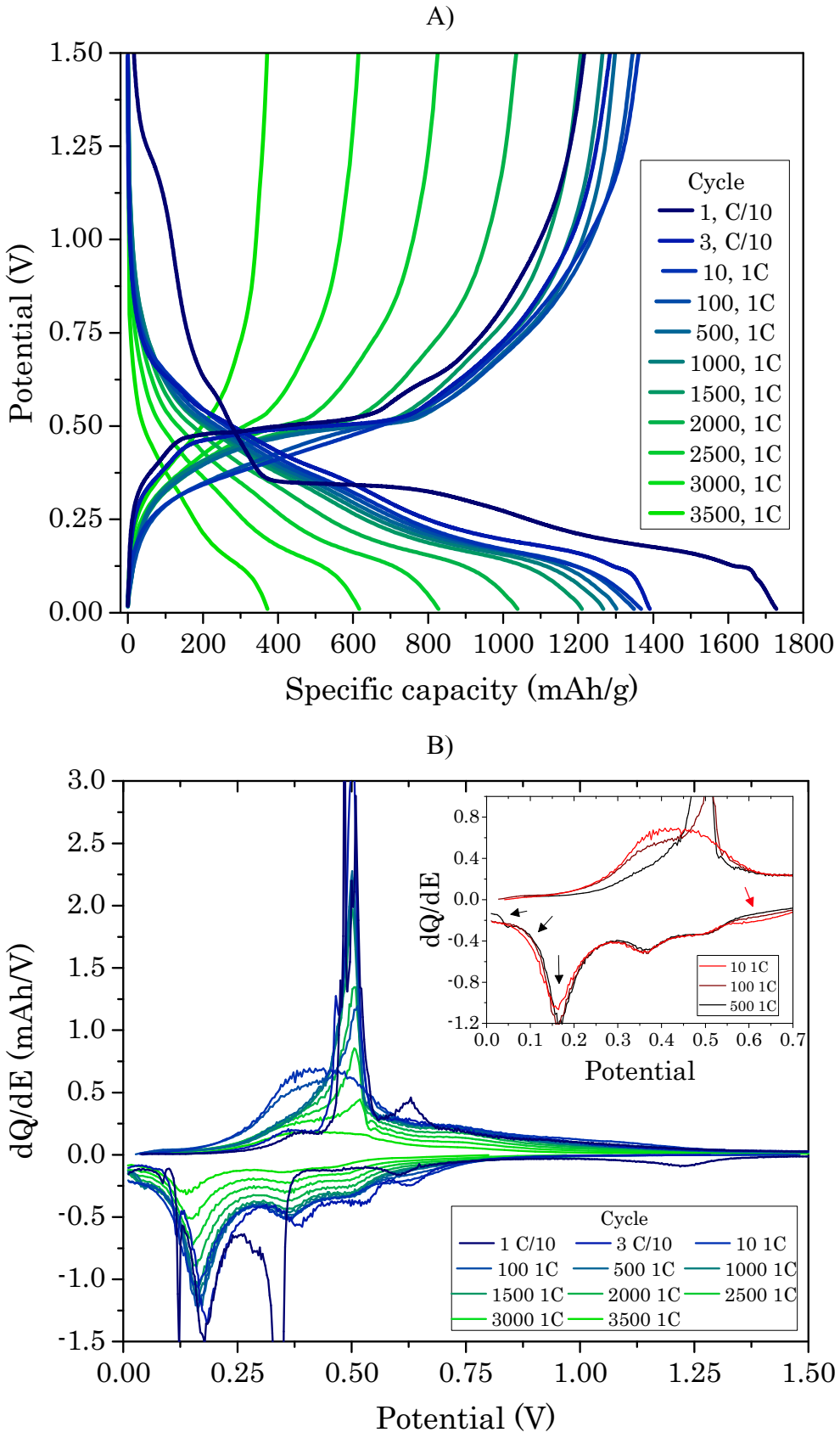

Figure 61: Galvanostatic profiles (A) of some cycles from the sample presented in Figure 59, together with their DCPs (B). A detail of the low potential part of the DCPs for the 10th, 100th and 500th cycles is shown in the inset of (B).

In summary, a result of this test, it can be guessed that etched cells are able to produce the final c-$Li_{15}Ge_4$ phase since their 1st cycle, for the low rate of C/10. When the rate is increased, a transient phase occurs: initially the Li-Ge reactions involve only amorphous phases; then, some reorganization process enables the electrodes to retrieve the final crystalline alloy. In the following cycles, the cell replicates the electrochemical reactions in a stable and efficient way. Finally, some deterioration process set off and the electrode gradually loose the capability to produce the c-$Li_{15}Ge_4$ phase. This corresponds to the smoothing down of the main details in both the DCP and the galvanostatic profiles.

As a last observation, it is important to note that the capacity is not affected by the modifications of the precise lithiation and de-lithiation mechanisms. This means that the capability to produce the final crystalline alloy, rather than stopping at the amorphous stage, only alters the shape of the galvanostatic profiles and not the cell capacity. Furthermore, the high CE demonstrates the high reversibility of the electrochemical processes, irrespective from the precise final lithiation product.

4.7.2. **Rate capability**

The remarkable capacity showed in the cycle-life test is accompanied by a good retention also at high current rates.

The rate capability test presented in this section demonstrates that even at C-rates as high as 40C the etched electrodes can deliver a capacity higher than the graphite theoretical one. Moreover, they are able to recover their initial capacity even after being stressed at the rate of 60C.

The test performed on a cell with etched electrode, realized on SS, is presented in Figure 62. The mass loading was of (0.24±0.02) mg and, as usual, the standard electrolyte solution was used. In this test, the cell was cycled increasing the c-rate each 10 cycles at the rates of C/10, C/8, C/4, C/2, 1C, 2C, 4C, 8C, 10C, 20C, 40C and 60C. As a last step, the cell was cycled again at C/10 for comparison with the initial cycles.

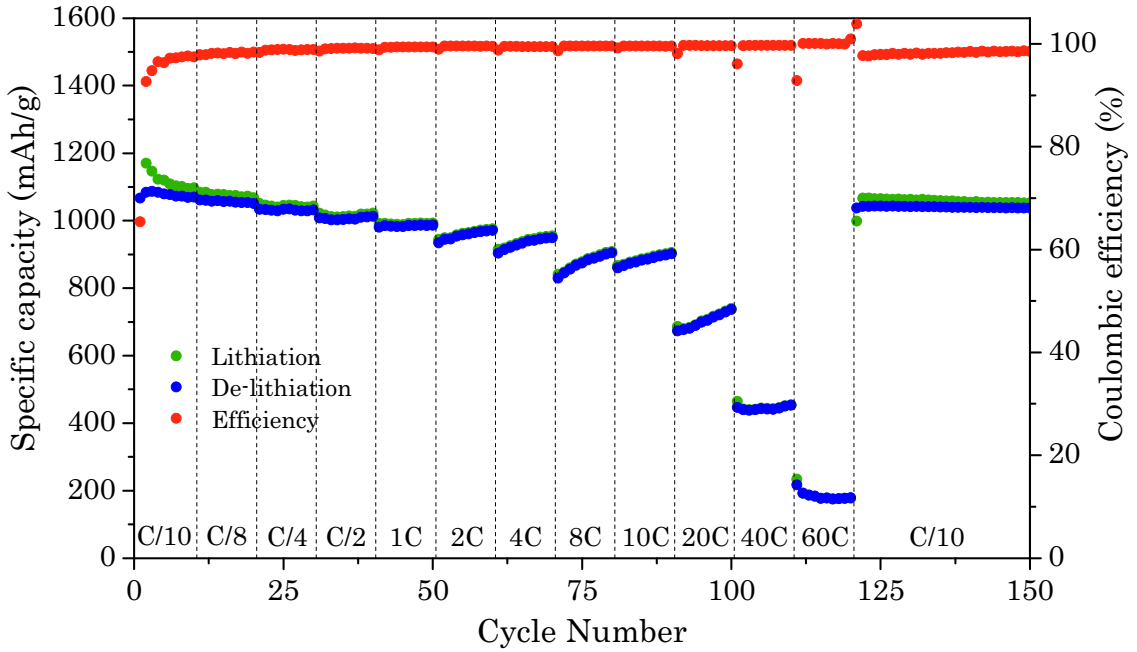

Figure 62: Rate capability of an etched cell, realized on SS substrate. The cell was tested starting from C/10 and increasing the C-rate each 10 cycles. At the end of the test, the cell is cycled again at C/10.

The cell shows interesting capacities of 1169 mAh/g and 1076 mAh/g in lithiation and de-lithiation, respectively, at C/10. This is retained stably up to 1C, with only slight reductions upon the rate changes. In particular, a good retention of about 85 % is observed at 1C with respect to the C/10 capacity.

A different behaviour arises between the rates of 2C and 20C: in this case, at each rate change, a capacity drop is followed by a partial recovery through the cycles. Further increasing the current at 40C and 60C, results in more marked capacity drops, without recovery through the cycles. Nevertheless, a stable behaviour can be identified also at these rates and the cell outperformed graphite even at 40C. Furthermore, when cycled again at C/10 at the end of the test, the cell fully recovered its initial capacity and retained it stably.

A good CE is observed at all rates, apart from the 1st cycle showing a mean efficiency of 65.44 %. As for the other cells, this is ascribed to irreversible processes like SEI formation or active material reorganizations. The CE continuously rise at each rate change up to 10C (see Table 15). Furthermore, very high efficiencies above the 99 % can be noted even at 20C, 40C and 60C. These high values permit to consider as “identical” the lithiation and de-lithiation capacities.

Considering the higher rates of this test, namely 10C, 20C, 40C and 60C, excellent capacity retentions of 76 %, 60 %, 38 % and 16 % are observed with respect to the initial C/10 cycles.

C-rate	Mean lithiation capacity (mAh/g)	Mean de-lithiation capacity (mAh/g)	Average efficiency (%)
C/10	1170	1076	93.27
C/8	1076	1056	98.18
C/4	1044	1032	98.80
C/2	1016	1007	99.07
1C	991	984	99.32
2C	962	957	99.49
4C	938	932	99.41
8C	879	875	99.48
10C	887	883	99.53
20C	706	703	99.50
40C	447	444	99.34
60C	186	184	99.40
C/10	1057	1040	98.44

Table 15: Average capacities and CE of the rate capability test of an etched sample.

Some of the galvanostatic profiles from the rate capability test are reported in Figure 63. Their evaluation permits to inspect how the shape of the final part of the lithiation profile affects that of the oxidation curves.

As in the previous Figure 61, even in this case the C/10 profiles terminate at low potential in a steeper way compared to those of the higher rates. Indeed, flatter regions followed by a steeper final segment are observed. Correspondingly, well-defined oxidation peaks at 0.5V are particularly evident in the DCP curves.
By raising the C-rate, the lithiation step-like termination of the galvanostatic profiles is lost. This is substituted by a single region with intermediate slope. Correspondently, a partial (C/2) or full (1C) abatement of the oxidation peak at 0.5V is observed in favour of the lower potential peak.

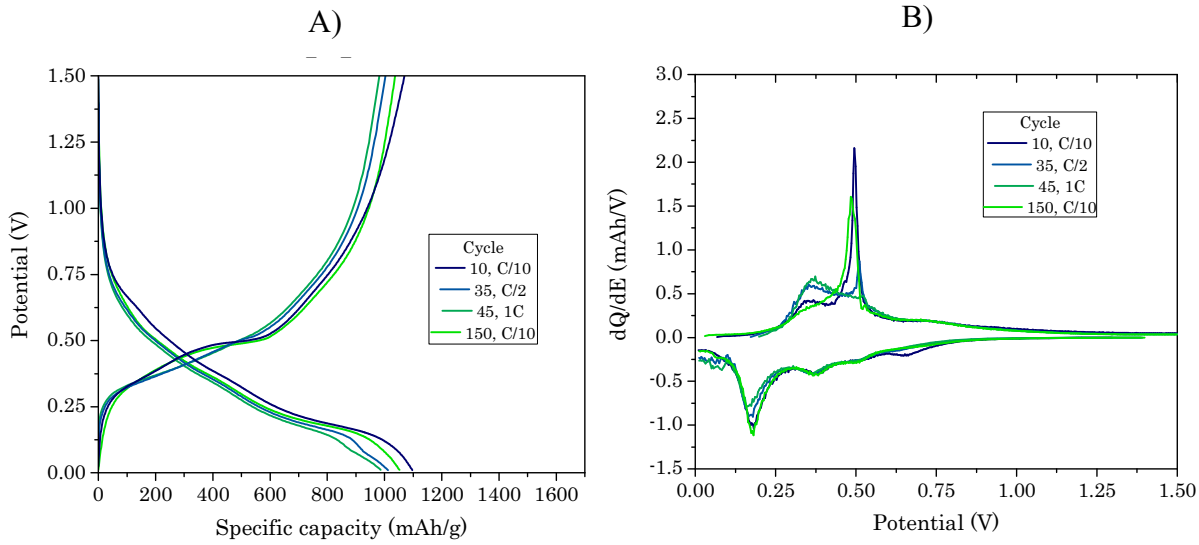

Figure 63: Selected galvanostatic profiles at C/10, C/2 and 1C, from the rate capability of the etched electrode (A) aside their corresponding DCPs (B).

Compared to the cycle-life, the final lithiation steps are less steep this time, as it can be clearly observed in part A of Figure 63. In addition, also the low potential segments of the DCP profiles are not going to zero in a steep way. On the anodic side of the DCPs, these things correspond to an increase of the segment at the left of the 0.5V peak (part B of Figure 63).

These observations perfectly agree with those made before and demonstrate that the C-rate influences the capability of a cell to convert the final lithiation product into its crystalline phase.

As a last remark about Figure 63, it is worth to note that the charge and discharge profiles of the 150th cycle recover the same features of the 10th one. This occurs in spite of the intermediate several cycles performed at higher rates.

4.7.3. **Temperature test**

A cell was tested in a wide temperature range to assess how the electrode capacity would have been affected. This test was carried out on a cell with mass loading of (0.29±0.02) mg, Mo substrate, and using the standard electrolyte solution.

After some initial cycles at C/10, the cell was cycled at the fixed rate of 1C and the temperature was lowered or raised by 5 °C each 10 cycles, in the range -30 °C ÷ 60 °C.

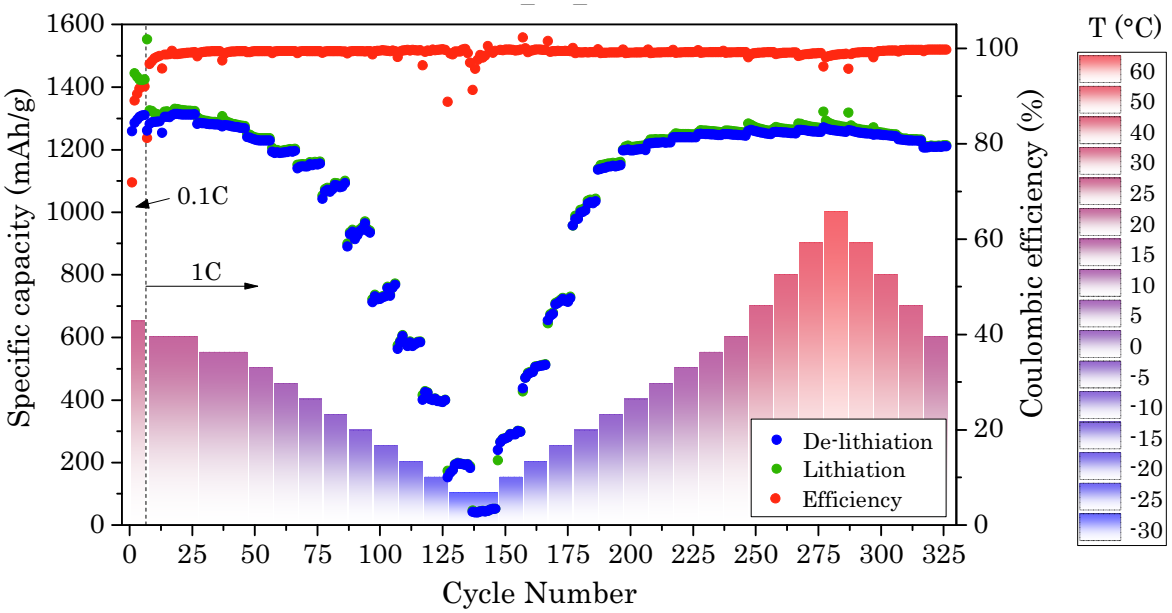

Figure 64: Temperature test of a cell with etched electrode realized on Mo substrate. After some initial cycles at C/10, the cell was tested at 1C, and the temperature varied by 5 °C each 10 cycles in the range -30 °C ÷ 60 °C.

Figure 64 reports the specific capacity of the cell as a function of the cycle number and the temperature. Even in this case, the initial coulombic efficiency (ICE) is the lowest, 71.89 %, and the mean lithiation and de-lithiation capacities are of 1483 mAh/g and 1294mAh/g in the C/10 cycles. The temperature in these cycles was of 25 °C, then it was lowered to 20 °C for the first 20 cycles at 1C.

As reported in Table 16, the average capacities at 20 °C are 1334 mAh/g and 1300 mAh/g during lithiation and de-lithiation. These are considered as reference values for the following cycles. A quite high efficiency of 97.6 % is observed in these cycles and, as before, the lithiation and de-lithiation capacities are considered as “identical” in the remainder of this section. Next to those at 20 °C, other 20 cycles were performed at 15 °C, observing only a shallow capacity reduction (-4 %) and even higher efficiency (99.16 %).

After these initial cycles, the temperature was lowered of 5 °C each 10 cycles up to -30 °C but, before analysing the low temperature behaviour, an important consideration must be done. As it can be seen, at -30 °C the capacity splits in two branches. This is ascribed to a short rest time between the tests at different temperature during the first descent, which

probably was not sufficient to guarantee that a uniform temperature was achieved inside the cells. Thus, in the second run of measurements, the rest time was increased to ensure that thermal equilibrium was reached. For this reason, only the data from the second branch are considered regarding the lower temperatures.

Starting from the performance at -30 °C, an almost negligible capacity of about 40 mAh/g is observed, while already at -25 °C it raises up to about 280 mAh/g. At -20 °C the capacity is approximately of 490 mAh/g, which is already higher than the graphite theoretical one. This value represents the 37 % of the 1C capacity, but it must be considered that at this temperature, when tested with similar electrolytes, standard cells with graphite anodes can deliver only the 6 % of their room temperature capacity [53]. In the next steps the capacity increases markedly with the temperature, and it reaches almost 1200 mAh/g at -5 °C, representing the 86 % of the room temperature capacity, with an efficiency above the 99 %.

	Not reliable data due to unsure thermal equilibrium			Temperature raise after ensured thermal equilibrium		
T (°C)	**Mean lith. cap. (mAh/g)**	**Mean de-lith. cap. (mAh/g)**	**Mean CE (%)**	**Mean lith. cap. (mAh/g)**	**Mean de-lith. cap. (mAh/g)**	**Mean CE (%)**
25 @C/10	1483	1294	87.83	/	/	/
20	1334	1300	97.60	1258	1248	99.20
15	1289	1278	99.16	1259	1249	99.21
10	1240	1232	99.37	1249	1239	99.22
5	1200	1192	99.38	1232	1222	99.19
0	1239	1231	99.37	1210	1200	99.17
-5	1200	1192	99.34	1154	1144	99.17
-10	1156	1149	99.34	1012	1004	99.24
-15	741	737	99.40	704	701	99.63
-20	584	581	99.43	492	491	99.91
-25	407	404	99.29	278	281	101.29
-30	188	185	98.02	46	45	97.82

Table 16: Average capacities and CE in the range -30 °C ÷ 25 °C during the first cooling and warming process. The data from the first cooling process can be considered only qualitatively due to unsure thermal equilibrium at the lower temperatures.

In the high temperature cycles, up to 60 °C, the capacity is essentially unaffected: the most relevant observation is only a small efficiency decrease (Table 17), indicating that some irreversible reaction is favoured at higher temperature. In the last cycles performed again at

20 °C, a mean capacity around 1200 mAh/g is observed, which is lower but still very close to the initial one (-10 %).

	Heating up to 60°C			Final temperature lowering to 20°C		
T (°C)	**Mean lith. cap. (mAh/g)**	**Mean de-lith. cap. (mAh/g)**	**Mean CE (%)**	**Mean lith. cap. (mAh/g)**	**Mean de-lith. cap. (mAh/g)**	**Mean CE (%)**
20	/	/	/	1213	1209	99.68
30	1269	1256	98,96	1235	1230	99.62
40	1267	1255	99,05	1255	1246	99.34
50	1275	1260	98,80	1271	1254	98.77
60	1284	1262	98,36	/	/	/

Table 17: Average capacities and CE in the range 20 °C ÷ 60 °C from the second part of the test.

As a last thing to note, an interesting increase of the capacity is observed through the cycles, at each temperature step below -5 °C in the rising branch (that in which thermal equilibrium was guaranteed). A reasonable explanation for this could be a current induced self-heating of the cell during the charge and discharge processes.

In conclusion, this test shows the high potential over a wide temperature range of the binder free anodes realized by means of LEPECVD and HF etching, with a capacity higher than 1000 mAh/g even at -5 °C. A poor capacity is observed only at the very low temperature of -30 °C, but this could be related to the semiconductive nature of Ge as well as to the unavoidable increase of the electrolyte resistance at such a low temperature [54][55] [56][57][58].

4.8. **Electrochemical performances of the ion implanted samples**

Ion Implantation was used as an alternative technique to nano-structure the electrodes. As presented in chapter 2.4, two ion implantation recipes were selected. Since also two substrate materials have been used, 4 possible combinations were possible and have been tested. In this section, the results of their cycle-life and rate capability tests are reported.

4.8.1. **Cycle-life**

Figure 65 reports the specific capacity as a function of the cycle number of samples realized by means of different ion implantation recipes on SS and Mo. The cells were realized using the usual electrolyte solution and the mass loadings were of (0.20±0.01) mg, (0.25±0.01) mg, (0.29±0.01) mg, (0.30±0.01) mg for samples realized by means of Ion1[3] recipe on SS and Mo and by means of Ion2[3] on SS and Mo, respectively.

After some initial cycles at C/10, the cycle-life tests were carried out at the constant rate of C/4. Thanks to the very high efficiencies registered (see Table 18), the lithiation and de-lithiation capacities are considered as "identical" in the remainder of this section.

As it can be seen in Figure 65, very high and stable capacities are achieved in all the cases, with high efficiencies too. Low ICEs are observed for all the samples with values of 87.44 %, 87.15 %, 76.12 % and 78.55 % for Ion1 on SS, Ion1 on Mo, Ion2 on SS, and Ion2 on Mo, respectively.

The highest capacity is observed for the Ion1 on Mo cell, which attains an average of 1358 mAh/g at C/4 with a mean efficiency of 99.77 %. This value represents the 84 % of the maximum thermodynamically conceivable (and 98 % of the theoretical capacity for $Li_{15}Ge_4$) and corresponds to 3.65 times the graphite theoretical one. A transient phase is observed up to about the 75th cycle in which the capacity gradually increases before stabilizing around 1360 mAh/g. The cells realized using the Ion1 on SS and Ion2 on Mo anodes show average capacities of 1186 mAh/g and 1200 mAh/g. Even in these cases, very high mean CE are observed, of 99.35 % for Ion1 on SS, and 99.63 % for Ion2 on Mo. Even this time some transients with increasing capacity are observed during the first 50-100 cycles. The lowest capacity is displayed by the Ion2 recipe on SS, with an average of 823 mAh/g at C/4. Although this, a very high average efficiency of 99.55 % is attained.

[3] With reference to the notation introduced in section 2.4.

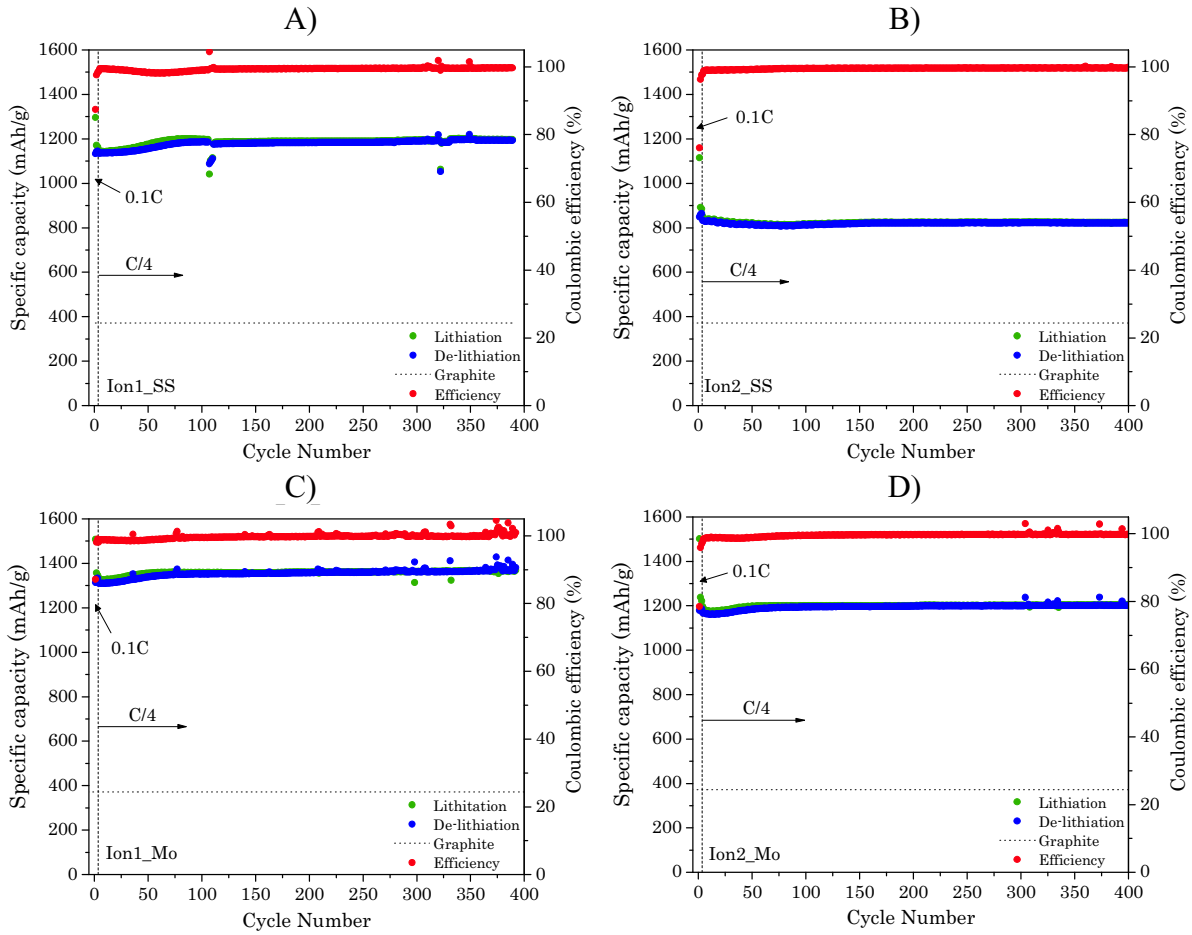

Figure 65: Specific capacity and CE as a function of the cycle number of half-cells with electrodes realized by means of different ion implantations recipes on SS and Mo. In particular, Ion1 on SS (A), Ion2 on SS (B), Ion1 on Mo (C), and Ion2 on Mo (D).

Besides the high capacities and efficiencies achieved, it must be noted that no hint of fading is observed in any cell. This could be related to the smaller and uniform size of the features observed in the implanted samples compared to the etched ones (cf. the morphological analysis in sect. 3.4), which could enable a better capacity retention through the cycles.

Sample	C-rate	Mean lithiation capacity (mAh/g)	Mean de-lithiation capacity (mAh/g)	CE (%)
Ion1 on SS	**C/10**	1210	1140	94.47
	C/4	1186	1178	99.35
Ion1 on Mo	**C/10**	1404	1326	94.76
	C/4	1358	1355	99.77
Ion2 on SS	**C/10**	964	858	90.02
	C/4	823	820	99.55
Ion2 on Mo	**C/10**	1321	1185	90.53
	C/4	1200	1195	99.63

Table 18: Average capacities and efficiencies of the cells using ion implanted anodes.

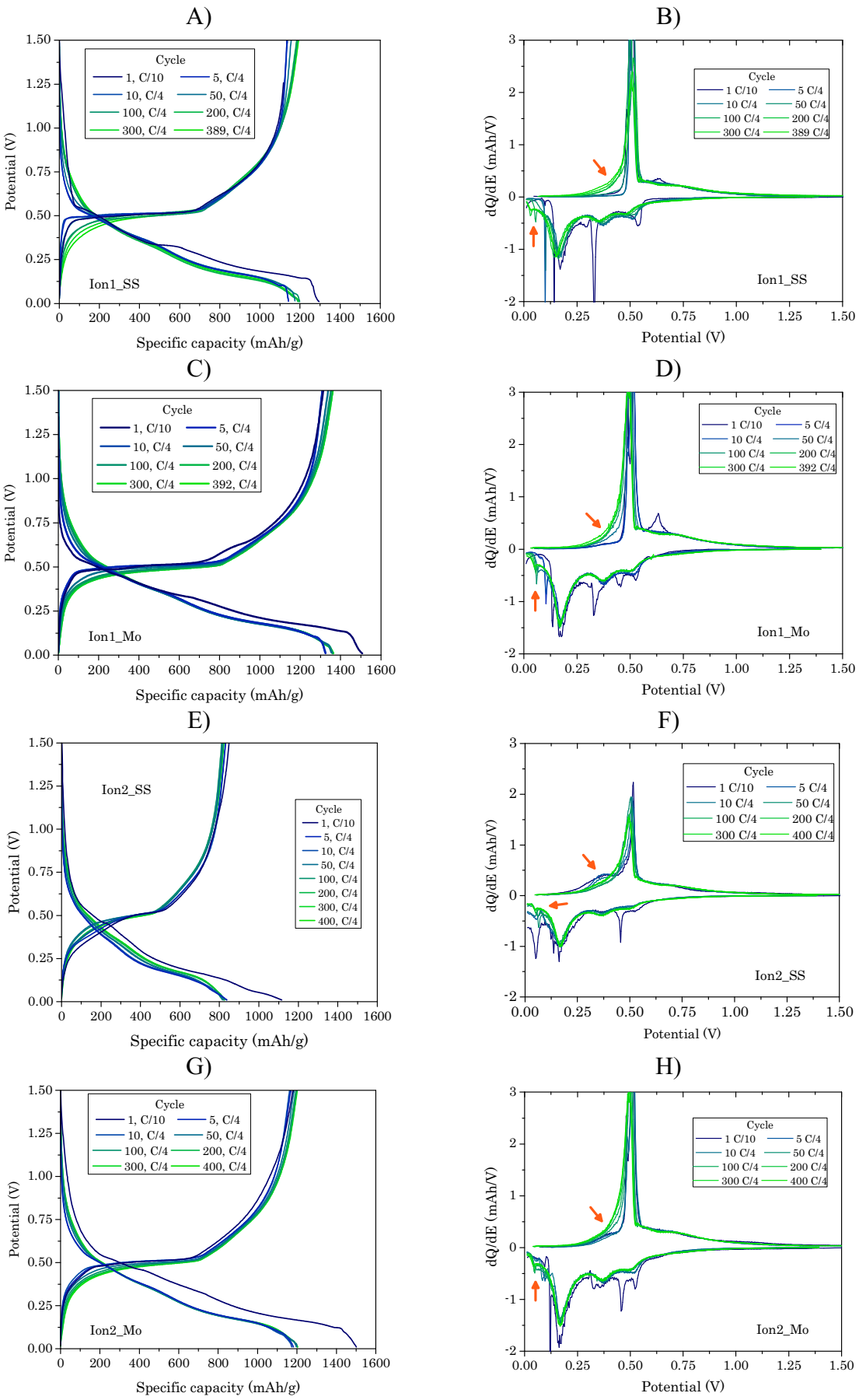

Figure 66: Selected cycles charge and discharge galvanostatic profiles of the cells with ion implanted anodes (A,C,E,G). The DCPs are presented aside their corresponding galvanostatic profiles (B,D,F,H).

The galvanostatic profiles of some cycles of the previous samples are presented in Figure 66, along with their DCPs. In all the cases, the 1st cycle differs from the following ones and shows the highest irreversible capacity. As for the other cells, this was ascribed to SEI production or structural reorganizations of the active material.
In the following cycles, the galvanostatic profiles are almost overlapped in all the cases, indicating a high reversibility of the electrochemical processes, as highlighted also by the high CE.

The DCP curves in Figure 66 confirm the similarity of the galvanostatic profiles as very similar behaviours can be recognized in all the samples, with only some differences for the Ion2 on SS sample.
The shape of these DCPs is also very similar to that of the electrochemically etched samples, although some striking differences can be noticed: firstly, the 1st cycles for the implanted samples do not differ significantly from the following ones, at least in their main details, while it was not the case for the etched samples. Secondly, the main oxidation peaks around 0.5 V are always present, for all the samples and all the cycles, with just some deviations in the case of Ion2 on SS.

The similar trend shared by the 1st cycles and the following ones is ascribed to a higher fraction of a-Ge in the implanted samples, with respect to the etched ones, as a consequence of the implantation process (cf. sec. 2.4.3). This is consistent with the works of Baggetto *et al.* and Laforge *et al.*, where a-Ge films were studied as anodic materials and whose galvanostatic profiles already displayed the lithiation multipeak shape since the 1st cycles, without the c-Ge sharp trough [44][59]. As a result, the 1st cycle DCPs of the ion implanted electrodes represent a sort of hybrid between those of etched samples and the multipeak curves that are classically ascribed to a-Ge.

The main reduction peaks are observed at 0.6 V (a), 0.53 V (b), 0.46 V (c), 0.33 V (d), 0.17 V (e), 0.14 V (f) and ~ 0.1 V (g)[4], matching well with those listed for 1st and 3rd cycles of the etched cell. However, different intensities are observed for the various samples and sometimes some peaks are missing.
The trough at 0.33 V, which can be seen in the Ion1 samples, highlights a residual presence of c-Ge. As introduced in section 2.4.7, this could be related to a not-perfect alignment of

[4] For the sake of clarity these are highlighted in Figure 67, where the 1st cycles of the etched and implanted samples are compared.

the samples inside the implantation masks, resulting in possible traces of bulk Ge at their borders.

The remaining peaks are all ascribed to the multi-lithiation steps of a-Ge: their higher intensity, compared to the following cycles, could be associated to a continuous SEI production during the 1st lithiation process.

To highlight the differences in the 1st cycles of the etched and implanted samples, their DCP profiles are reported together in Figure 67. Since the integral of the DCP curves represents the total amount of charge fluxed, the curves are normalised with respect to that value to enable a reliable comparison.

A marked difference can be recognized between 1.5 V and 0.33 V, in lithiation, while they become quite similar at low potential (apart from the Ion2 on SS sample, that is deepened afterward). In oxidation, a similar behaviour is observed for all the samples with an intense peak at 0.5 V (h).

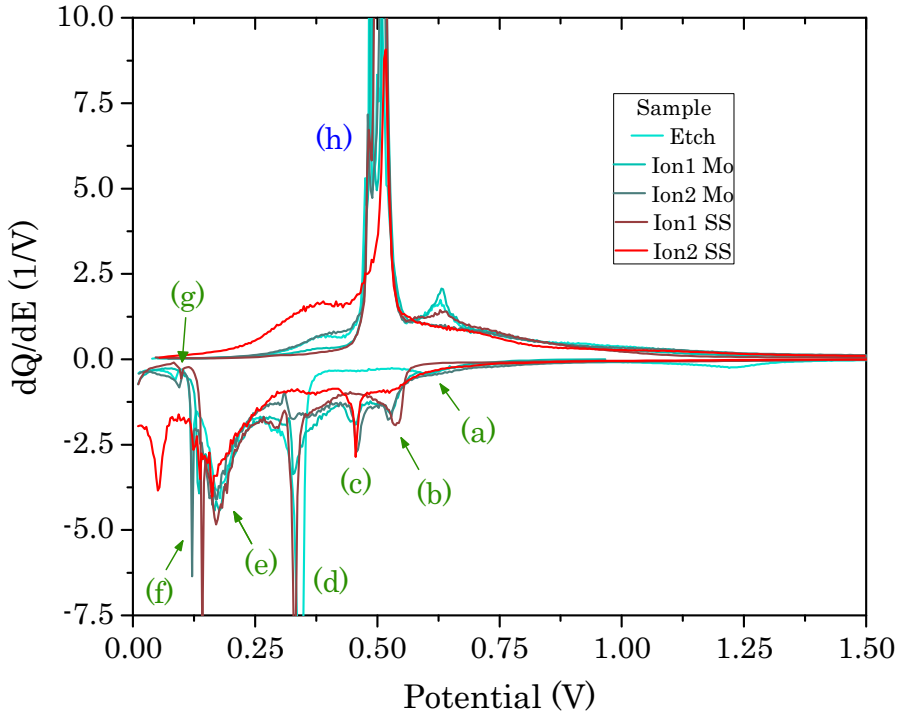

Figure 67: Comparisons of the 1st cycle DCPs of ion implanted and etched samples, all normalised with respect to the corresponding charge fluxed. The letters highlight the lithiation (green characters) and de-lithiation (blue letters) peaks.

The similarities in final parts of the cathodic steps as well as that of the anodic curves point out that the same lithiation products were obtained, irrespective of the specific nano-structuration technique employed, as the oxidation pathways are the same.

This perfectly agrees with the observations done about the cycle-life and rate capability of the etched samples, which were presented in the sections 4.7.1 and 4.7.2. In particular, this further confirms the relation between the step-like termination of the lithiation galvanostatic profiles and the development of the c-$Li_{15}Ge_4$ phase.

Even the anomalous behaviour of the Ion2 on SS sample can be easily interpreted by observing the analogies with the curves reported in Figure 63 (rate capability of the etched sample). Indeed, making analogous considerations as those of section 4.7.2, it can be thought that the lithiation process is not completed for this sample. For this reason, the final "step-like" segment of the cathodic galvanostatic profile is suppressed and the same occurs for the 0.5 V oxidation peak, while the low potential part of the oxidation DCP curve raises.

The normalised DCPs of the 2nd cycles of the etched and implanted samples are reported in Figure 68. A high similarity between each other and with the 1st cycle curves of the ion implanted samples can be observed (cf. Figure 67). Even in this case, the Ion2 on SS sample differs from the others, but similar considerations can be made as before.

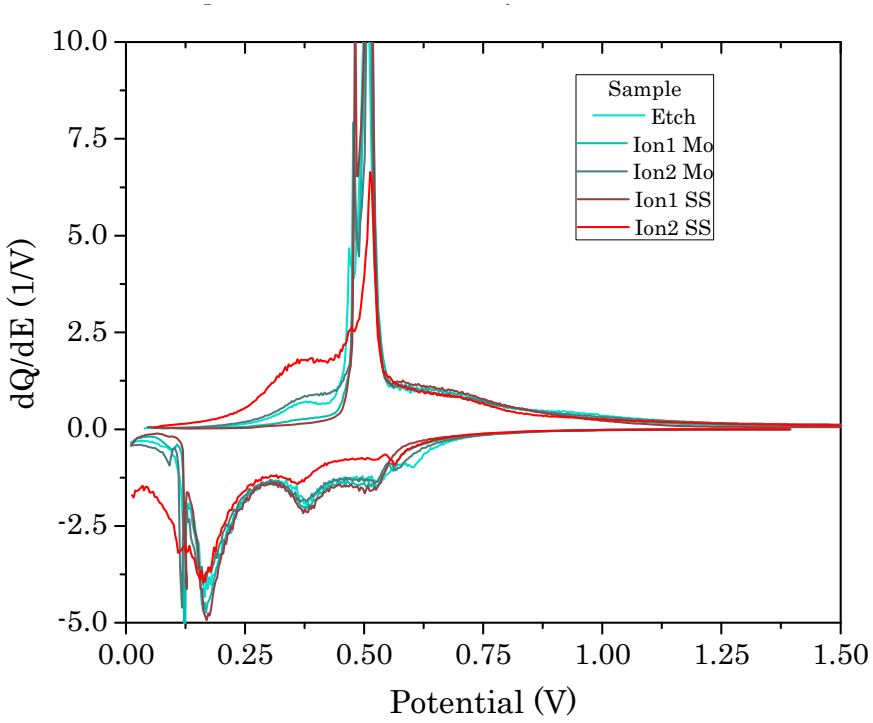

Figure 68: Comparisons of the 2nd cycle DCPs of ion implanted and etched samples, all normalised with respect to the corresponding charge fluxed.

Returning to Figure 66, where the galvanostatic profiles and DCP for many cycles of the cells are reported, an impressive similarity can be noticed between the subsequent cycles

for all the samples. Indeed, both the galvanostatic profiles and the DCPs are always essentially superposed.
This is an evidence that highly reversible processes occurred, as it is supported also by the high efficiencies reported in the Table 18.

The evolution of the curves reported in Figure 66 through the cycles produces just one main difference that is pointed out by the orange arrows in the DCP graphs. This is represented by an "expansion" towards 0 V of their low potential segment, resulting in a small side peak that was not present in the initial cycles. Upon inspection of the galvanostatic profiles, this can be recognized as a downshift of the step-like termination, with its steeper final segment becoming shorter.
On the oxidation side, all of this corresponds to an increase of the low potential segment of the oxidation curves.
Interestingly, a reversed process is observed for the Ion2 on SS sample. There, the low potential segment of the lithiation DCPs "sharpens" through the cycles. Correspondingly, the oxidation peak at 0.5V loses its low potential shoulder.

All these considerations are consistent with the previous observations, further supporting the relation between the sharp step-like termination of the lithiation galvanostatic profile and the complete development of the c-$Li_{15}Ge_4$ phase. This corresponds in turn to the presence of the sharp 0.5 V peak in oxidation.

As a last remark about these samples, it is interesting to note the SEI peak around 1.2 V is not visible from the DCP curves. However, the SEI production can be recognized from the galvanostatic profiles in Figure 66, where a clear charge flow is visible in almost all the cases around 1.2 V ÷ 1.3 V.

4.8.2. **Rate capability**

The last characterization presented is the rate capability of the ion implanted samples, whose graphs are reported in Figure 69. As always, the standard electrolyte solution was used. The electrode mass loadings were of (0.24±0.01) mg, (0.23±0.01) mg, (0.22±0.01) mg, (0.27±0.01) mg for Ion1 on SS, Ion1 on Mo, Ion2 on SS, and Ion2 Mo, respectively.

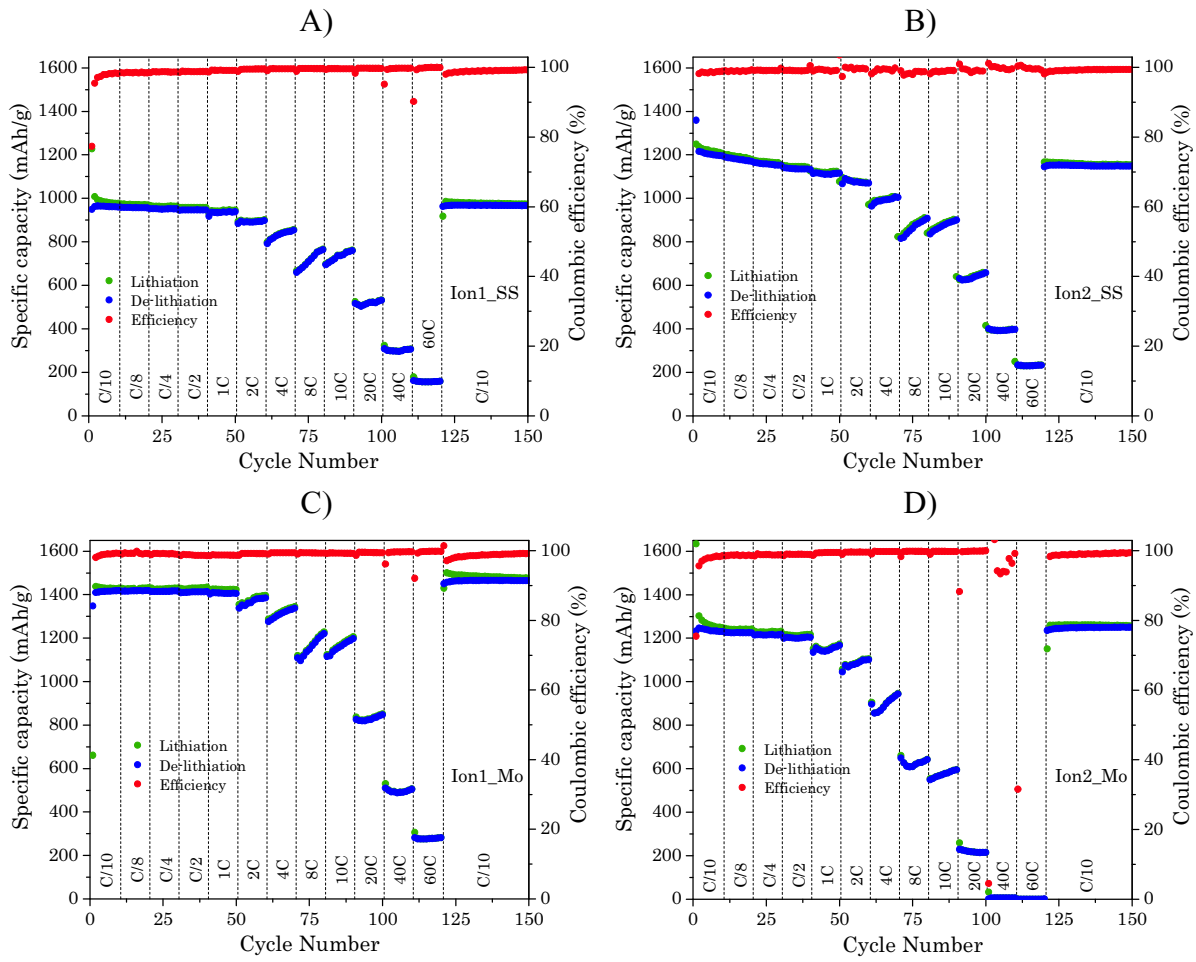

Figure 69: Rate capability tests of the ion implanted samples.

Even in this case, the highest capacity is observed for the Ion1 on Mo sample, which outperformed all the others and that showed an outstanding reversible capacity of 1482 mAh/g when cycled again at C/10. This is even higher than the theoretical capacity of $Li_{15}Ge_4$ (107 %) and could be due to over-lithiated phases (analogous phases were observed also by Jung *et al* and Al-Obeidi *et al* [60][61]).

Even all the other samples display good capacities with high retention even at the elevated rates, as it can be argued by the graphs and by the values listed in Table 19. Only Ion2 on Mo showed a bad retention at 40C and 60C, however it recovered its initial capacity when cycled again at C/10. Interestingly, the sample Ion2 on SS has a very high capacity compared to its twin of the cycle-life test, which is ascribed to some intrinsic poor characteristic of that electrode.

As a last remark, some failure of the galvanostat occurred during the first cycles for the electrodes Ion2 on SS and Ion1 on Mo, which produced unrealistic capacity values for their 1st cycles. However, this has not affected the remaining cycles, as it can be easily seen by

the graphs themselves. These data have been discarded in the calculation of the average values.

	Ion1 on SS			Ion2 on SS		
C-rate	**Mean lith. cap. (mAh/g)**	**Mean de-lith. cap. (mAh/g)**	**Mean CE (%)**	**Mean lith. cap. (mAh/g)**	**Mean de-lith. cap. (mAh/g)**	**Mean CE (%)**
C/10	1010	961	95.63	1220	1203	98.63
C/8	972	957	98.51	1191	1179	99.00
C/4	964	951	98.70	1167	1158	99.20
C/2	958	947	98.80	1145	1136	99.25
1C	943	934	99.12	1118	1114	99.64
2C	897	892	99.47	1071	1075	100.55
4C	835	831	99.56	979	990	101.51
8C	717	714	99.60	870	865	99.45
10C	734	731	99.61	856	873	103.03
20C	520	518	99.60	617	638	105.25
40C	304	301	99.25	380	395	105.91
60C	159	157	98.89	231	231	99.67
C/10	976	967	99.15	1159	1150	99.26
	Ion1 on Mo			**Ion2 on Mo**		
C-rate	**Mean lith. cap. (mAh/g)**	**Mean de-lith. cap. (mAh/g)**	**Mean CE (%)**	**Mean lith. cap. (mAh/g)**	**Mean de-lith. cap. (mAh/g)**	**Mean CE (%)**
C/10	1431	1415	98.90	1302	1236	95.52
C/8	1428	1418	99.28	1242	1225	98.69
C/4	1428	1415	99.11	1230	1215	98.84
C/2	1430	1412	98.74	1215	1202	98.95
1C	1424	1406	98.74	1156	1149	99.39
2C	1378	1367	99.16	1086	1082	99.56
4C	1319	1311	99.37	900	897	99.72
8C	1165	1158	99.35	628	626	99.69
10C	1167	1158	99.31	575	573	99.76
20C	834	829	99.41	222	219	98.73
40C	500	496	99.30	7	5	178.37
60C	281	278	98.99	0	0	\
C/10	1482	1464	98.76	1256	1248	99.34

Table 19: Average capacities and efficiencies for the rate capabilities of the ion implanted samples.

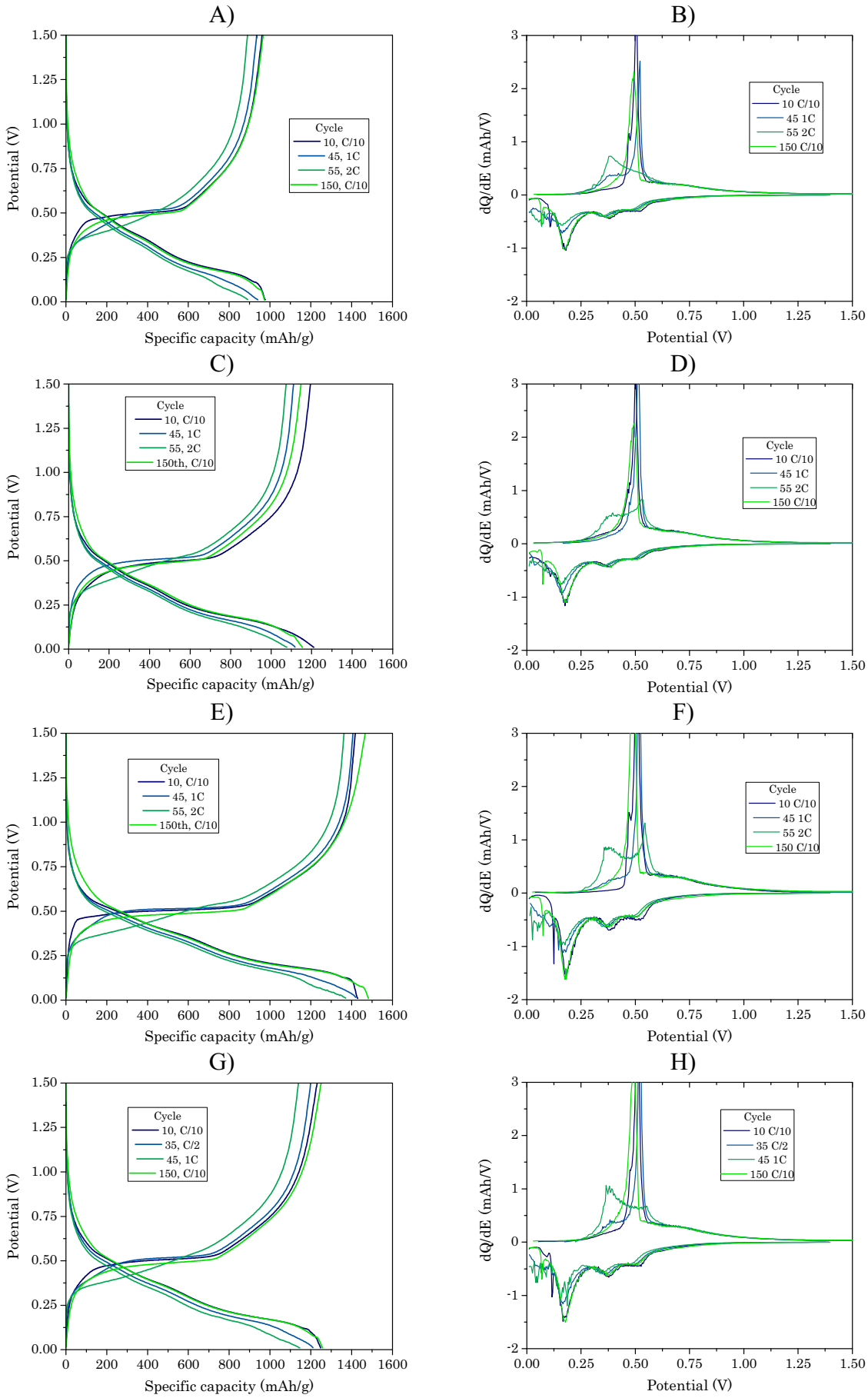

Figure 70: Selected galvanostatic profiles from the rate capabilities of the ion implanted electrodes (A) beside their related DCPs (B).

The analysis of the shapes of galvanostatic profiles for these samples leads to similar results as those presented in section 4.7.2, where the etched sample rate capability was presented. These profiles are reported in Figure 70: as it can be seen, in all the cases, the suppression of the final lithiation step implies a proportional abatement of the oxidation peak at 0.5 V plus a gradual enhancement of its lower potential component.
Again, this further supports the correlation between the shape of the final part of the lithiation curves and the cells capability to produce the final c-$Li_{15}Ge_4$ phase.

It is interesting to note that this time, the loss of the oxidation peak at 0.5 V is observed at higher rates compared to the etched samples. This could be related to the smaller morphological features observed in the implanted samples, compared to the etched ones (cf. sect. 3.4.2). Indeed, such structures could be fully lithiated more easily, as the lithium diffusion lengths are shorter. Therefore, this smaller diffusion length could compensate for the increased rate and render accessible the final crystalline phase even at higher rates.

4.9. **"Stable cycles" comparison**

In conclusion of this chapter, a comparison of the DCPs of selected cycles from many of the samples previously presented is reported in Figure 71. Precisely as in Figure 67, all the curves are normalised with respect to the corresponding charge fluxed.

The cycles are selected from cells that showed a smooth capacity trend, without irregularities like those of the samples using VC (cf. sections 4.3 and 4.4) nor abrupt variations within few cycles like observed in the bulk or half-bulk samples (see sections 4.3 and 4.5).

These cycles are here referred to as "stable cycles". These cycles are all selected from the 100^{th} onward, preferring the lowest rate ones, since it is reasonable that these are less affected by the transient phenomena that may afflict the initial ones, like SEI production or material reorganizations. Furthermore, the curves for the lower rates are expected to be less affected by the overpotentials [7][2].

This comparison if presented in Figure 71, where a striking similarity can be recognized between all the curves. This clearly demonstrates that the same electrochemical reactions occurred in all the cases, independently of:

A. The substrate material (further proof),
B. The nano-structuration techinque employed (etching or ion implantation),
C. The kind of test performed or, in other words, the "history" of the cell (cycle-life, rate capability, temperature test)

Only a slight dependence from the C-rate can observed in the low potential segments of these curves, both in reduction and in oxidation. Indeed, it can be noticed that the lithiation profiles do not terminate in a sharp way at low potential, with a shift towards lower potential that gradually increases as the rate is raised.
This is more evident in part B of Figure 71, where the low potential region of part A is magnified. The blue arrow highlights the low potential shift for the higher rates, while the blue circle underlines the vanishing of the sharp terminations. In fact, it can be clearly observed that the green curves (C/10 rate) are all close to zero while the red (C/4 rate), blue and orange (1C rate) ones are progressively displaced.
Correspondingly, on the oxidation side, the left side of the 0.5 V peak increases (violet arrow), this being more evident for the higher rate profiles (red, blue, and orange curves).

This analysis perfectly agrees with the considerations previously made about the shapes of the galvanostatic curves for the cycle-life and the rate capabilities of both the implanted and etched samples. This further supports the conclusions about the influence of the C-rate on the capability to convert the final lithiation product into its crystalline phase.

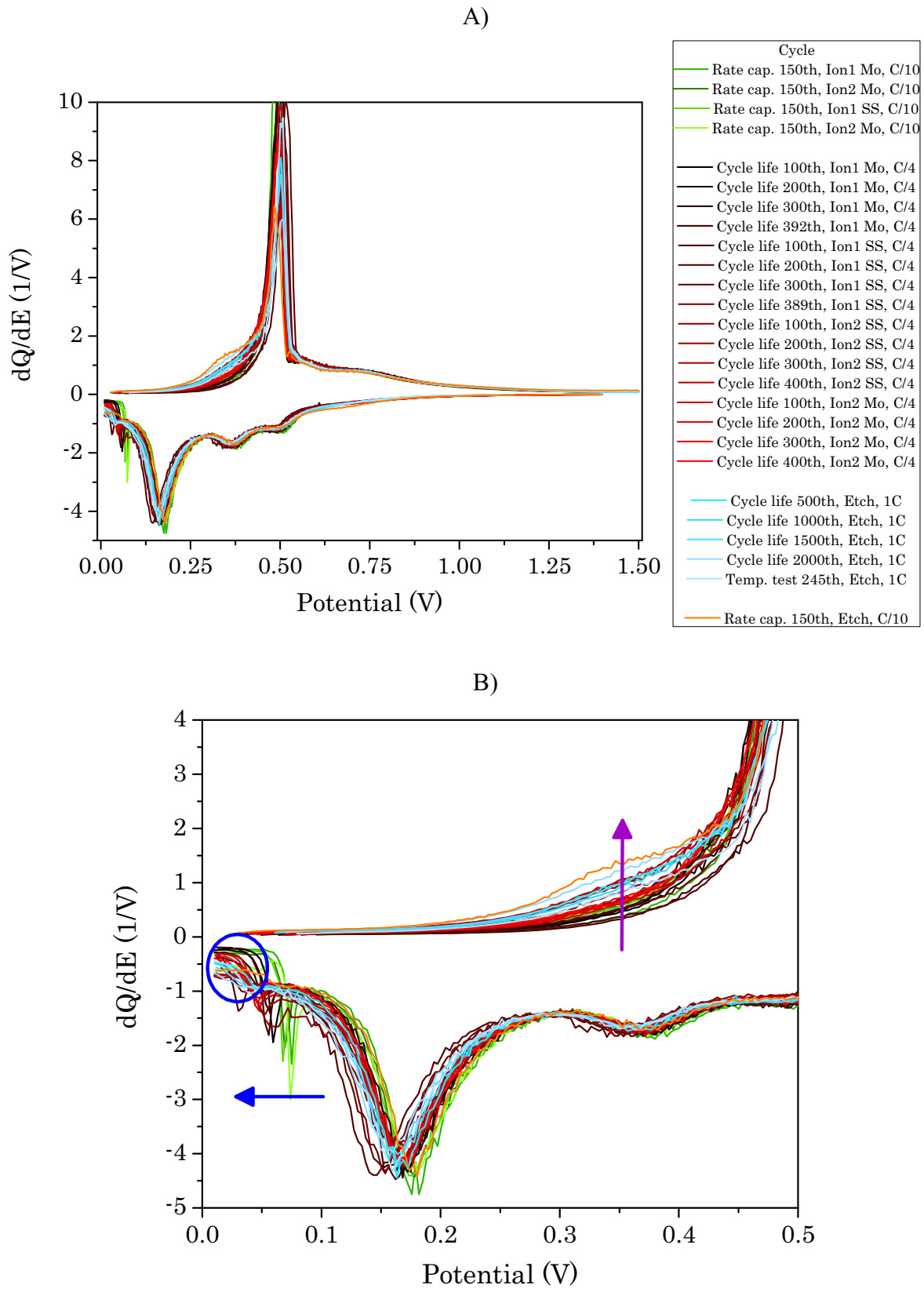

Figure 71: Comparison of the DCPs from stable cycles of different cells (A) and a magnification of its low potential part (B). The curves were normalized with respect to the charge fluxed in the corresponding cycles. The same colour meaning holds for both the graphs.

4.10. Summary and conclusions to Chapter 4

In this chapter, the electrochemical characterizations of the electrodes and some of the best results achieved so far were presented, starting from the electrochemically etched anodes, and then presenting the ion-implanted ones.

The main characterization techniques were cyclic voltammetry and galvanostatic cycles of charge and discharge.
The first was used to assess the principal features of the electrochemical reactions of the binder-free electrodes, demonstrating their independence from the substrate materials. Indeed, these can be considered as inert as they do not contribute to the overall capacity nor influence the dynamics of the electrochemical reactions between lithium and germanium. The CV curves were compared with the literature and the typical germanium and electrolyte reactions with lithium were recognized.

The importance of the nano-structuration step was also presented, as the bulk electrode showed a rapid capacity fading already in the first cycles, while the nano-structured ones performed several hundreds of cycles without degenerative trends.
Then, the choice of the standard etching recipe was explained, based on the best trade-off between high capacity and lowest fading. Etch1 was chosen thanks to its “fading-less” behaviour in these preliminary tests.
The FEC was also selected as standard additive for the electrolyte solution thanks to its beneficial effects on the overall electrode capacity and in its stabilization, with respect to VC.

Galvanostatic charge and discharge cycles for both the kinds of nano-structured electrodes have been performed to assess their cycle-life behaviours and rate capabilities. These showed very promising results, with high capacities well above that of graphite that were retained for hundreds or even thousands of cycles.
In addition, remarkable capacity retention was observed at elevated rates in both the cases. Moreover, when cycled back at low rates, all the electrodes recovered their initial capacities. Just a slightly better rate capability was observed for the ion-implanted samples, which was ascribed to their “finer” morphology. This could favour the electrode kinetics by reducing the diffusion length of lithium from the electrolyte into the active material.

All of this testifies the elevated reliability of the sample realized by means of the fabrication process presented in this thesis. This also represents an experimental evidence that the binder-free electrodes were able to reversibly accommodate the volumetric changes during the cycles, as no abrupt capacity fading were observed (apart for the bulk or the half-bulk samples) while high efficiencies were always attained.

The galvanostatic cycling of an etched sample over a wide temperature range, between -30 °C and 60 °C, was also presented, showing a remarkable capacity retention that could be particularly promising for aerospace applications.

In the whole chapter, particular attention was devoted to the electrochemical features of the lithiation and de-lithiation processes. The typical "signature" of the lithiation and de-lithiation of germanium was recognised, as suggested by the most reliable and recent literature. These features were compared for samples realized by means of the different techniques and for the various tests performed. The striking analogies found clearly demonstrate the occurrence of the same electrochemical reactions in all the cases, independently from the substrate material, the specific nano-structuration technique used or the cell testing procedure (their "history"). In other words, apart from the first few cycles in which electrolyte side reactions were identified (SEI), the electrochemical reactions can be uniquely ascribed to germanium as active material.
Finally, an interesting correlation between the precise form of the lithiation and de-lithiation curves and the electrode capability to produce the final c-$Li_{15}Ge_4$ phase was deepened, based on the literature and on comparisons between different cells and different C-rates. Although the precise final lithiation step was identified as the crystalline phase in some cases, or the amorphous one in other cases, this did not affect the overall capacity of the cells.

References

[1] E. Talaie, P. Bonnick, X. Sun, Q. Pang, X. Liang, and L. F. Nazar, "Methods and protocols for electrochemical energy storage materials research," *Chemistry of Materials*, vol. 29, no. 1. 2017, doi: 10.1021/acs.chemmater.6b02726.

[2] R. Nölle, K. Beltrop, F. Holtstiege, J. Kasnatscheew, T. Placke, and M. Winter, "A reality check and tutorial on electrochemical characterization of battery cell materials: How to choose the appropriate cell setup," *Materials Today*, vol. 32. 2020, doi:

10.1016/j.mattod.2019.07.002.
[3] B. Scrosati and J. Garche, “Lithium batteries: Status, prospects and future,” *Journal of Power Sources*, vol. 195, no. 9. 2010, doi: 10.1016/j.jpowsour.2009.11.048.
[4] Y. Jin *et al.*, “Understanding Fluoroethylene Carbonate and Vinylene Carbonate Based Electrolytes for Si Anodes in Lithium Ion Batteries with NMR Spectroscopy,” *J. Am. Chem. Soc.*, vol. 140, no. 31, 2018, doi: 10.1021/jacs.8b03408.
[5] A. M. Chockla, K. C. Klavetter, C. B. Mullins, and B. A. Korgel, “Solution-grown germanium nanowire anodes for lithium-ion batteries,” *ACS Appl. Mater. Interfaces*, vol. 4, no. 9, 2012, doi: 10.1021/am3010253.
[6] T. Kennedy, E. Mullane, H. Geaney, M. Osiak, C. O’Dwyer, and K. M. Ryan, “High-performance germanium nanowire-based lithium-ion battery anodes extending over 1000 cycles through in situ formation of a continuous porous network,” *Nano Lett.*, vol. 14, no. 2, pp. 716–723, 2014, doi: 10.1021/nl403979s.
[7] R. A. Huggins, *Advanced batteries: Materials science aspects*. 2009.
[8] M. Winter and R. J. Brodd, “What are batteries, fuel cells, and supercapacitors?,” *Chem. Rev.*, vol. 104, no. 10, 2004, doi: 10.1021/cr020730k.
[9] T. B. Reddy, *Linden’s Handbook of Batteries, Fourth Edition*, 4th ed. New York: McGraw-Hill Education, 2011.
[10] A. A. Franco, *Rechargeable Lithium Batteries: From Fundamentals to Applications*. 2015.
[11] D. A. C. Brownson, D. K. Kampouris, and C. E. Banks, “Graphene electrochemistry: Fundamental concepts through to prominent applications,” *Chem. Soc. Rev.*, vol. 41, no. 21, 2012, doi: 10.1039/c2cs35105f.
[12] A. J. Bard and L. R. Faulkner, *Electrochemical Methods: Fundamentals and Applications* . John Wiley & Sons, Inc., 2001.
[13] T. Kim *et al.*, “Applications of voltammetry in lithium ion battery research,” *Journal of Electrochemical Science and Technology*, vol. 11, no. 1. 2020, doi: 10.33961/jecst.2019.00619.
[14] J. Hao *et al.*, “A general method for high-performance Li-ion battery Ge composites electrodes from ionic liquid electrodeposition without binders or conductive agents: The cases of CNTs, RGO and PEDOT,” *Chem. Eng. J.*, vol. 346, 2018, doi: 10.1016/j.cej.2018.04.007.
[15] W. Li, X. Sun, and Y. Yu, “Si-, Ge-, Sn-Based Anode Materials for Lithium-Ion Batteries: From Structure Design to Electrochemical Performance,” *Small Methods*, vol. 1, no. 3. 2017, doi: 10.1002/smtd.201600037.
[16] Z. Hu, S. Zhang, C. Zhang, and G. Cui, “High performance germanium-based anode materials,” *Coordination Chemistry Reviews*, vol. 326. 2016, doi: 10.1016/j.ccr.2016.08.002.
[17] S. Choi *et al.*, “Mesoporous Germanium Anode Materials for Lithium-Ion Battery with Exceptional Cycling Stability in Wide Temperature Range,” *Small*, vol. 13, no. 13, 2017, doi: 10.1002/smll.201603045.
[18] J. Hao, Y. Wang, Q. Guo, J. Zhao, and Y. Li, “Structural Strategies for Germanium-Based Anode Materials to Enhance Lithium Storage,” *Particle and Particle Systems Characterization*, vol. 36, no. 9. 2019, doi: 10.1002/ppsc.201900248.
[19] S. Geier, R. Jung, K. Peters, H. A. Gasteiger, D. Fattakhova-Rohlfing, and T. F. Fässler, “A wet-chemical route for macroporous inverse opal Ge anodes for lithium ion batteries with high capacity retention,” *Sustain. Energy Fuels*, vol. 2, no. 1, 2018, doi: 10.1039/c7se00422b.
[20] L. Chen, K. Wang, X. Xie, and J. Xie, “Effect of vinylene carbonate (VC) as electrolyte additive on electrochemical performance of Si film anode for lithium ion batteries,” *J. Power Sources*, vol. 174, no. 2, 2007, doi: 10.1016/j.jpowsour.2007.06.149.
[21] M. Ulldemolins, F. Le Cras, B. Pecquenard, V. P. Phan, L. Martin, and H. Martinez, “Investigation on the part played by the solid electrolyte interphase on the electrochemical performances of the silicon electrode for lithium-ion batteries,” *J. Power Sources*, vol. 206, 2012, doi: 10.1016/j.jpowsour.2012.01.095.
[22] A. Andreoli, “Porous germanium films as anode materials for lithium ion batteries,” University of Ferrara, Ferrara, 2016.
[23] J. T. Warner, *Lithium-Ion Battery Chemistries: A Primer*. Elsevier Science, 2019.
[24] S. J. An, J. Li, C. Daniel, D. Mohanty, S. Nagpure, and D. L. Wood, “The state of

understanding of the lithium-ion-battery graphite solid electrolyte interphase (SEI) and its relationship to formation cycling," *Carbon*, vol. 105. 2016, doi: 10.1016/j.carbon.2016.04.008.

[25] H. Wu, H. Jia, C. Wang, J. G. Zhang, and W. Xu, "Recent Progress in Understanding Solid Electrolyte Interphase on Lithium Metal Anodes," *Advanced Energy Materials*, vol. 11, no. 5. 2021, doi: 10.1002/aenm.202003092.

[26] P. Verma, P. Maire, and P. Novák, "A review of the features and analyses of the solid electrolyte interphase in Li-ion batteries," *Electrochimica Acta*, vol. 55, no. 22. 2010, doi: 10.1016/j.electacta.2010.05.072.

[27] E. Peled and S. Menkin, "Review—SEI: Past, Present and Future," *J. Electrochem. Soc.*, vol. 164, no. 7, 2017, doi: 10.1149/2.1441707jes.

[28] T. Kennedy, M. Brandon, and K. M. Ryan, "Advances in the Application of Silicon and Germanium Nanowires for High-Performance Lithium-Ion Batteries," *Adv. Mater.*, vol. 28, no. 27, 2016, doi: 10.1002/adma.201503978.

[29] T. D. Bogart, A. M. Chockla, and B. A. Korgel, "High capacity lithium ion battery anodes of silicon and germanium," *Current Opinion in Chemical Engineering*, vol. 2, no. 3. 2013, doi: 10.1016/j.coche.2013.07.001.

[30] Z.-C. Wang, J. Xu, W.-H. Yao, Y.-W. Yao, and Y. Yang, "Fluoroethylene Carbonate as an Electrolyte Additive for Improving the Performance of Mesocarbon Microbead Electrode," *ECS Trans.*, vol. 41, no. 41, 2012, doi: 10.1149/1.4717960.

[31] K. Schroder *et al.*, "The Effect of Fluoroethylene Carbonate as an Additive on the Solid Electrolyte Interphase on Silicon Lithium-Ion Electrodes," *Chem. Mater.*, vol. 27, no. 16, 2015, doi: 10.1021/acs.chemmater.5b01627.

[32] K. C. Klavetter *et al.*, "A high-rate germanium-particle slurry cast Li-ion anode with high Coulombic efficiency and long cycle life," *J. Power Sources*, vol. 238, 2013, doi: 10.1016/j.jpowsour.2013.02.091.

[33] C. C. Nguyen and B. L. Lucht, "Comparative Study of Fluoroethylene Carbonate and Vinylene Carbonate for Silicon Anodes in Lithium Ion Batteries," *J. Electrochem. Soc.*, vol. 161, no. 12, 2014, doi: 10.1149/2.0731412jes.

[34] S. Fugattini, "Binder-free porous germanium anode for Li-ion batteries," University of Ferrara, Ferrara, 2018.

[35] M. Nie *et al.*, "Effect of Vinylene Carbonate and Fluoroethylene Carbonate on SEI Formation on Graphitic Anodes in Li-Ion Batteries," *J. Electrochem. Soc.*, vol. 162, no. 13, 2015, doi: 10.1149/2.0021513jes.

[36] A. L. Michan *et al.*, "Fluoroethylene carbonate and vinylene carbonate reduction: Understanding lithium-ion battery electrolyte additives and solid electrolyte interphase formation," *Chem. Mater.*, vol. 28, no. 22, 2016, doi: 10.1021/acs.chemmater.6b02282.

[37] Y. Jin *et al.*, "Identifying the Structural Basis for the Increased Stability of the Solid Electrolyte Interphase Formed on Silicon with the Additive Fluoroethylene Carbonate," *J. Am. Chem. Soc.*, vol. 139, no. 42, 2017, doi: 10.1021/jacs.7b06834.

[38] E. Markevich, G. Salitra, and D. Aurbach, "Fluoroethylene Carbonate as an Important Component for the Formation of an Effective Solid Electrolyte Interphase on Anodes and Cathodes for Advanced Li-Ion Batteries," *ACS Energy Letters*, vol. 2, no. 6. 2017, doi: 10.1021/acsenergylett.7b00163.

[39] T. P. Barrera and M. L. Wasz, "Spacecraft li-ion battery power system state-of-practice: A critical review," 2018, doi: 10.2514/6.2018-4495.

[40] V. Knap, L. K. Vestergaard, and D. I. Stroe, "A review of battery technology in cubesats and small satellite solutions," *Energies*, vol. 13, no. 15. 2020, doi: 10.3390/en13164097.

[41] U. Gulzar, "Nitrogen doped single walled carbon nanohorns for energy storage applications," University of Genova and Italian Institute of Technology, Genova, 2018.

[42] S. Goriparti *et al.*, "Facile synthesis of Ge-MWCNT nanocomposite electrodes for high capacity lithium ion batteries," *J. Mater. Chem. A*, vol. 5, no. 37, 2017, doi: 10.1039/c7ta04971d.

[43] D. McNulty, S. Biswas, S. Garvey, C. O'Dwyer, and J. D. Holmes, "Directly Grown Germanium Nanowires from Stainless Steel: High-performing Anodes for Li-Ion Batteries," *ACS Appl. Energy Mater.*, vol. 3, no. 12, pp. 11811–11819, 2020, doi: 10.1021/acsaem.0c01977.

[44] L. Baggetto and P. H. L. Notten, “Lithium-Ion (De)Insertion Reaction of Germanium Thin-Film Electrodes: An Electrochemical and In Situ XRD Study,” *J. Electrochem. Soc.*, vol. 156, no. 3, 2009, doi: 10.1149/1.3055984.

[45] U. Gulzar *et al.*, “Nitrogen-doped single walled carbon nanohorns enabling effective utilization of Ge nanocrystals for next generation lithium ion batteries,” *Electrochim. Acta*, vol. 298, 2019, doi: 10.1016/j.electacta.2018.11.130.

[46] M. A. González, A. C. Marschilok, and E. Reichmanis, “Perspective—Enhancing Active Anode Material Performance for Lithium-Ion Batteries via Manipulation of Interfacial Chemistry,” *J. Electrochem. Soc.*, vol. 167, no. 5, 2020, doi: 10.1149/1945-7111/ab6a8a.

[47] D. C. Bock, A. C. Marschilok, K. J. Takeuchi, and E. S. Takeuchi, “Deliberate modification of the solid electrolyte interphase (SEI) during lithiation of magnetite, Fe3O4: Impact on electrochemistry,” *Chem. Commun.*, vol. 53, no. 98, 2017, doi: 10.1039/c7cc07142f.

[48] E. Mullane, T. Kennedy, H. Geaney, and K. M. Ryan, “A rapid, solvent-free protocol for the synthesis of germanium nanowire lithium-ion anodes with a long cycle life and high rate capability,” *ACS Appl. Mater. Interfaces*, vol. 6, no. 21, pp. 18800–18807, 2014, doi: 10.1021/am5045168.

[49] J. Doherty *et al.*, “Germanium tin alloy nanowires as anode materials for high performance Li-ion batteries,” *Nanotechnology*, vol. 31, no. 16, 2020, doi: 10.1088/1361-6528/ab6678.

[50] D. McNulty, H. Geaney, D. Buckley, and C. O’Dwyer, “High capacity binder-free nanocrystalline GeO2 inverse opal anodes for Li-ion batteries with long cycle life and stable cell voltage,” *Nano Energy*, vol. 43, 2018, doi: 10.1016/j.nanoen.2017.11.007.

[51] K. Mishra, X. C. Liu, F. S. Ke, and X. D. Zhou, “Porous germanium enabled high areal capacity anode for lithium-ion batteries,” *Compos. Part B Eng.*, vol. 163, 2019, doi: 10.1016/j.compositesb.2018.10.076.

[52] L. Y. Lim, N. Liu, Y. Cui, and M. F. Toney, “Understanding phase transformation in crystalline Ge anodes for Li-ion batteries,” *Chem. Mater.*, vol. 26, no. 12, 2014, doi: 10.1021/cm501233k.

[53] Y. G. Cho, Y. S. Kim, D. G. Sung, M. S. Seo, and H. K. Song, “Nitrile-assistant eutectic electrolytes for cryogenic operation of lithium ion batteries at fast charges and discharges,” *Energy Environ. Sci.*, vol. 7, no. 5, 2014, doi: 10.1039/c3ee43029d.

[54] K. L. Chopra and S. K. Bahl, “Structural, electrical, and optical properties of amorphous germanium films,” *Phys. Rev. B*, vol. 1, no. 6, 1970, doi: 10.1103/PhysRevB.1.2545.

[55] S. Ma *et al.*, “Temperature effect and thermal impact in lithium-ion batteries: A review,” *Progress in Natural Science: Materials International*, vol. 28, no. 6. 2018, doi: 10.1016/j.pnsc.2018.11.002.

[56] E. J. Plichta and W. K. Behl, “Low-temperature electrolyte for lithium and lithium-ion batteries,” *J. Power Sources*, vol. 88, no. 2, 2000, doi: 10.1016/S0378-7753(00)00367-0.

[57] J. Shi *et al.*, “Improving the graphite/electrolyte interface in lithium-ion battery for fast charging and low temperature operation: Fluorosulfonyl isocyanate as electrolyte additive,” *J. Power Sources*, vol. 429, 2019, doi: 10.1016/j.jpowsour.2019.04.113.

[58] G. Zhu *et al.*, “Materials insights into low-temperature performances of lithium-ion batteries,” *Journal of Power Sources*, vol. 300. 2015, doi: 10.1016/j.jpowsour.2015.09.056.

[59] B. Laforge, L. Levan-Jodin, R. Salot, and A. Billard, “Study of Germanium as Electrode in Thin-Film Battery,” *J. Electrochem. Soc.*, vol. 155, no. 2, 2008, doi: 10.1149/1.2820666.

[60] H. Jung *et al.*, “Elucidation of the local and long-range structural changes that occur in germanium anodes in lithium-ion batteries,” *Chem. Mater.*, vol. 27, no. 3, 2015, doi: 10.1021/cm504312x.

[61] A. Al-Obeidi, D. Kramer, R. Mönig, and C. V. Thompson, “Mechanical stresses and crystallization of lithium phosphorous oxynitride-coated germanium electrodes during lithiation and delithiation,” *J. Power Sources*, vol. 306, 2016, doi: 10.1016/j.jpowsour.2015.12.057.

5. Conclusion

This thesis work demonstrated two processes to fabricate efficient and reliable germanium-based anodes for LIBs, whose electrochemical performances have been extensively characterized and whose morphological, compositional, and structural properties were thoroughly presented.

The details of the two fabrication processes, both consisting in the realization of a thin germanium film and its subsequent nano-structuration, were presented in Chapter 2.
Some basic insights of the deposition technique, the LEPECVD, and of the two nano-structuration methods, the HF etching and the Ion Implantation, were introduced.
Besides, a review of the experimental data was carried out and was found in complete agreement with the results from previous works, the theoretical models, or the literature.

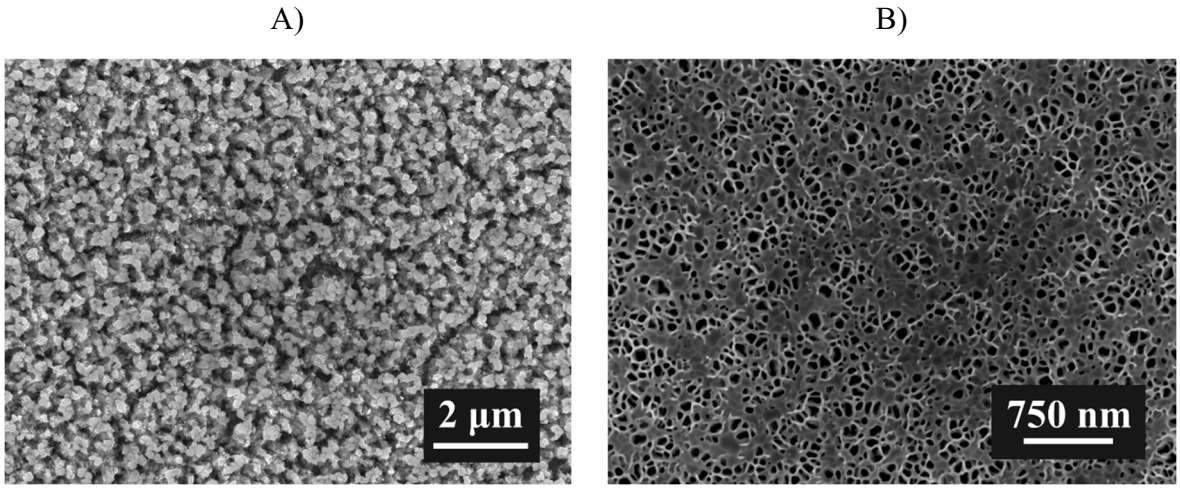

Figure 72: Representative top-view SEM images of an etched (A) and an ion implanted (B) sample.

The sample physical properties were thoroughly characterised in Chapter 3, where the analyses performed on the bare substrates, the as deposited samples and the nano-structured ones were presented. The role of the former was observed to influence only the macroscopic features of the thin films.
Structural evaluations demonstrated that the germanium layers are composed by an amorphous matrix in which germanium is locally organized into crystalline domains, for

both the sample thicknesses of 1 µm and 350 nm. The crystalline structure is not affected by the electrochemical etching, while ion implantation results in amorphization.

The compositional analysis demonstrated that highly pure germanium films were fabricated, with only some traces of contaminants from pollutants in the deposition process (mainly C, O and Si).

The sample morphology was evaluated, showing completely different features for the etched samples and the ion-implanted ones, as it can be noticed from the representative SEM images of Figure 72. The firsts have a "mountain-shaped" aspect, with irregular features. The seconds appear to be arranged in more even structures, which are compatible with the "honeycomb" structures described in the literature.

In all the cases, void spaces were produced to allow for the volumetric expansion of germanium through the cycles.

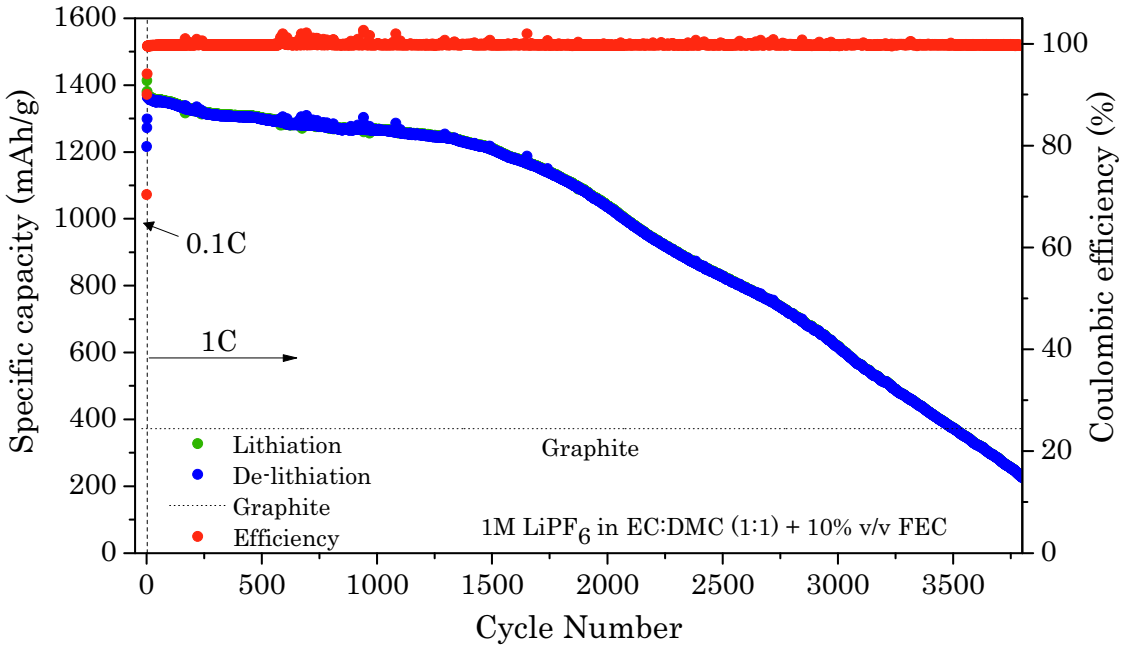

Figure 73: Cycle life performance of an etched electrode

In Chapter 4 the electrochemical characterizations of the electrodes were presented. They showed very high capacities, well above that of graphite, which were retained for hundreds or even thousands of cycles, like the sample depicted in Figure 73.

A remarkable retention at elevated rates was also observed, with a full recovery of the initial capacity when the electrodes were cycled back at low rates. These remarkable results were completely and uniquely ascribed to germanium, since the independence from the

substrate materials, the nano-structuration technique used, or the cell testing procedure was demonstrated.
Just a slightly better performance in the rate capability of the ion-implanted samples was observed, due to their "finer" morphology. The best rate capabilities of these samples are presented again here, in Figure 74.
The importance of the nano-structuration step was also presented, as well as the impact of FEC in stabilizing and enhancing the cell capacity. Furthermore, the test of an electrochemically etched electrode in a wide temperature range (-30 °C ÷ 60 °C) was presented, showing a promising retention even at very low and high temperatures.

The high capacity and the stability shown in the electrochemical tests as well as the elevated efficiencies, represent an experimental evidence that the binder-free electrodes presented in this work are able to reversibly accommodate the volumetric changes during the cycles.
Particular attention was devoted to the electrochemical features of the lithiation and de-lithiation processes, since useful insight was enabled by the lack of any interference from inert materials like binders, conductive agents, or seed-layers. The features found match well with the most recent and reliable literature regarding the lithiation and de-lithiation mechanisms of germanium.
Finally, an interesting correlation between the precise electrode behaviour and its capability to produce the final c-$Li_{15}Ge_4$ phase was deepened, with this phenomenon not affecting the overall capacity of the cells.

Thanks to the promising results observed since the first prototypes, the fabrication process consisting in the deposition and the subsequent HF dissolution led to the registration of an Italian patent (priority IT201800006103A), subsequently extended as PCT (WO2019234666A1) and actually under extension in China (CN112789748A).
The attractivity of this technology and of the process presented in this thesis, is testified by two research projects on this subject granted by the Italian Space Agency. Part of the activities of this work were carried out in the former of these projects, named ANGELS (see section 1.8). A new project, named GLITTERY (see section 1.8), started in 2021 and aims to bring the germanium-anodes technology up to a TRL 6, corresponding to system adequacy demonstrated in simulated relevant environment.

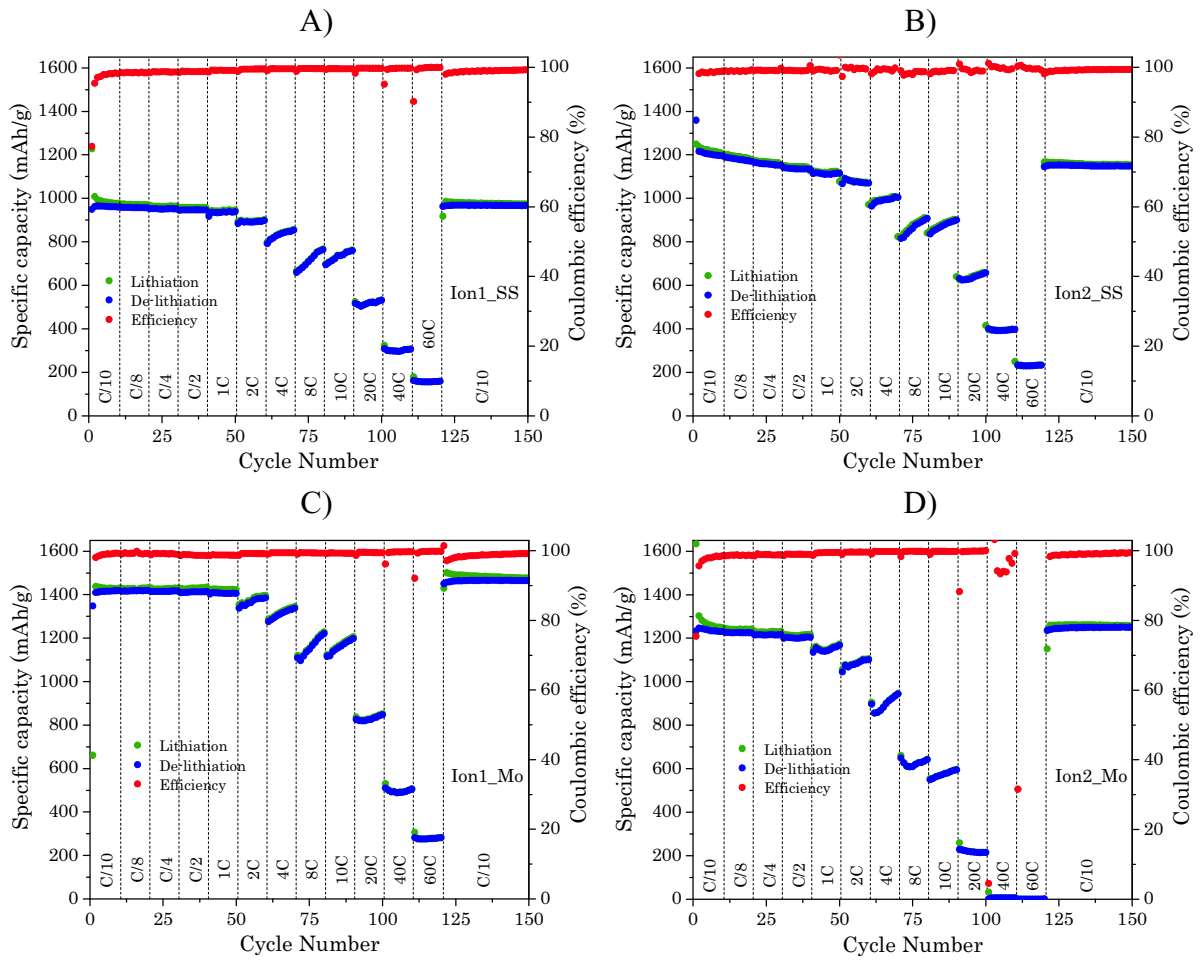

Figure 74: Rate capabilities of the ion implanted samples.